

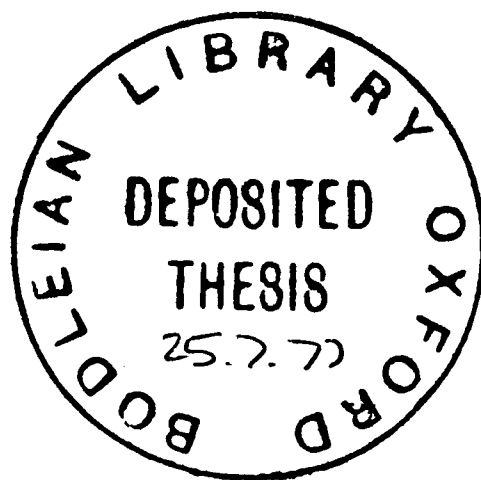
THE CHICAGO CYCLOTRON MAGNET

TO MY PARENTS

DEEP INELASTIC MUON-NUCLEON SCATTERING

Vinod Kumar Bharadwaj

Balliol College



Thesis submitted for the degree of
Doctor of Philosophy at the University of Oxford

February 1977

ABSTRACT

This thesis reports some results from an experiment using a high energy muon beam incident upon a liquid hydrogen target performed at the Fermi National Accelerator Laboratory, Illinois, USA. It is solely concerned with the inclusive muon scattering distributions. The results reported are derived from the analysis of data taken at two incident momenta, 96 GeV/c and 147 GeV/c. Values of the inelastic structure function νW_2 are presented for ω up to 1000, albeit with different Q^2 ranges at different ω . The values of R , the ratio of the longitudinal to transverse virtual photon cross-sections are extracted in a limited kinematic region, but with large errors. Overall fits are made to the data assuming R has a constant form. The Callan-Gross sum rule is evaluated using data from this experiment in conjunction with previous electron scattering experiments.

ACKNOWLEDGEMENTS

All high energy physics experiments of necessity involve the co-operation of many people and institutions and I would like first and foremost to thank everyone concerned in the construction and successful operation of this experiment.

The following people are deserving of explicit mention:-

Sir Denys Wilkinson for a place in the Oxford Nuclear Physics Department.

Bill Williams, my supervisor, for his constant interest in and encouragement for the prompt and successful completion of this thesis.

Norman Booth for his readiness to advise on and discuss any questions put to him.

Andris Skuja for patiently introducing me to the rigours of experimental setup.

Tom Quirk for masterminding the analysis of the data without which this thesis would not exist.

Luke Mo for his interest in me and my development as a physicist.

Ian Kirkbride, who was a fellow graduate student at Oxford for four years, for many and varied discussions both inside and outside of physics.

Philip Burton for contributing so much to the success of the Oxford group at Fermilab.

Bruce Gordon for proof-reading most of this thesis.

Tricia Falconer Smith for her excellent and efficient typing of this thesis.

Dorothy Carter and Elsa Mason for the speedy and skilful drawing of the figures.

Finally I would like to draw attention to the excellent and complementary facilities that the Fermilab and the computer section of the Rutherford Laboratory have allowed this experiment.

CONTENTS

Page

ABSTRACT

ACKNOWLEDGEMENTS

CHAPTER 1 EXPERIMENTAL AND THEORETICAL BACKGROUND

1.A	Introduction	1
1.B	Kinematic Variables and Cross-section Formulae	2
1.C	Experimental Status of Deep Inelastic Scattering	7
1.D	Theoretical Speculations in Deep Inelastic Scattering	11
1.E	Related Topics	13

CHAPTER 2 THE APPARATUS

2.A	Introduction	17
2.B	Muon Beam Transport	18
2.C	Beam Detection	20
2.D	The Spectrometer	22

CHAPTER 3 SET-UP AND DATA TAKING

3.A	Introduction	29
3.B	Fast Electronics	29
3.C	Gating and Event Logging	33
3.D	On-line Control and Monitoring	35
3.E	Trigger Set-up and Data Taking	38
3.F	Pion Contamination of the Muon Beam	44
3.G	The Magnetic Field of the CCM	46

CHAPTER 4	DATA ANALYSIS -I	<u>page</u>
4.A	Introduction	50
4.B	Event Reconstruction - Tape Sequencing	51
4.C	Counter Positions and Efficiencies	62
4.D	Event Reconstruction - Muon Selection and Kinematics	68
4.E	Data Reduction	76

CHAPTER 5	DATA ANALYSIS - II	
5.A	Introduction	80
5.B	Normalisation Corrections and Weighted Events	81
5.C	Radiative and Resolution Corrections	90
5.D	Results and Comments	97

APPENDIX A	SUMMARY OF THE KINEMATICS OF CHARGED LEPTON-NUCLEON SCATTERING.	
------------	--	--

REFERENCES.

DATA TABLES

LIST OF FIGURES

CHAPTER 1

- 1.1 One photon exchange
- 1.2 Kinematic region for incident energy up to 150 GeV
- 1.3 Kinematic region of the SLAC experiments
- 1.4 Illustration of the Bjorken scaling of νW_2 and $2M\nu W_1$.
- 1.5 Neutron to proton ratio for νW_2
- 1.6 Variation of R
- 1.7 Separated values νW_2 and $2M\nu W_1$
- 1.8 Vector Meson Dominance

CHAPTER 2

- 2.1 Co-ordinate system
- 2.2 Beam Transport
- 2.3 Beam triggering and tagging system
- 2.4 Size of the elements of the beam apparatus
- 2.5 Beam momentum distributions
- 2.6 Beam phase space for the 147 GeV/c data
- 2.7 The spectrometer apparatus
- 2.8 Wire chamber nomenclature
- 2.9 The downstream scintillation counter hodoscopes.
- 2.10 Central area of Muon hodoscopes

CHAPTER 3

- 3.1 A muon's view of the triggering and veto hodoscopes
- 3.2 Simplified trigger logic
- 3.3 Fast electronics
- 3.4. Counter latching and chamber firing logic

List of Figures (continued)

CHAPTER 3

- 3.5 Trigger and interrupt sequence
- 3.6 Gating Logic
- 3.7 Block diagram of the on-line program
- 3.8 Clipping of electronic pulses
- 3.9 Counter plateauing
- 3.10 Counter timing
- 3.11 G hodoscope timing
- 3.12 Pion absorption by the polythene absorber
- 3.13 Extent of the CCM magnetic field maps
- 3.14 Sketch of the measuring apparatus used to map the CCM magnetic field
- 3.15 CCM magnetic field plots
- 3.16 The geometry of a charged particle trajectory through a cylindrically symmetric magnetic field

CHAPTER 4

- 4.1 Illustration of magnetostrictive wand non-linearities
- 4.2 Linking of upstream to downstream beam track segments at the centre of the beam tagging magnets
- 4.3 Schematic example of track-finding in the Muon and 6-metre spark chambers
- 4.4 Linking of upstream tracks to downstream tracks through the CCM
- 4.5 Matching of the X-slopes of downstream tracks with those of the Muon chamber tracks.
- 4.6 Matching of the X-intercepts of downstream tracks with those of the Muon chamber tracks.
- 4.7 Scatter plot of beam events at the N-hodoscope
- 4.8 N-counter positions found using the imbedded beam triggers.

List of Figures (continued)

CHAPTER 4

- 4.9 Examples of counter positions found using the event trigger data
- 4.10 Comparison of the event data with the Monte-Carlo data to find the limits of the hole in the muon hodoscopes
- 4.11 Event vertex distribution in Z
- 4.12 Some event pictures
- 4.13 Momentum calibration for the 96 GeV/c data
- 4.14 Momentum calibration for the 147 GeV/c data
- 4.15 Raw event distribution for the 96 GeV/c data
- 4.16 Raw event distribution for the 147 GeV/c data

CHAPTER 5

- 5.1 Circles of constant ν and Q^2 at the M hodoscope for the 96 GeV/c data.
- 5.2 Circles of constant ν and Q^2 at the M hodoscope for the 147 GeV/c data.
- 5.3 : Track-finding efficiency in the beam region of the downstream spark chambers.
- 5.4 K-veto showering correction
- 5.5 Smoothed background subtraction
- 5.6 ν and Q^2 distributions of weighted events for the 96 GeV/c data.
- 5.7 ν and Q^2 distributions of weighted events for the 147 GeV/c data.
- 5.8 Radiative processes
- 5.9 Radiative Correction Triangle
- 5.10 Energy and Q^2 balance in muon-electron scatters
- 5.11 Muon inclusive cross-section, $\frac{d^2\sigma}{d\nu dq^2}$, vs. Q^2 for fixed ν .

List of Figures (continued)

CHAPTER 5

- 5.12 Muon inclusive cross-section, $\frac{d^2\sigma}{d\nu dq^2}$, vs. ν for fixed Q^2 .
- 5.13 νW_2 average over all Q^2 vs. ω for both the 96 GeV/c and 147 GeV/c datasets.
- 5.14 νW_2 vs. Q^2 for various bands of ω (96 GeV/c data).
- 5.15 νW_2 vs. Q^2 for various bands of ω (147 GeV/c data).
- 5.16 νW_2 vs. Q^2 for various bands of ω (combined data)
- 5.17 νW_2 vs. ω for various bands of Q^2 (combined data)
- 5.18 Scaling violation vs. x
- 5.19 Comparison of νW_2 with the predictions of the generalised vector meson dominance theory.
- 5.20 Total virtual photoabsorption cross-section vs. Q^2 for various bands of W^2 .
- 5.21 Total virtual photoabsorption cross-section vs. W^2 for various bands of Q^2 .
- 5.22 Total virtual photoabsorption cross-section vs. ϵ in various (W^2, Q^2) bins.

LIST OF TABLES

CHAPTER 3

- 3.1 Scaler outputs for a few typical runs
- 3.2 Scaler rates for a few typical runs
- 3.3 Trigger rates for the calculation of the pion contamination
of the muon beam
- 3.4 Grid points of the CCM field maps

CHAPTER 4

- 4.1 Some typical beam reconstruction statistics
- 4.2 Counter efficiencies
- 4.3 Data reduction statistics

CHAPTER 5

- 5.1 Values of σ_L , σ_T and R
- 5.2 Fits for R and νW_2
- 5.3 Results for the Callan-Gross sum rule

LIST OF DATA TABLES

- DT1 Geometric acceptance
- DT2 Elastic Radiative tail cross-sections, $\frac{d^2\sigma}{d\Omega dE'}$
- DT3 Inelastic radiative corrections
- DT4 Momentum smearing corrections
- DT5 Muon inclusive cross-section, $\frac{d^2\sigma}{d\nu dq^2}$ for the 96 GeV/c data
- DT6 Muon inclusive cross-section, $\frac{d^2\sigma}{d\nu dq^2}$, for the 147 GeV/c data
- DT7 Inelastic structure function, νW_2 , for the 96 GeV/c data
- DT8 Inelastic structure function, νW_2 , for the 147 GeV/c data.
- DT9 Total virtual photoabsorption cross-section for the 96 GeV/c data
- DT10 Total virtual photoabsorption cross-section for the 147 GeV/c data

CHAPTER 1

EXPERIMENTAL AND THEORETICAL BACKGROUND

1.A INTRODUCTION

This experiment uses an electromagnetically interacting beam of particles to probe the structure of matter. Past experience in the use of such beams has been extremely profitable in furthering understanding of this structure. Rutherford's use of alpha particles with energies of a few MeV led to the discovery of the existence of the nucleus within the atom. Experiments by Hofstadter⁽¹⁾ and others using electrons with energies of a few hundred MeV determined the charge and magnetic moment distributions of nuclei and nucleons. Most recently, experiments at SLAC using electrons with energies of up to 20 GeV have represented evidence for the existence of point-like constituents within the nucleon. These experiments are extensively discussed in Section 1.C.

As can be seen from these examples, the use of higher incident energies enables one to probe progressively shorter distances. In order to gain information about any structure, the de Broglie wavelength of the probing particle must be of the same order of magnitude as the size of such structures. In the above experiments one can look upon the four momentum transfer squared between the incident and target particles as a measure of the distances being probed. Naively speaking a small four momentum transfer squared corresponds to a glancing blow and will give information only on the overall shape of the object being examined, whereas large values of the four momentum transfer squared correspond to much more violent collision and will give information as to the internal structure of the target.

Figure 1.1 represents the lowest order Feynman diagram for the charged lepton-nucleon reaction $\ell^\pm + N \rightarrow \ell^\pm + \text{"anything"}$ - this is also called the one-photon exchange diagram. The major advantage of this reaction over hadron-nucleon reactions in the study of nucleon structure is that the electromagnetic vertex is well understood from QED and thus the photon-nucleon vertex may be explicitly studied. Two assumptions are made when discussing charged lepton-nucleon scattering. Firstly, one photon exchange is believed to be the dominant process and secondly, muon-electron universality is assumed to hold. A statement of the latter is that there is no difference between the $e\bar{e}\gamma$ and $\mu\bar{\mu}\gamma$ vertices apart from very small effects arising from the difference in mass between the electron and muon. The basis for these assumptions is briefly examined in Section 1.E. In subsequent discussions one photon exchange is considered to be the only process in μ -N and e-N scattering and electrons and muons are considered to be completely equivalent sources of virtual photons.

This chapter reviews various aspects of charged lepton-nucleon scattering. Section 1.B lists the variables and formulae conventionally used. The current status of experiment and theory is briefly reviewed in Section 1.C and 1.D respectively. Lastly, Section 1.E looks at various related topics.

1.B KINEMATIC VARIABLES AND CROSS-SECTION FORMULAE

Variables - Referring to Figure 1.1, it is seen that for the charged lepton, the kinematic quantities experimentally measured are essentially p and p' , its initial and final four-momenta. From these it is conventional and convenient to construct and use the following variables when discussing the lepton scattering distributions.

The square of the four-momentum transferred from the lepton to the nucleon, q^2 , is defined as

$$q^2 = (p - p')^2 = -2(EE' - \vec{p} \cdot \vec{p}' - m_\ell^2) \\ = -4EE' \sin^2(\theta/2) \text{ in the limit } E, E' \gg m_\ell -$$

where E, \vec{p} are the energy and three-momentum of the incident muon,

E', \vec{p}' are the energy and three-momentum of the scattered muon,

θ is the angle of scatter - i.e. angle between \vec{p} and \vec{p}'

m_ℓ is the mass of the lepton.

For the reaction being considered, q^2 is always a negative quantity - i.e. q is a space-like four vector - and for ease of discussion the quantity $Q^2 = -q^2$ is used. It is seen that q is the four momentum of the exchanged virtual photon, so that q^2 may be thought of as the mass of an off mass-shell photon. For a given E and E' , it is apparent that Q^2 is a minimum for $\theta = 0$, i.e.

$$Q_{\min}^2 = 2(EE' - |\vec{p}| |\vec{p}'| - m_\ell^2) \\ \frac{m_\ell^2 (E-E')^2}{EE'} \text{ in the limit where terms of order higher than } \frac{m_\ell^2}{E^2} \text{ are ignored. Taking an extreme case, for a muon with } E = 150 \text{ GeV and } E' = 10 \text{ GeV, } Q_{\min}^2 = 0.11 \text{ (GeV/c)}^2.$$

The laboratory energy loss of the lepton and consequently the energy of the virtual photon is

$$\nu = E_{\text{lab}} - E'_{\text{lab}}$$

It is easy to show that ν is equal to the Lorentz invariant $\frac{P \cdot q}{M}$

where P is the four-momentum of the target nucleon and M is its mass.

The centre of mass energy of the hadronic system, W , is also of interest. It is seen that

$$W^2 = (q + P)^2 = M^2 + 2M\nu - Q^2$$

The quantities ω , x , ω' , x' are defined as follows:

$$\omega = \frac{2M\nu}{Q^2} \quad ; \quad x = \frac{1}{\omega}$$

$$\omega' = 1 + \frac{W^2}{Q^2} \quad ; \quad x' = \frac{1}{\omega'}$$

These are called "scaling variables" and their usefulness will become apparent in Sections 1.C and 1.D.

The quantity $y = \frac{\nu}{E}$ is sometimes used.

Finally the quantity $K = \frac{W^2 - M^2}{2M}$ is defined. This is known as the "equivalent photon energy" and corresponds to the energy of a real photon that produces the same final state - i.e. same W^2 - as a virtual photon of energy ν .

Figure 1.2 shows the kinematic plane in (ν, Q^2) for E up to 150 GeV. Elastic scattering is given by $Q^2 = 2M\nu$ and resonances lie in the region $W^2 < 4 \text{ (GeV)}^2$. The real photoproduction limit is obviously at $Q^2 = 0$. The region with $W^2 > 4 \text{ (GeV)}^2$ and $Q^2 > 1 \text{ (GeV/c)}^2$ is traditionally known as the "deep inelastic scattering" region.

Elastic Scattering - The differential cross-section for the process $\ell^\pm + N \rightarrow \ell^\pm + N$ may be written, assuming that the lepton mass is negligible, as⁽²⁾

$$\frac{d\sigma}{dq^2} = \frac{4\pi\alpha^2}{Q^4(S - M^2)^2} \left[\frac{Q^4}{2} G_M^2 + \frac{\left(G_E^2 + \frac{Q^2}{4M^2} G_M^2 \right)}{1 + \frac{Q^2}{4M^2}} ((S - M^2)^2 - Q^2 W^2) \right] \quad \begin{array}{l} S = \text{centre of mass} \\ \text{energy squared of} \\ \text{muon - proton system.} \end{array}$$

This is the Rosenbluth formula and $G_E(Q^2)$ and $G_M(Q^2)$ are called the electric and magnetic elastic form factors of the nucleon.

Inelastic Scattering - The differential cross-section for the inelastic scattering of muons of incident energy E to a final energy E' through an angle θ is given by⁽³⁾

$$\frac{d^2\sigma}{d\nu dq^2} = \frac{\pi}{|\vec{p}| |\vec{p}'|} \frac{2\alpha^2}{Q^4} \left| \frac{\vec{p}'}{\vec{p}} \right| \left[\left(2EE' - \frac{Q^2}{2} \right) W_2(Q^2, \nu) + (Q^2 - 2m_\ell^2) W_1(Q^2, \nu) \right]$$

This may also be written, so as to show angular dependences more explicitly, as

$$\frac{d^2\sigma}{d\Omega dE'} = \sigma_{\text{Mott}} [W_2(Q^2, \nu) + 2 \tan^2(\frac{\theta}{2}) W_1(Q^2, \nu)]$$

where $\sigma_{\text{Mott}} = \frac{\alpha^2}{4E^2} \frac{\cos^2(\theta/2)}{\sin^4(\theta/2)}$, the form of the scattering between a spin $\frac{1}{2}$ charged point particle incident on a spinless charged point particle.

The functions $W_1(Q^2, \nu)$ and $W_2(Q^2, \nu)$ are called the inelastic structure functions of the nucleon and contain information about the inelastic virtual photon-nucleon vertex.

Virtual Photon Cross-sections - A physically more direct formulation of the differential cross-section formulae, completely equivalent to that using the structure functions $W_1(Q^2, \nu)$ and $W_2(Q^2, \nu)$, was devised by Hand^(4,5). In this description the cross-section is separated into a part, $\sigma_T(Q^2, \nu)$ which is the absorption cross-section for transverse virtual photons and a part $\sigma_L(Q^2, \nu)$ which is the absorption cross-section for longitudinal virtual photons, i.e.

$$\frac{d^2\sigma}{d\nu dq^2} = \Gamma(E, E', \theta) \left[\sigma_T(Q^2, \nu) + (\epsilon + \delta) \sigma_L(Q^2, \nu) \right]$$

where $\Gamma(E, E', \theta)$ is the flux of transverse virtual photons, ϵ is the ratio of the longitudinal virtual photon flux to the transverse virtual photon flux and δ is a very small kinematic factor that arises from the finite mass of the lepton. Explicitly, Γ , ϵ and δ are given by

$$\Gamma(E, E', \theta) = \frac{\alpha}{2\pi^2} \frac{K}{Q^2} \frac{E'}{E} \frac{1}{1-\epsilon} \frac{\pi}{EE'},$$

$$\epsilon = \frac{1}{\left(1 + \frac{2(Q^2 + v^2) \tan^2(\theta/2)}{Q^2 \left(1 - \frac{Q_{\min}^2}{Q^2}\right)^2}\right)}$$

$$\text{and } \delta = \frac{2m_l^2(1-\epsilon)}{Q^2}$$

A word about the factor K is appropriate at this point. Its choice is arbitrary so long as it reduces to the correct form as $Q^2 \rightarrow 0$ - i.e. for real photons K must equal v . The above definition of K is that of Hand. Because of this arbitrary definition of K the virtual photo-absorption cross-sections $\sigma_T(Q^2, v)$ and $\sigma_L(Q^2, v)$ are also arbitrary quantities.

Comparing the two forms of the differential cross-sections, it is seen that W_1 , W_2 , σ_T , σ_L are related by

$$W_1(Q^2, v) = \frac{K}{4\pi^2\alpha} \sigma_T(Q^2, v)$$

$$W_2(Q^2, v) = \frac{K}{4\pi^2\alpha} \frac{Q^2}{Q^2 + v^2} (\sigma_T(Q^2, v) + \sigma_L(Q^2, v))$$

Finally one defines the quantity

$$R(Q^2, v) = \frac{\sigma_L(Q^2, v)}{\sigma_T(Q^2, v)} \quad \text{obviously named the ratio of the}$$

longitudinal to transverse virtual photon cross-sections. It may be noted that the definition of $R(Q^2, v)$ does not depend on the arbitrary factor K .

The above kinematic variables, cross-section formulae and other relevant information are summarized in

Appendix A.

1.C EXPERIMENTAL STATUS OF DEEP INELASTIC SCATTERING

This section concerns itself with the current status of muon-nucleon and electron-nucleon scattering data⁽⁶⁻¹⁸⁾ and the next section mentions a few of the theoretical ideas⁽¹⁹⁻³⁴⁾ generated by and motivating such scattering experiments. More complete compilations of this information may be found in review talks⁽³⁵⁻⁴¹⁾ given at various International Conferences in the past few years. One can comment that the most extensive experimental data comes from experiments using the electron beam at SLAC.

Elastic Scattering - Before discussing the behaviour of the inelastic structure functions and differential cross-sections, it is instructive to look at the Q^2 dependence of the elastic scattering cross-section. Experimentally^(6,7,37) it is found that the elastic form factors have a Q^2 dependence given by

$$G_E^{\bar{p}}(Q^2) = \frac{G_M^p(Q^2)}{\mu_p} = \frac{G_M^n(Q^2)}{\mu_n} = \frac{1}{(1 + Q^2/0.71)^2}$$

and

$$G_E^n(Q^2) \lesssim 0.1 G_E^p(Q^2)$$

where the p, n superscript refer to the proton or neutron, μ_p and μ_n are the static proton and neutron magnetic moments, and Q^2 is expressed in $(\text{GeV}/c)^2$.

For the proton, the cross-section in the limit of $s \gg M^2$ and $s \gg Q^2$ simplifies to

$$\frac{d\sigma}{dq^2} = \frac{4\pi\alpha^2}{Q^4} \left[\frac{1 + \mu_p Q^2/4M^2}{1 + Q^2/4M^2} \right] \left[\frac{1}{(1 + Q^2/0.71)^4} \right]$$

For large Q^2 this further simplifies and the elastic cross-section falls as $(Q^2)^{-6}$ where a factor $1/Q^4$ comes from the Mott cross-section - i.e. the scattering cross-section between two charged point particles - and a factor $1/Q^8$ comes from the square of the elastic form

factors. Furthermore, it is found that the resonance cross-sections in the virtual-photon/nucleon system fall at least as rapidly as a function of Q^2 .

Inelastic Structure Functions - A large body of data exists for the measurement of $W_1(Q^2, \nu)$ and $W_2(Q^2, \nu)$ for both the proton and neutron - the data for the latter being derived from experiments using deuterium targets. The series of experiments conducted at SLAC - by a SLAC-MIT group⁽⁸⁻¹⁴⁾ and the SLAC group A^(15,16) - provide the most comprehensive base for discussion of inelastic charged lepton-nucleon scattering. The kinematic region covered by these experiments is indicated in Figure 1.3. The inelastic structure functions $W_1(Q^2, \nu)$ and $W_2(Q^2, \nu)$ may be written as

$$W_1(Q^2, \nu) = \frac{\sigma_{\text{experimental}}}{\sigma_{\text{Mott}}} \left[\left((1 + R) \frac{Q^2}{Q^2 + \nu^2} \right) + 2 \tan^2 \frac{\theta}{2} \right]^{-1}$$

$$W_2(Q^2, \nu) = \frac{\sigma_{\text{experimental}}}{\sigma_{\text{Mott}}} \left[1 + 2 \left(\frac{1}{1+R} \right) \frac{Q^2 + \nu^2}{Q^2} \tan^2 \frac{\theta}{2} \right]^{-1}$$

In the SLAC kinematic region the value of R is found to lie between 0.0-0.5 and in this range W_1 and W_2 are only weakly dependent on its exact value. Figures 1.4⁽¹¹⁾ show plots of the values of νW_2 and $2MW_1$ for the proton extracted from the SLAC data. Figure 1.5⁽³⁹⁾ shows a plot of the ratio of νW_2 for the neutron to νW_2 for the proton. In all these plots R is assumed to be 0.18. It is immediately apparent that the Q^2 dependence of the structure functions is nowhere near a $1/Q^8$ fall-off as it is for the square of the elastic form factors and that at high Q^2 values, the inelastic cross-section will be much larger than the elastic and resonance contributions to the total cross-section.

Scaling - Bjorken⁽²²⁾ predicted that in the limit of $\nu \rightarrow \infty$ and $Q^2 \rightarrow \infty$ but keeping $\omega = 2M\nu/Q^2$ fixed, the structure functions $2MW_1$ and νW_2 would depend only on this variable ω , i.e.

$$\begin{array}{ccc} \nu W_2(Q^2, \nu) & \xrightarrow{\substack{Q^2 \rightarrow \infty \\ \nu \rightarrow \infty \\ \omega \text{ fixed}}} & F_2(\omega) \quad ; \quad 2MW_1(Q^2, \nu) \xrightarrow{\substack{Q^2 \rightarrow \infty \\ \nu \rightarrow \infty \\ \omega \text{ fixed}}} F_1(\omega) \end{array}$$

This behaviour is termed "scaling". Looking at Figures 1.4 and 1.5, it is obvious that to first order the functions $2MW_1$ and νW_2 do scale. One may comment also that this Bjorken scaling occurs at remarkably non-infinite values of ν and Q^2 . Scaling variables other than ω have been devised and used - i.e. ω' , and some others listed in Ref.⁽¹¹⁾. These all approach ω in the asymptotic - i.e. ω fixed, $\nu \rightarrow \infty$ and $Q^2 \rightarrow \infty$ - limit and improve the scaling behaviour in overall and/or specific kinematic regions. The gross features of scaling in the various scaling variables however are similar to scaling in the variable ω . From the time that scaling was first observed and mentioned⁽³⁵⁾, activity in the deep inelastic - i.e. scaling - kinematic region has been focussed experimentally in the exactness of the scaling relations and in the form of any scaling violations and theoretically in deducing models that predict the gross scaling behaviour and its violations.

Virtual Photo-absorption Cross-section and R. - The SLAC-MIT electron scattering experiments were carried out at different energies incident on the target. For a given ν , Q^2 - or indeed any other pair of kinematic variables, such as W^2 , Q^2 - the ratio of the longitudinal to transverse virtual photon fluxes, ϵ , depends on this incident energy. If the quantity $\frac{d^2\sigma}{d\nu dq^2} / \Gamma(E, E', \theta)$ for the various values of E at fixed ν , Q^2 is plotted against ϵ , the graph should be a straight line whose slope is $\sigma_L(Q^2, \nu)$ and whose intercept at $\epsilon = 0$ is $\sigma_T(Q^2, \nu)$.

From the virtual photoabsorption cross-sections so generated, it is trivial to construct the value of R at the ν, Q^2 point being considered. For the SLAC-MIT data this was done for 75 points on the W^2, Q^2 kinematic plane - these points define the separation region shown in Figure 1.3. Figure 1.6⁽⁴⁰⁾ gives the results for R for the proton and the deuteron. Analysis of these results show that R proton is consistent with having a constant value, i.e.

$$R_{\text{proton}} = 0.14 \pm 0.011 \text{ statistical} \\ \pm 0.056 \text{ systematic}$$

It is also found that R is consistent with a $1/Q^2$ or a $1/\log(Q^2)$ behaviour. A full description of the extraction of R and its possible functional forms is given in Ref.⁽¹⁴⁾. Results for the deuterium data from the SLAC-MIT collaboration indicate that $R_{\text{proton}} = R_{\text{deuteron}}$ and so by implication that $R_{\text{proton}} = R_{\text{neutron}}$.

Separated Structure Functions and Scaling Violations - Having

obtained a value of R at any kinematic point, it may be used to calculate the structure functions W_1 and W_2 . Figure 1.7⁽⁴⁰⁾ shows some plots of νW_2 and $2MW_1$ for both the proton and the deuteron. It is clearly seen that these exhibit a Q^2 dependence at constant x and hence violate exact scaling. Scale violating effects in the SLAC data are parameterized and extensively discussed by Taylor⁽⁴⁰⁾.

In addition scaling violations have been observed in an experiment using high energy muons⁽¹⁷⁾. A brief summary of scale violating effects would say that:

- (a) the maximum scaling violations are less than 30%,
- (b) the SLAC data shows that the use of the scaling variable x' , instead of x , gives better fits to data. In x' , the structure functions decrease by approximately 1% per $(\text{GeV}/c)^2$ rise in Q^2 .

- (c) the muon data does not disagree with the SLAC data and also tends to indicate that νW_2 rises with Q^2 for values of $x < 0.2$.
- (d) looking at the deuterium data, the neutron appears to break scaling differently from the proton.

1.D THEORETICAL SPECULATIONS IN DEEP INELASTIC SCATTERING

This section will give a brief and by no means complete list of various theoretical ideas concerning deep inelastic scattering. A more complete review is given by Llewellyn-Smith⁽⁴¹⁾.

Vector Meson Dominance - When the scaling phenomenon was first discovered, two theories were immediately put forward, the vector meson dominance model and the various parton models. The vector meson dominance model⁽²⁹⁾, see Figure 1.8, of the virtual photon - nucleon interactions says that the virtual photon couples to vector mesons - such as ρ , ω , ϕ - which then interact strongly with the nucleon. The simplest version of this model, using just the ρ , ω and ϕ vector mesons is not very good at explaining the data. To follow completely all the trends of the data, the vector dominance picture has to be generalised to such an extent that the model loses most of its predictive power.

Parton Models - All parton models start off with the assumption that the nucleon is made up of point-like constituents called "partons". These are assumed to have definite masses and internal quantum

numbers and are held together by forces that are at least as strong as the strong force.

The quark model⁽¹⁹⁾ is a simple model that explains the spectroscopy of the hadron multiplets. Another example of a parton model was proposed by Kuti and Weisskopf⁽²⁸⁾ in which the nucleon consists of three valence quarks and a sea of quark-antiquark pairs. In parton models, the crucial assumption on which scattering calculations are based is that in the limit of $\nu \rightarrow \infty$ and $Q^2 \rightarrow \infty$, the virtual photon interacts with only one of the partons which during the time scale of the interaction is effectively free. Parton models lead directly to Bjorken scaling and the scaling variable x is identified with the fraction of the nucleon momentum carried by the interacting parton. The structure functions are related to probability distributions of the constituent partons in x . The value of R is related to the spins of the partons. Spin $\frac{1}{2}$ constituents give a value of $R = 0$ and for spin 1 constituents $R = \infty$. The experimental value of R indicates a predominance of spin $\frac{1}{2}$ objects in the nucleon.

So far there is no experimental evidence for unbound parton states and quark confinement models⁽³⁰⁾ have been devised. Various renormalisable field theories attempt to explain both the experimental non-observation of free partons and their small couplings - zero for asymptotically free theories - in the Bjorken limit. In these it is argued that the strength of the parton-parton coupling increases with their separation.

Sum Rules - It is possible to write down relations for various integrals of the structure functions $F_1(x) = 2M\nu W_1$ and $F_2(x) = \nu W_2$ without knowing theoretically the exact form of these functions. These

relations are known as "sum rules". Specifically two such sum rules may be mentioned.

(a) Callan-Gross⁽²¹⁾ Sum Rule

$$\int_0^1 dx F_2(x) = \sum_N \left[\frac{P(N) \sum_{i=1}^N Q_i^2}{N} \right]$$

(b) Gottfried⁽²⁰⁾ Sum Rule

$$\int_0^1 \frac{dx F_2(x)}{x} = \sum_N \left[P(N) \sum_{i=1}^N Q_i^2 \right]$$

where $P(N)$ is the probability of finding N quarks in the nucleon and the Q_i 's are the individual quark charges.

It is seen that (a) corresponds the mean of the squares of the parton charges and (b) corresponds the sum of the squares of the parton charges. These sum rules may be used to experimentally check the various parton models.

Other Theoretical Ideas - Some authors have attempted to use duality⁽²⁵⁾ and Regge exchange ideas⁽²⁶⁾ to explain the deep inelastic scattering data.

1.E RELATED TOPICS

This section contains a brief list of some related and complementary areas of research. Much more detailed information may be found in review talks given at the 1975 SLAC Conference⁽⁴²⁾.

One Photon Exchange - In charged lepton-nucleon scattering it is assumed that the one photon exchange mechanism - see Figure 1.1 - is the dominant process. Estimates of the contribution of two-photon exchange to the cross-sections are made by comparing ℓ^+N scattering data with ℓ^-N data - the interference term between 1γ exchange and 2γ exchange changes sign in going from an ℓ^+ incident beam to an ℓ^- incident beam. For electrons at SLAC e^+p and e^-p are equal to within 2%⁽⁴³⁾. Comparisons of μ^+N data to μ^-N data at Fermilab⁽¹⁷⁾ indicates that the two photon mechanism contributes less than a few percent to the cross-section.

Muon-Electron Universality - A large number of experiments have been done scattering muons off nucleons. Using incident muon energies similar to that of the SLAC electron beam, both elastic⁽⁴⁴⁾ and inelastic⁽⁴⁵⁾ scattering was investigated. Although in principle these experiments also yielded the elastic form factors and inelastic structure functions for the nucleon, the prime objectives were to look for differences between the muon data and the electron data. Another method of looking for breakdowns of muon-electron universality is to determine the $(g-2)$ for the muons⁽⁴⁶⁾.

These experiments conclude that there is no significant breakdown of muon-electron universality for $Q^2 < 3(\text{GeV}/c)^2$ in elastic scattering and $Q^2 < 5(\text{GeV}/c)^2$ in inelastic scattering.

Virtual Photoproduction - Another useful area of research is to study the hadrons produced in the virtual photoproduction process. One may comment that the experiment described in the thesis was also designed to detect and measure the hadrons produced in deep inelastic muon-

nucleon scattering and some data has been published^(18,47). In addition extrapolation of the data for $\sigma_T(Q^2, \nu)$ to $Q^2 = 0$ will generate measurements of the real photoproduction cross-sections.

Polarised Deep Inelastic Scattering - Inelastically scattering a polarised lepton beam off a polarised target introduces two extra structure functions into the differential cross-section formula⁽⁴⁸⁾. Experiments using a polarised electron source at SLAC are proceeding and some preliminary data has been published⁽⁴⁹⁾.

Neutrino Scattering - Inelastic νN scattering cross-sections can be described using three structure functions. These may be related to the inelastic charged lepton-nucleon scattering structure functions⁽³²⁾ in parton models of the nucleus.

Background Processes - The reaction this experiment is interested in is $\mu^+ + N \rightarrow \mu^+ + \text{hadrons}$. There are two additional processes seen in the apparatus which constitute major sources of background events.

The first of these is elastic muon-electron scattering - i.e. $\mu^+ + e^- \rightarrow \mu^+ + e^-$. For this process $Q^2 = 2 M_e \nu$ and the differential cross-section may be written as

$$\frac{d\sigma}{dq^2} = \frac{4\pi\alpha^2}{Q^4} \frac{E}{|\vec{P}|} \left[1 - \frac{|\vec{P}|^2}{E^2} \frac{\nu}{\nu_{\max}} + \frac{\nu^2}{2E^2} \right]$$

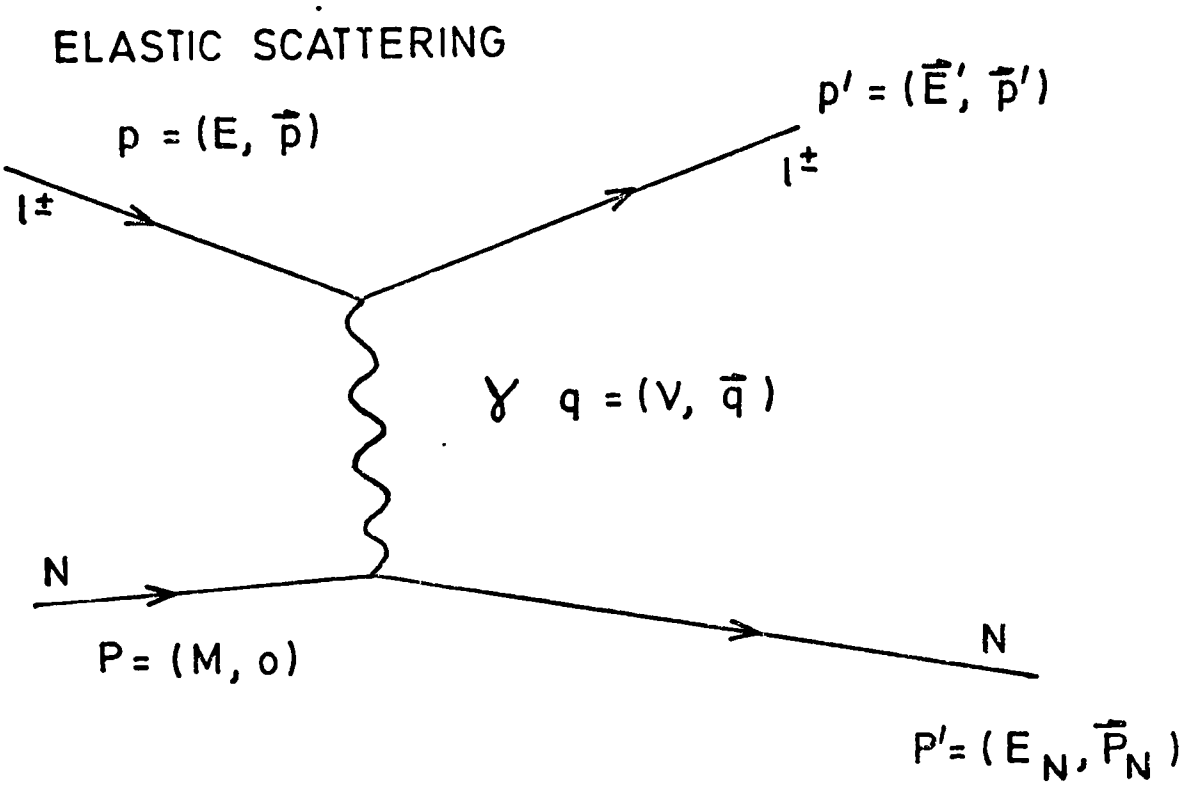
where $\nu_{\max} = \frac{2m_e |\vec{P}|^2}{2m_e E + M_\mu^2 + M_e^2}$ is the maximum

kinematically allowed muon energy loss, E and P are the incident muon energy and three momentum, and m_e , m_μ are the electron and muon masses.

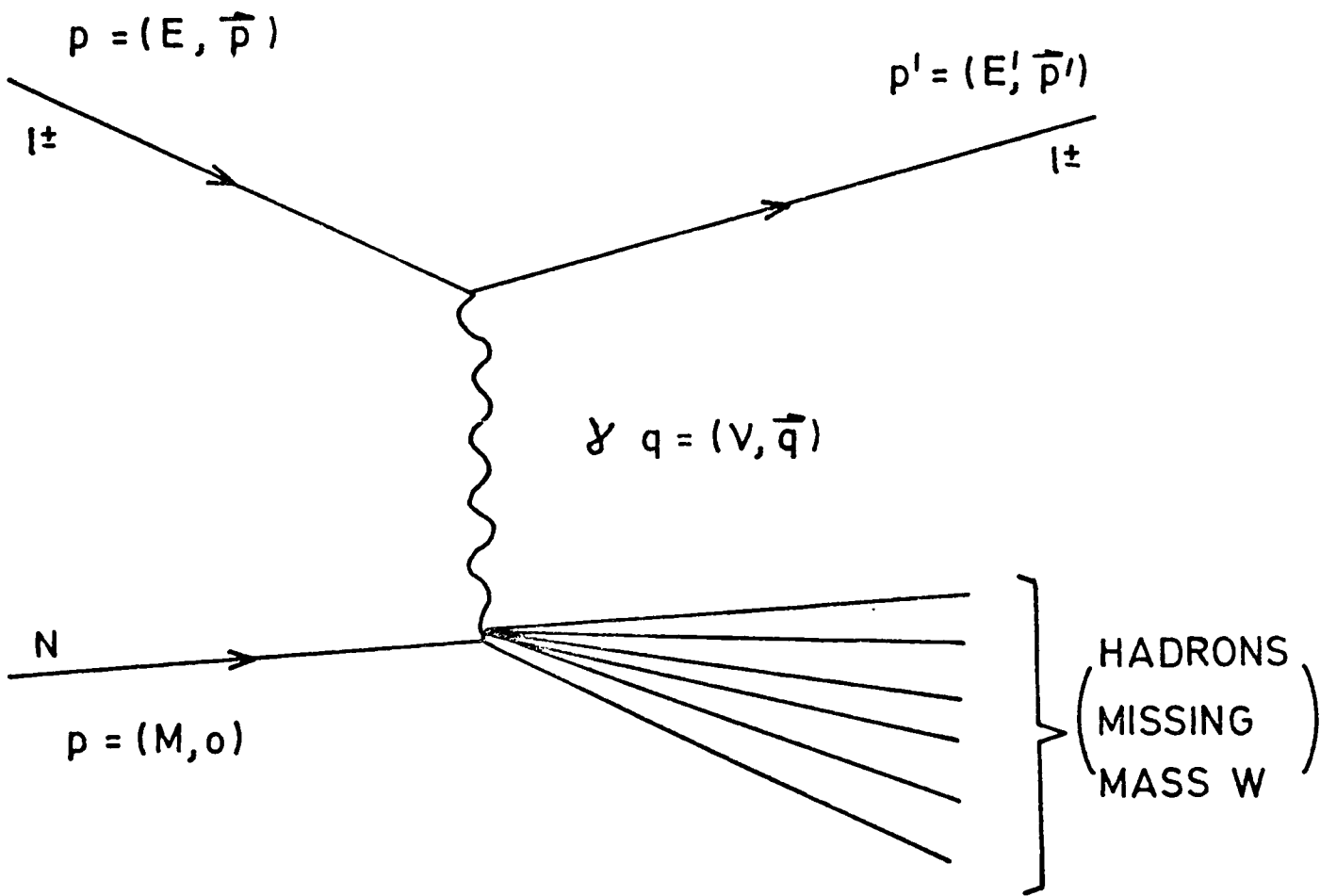
The cross-section integrated over the apparatus acceptance is large - the number of muon electron scatters seen by the apparatus is several times larger than the number of $Q^2 > 0.2 \text{ (GeV/c)}^2$ inelastic muon-nucleon scatters.

The second source of background events is loosely termed bremsstrahlung. In this case the muon loses energy by radiating a real photon in the presence of nuclear charges. The unfolding of radiative effects from the data is more fully discussed in Section 5.C under "Radiative Corrections".

FIG. 1-1 ONE PHOTON EXCHANGE



INELASTIC SCATTERING



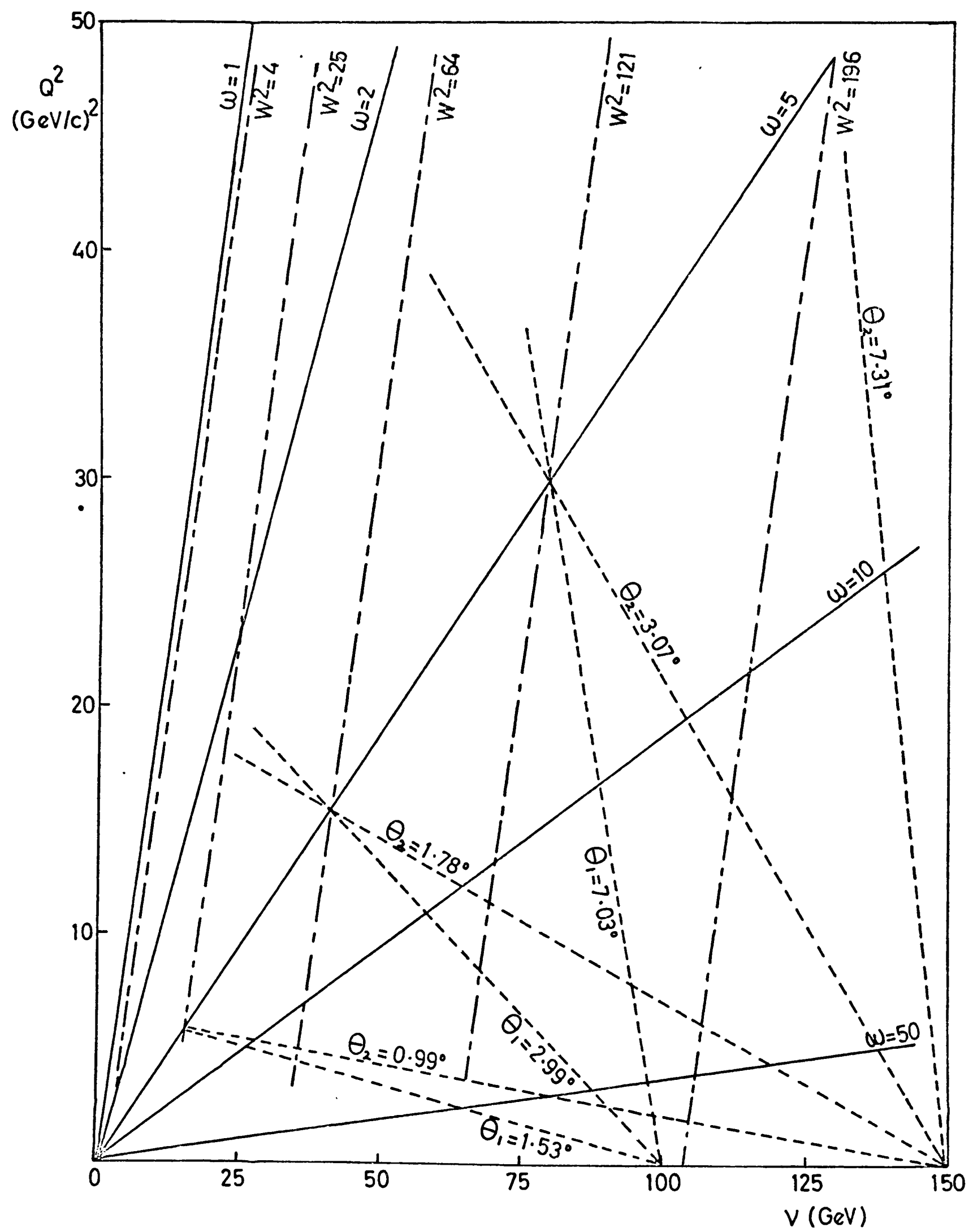
l^\pm CHARGED LEPTON

γ VIRTUAL PHOTON

N NUCLEON

SEE APPENDIX A FOR DEFINITION OF THE VARIABLES

FIG.1-2
 KINEMATIC REGION FOR INCIDENT ENERGY UP TO 150 GeV.

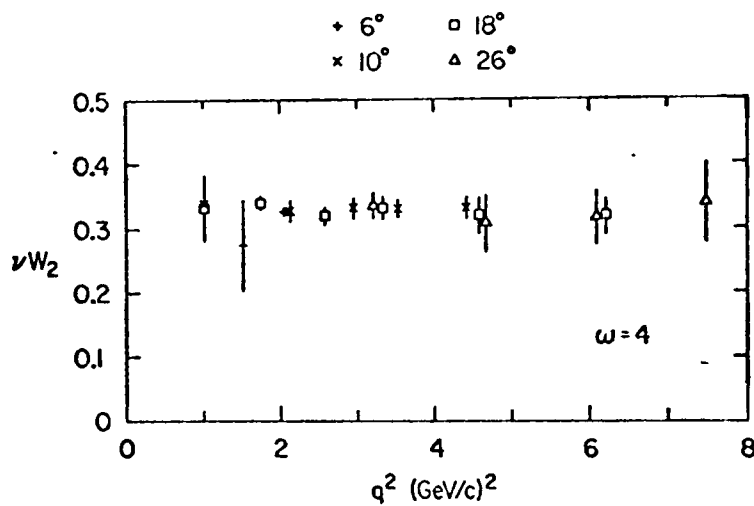
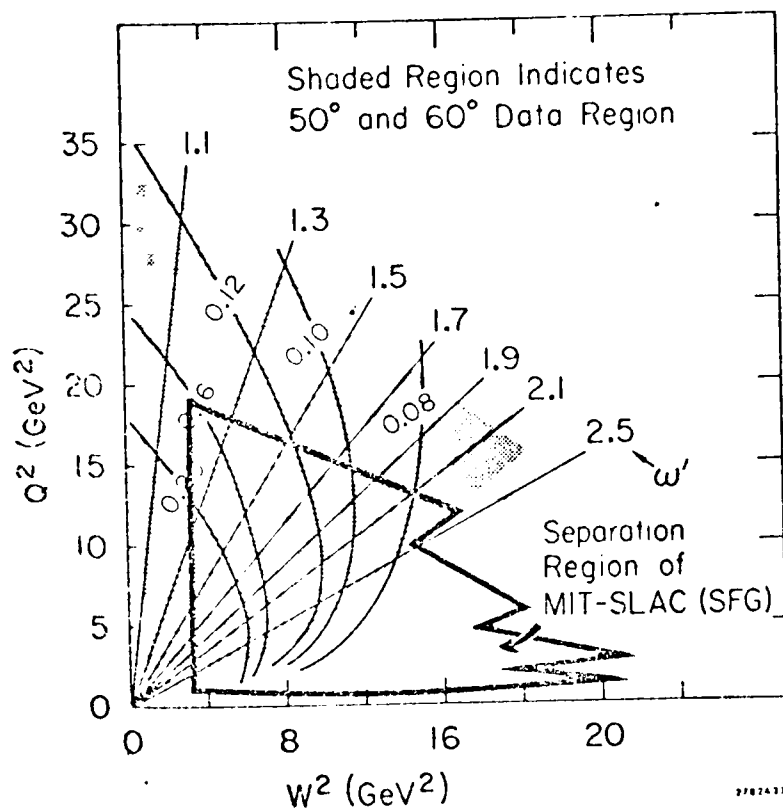


θ_1 = SCATTERING ANGLE FOR
 100 GeV INCIDENT BEAM.

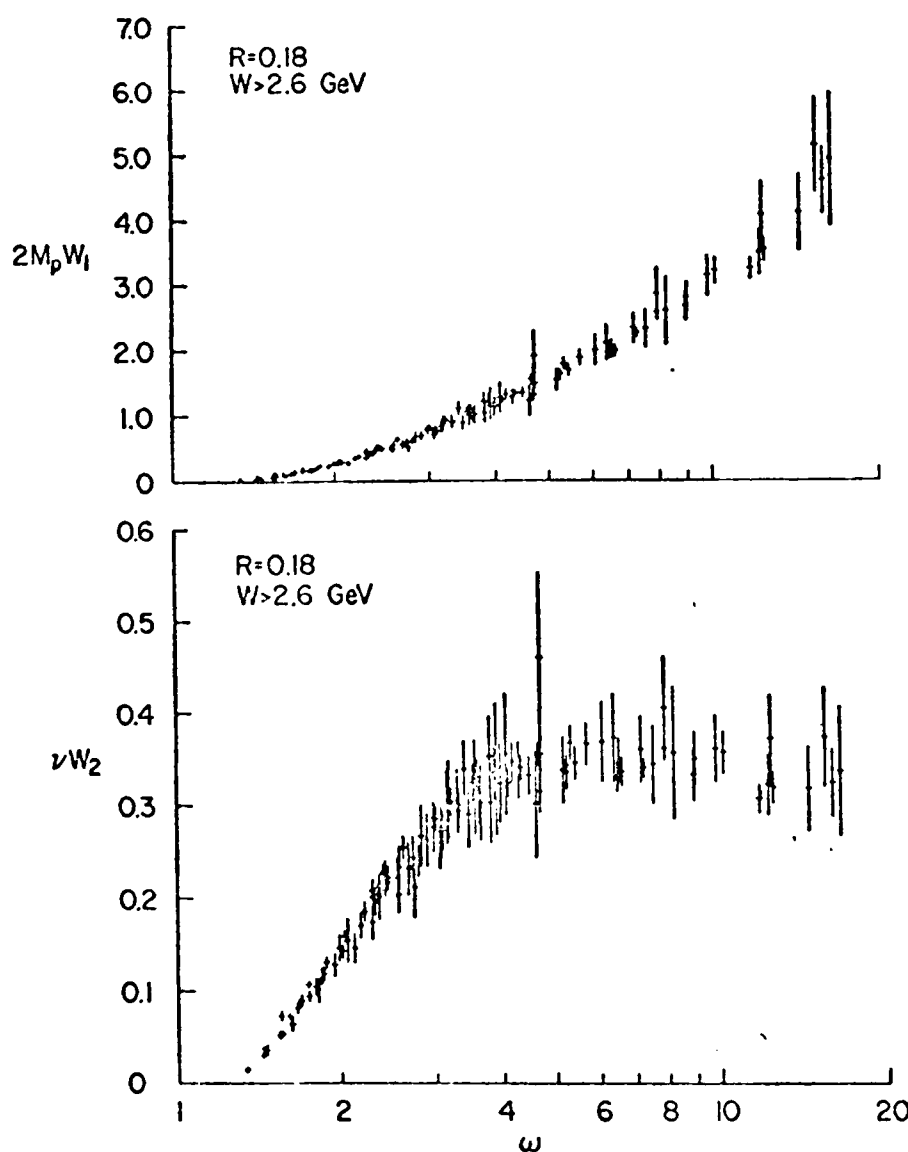
θ_2 = SCATTERING ANGLE FOR
 150 GeV INCIDENT BEAM.

FIG. 1.3

KINEMATIC REGION OF
SLAC EXPERIMENTS.
THE CURVED LINES
ARE LINES OF CONST
 $\epsilon(\theta = 60^\circ)$



(a)

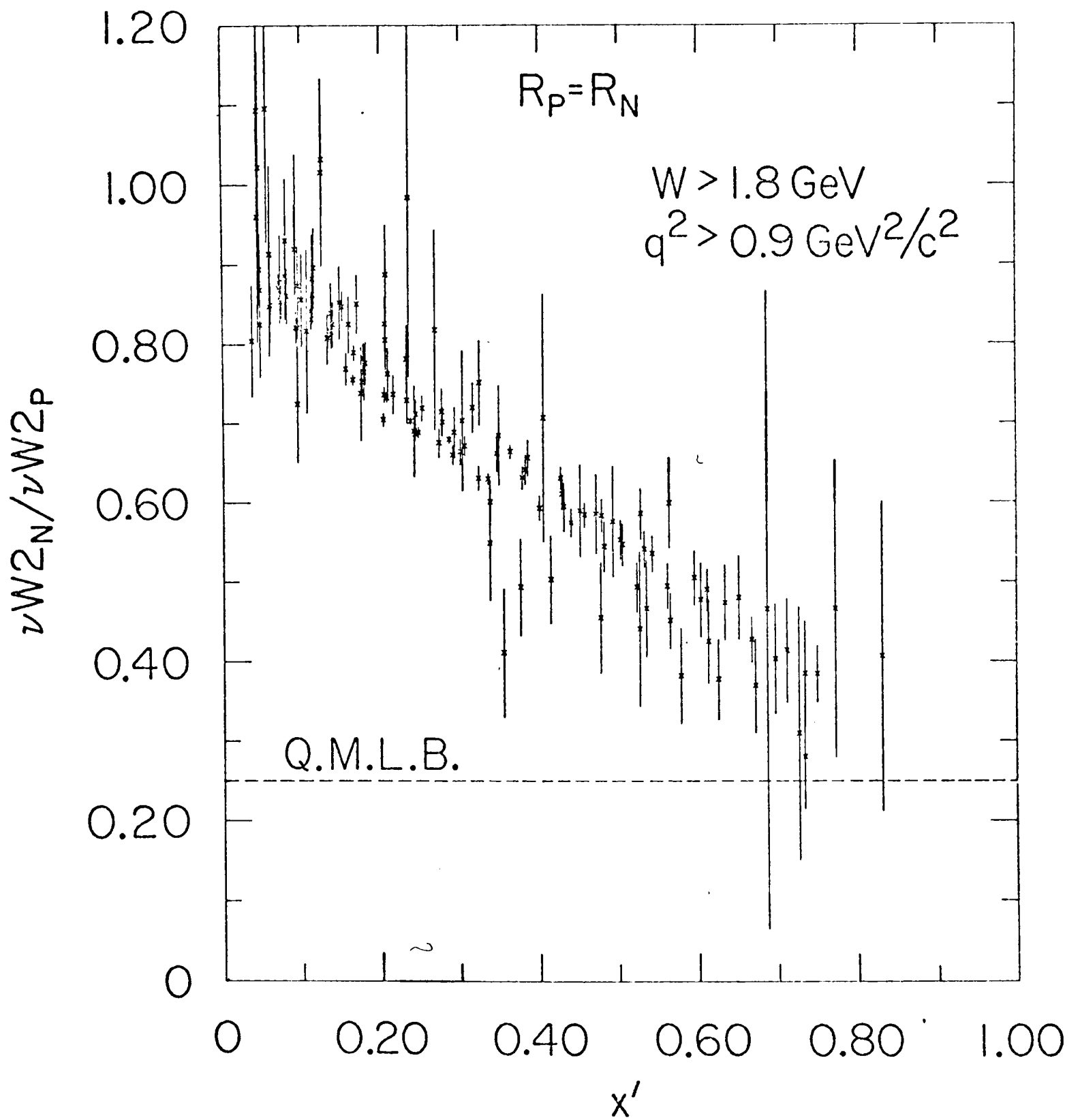


(b)

FIG. 1.4

Illustrations of the Bjorken scaling of νW_2 and W_1 : (a) for a fixed value of ω , and (b) for a range of ω values. The points in (b) are for many different $|q^2|$ values in the range of 1 to 12 (GeV/c)². The near overlap of the points at a particular ω indicates scaling

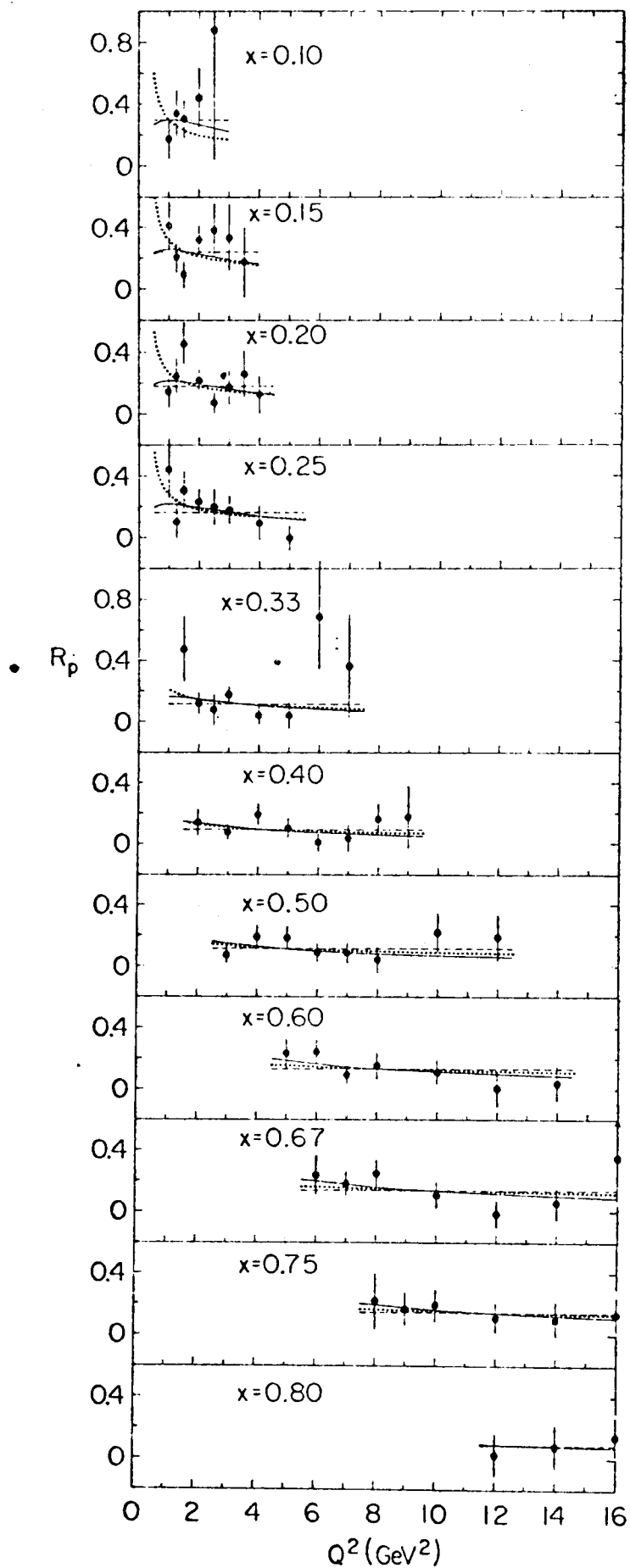
FIG. 1.5



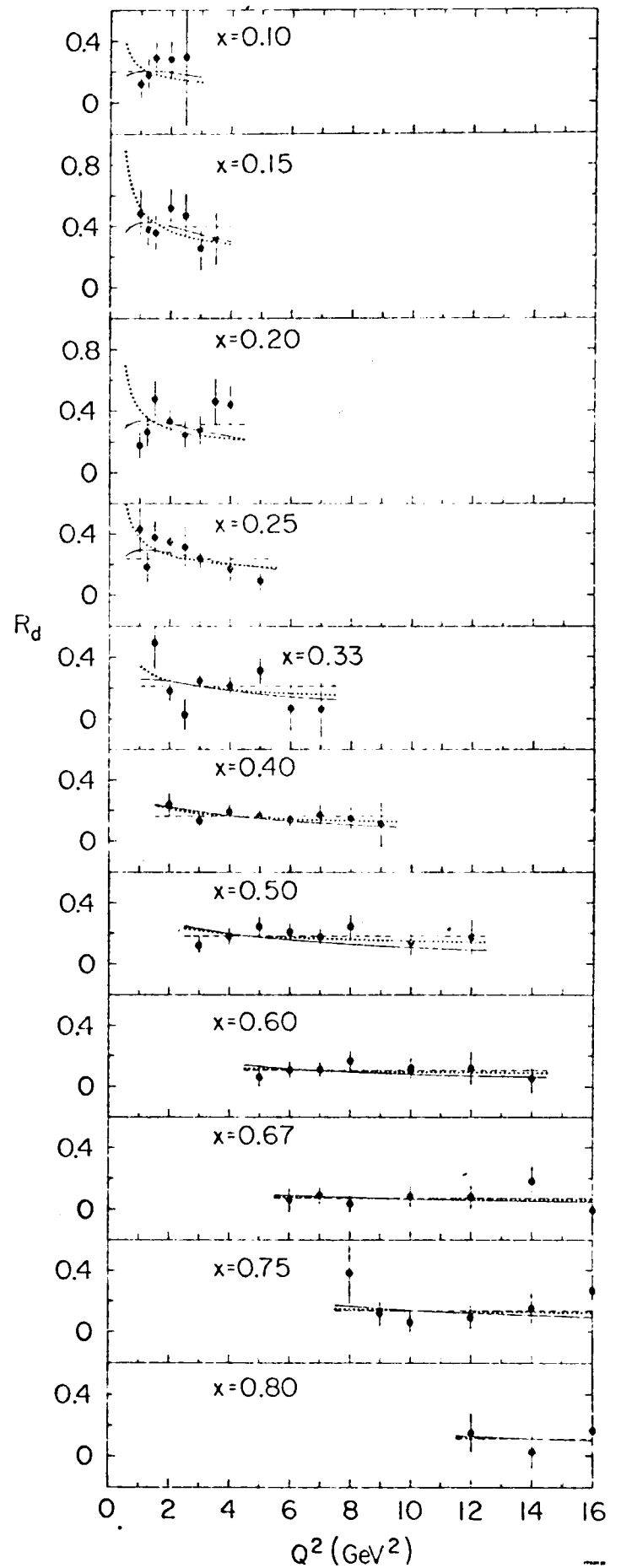
Q. M. L. B. =
QUARK MODEL
LOWER BOUND.

FIG. 1-6
VARIATION OF R (SLAC-MIT)

PROTON DATA



DEUTERON DATA



THE CURVES REPRESENT THE FOLLOWING FITS TO THE DATA.

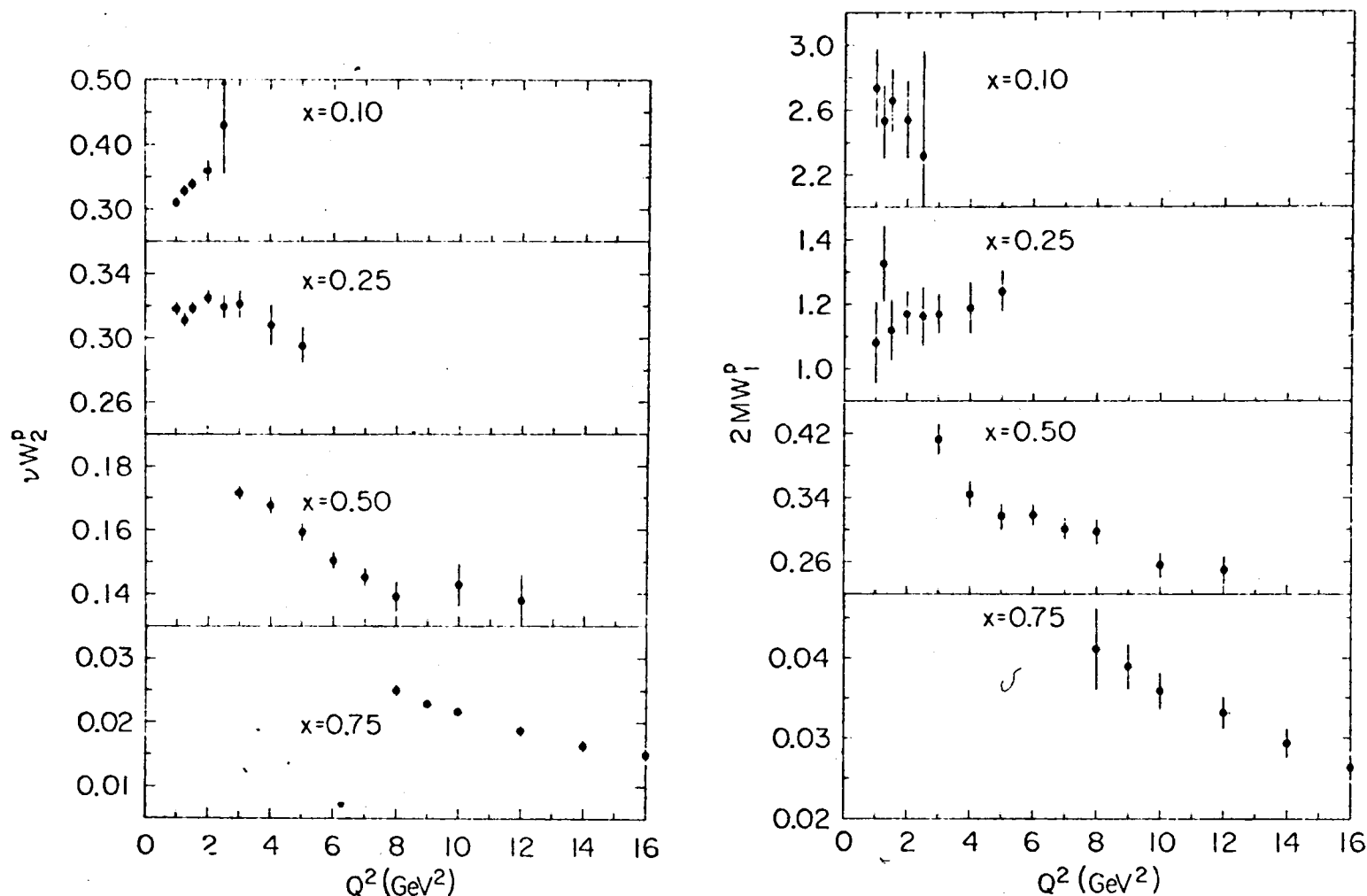
DASHED LINE $R = \text{const}$

SOLID LINE $R = C(x) \frac{Q^2}{(Q^2 + d^2)^2}$

DOTTED LINE $R = \frac{\alpha^2(x)}{\ln(Q^2/B^2)}$

FIG.1-7
SEPARATED VALUES OF νW_2 & $2M W_1$

PROTON DATA



DEUTERON DATA

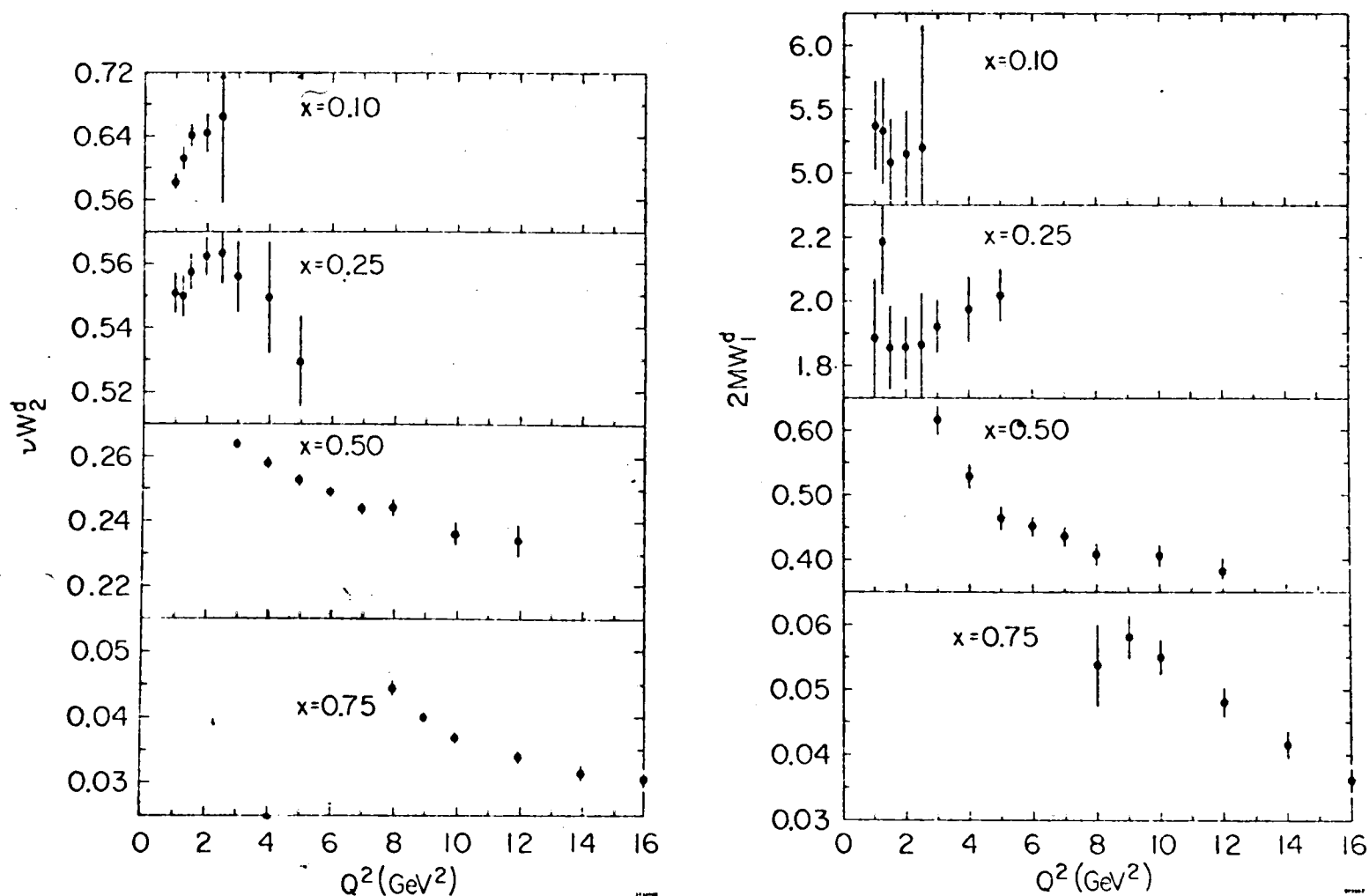
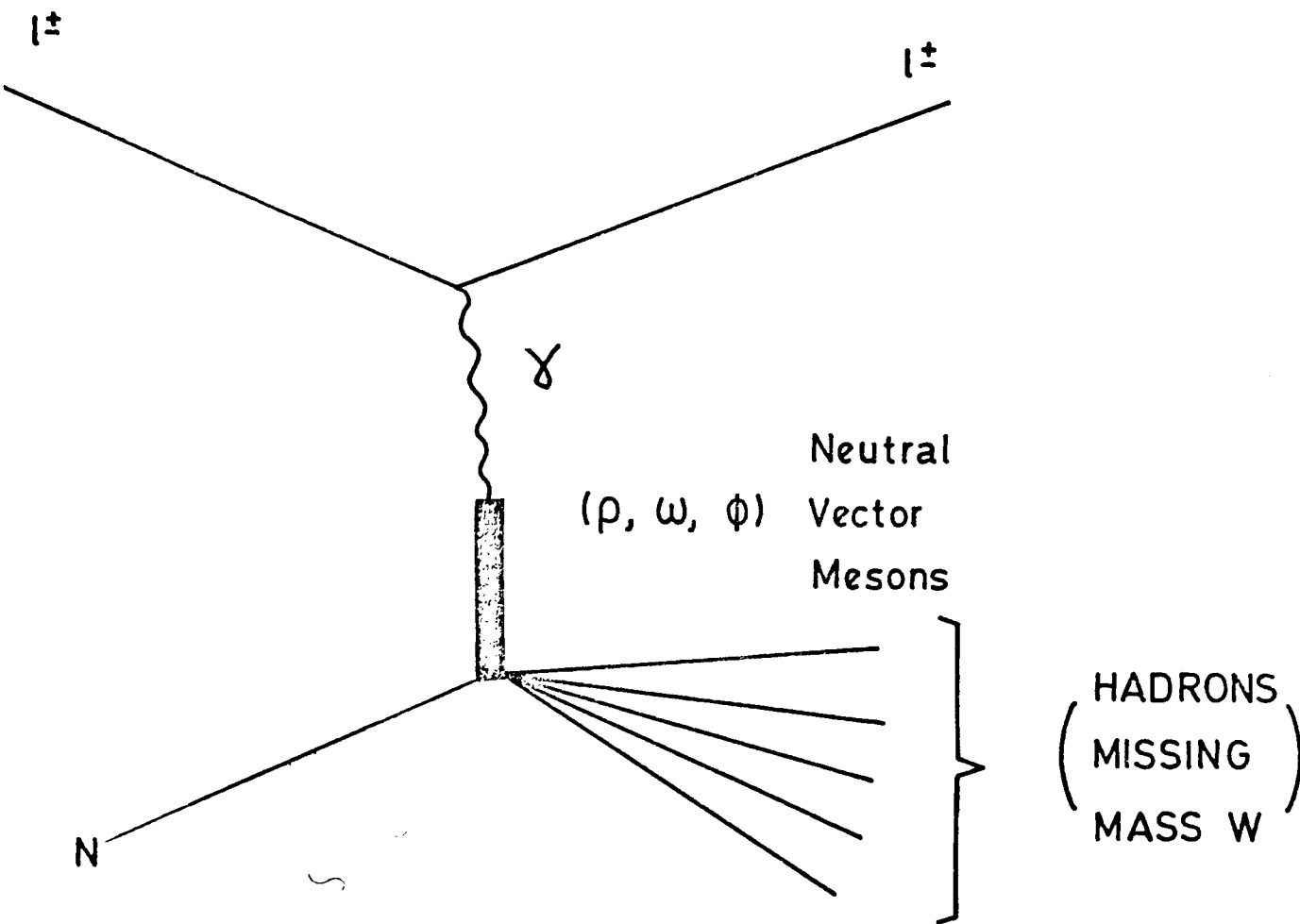


FIG. 1.8

VECTOR MESON DOMINANCE



l^\pm CHARGED LEPTON

γ VIRTUAL PHOTON

N NUCLEON

CHAPTER 2

THE APPARATUS

2.A INTRODUCTION

This chapter contains a brief description of the experimental apparatus. The set up consists basically of a large solid angle, particle spectrometer in which the interaction products of a muon beam incident on a liquid hydrogen target may be studied. The description is divided into three parts. The first part, Section 2.B, looks at the Muon Beam Transport system that produces and delivers a beam of muons to the experimental site. Section 2.C describes the beam defining and tagging apparatus that detects the muon beam as it enters the Muon Laboratory. Lastly, Section 2.D lists and says a few words on the various elements of the spectrometer apparatus.

Before starting on this description of the apparatus, it is convenient to define the experimental co-ordinate system. The origin of the co-ordinate system is on the axis of cylindrical symmetry of the Chicago cyclotron magnet midway between its two pole-faces - this is the momentum analysing magnet of the spectrometer, see Section 2.D and Figure 2.7. The +Z direction points along the nominal direction of travel of the muon beam as it enters the Muon Laboratory. The +Y direction points vertically upwards and the +X direction is defined such that X, Y, Z form a right-handed cartesian co-ordinate system. One may also note that +Z and +X point approximately north and west respectively. In addition to these axes, two extra directions, U and V, are defined for ease in discussing the spark chambers in the spectrometer. Both the U and V axes lie in the X, Y plane, at angles of $+7.125^\circ$ and -7.125° to the +X direction respectively ($7.125^\circ = \tan^{-1}(1/8)$). The five co-ordinate axes are illustrated in Figure 2.1.

2.B MUON BEAM TRANSPORT

A beam of muons is produced by the decay in flight of pions and kaons produced in high energy proton-nucleon collisions.

Magnet Lay-Out - Figures 2.2(a) and 2.2(b) are schematic outlines of the FNAL Muon Beam Transport system. More detailed drawings may be obtained from the FNAL Neutrino Section.

A 300 GeV extracted proton beam from the FNAL accelerator impinges on a 30 cm aluminium target. The secondaries produced in the resulting interactions are strongly focussed by a triplet of quadrupole magnets Q1 into a 500 metre evacuated decay pipe. The beam-line has four bending stations D1, D2, D3 and D4, each consisting of three dipole magnets with a total bend at each station of 27 mr and an aperture of 10 cm. These bends serve to momentum select the muons and to separate the muon beam line from the neutrino beam line. The beam coming out of the 500 metre decay pipe is bent at D1, refocussed by quadrupole doublets Q2 and Q3 and bent again at D2. The dipole magnets at D3 contain approximately 23 metres of high density polyethylene. This absorbs the hadrons that have not yet decayed so that the beam emerging from D3 is a highly pure muon beam. An estimate made of the residual hadron contamination of this beam is described in Chapter 3. The beam is further refocussed at Q4 and is bent at D4 into the Muon Laboratory. The bending station at D4 contains the momentum tagging magnets for the muon beam. Looking at Figure 2.2(b) it is seen that quadrupoles Q3 focus the beam onto the polyethylene absorber and quadrupoles Q4 focus the beam onto the experimental target in the Muon Laboratory.

Intensity Optimisation - The decay of the pion or kaon is isotropic in its rest frame. Simple kinematics show that the forward muons from the decays of high energy pions and kaons take almost all of the meson energy. Therefore to achieve the maximum muon yield, the beam-line magnets are all set for particles at the nominal muon beam energy. This enables some pions and kaons to follow the beam-line and decay into beam muons right up to the hadron absorber in D3. Incidentally, the process of selecting the forward decays of the pions and kaons produces a polarised beam of muons, their spins being anti-parallel to their momenta. In addition the polarity of the beam line is set for positive particles. μ^+ beams are more intense - in practice by a factor of 3 or so - than μ^- beams simply because the pion and kaon secondaries are produced from initial states - i.e. proton-proton or proton-neutron - that have a net positive charge. This gives rise to more positive than negative mesons and subsequently a higher μ^+ yield than a μ^- yield. Assuming the one photon exchange picture holds for the muon-proton interaction it does not matter if the beam is μ^+ or μ^- , the muons being used simply as a source of virtual photons. The beam line thus set up has a muon/(incident proton) yield of the order of 10^{-7} .

Halo - High energy muons are highly penetrating particles. This means that any muons that have been scattered or bent out of the beam line have a substantial probability of entering the Muon Laboratory. These muons are called halo muons and are spread over the entire aperture of the experimental apparatus, their numbers being of the same order of magnitude as the number of beam muons. Attempts to minimise this halo, including an earth shield around the beam pipes right up to the Muon Laboratory, are made, but the experiment has to rely on electronic collimation to adequately define the beam and reject the halo.

R.F. Structure - Proton synchro-cyclotrons use r.f. cavities⁽⁵⁰⁾ to accelerate the beam. This r.f. tends to bunch the protons around the accelerator ring. At FNAL these bunches are typically 2 nsec long and are separated by 18 nsec. Any secondary beam produced from these protons will necessarily reproduce this time structure. The muons therefore come in 2 nsec "buckets" every 18 nsec. As the beam intensity is typically $10^6/\text{sec}$ - i.e. approximately 10^6 for 50×10^6 r.f. buckets - in general there is a small probability that there will be more than one muon in a particular r.f. bucket.

2.C BEAM DETECTION

Figure 2.3 gives the disposition of all the elements of the beam defining and tagging apparatus. Figure 2.4 gives the shapes and sizes in the X, Y plane of the various counters and chambers in this apparatus.

Beam Definition - The purpose of the beam defining system is to electronically collimate the beam and to register particles in the beam as they enter the Muon Laboratory. The collimation of the beam is effected by five sets of scintillation counters V1, V2, V3, V4 and V5. These are veto counters and have a circular hole in each set corresponding to the aperture of the D4 dipole magnets. T1, T1A, T2, T3 are small scintillation counters centred on the nominal beam line. A beam particle is defined and registered by giving a coincidence between T1, T1A, T2 and T3 and by not passing through any of the five sets of veto counters. The halo muons further out from the beam line are vetoed by the Halo Veto scintillation counter hodoscope.

Beam Tagging - The purpose of the beam tagging system is to measure the momentum of the incoming beam particle and to determine its trajectory

as it enters the experimental target. This is achieved by the use of eight Multi-Wire Proportional Chambers⁽⁵¹⁾ and six small scintillation counter hodoscopes. The MWPCs are 20 cm x 20 cm in area and have a wire spacing of 2 mm. There is one read-out plane per chamber. Chambers with vertical read-out wires are described as X chambers, and those with horizontal wires as Y chambers. The most upstream beam hodoscope, BH1, is 20 cm x 20 cm in total area. The other five hodoscopes are all 15 cm x 15 cm. Each hodoscope has eight elements. In exactly the same way as with the beam chambers, the hodoscopes are designated X or Y according to the direction of spatial information they output. Looking at Figure 2.3, it is seen that these chambers and hodoscopes are distributed at four stations along the beam line. Stations 1 and 2 are upstream of the D4 dipole magnets and each consists of one X chamber and one X hodoscope. Beam station 3 consists of an X, Y pair of chambers and an X, Y pair of hodoscopes and lies at the exit of the D4 tagging magnets. Station 4 lies just upstream of the experimental target and consists of two X, Y pairs of chambers and one X, Y pair of hodoscopes. The X information from stations 1-4 gives the X-bend of the beam track in the D4 tagging magnets and consequently the momentum of the beam particle. The X and Y information from Stations 3 and 4 give the track of the beam particle as it enters the experimental target. It may be noted that as the total thickness of scintillator at any one station may be up to 2 cm, the beam chambers are always the most upstream elements in their respective beam stations. This prevents the chambers from seeing any knock-on electrons from the scintillator thereby causing track confusion in the beam tagging system.

Beam Phase Space - This is an appropriate point at which to look at the characteristics of the muon beam generated by the Beam Transport system and defined by the beam apparatus. The (muon beam)/(incident proton) yield lies between 1×10^{-7} and 2×10^{-7} and the muon halo is larger than the beam itself. The best beam yields and the smallest halo/beam ratios arise when the beam momentum is set at approximately one half of the primary proton momentum - e.g. the halo/beam ratio is approximately 1.5 for the 147 GeV/c data and 3.0 for the 96 GeV/c data, the primary proton energy being 300 GeV/c. Figures 2.5(a) and 2.5(b) give the momentum distributions of beam particles for the 96 GeV/c and 147 GeV/c datasets. Figure 2.6(a) - 2.6(g) give some results for the phase space distribution of the 147 GeV/c beam data, the results for the 96 GeV/c beam data being similar.

2.D THE SPECTROMETER

Figure 2.7 is a diagram of the spectrometer apparatus. This section lists and briefly describes the various elements of this spectrometer.

Target - The target flask stands approximately 6 metres upstream of the centre of the Chicago Cyclotron Magnet - the origin of the experimental co-ordinate system. It is 18 cm in diameter and 120 cm long and may be filled with either liquid hydrogen or liquid deuterium. For liquid hydrogen this corresponds to a target thickness of approximately 8.3 gm/cm^2 - compared with the flask material which presents 0.4 gm/cm^2 to the beam. The filling and emptying of the target flask is done from and to a reservoir of liquid hydrogen - or deuterium- thus ensuring that the target can be filled or emptied quickly. The target pressure is slightly above atmospheric and is monitored continuously.

Halo Veto Wall - Immediately upstream of the target stands the halo veto wall. This wall is made of concrete blocks and is one metre thick. It has a hole in its centre to allow the beam through and covers the entire X, Y extent of the halo veto. This wall ensures that any backscattered particles from an interaction in the target do not veto the event by hitting the Halo Veto counter hodoscope.

1m x 1m Multiwire Proportional Chambers - Immediately downstream of the target is a bank of eight large MWPCs.⁽⁵²⁾ There is an additional pair of such chambers near the centre of the Chicago Cyclotron Magnet. These chambers are arranged so that the read-out planes - of which there is one per chamber - have wires that are alternately vertical and horizontal. This gives five X views alternating with five Y views. The wire spacing in the chambers is 1.5 mm which gives a resolution in each view of about 0.5 mm. These ten MWPCs record the trajectories of all the forward going charged particles from an interaction in the target. The most important reason for using proportional chambers in this region arises from the short memory times of such chambers - typically 120 nsec for the ones being described. As a large fraction of the products of interactions in the target have trajectories very close to the beam, having a short memory time ensures that the tracks of the interaction products are not confused with additional tracks due to stale beam and halo.

Chicago Cyclotron Magnet - This large volume magnet - which used to be the magnet for the 0.5 GeV cyclotron at the University of Chicago - is the momentum analysing magnet of the spectrometer. It has a pole tip radius of 220 cm and a gap between the pole faces of 125 cm. It takes a current of 5000 Amps at 400 Volts to generate the maximum field of 15 Kilogauss. The field integral, $B \cdot dl$, is approximately 75 Kilogauss-

metre at full field. This corresponds to a transverse momentum kick of about 2.2 GeV/c to particles going through it. At full field the Chicago Cyclotron Magnet - CCM - has a momentum cut-off of about 7 GeV/c, particles less energetic than this bend out of the acceptance of the detectors downstream of the magnet. The polarity of the magnetic field is such that positive particles bend towards the negative X direction. Incidentally, the CCM has supports that are sunk to the bed-rock of the FNAL site and this fact makes it an ideal reference point from which to survey the apparatus in the Muon Laboratory. A negative aspect of the CCM arises from its use as a cyclotron magnet, namely that the pole-tips have a high residual radio-activity.

2m x 4m Shift Register Chambers - Downstream of the CCM there are 6 shift register spark chambers⁽⁵³⁾ presenting an area of 2m x 4m in the Y-X plane. Each chamber has two planes of capacitatively read-out wires separated by a 1.25 cm gap. The wire spacing in the read-out planes is 1.25 mm and the resolutions of individual planes are typically 0.3 to 0.5 mm in the read-out direction.. These chambers have a memory time of 2-9 microseconds and may be sparked up to 50 times a second. With spark chambers of this size it turns out to be very difficult to support the fine wires - that are necessary for such small interwire spacing - horizontally, the effect of gravity causing them to sag in the middle. So in the construction of these chambers and of all the magnetostrictive chambers described below, the wires are wound vertically or at $\pm\theta$ ($\theta \equiv \tan^{-1} 1/8 = 7.125^\circ$) to the vertical direction. Again the read-out planes are labelled according to the direction of spatial information they provide. Looking at Figure 2.8, X-planes have vertical wires, U-planes have wires rotated in an anti-clockwise direction looking downstream, V-planes have wires rotated in a clockwise direction from the vertical looking downstream.

In this convention the twelve capacitative read-out planes of the shift register chambers consist of three sets of UXXV type planes.

2m x 6m Spark Chambers - Approximately nine metres downstream of the centre of the CCM, there are four 2m x 6m magnetostrictive spark chambers. Each chamber has two planes of read-out wires separated by 1.25 cm. The wire spacing is again 1.25 mm giving resolutions typically 0.3-0.5 mm in the read-out direction. These chambers have memory times of 1-2 microseconds. They are deadened in the beam region by epoxying a 10 cm radius plastic disc of the appropriate thickness in between the chamber gaps. Using the convention defined above the eight read-out planes are of type UXUXVUXV. These and the 2m x 4m shift register planes constitute the twenty measuring planes which are used to determine the trajectories of the charged particles that go through the CCM. A comparison of tracks upstream and downstream of the CCM gives the momenta and charges of these particles. It should be mentioned that the magnetostrictive chambers used in this experiment require a large amount of energy for sparking and consequently a limit of 10-15 triggers per second is set by the recovery times of the power supplies and the main charge-storing capacitors of these chambers. A more complete description of the magnetostrictive chambers and associated electronics used in this experiment may be found in Ref. 54.

G and H Hodoscopes - Immediately downstream of the 2m x 6m spark chambers lie two large scintillation counter hodoscopes. The sizes and dispositions of their elements are indicated in Figures 2.9(a) and 2.9(b). The H hodoscope has twenty-four vertical elements and cover an area of 2m x 4m. The elements are arranged to overlap by 1 cm. The hodoscope is deadened in the beam region by replacing

the central 30 cm of scintillator of elements H11 and H12 with lucite. The G hodoscope covers an area of 2m x 6m. It has eighteen large horizontal elements - slightly overlapped - and two small elements G19 and G20. Referring to Figure 2.9(a) one can see that element G9 is pulled out so as to make a hole 25 cm wide horizontally between it and element G10. This hole is covered by G19 and G20 and accommodates the beam region. The G and H hodoscopes - with their time resolutions of about 30 nsec - are used to determine the in-time event associated tracks from those tracks found in the downstream measuring planes. Elements G1-G18 are also used for triggering, a use more fully discussed in Chapter 3.

e, γ , π^0 Identification - The 5 cm thick steel wall and the 2m x 4m spark chambers - called the Photon chambers - immediately downstream of it provide a basis for a crude identification of electrons, photons and π^0 s. The steel wall corresponds to approximately 3 radiation lengths. The four spark chambers are of the same type as the 2m x 6m chambers and have eight planes - UVUXUXUV - of magnetostrictive read-out. There is a large probability that electrons, photons and π^0 s will form electromagnetic showers in the steel which will form clusters of sparks in the chambers. Spark counting in these chambers in the regions indicated by the downstream tracks will help identify the above particles.

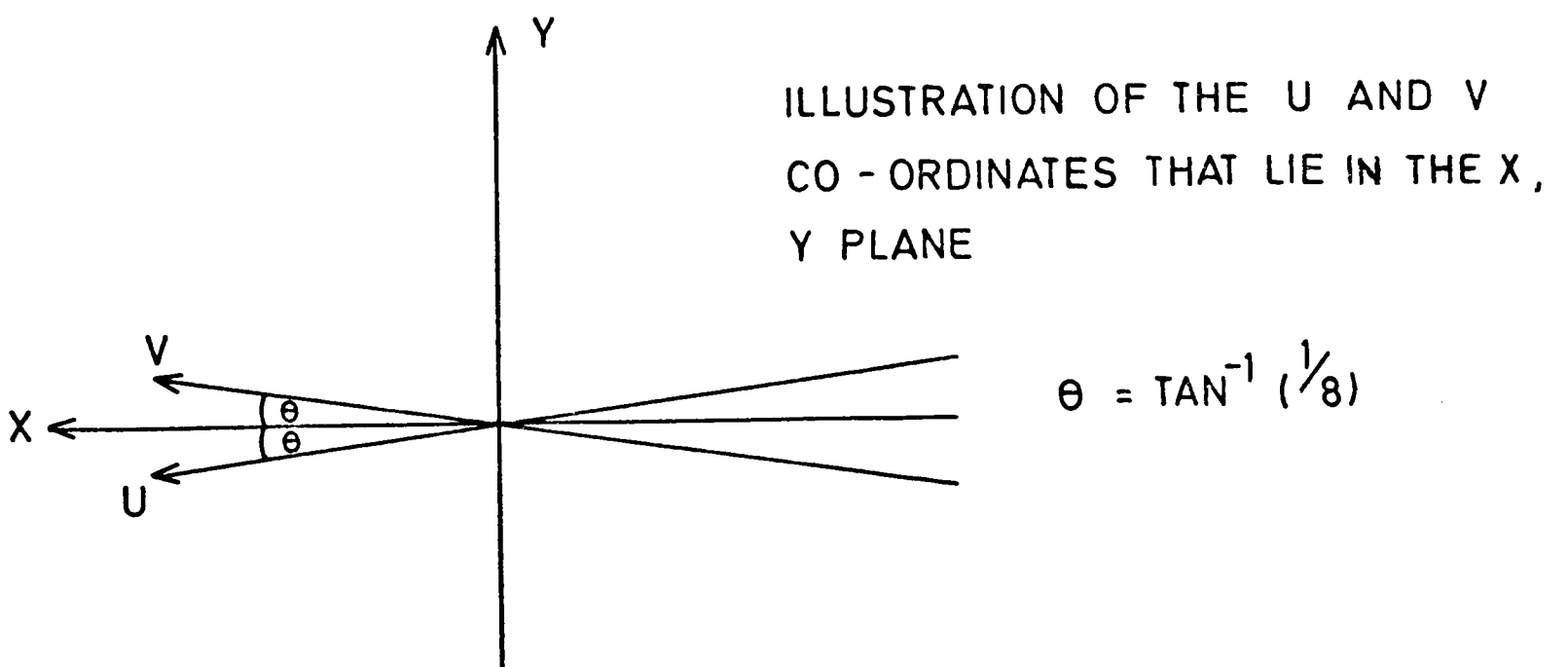
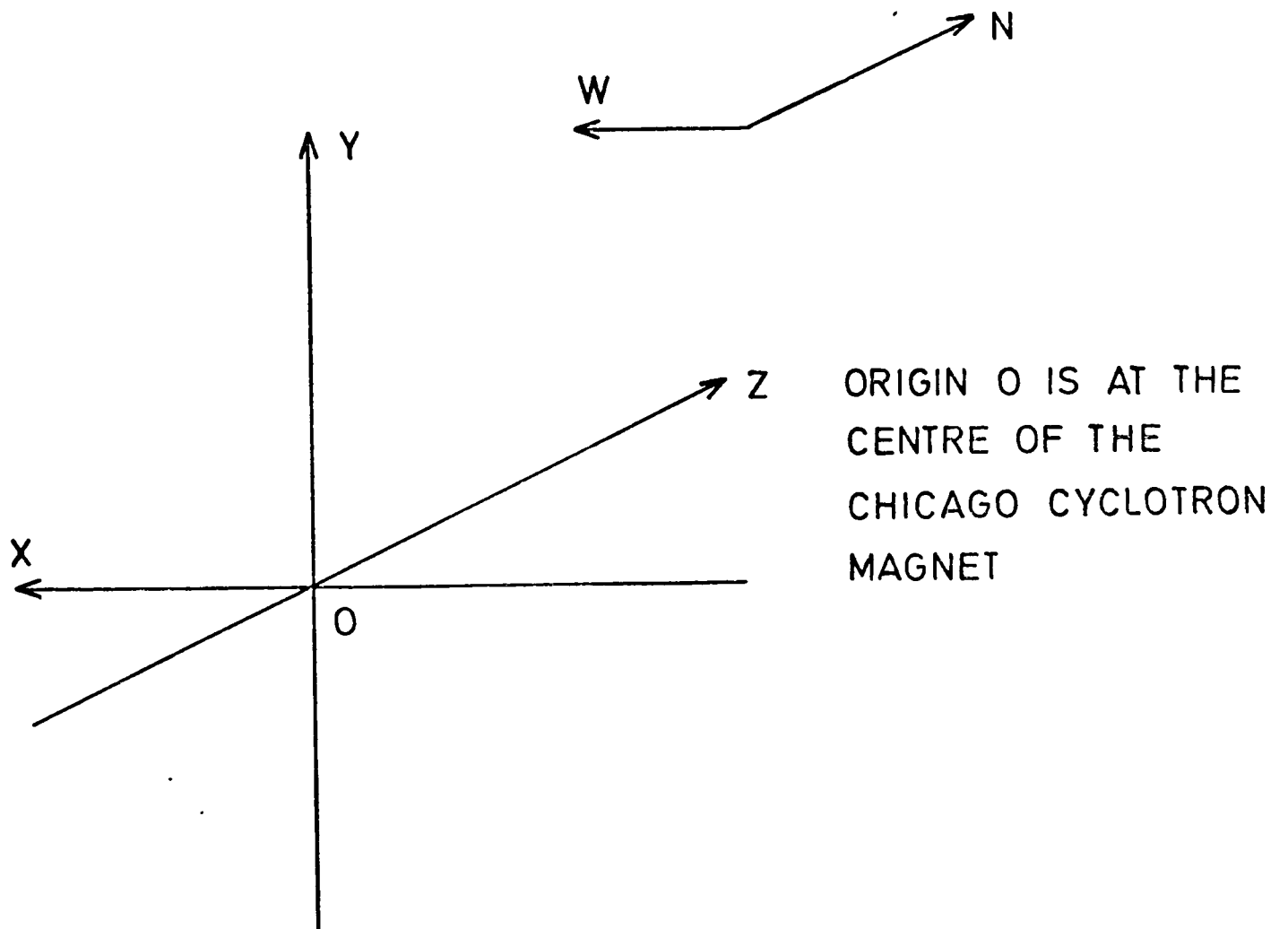
Neutral Hadron Identification - Downstream of the Photon chambers lies a 40 cm thick lead wall followed by three 2m x 4m spark chambers. These chambers - called the Neutron chambers - are of the same type as the 2m x 6m chambers and have six planes - XVUXXV - of magnetostrictive readout. The lead wall corresponds to about 70 radiation lengths, and this is sufficient to kill almost all of the showers produced in the 5cm steel wall. The lead wall also provides a large cross-section for neutral

hadrons - such as K^0 's and neutrons - to interact and form showers, producing a cluster of sparks in the Neutron chambers. Spark counting in these chambers gives us further information as to the nature of the downstream particles.

Muon Identification - The purpose of the muon identification system is to detect a scattered muon and to record its track. After the Neutron chambers there are the remaining hadrons from the interaction in the experimental target and the particles from the secondary interactions in the material of the apparatus along with the scattered muon. Muons are distinguished by their unique ability to penetrate the 240 cm - corresponding to about 15 interaction lengths - steel wall. Incidentally, the steel for this wall used to be a part of the Rochester Cyclotron.

The K-veto consists of three scintillation counters 30 cm in X by 23 cm in Y lying one behind another in Z. The K counters veto any triggers in which the muon has not scattered and is still in the beam region. Muons interact electromagnetically - i.e. muon-electron scattering and bremsstrahlung - when passing through the steel and lead walls. If the resulting electrons or photons have a high enough energy, they will further interact to form electromagnetic showers. To minimise the probability of an electron - from a shower produced by a good scattered muon near the downstream surface of the 240 cm steel wall - accidentally vetoing the event, the K-counters lie just downstream and up against 4 cm of steel. Figures 2.9(c), 2.9(d), 2.9(e) are diagrams indicating the sizes and shapes of the M, N, M' scintillation counter hodoscopes. The disposition of the K, M, M' and N1, N3, N13 elements in the central region is shown in Figure 2.10. Although the layout of these hodoscopes is quite complicated, it does give the experiment great flexibility in choosing acceptances for the various kinematic regions to suit external beam conditions. The M, N, M' hodoscopes are used

for timing spark chamber tracks and for triggering, the latter use being more fully discussed in Chapter 3. The tracks of particles that pass through the steel muon filter are recorded in the Muon spark chambers. These again are exactly of the same type as the 2m x 6m spark chambers, there being eight planes - UXXVUVUX - of magnetostrictive read-out 2m x 4m in area in the X-Y plane.



CO - ORDINATE SYSTEM.

FIG. 2-1

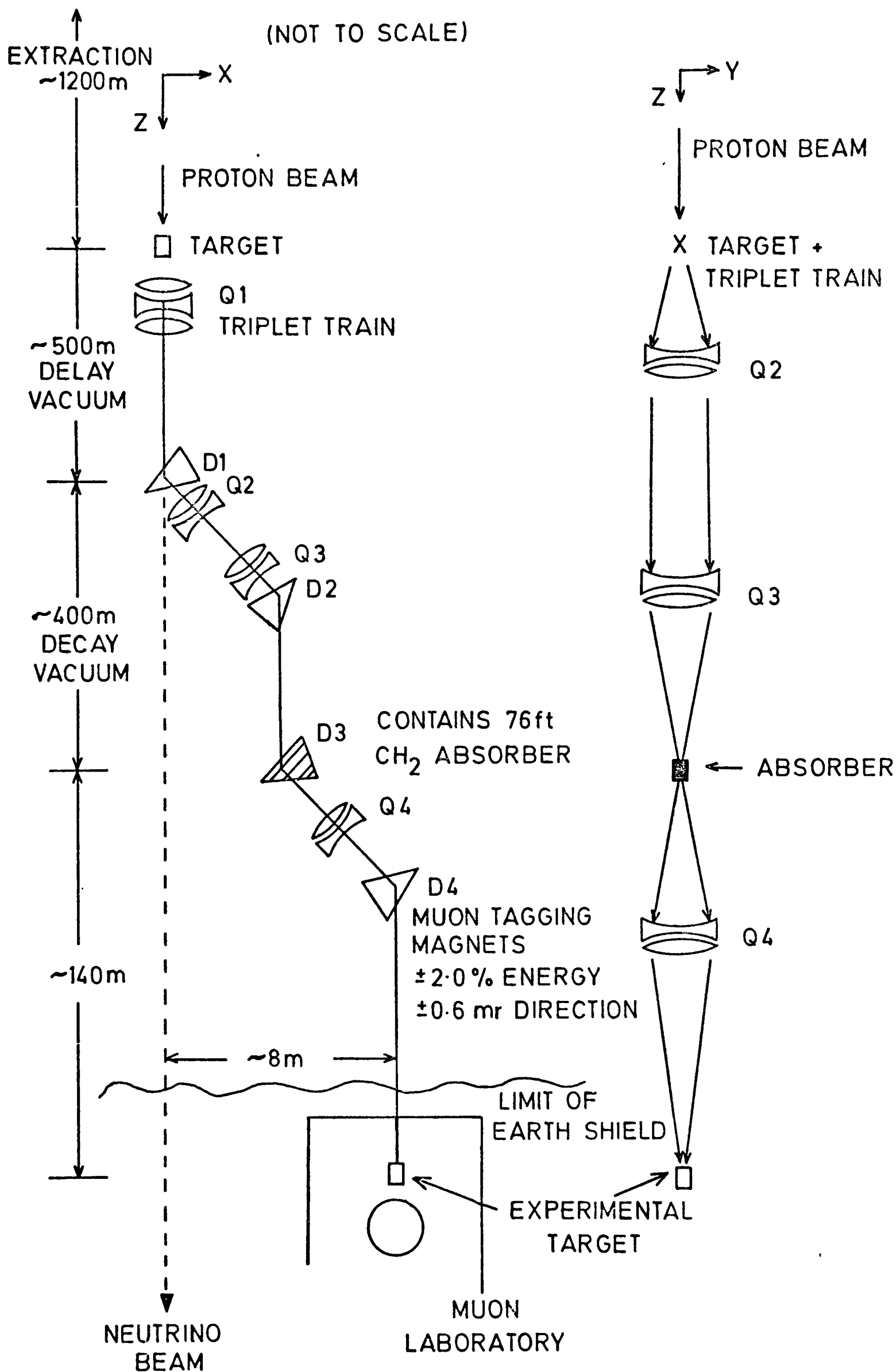
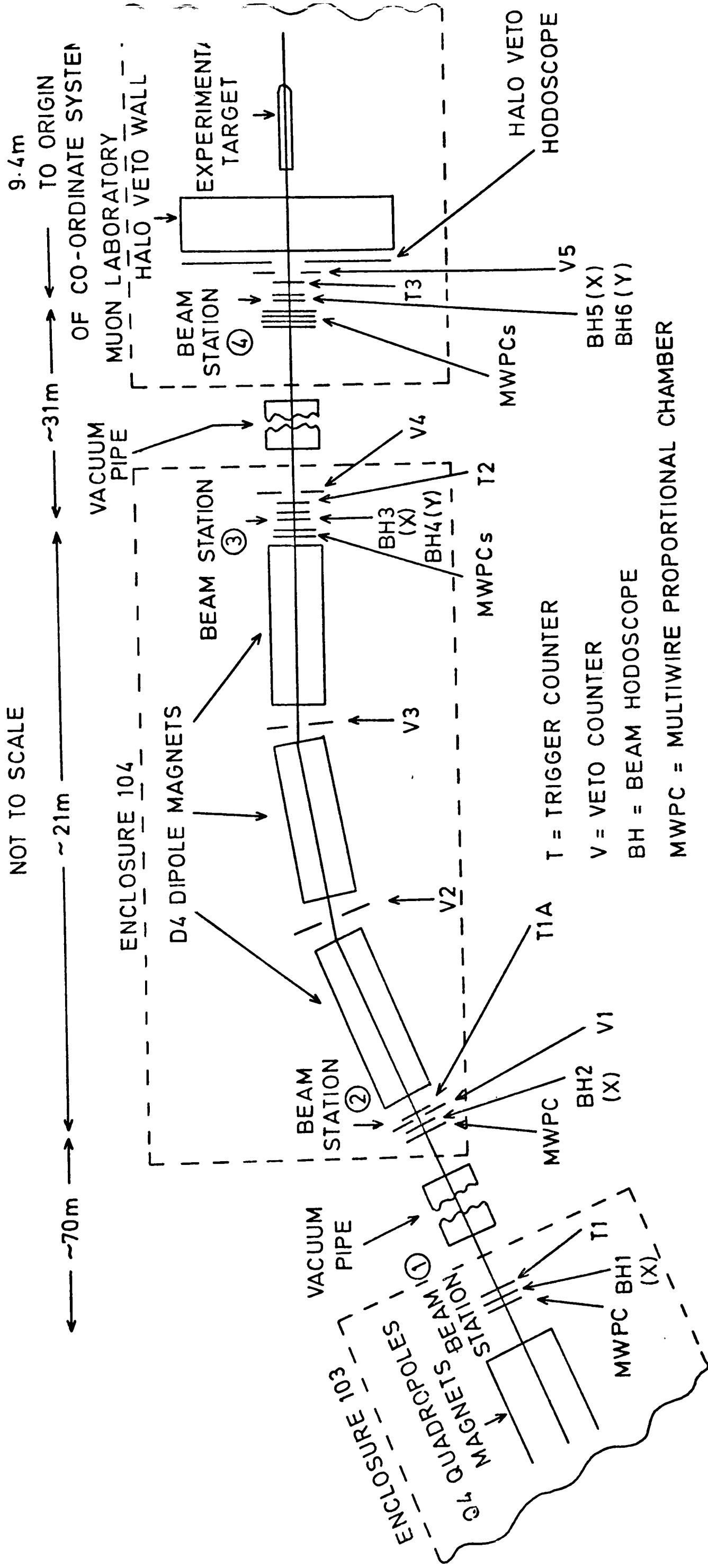


FIG. 2.2(a)

FIG. 2.2(b)

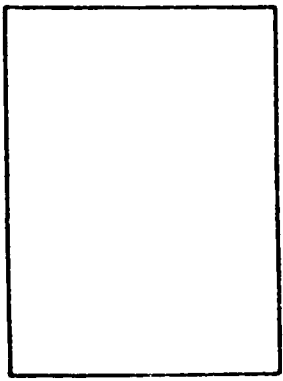
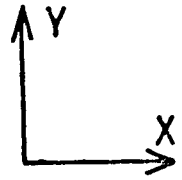


BEAM TRIGGERING AND TAGGING SYSTEM

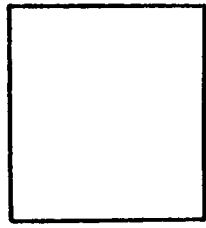
FIG. 2-3

SCALE UNLESS OTHERWISE INDICATED

0 10 20 30 cms



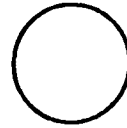
T1



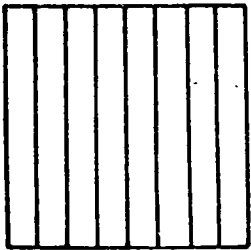
T1A



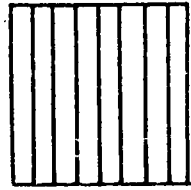
T2



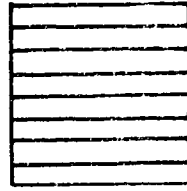
T3



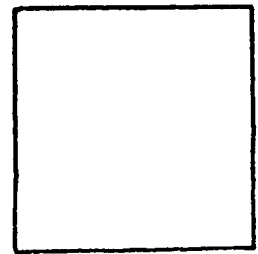
BH1



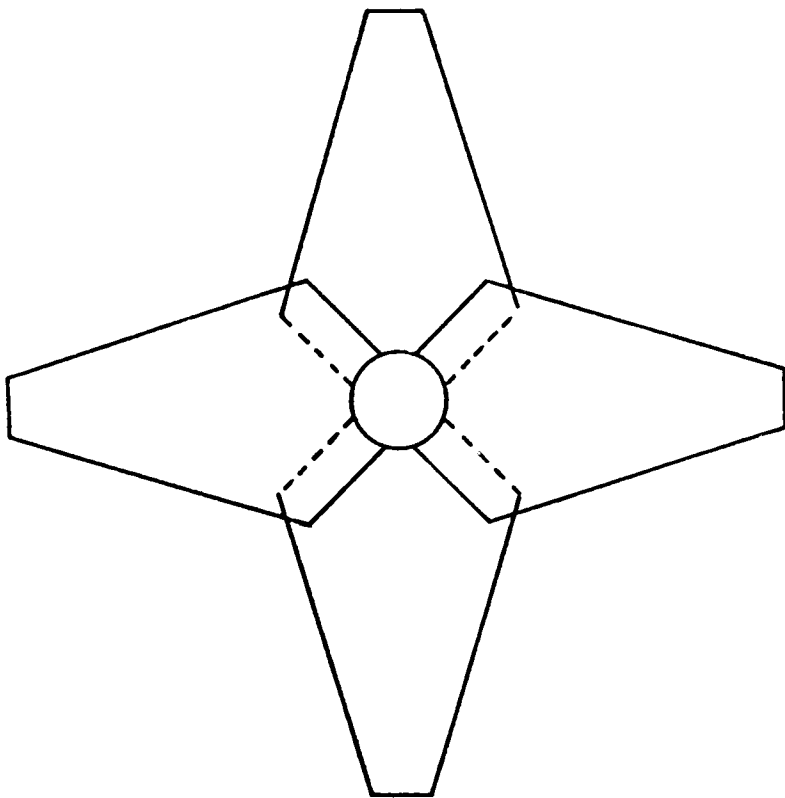
BH2,3,5



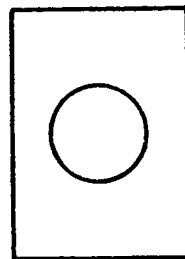
BH4,6



MWPC
2mm wire spring

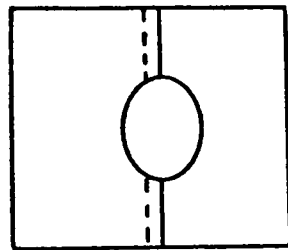


V5 4 ELEMENTS

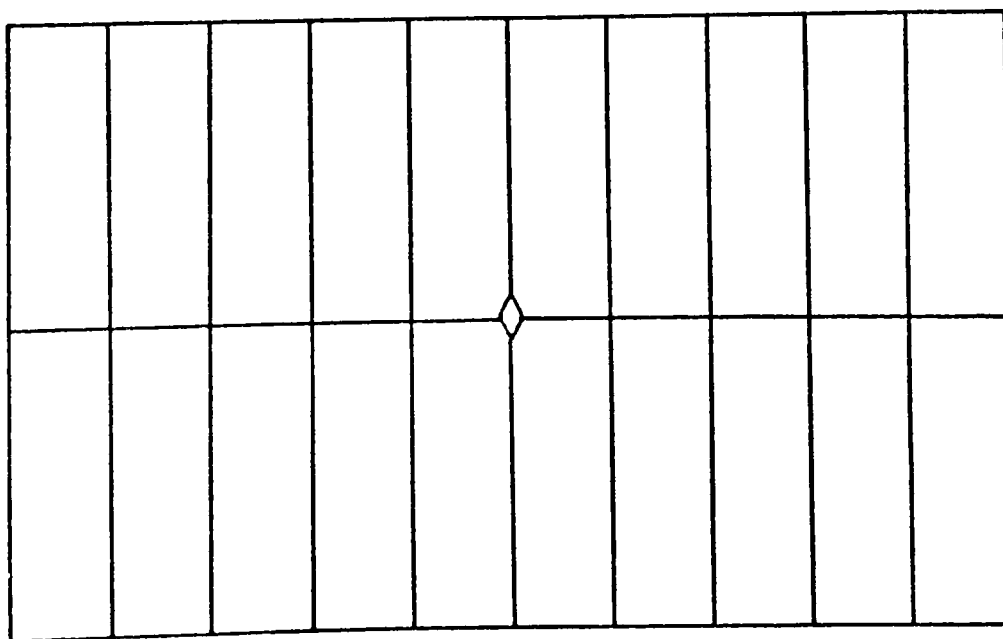


V1

FIG.2.4
SIZE OF THE
ELEMENTS OF
THE BEAM
APPARATUS.



V2, V3, V4,
2 ELEMENTS EACH

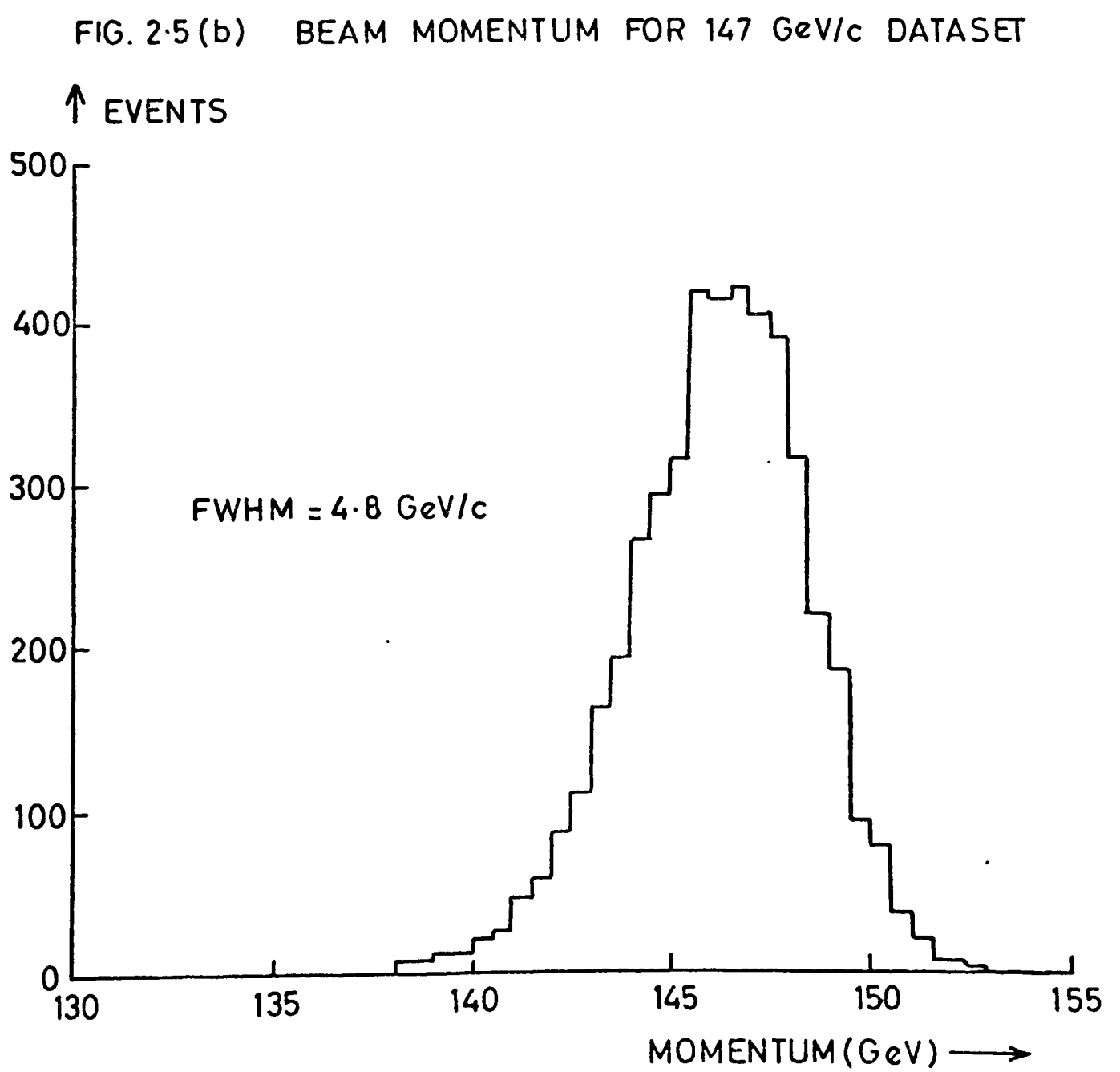
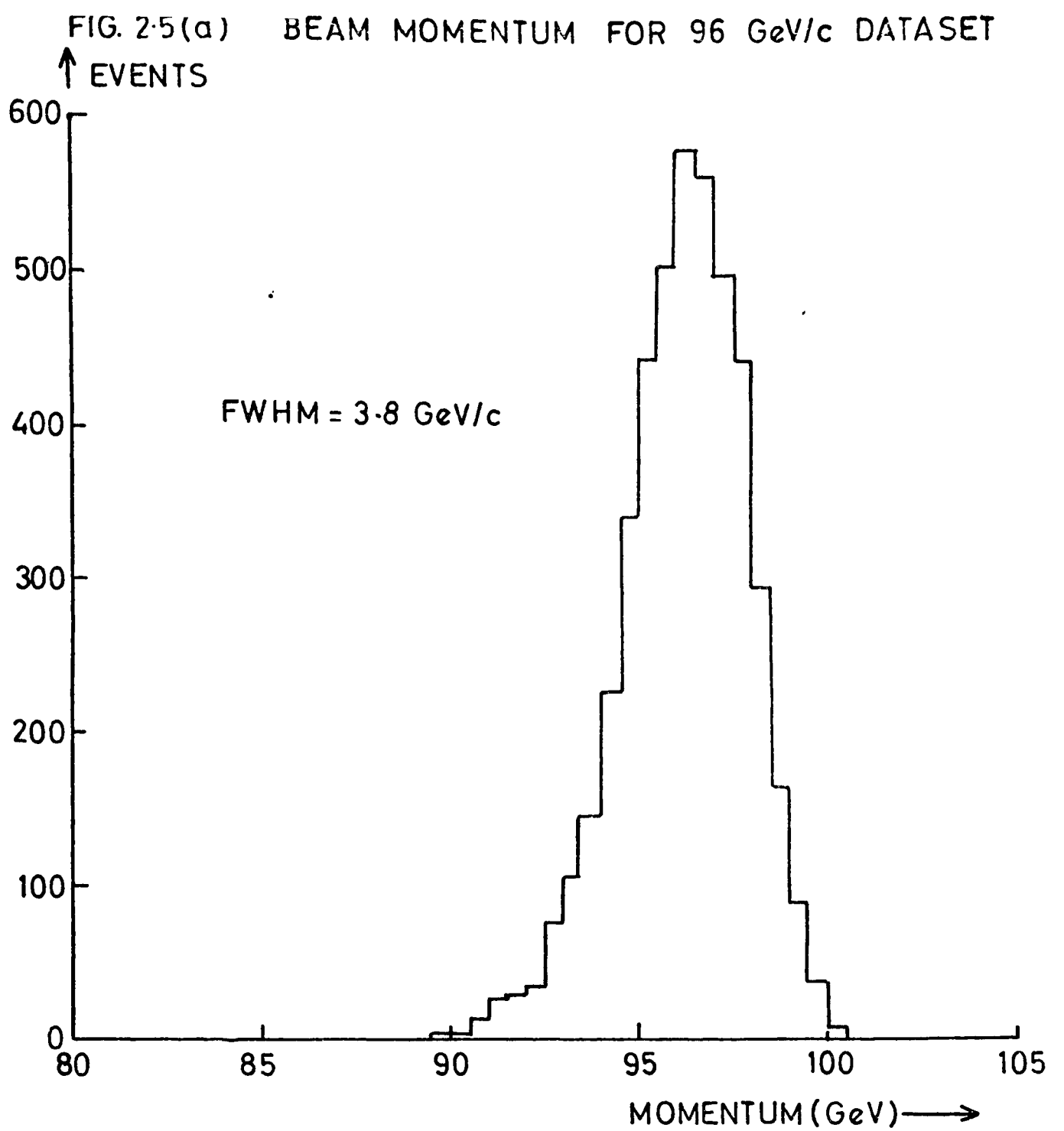


HALO VETO HODO.
20 ELEMENTS

3 metres

ELEMENTS
OVERLAPPED
BY 4cms

5 metres



BEAM PHASE SPACE FOR 147 GEV/C DATA

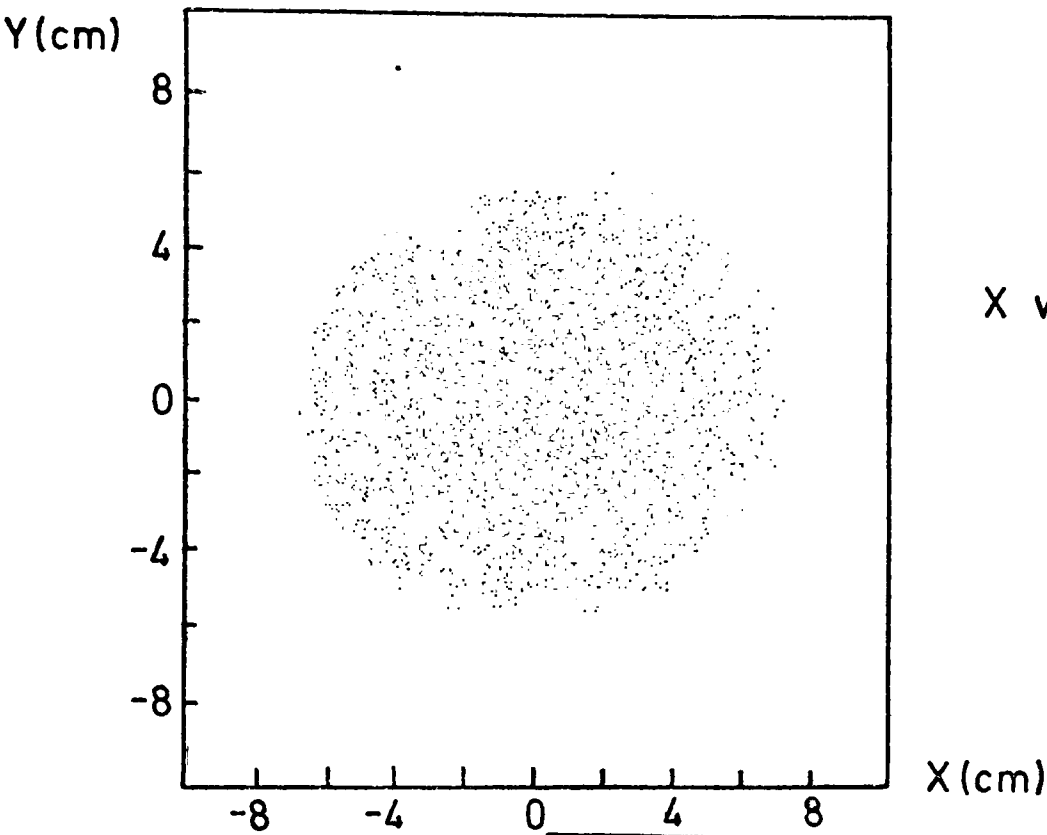


FIG. 2·6 (a)

X vs Y

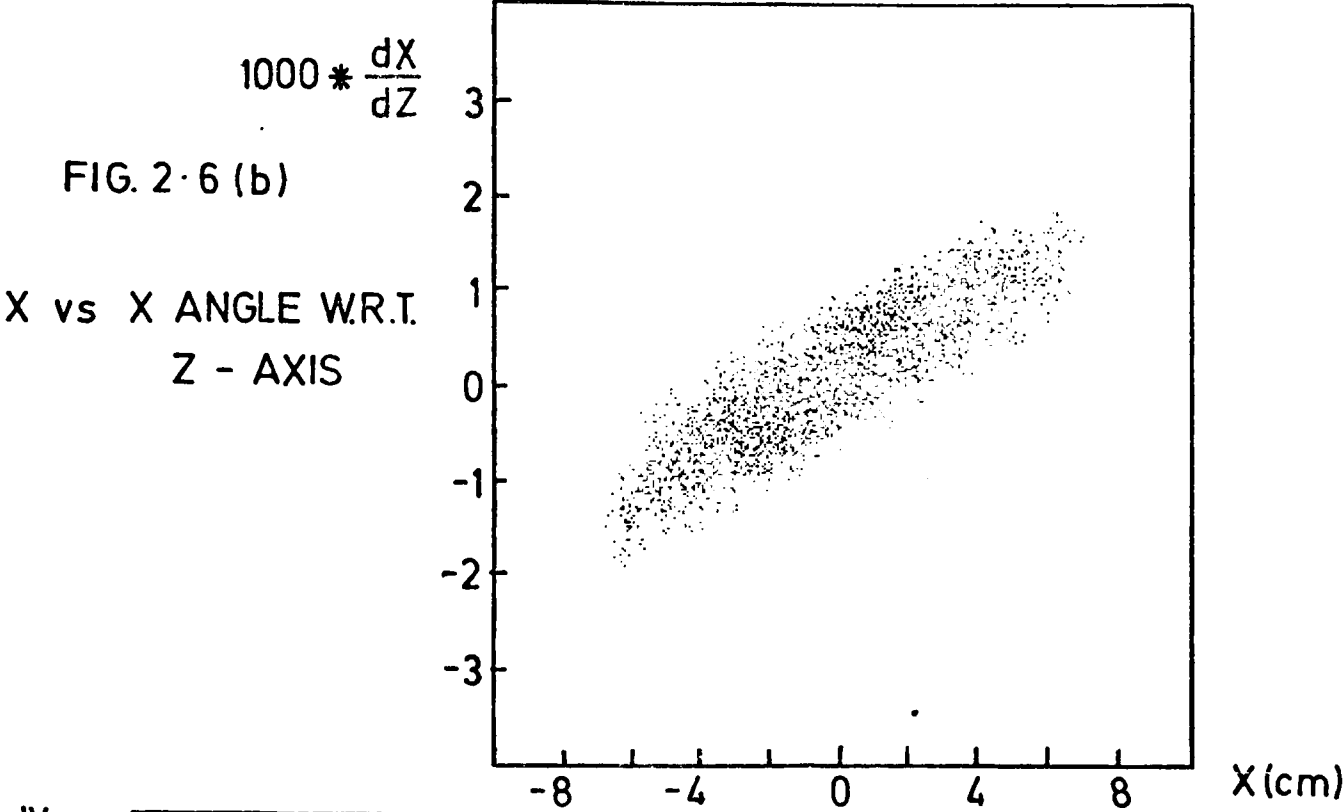


FIG. 2·6 (b)

X vs X ANGLE W.R.T.
Z - AXIS

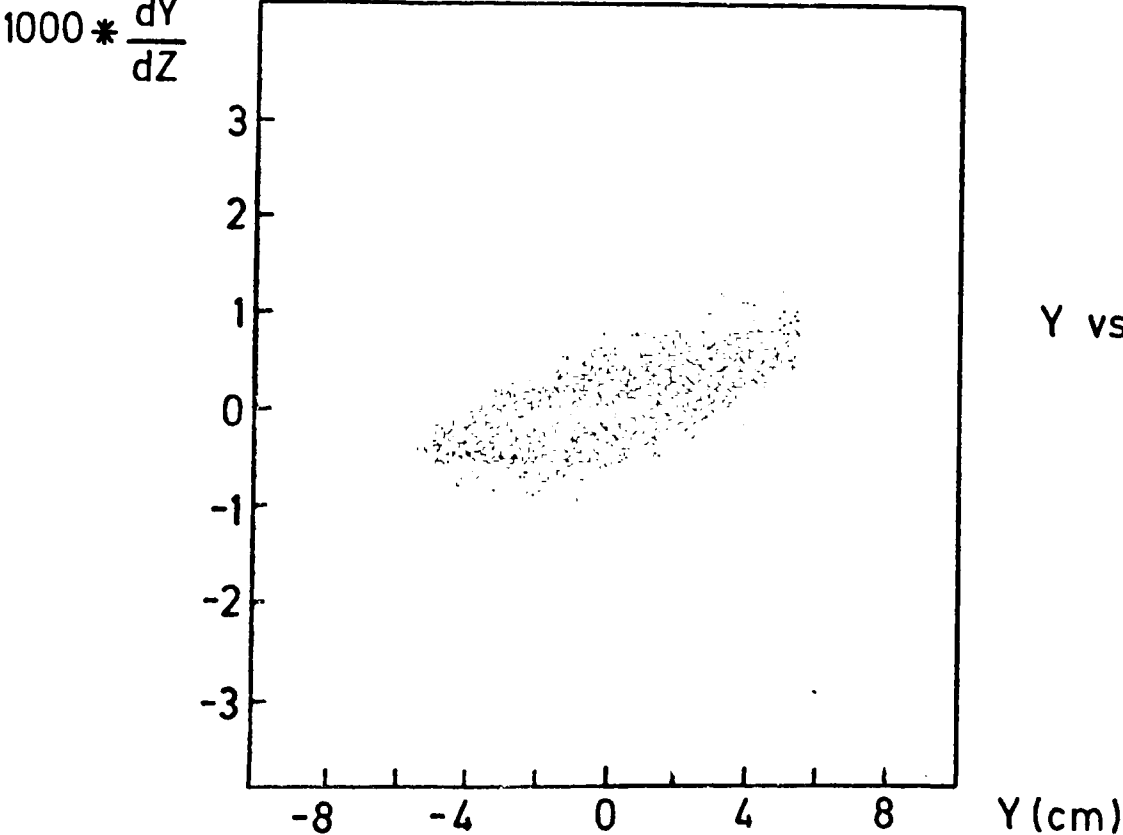


FIG. 2·6 (c)

Y vs Y ANGLE W.R.T.
Z - AXIS

BEAM PHASE SPACE FOR 147 GeV/c DATA

FIG 2.6(d)
X-DISTRIBUTION

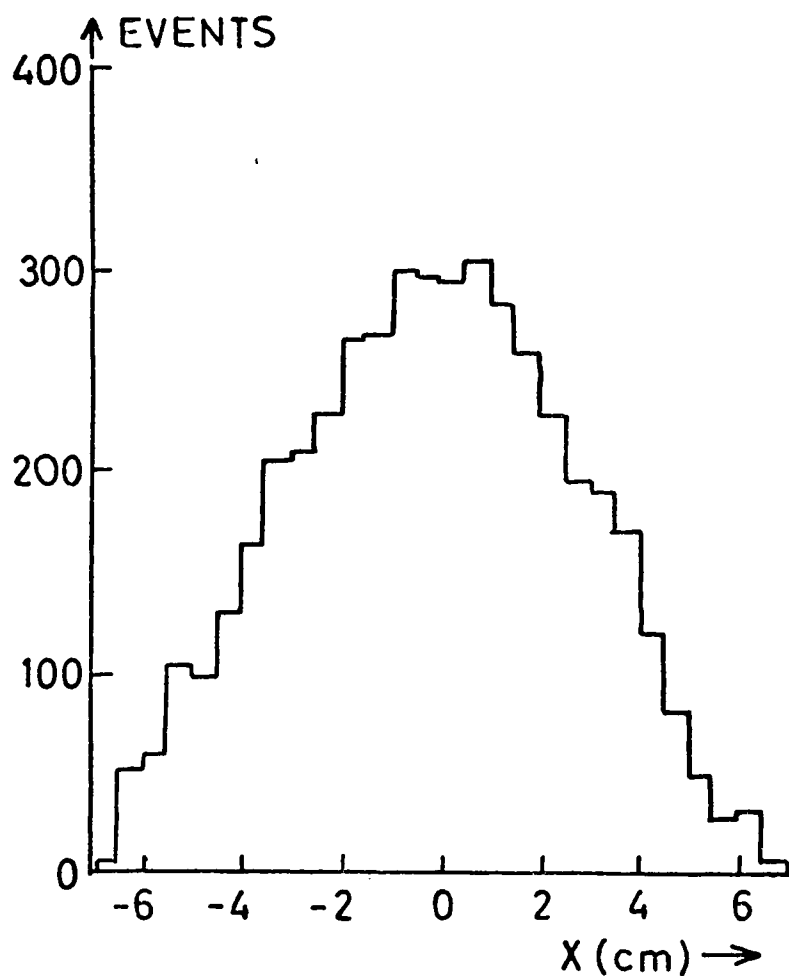


FIG 2.6(e)
Y-DISTRIBUTION

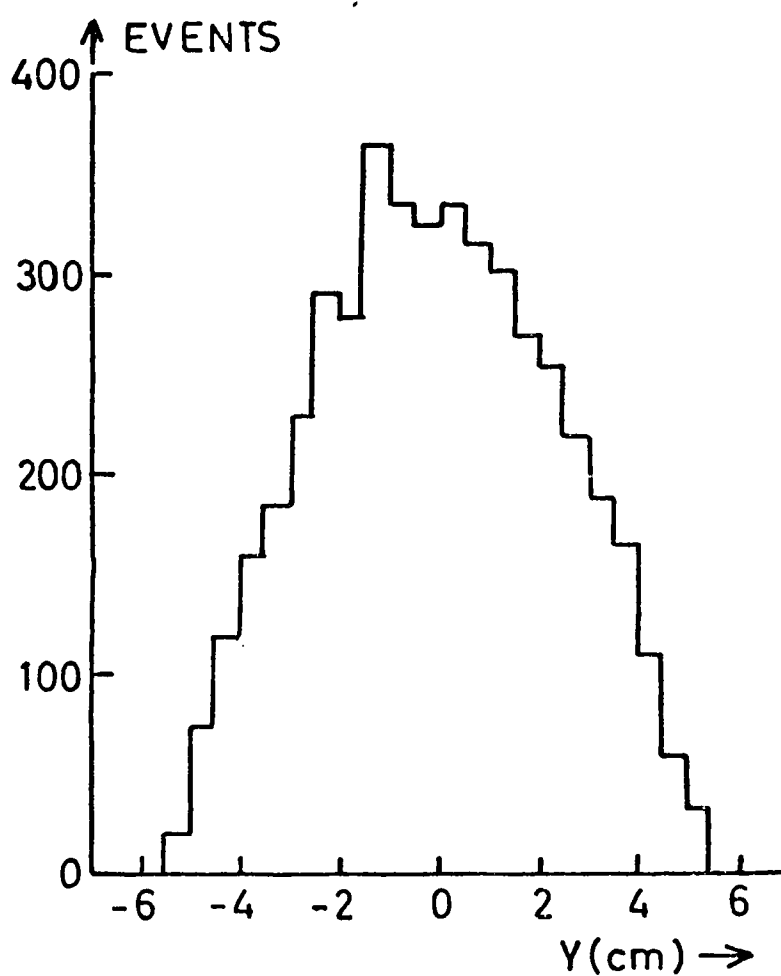


FIG 2.6(f)
X-ANGLE W.R.T.
Z-DIRECTION

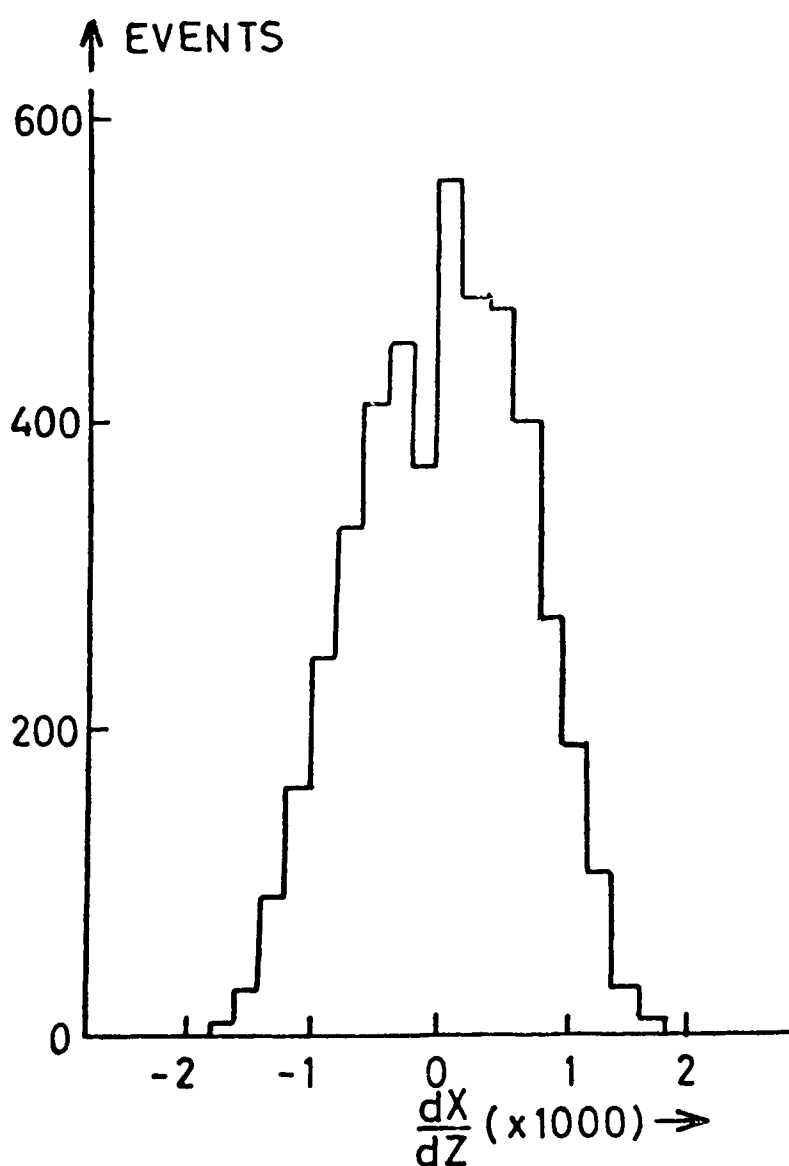
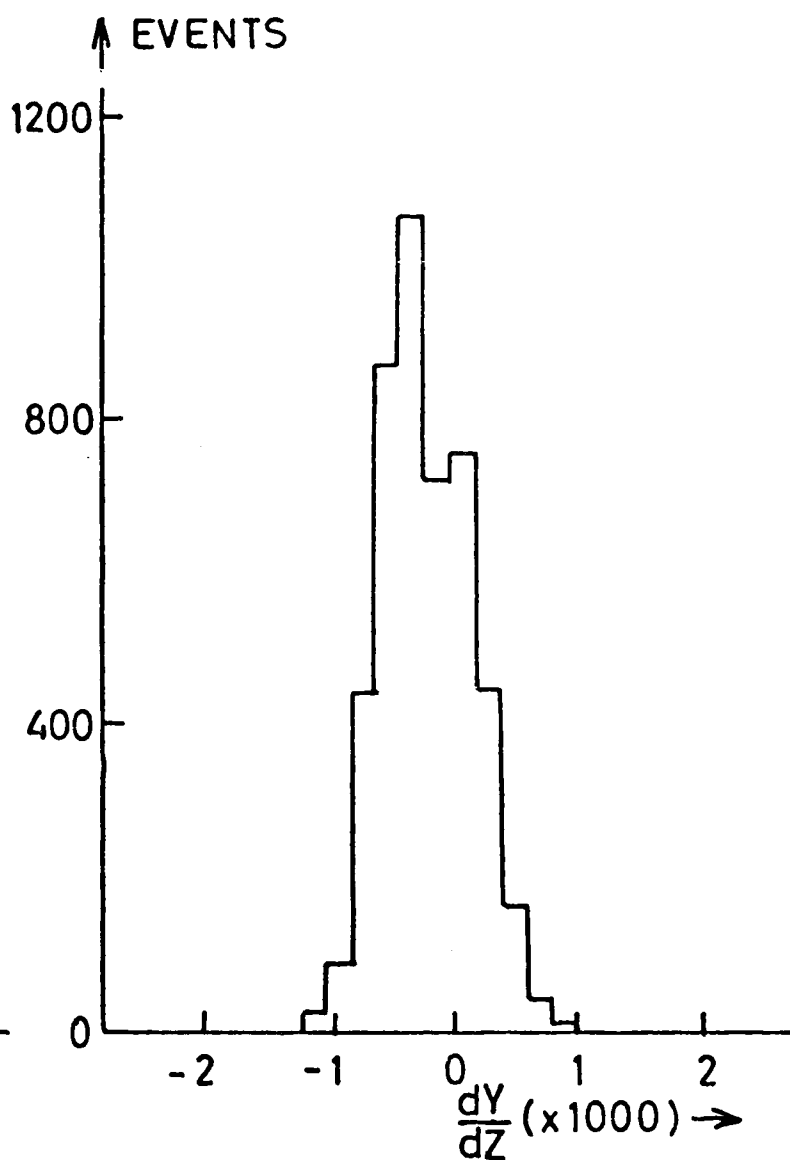


FIG 2.6(g)
Y-ANGLE W.R.T.
Z-DIRECTION



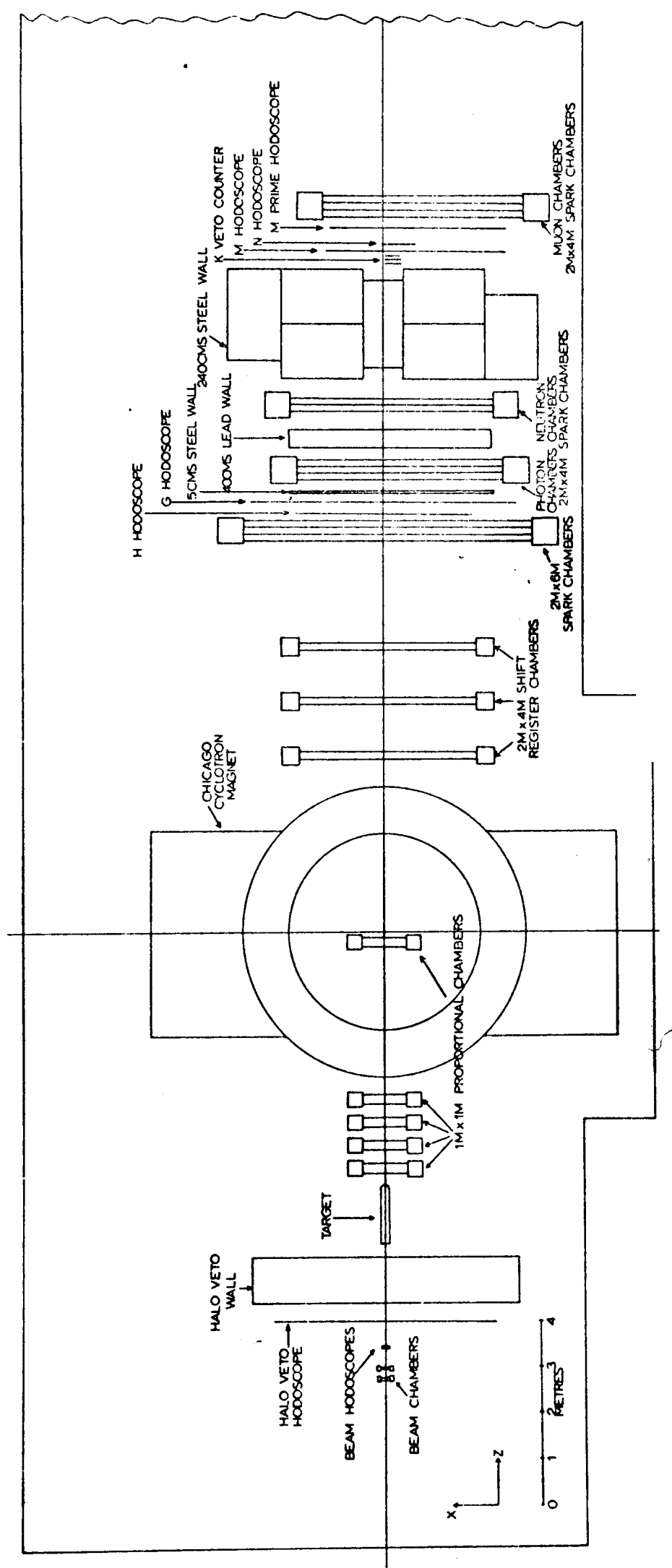
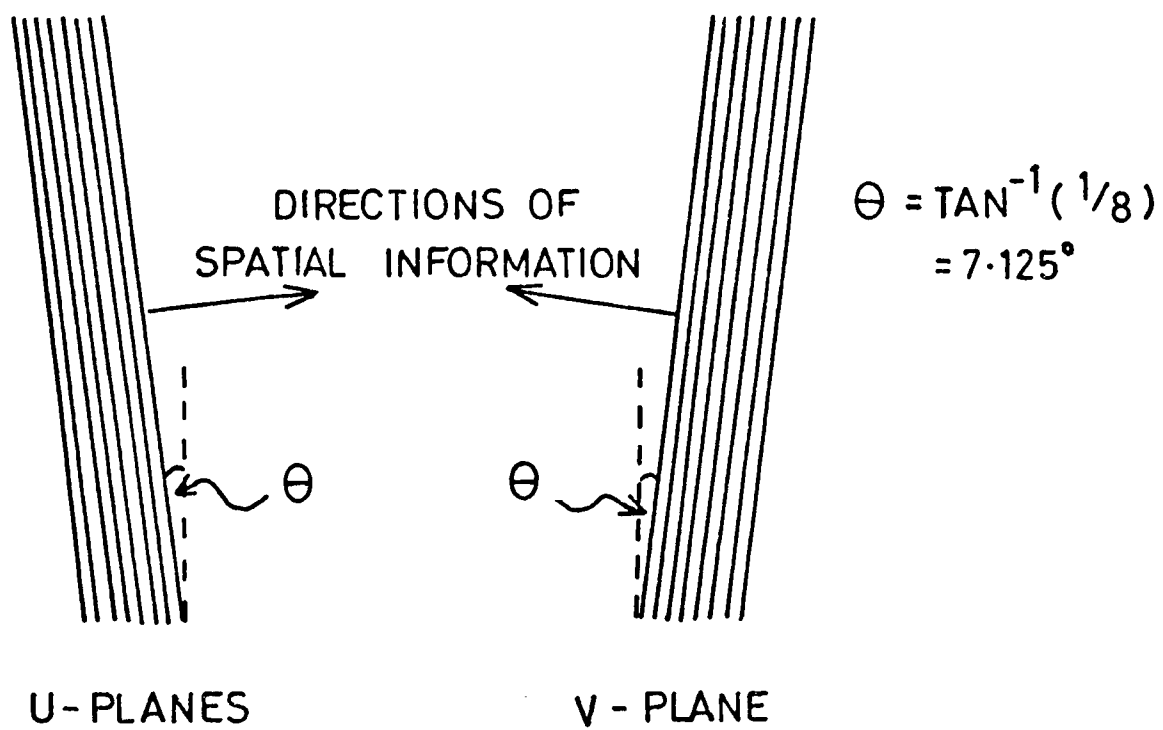
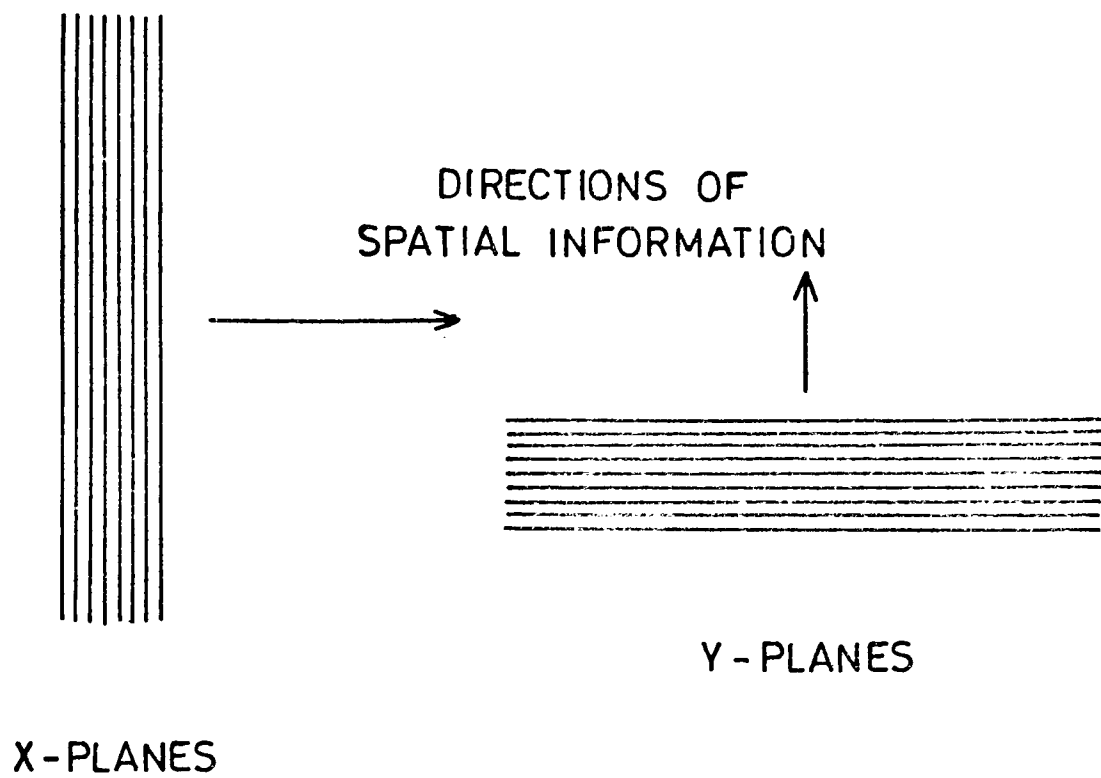


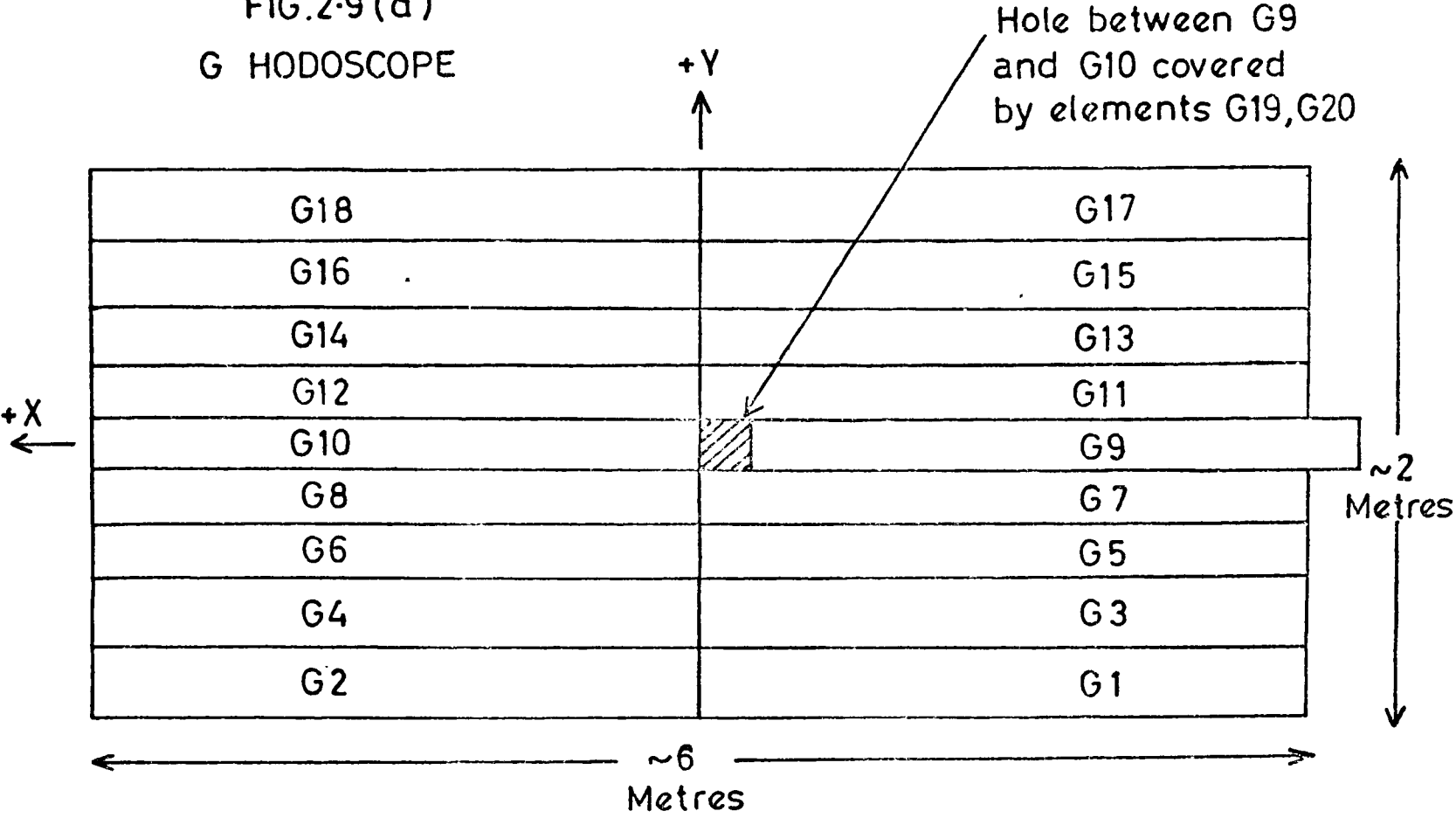
FIG.2-7 DIAGRAM OF THE SPECTROMETER APPARATUS.



WIRE CHAMBER NOMENCLATURE.

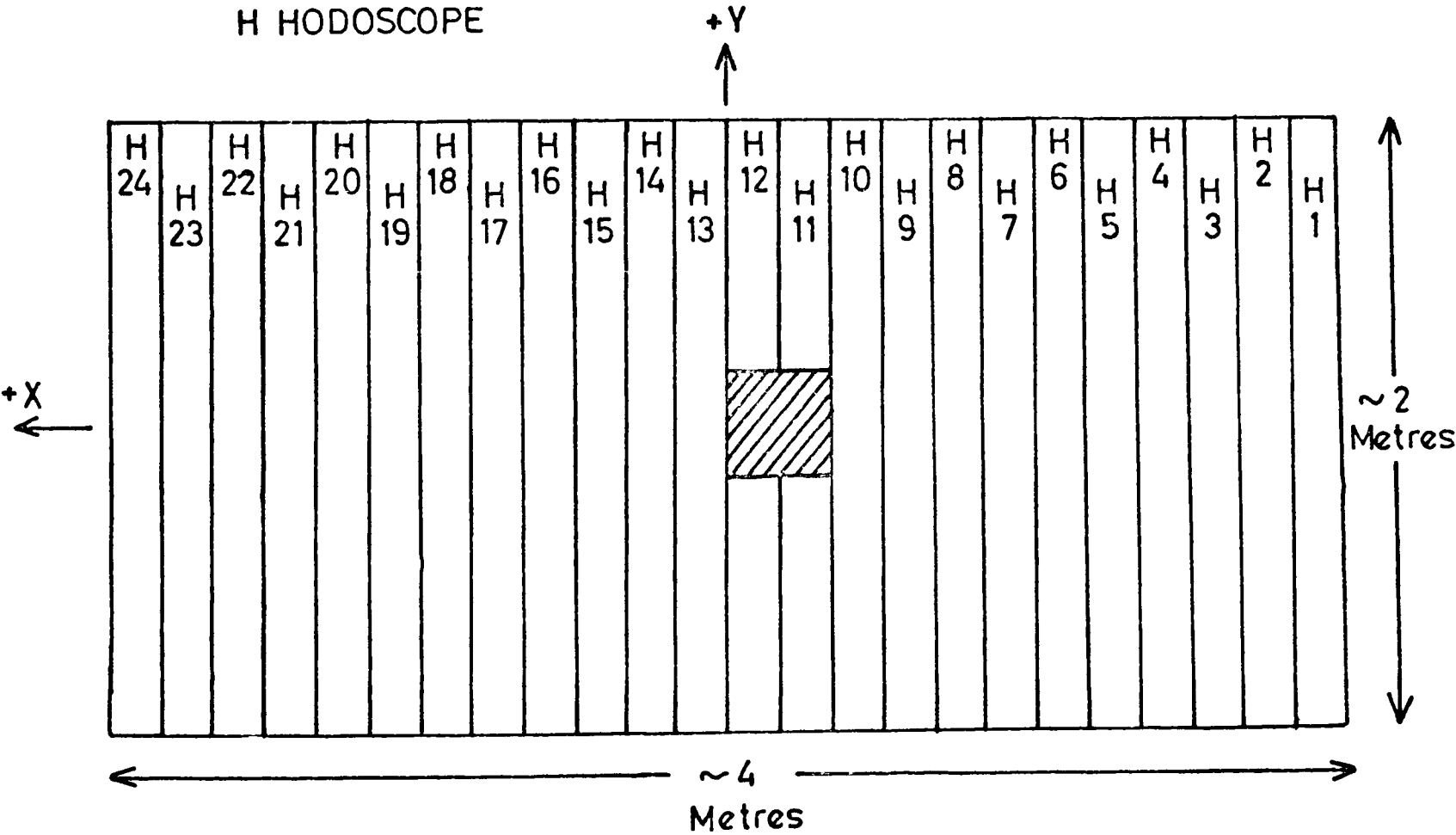
FIG. 2-8

FIG.2-9 (a)
G HODOSCOPE



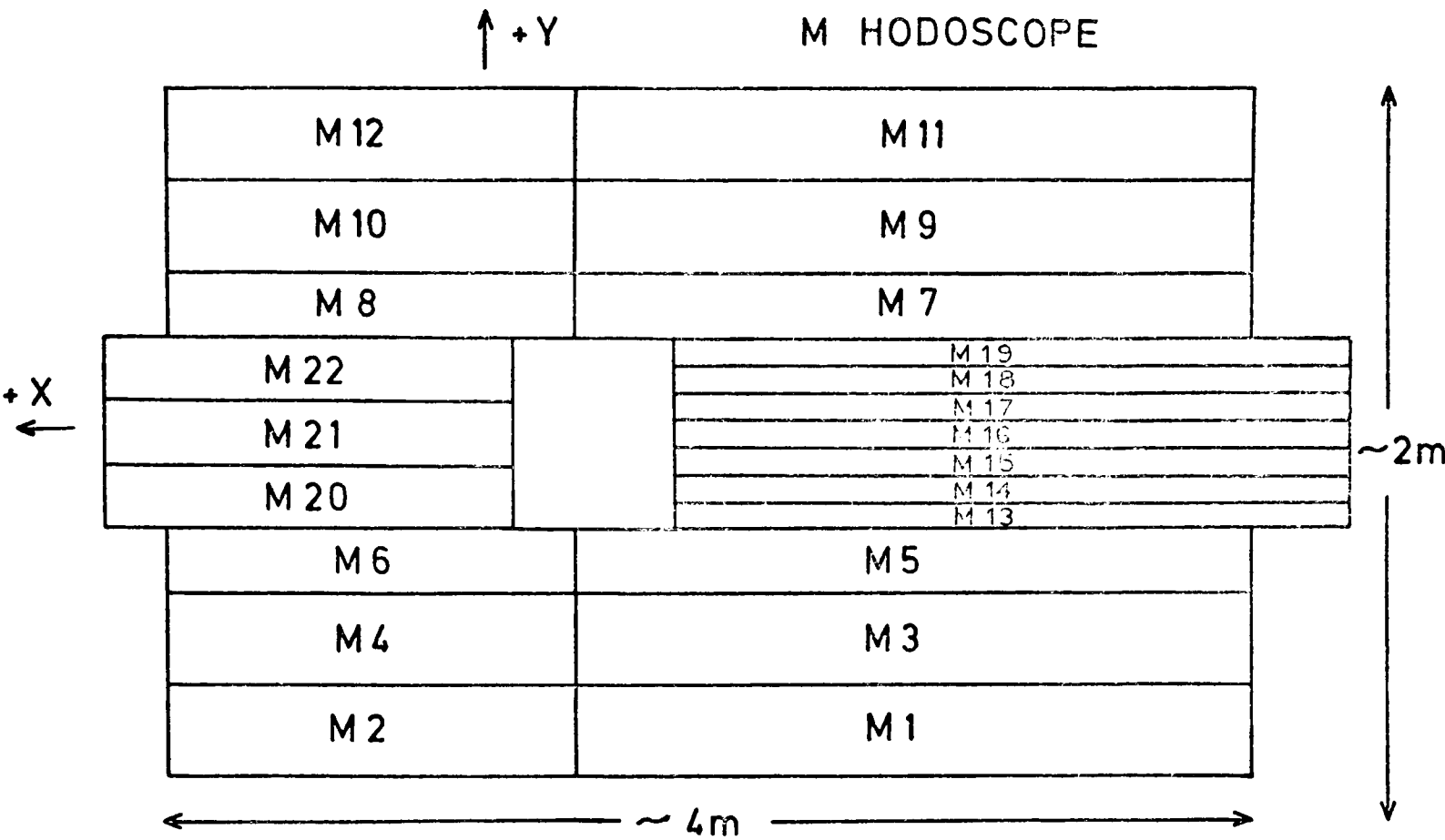
COUNTER ELEMENT	DIMENSION
G1 - G4 , G15 - G18 G5 - G14	27.5cm x 300cm x 2cm 18 cm x 300cm x 2cm Overlapped 1/2 cm
H1 - H24	18 cm x 200 cm x 2cm Overlapped 1cm

FIG. 2-9 (b)
H HODOSCOPE



LOOKING DOWNSTREAM ALONG Z AXIS.

FIG, 2.9 (c)



LOOKING DOWNSTREAM
ALONG Z DIRECTION

COUNTER	DIMENSIONS	COUNTER	DIMENSIONS
M1, M3, M9, M11	27.5cm x 250cm x 2cm	M13 - M19	7.7cm x 250cm x 2cm
M2, M4, M10, M12	27.5cm x 150cm x 2cm	M20 - M22	18.0cm x 150cm x 2cm
M5, M7	18.0cm x 250cm x 2cm	ELEMENTS SLIGHTLY OVER LAPPED	
M6, M8	18.0cm x 150cm x 2cm		

FIG. 2.9(d)
N HODOSCOPE

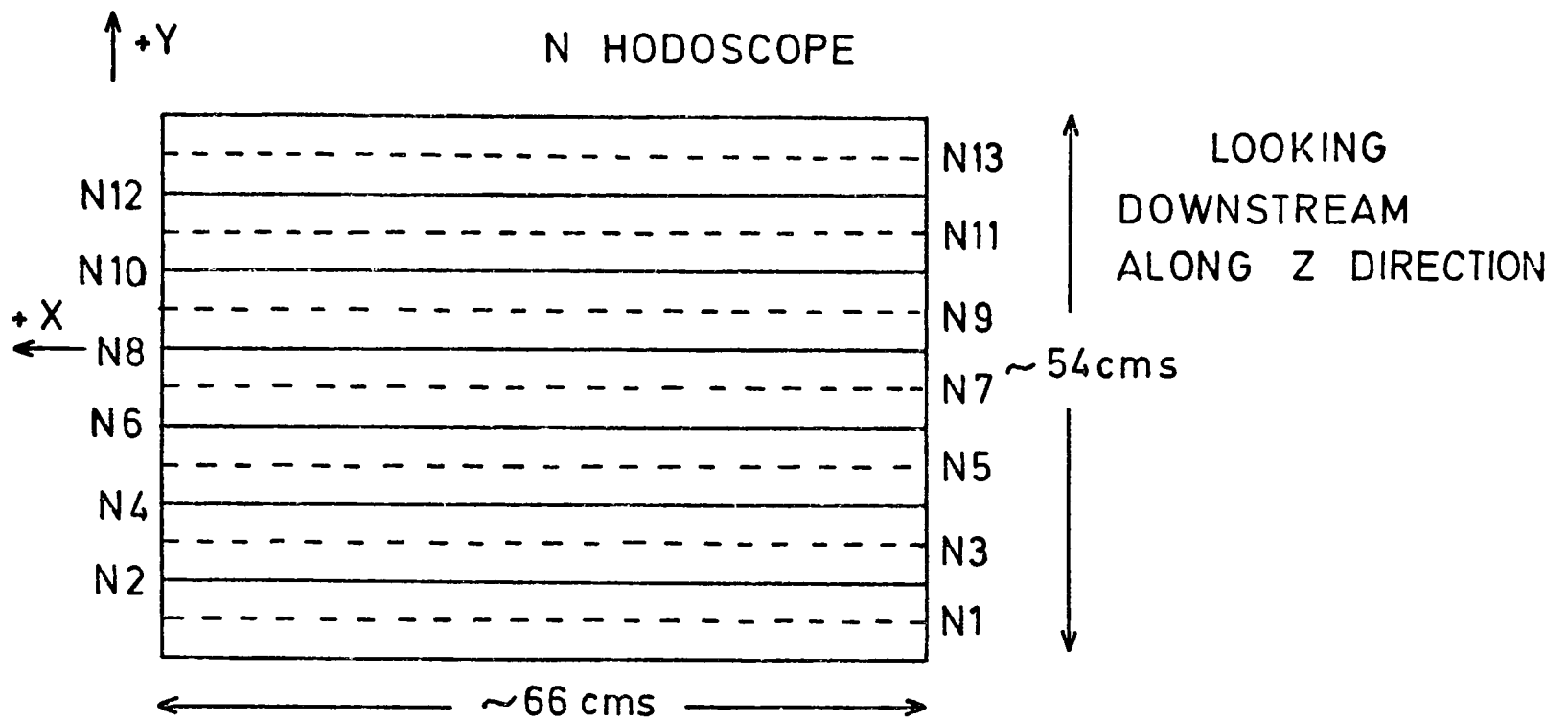


FIG. 2.9(e)
M' HODOSCOPE

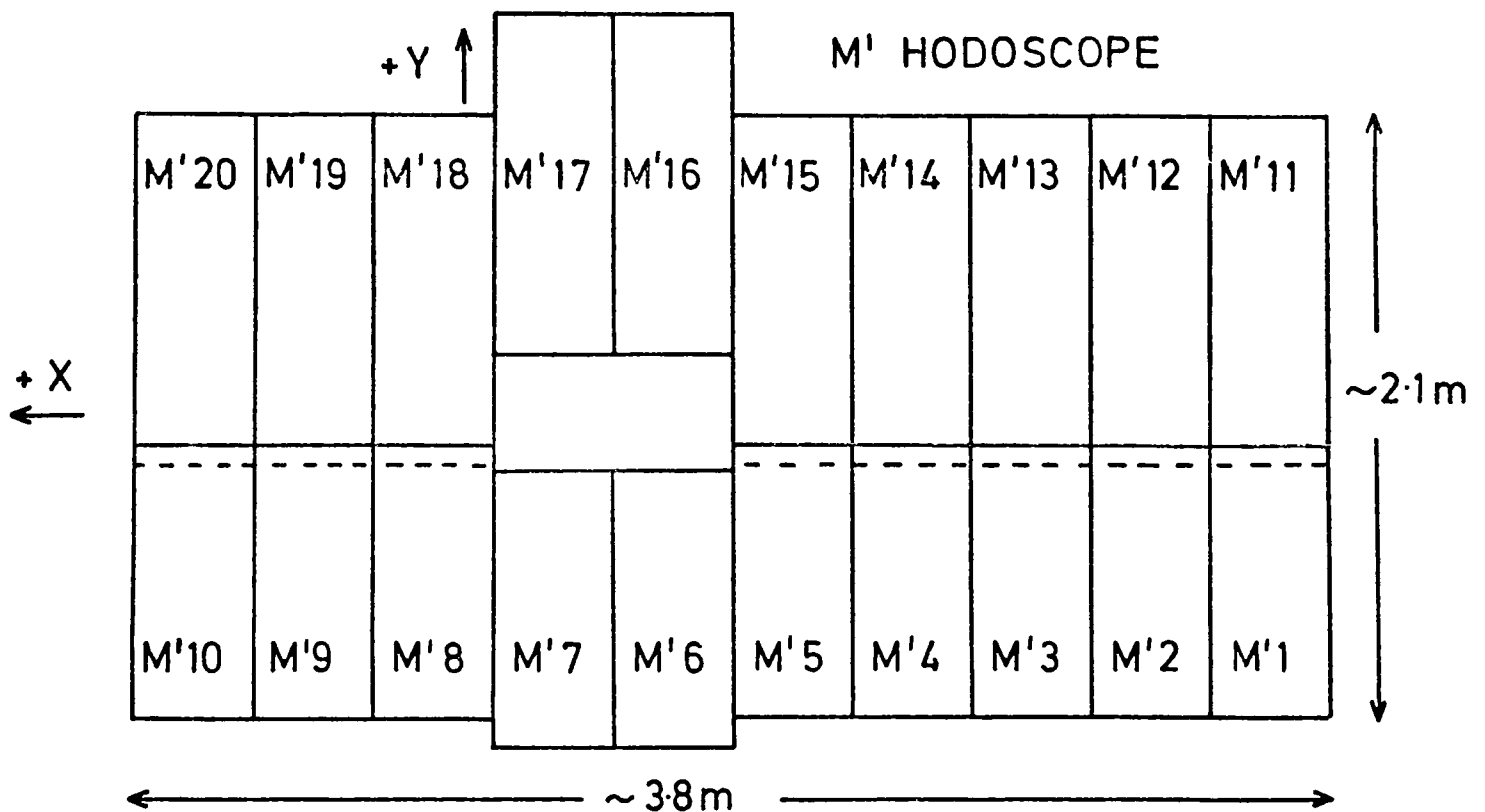
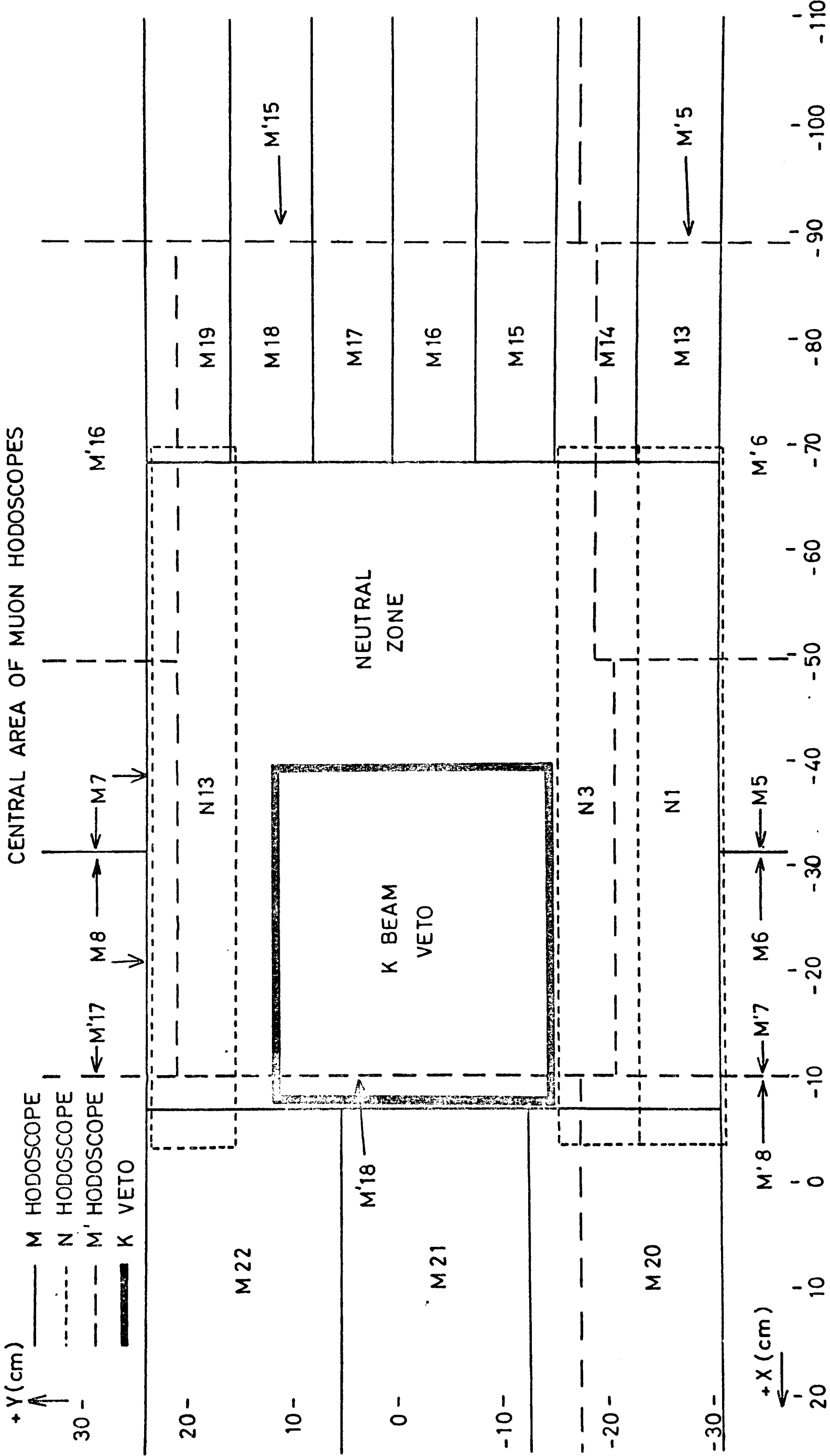


FIG. 2-10



CHAPTER 3

SET-UP AND DATA-TAKING

3.A INTRODUCTION

This Chapter describes some aspects of the set-up and data-taking in the experiment. Sections 3.B and 3.C are mainly concerned with the electronic logic, the first describing the philosophy of the trigger and its associated fast electronics, the second looking at the gating and read-out logic. Section 3.D contains a description of the on-line program and of the various monitors necessary for the running of the experiment. Section 3.E contains some details of the setting-up of the scintillation counters and the trigger. Two additional necessary measurements are described in the last two sections of this Chapter. Section 3.F looks at an experimental estimate of the residual pion contamination of the muon beam and Section 3.G describes the measurement of the magnetic field of the CCM.

3.B FAST ELECTRONICS

The purpose of the fast electronics is two-fold. Firstly, it recognises and provides a trigger signal when a muon scatters out of the beam. Secondly, it forms various coincidences which are recorded on visual and CAMAC scalars. This scaler information is useful for hardware debugging and for the setting up of the trigger and essential for various calculations in the analysis.

Muon Scattering Trigger - Figure 3.1 is a schematic attempt at a three-dimensional picture of how a scattered muon "sees" the triggering counters

and hodoscopes. Figure 3.2 is a simplified diagram of the apparatus showing the trigger logic. Basically the requirements for a scattered muon are that:

- (a) it should be in the beam upstream of the target,
- (b) it should not be in the beam at the K beam veto counter,
- (c) it should go through one of the elements G1-G18 in the G hodoscope,
- (d) it should go through at least one of the M, N, M' hodoscope elements that are in the chosen acceptance region. For the datasets on which this thesis is based, these elements are M1-M22, M'1-M'20 and N1, N2, N3 and N13.

From these requirements it is seen that the coincidence defining a scattered muon is $B.\bar{K}.G.M$, the "." symbol representing a logical AND. Using the "+" symbol to represent a logical OR, K, G and M are defined as follows:

$$K = K1 + K2 + K3$$

$$G = \sum_{i=1}^{18} G_i$$

$$M = \sum_{i=1}^{22} M_i + \sum_{i=1}^{20} M'_i + N1 + N2 + N3 + N13$$

The definition of the beam, B, is slightly more complicated. The simplest construction of B, which is a coincidence of $T = T1.T1A.T2.T3$ vetoed by a hit in any of the beam veto counters V1, V2, V3, V4, V5 and the Halo Veto hodoscope, has to be modified to allow for two effects of the time structure of the muon beam. The first effect arises when there are two or more muons in the same r.f. bucket - see Section 2.B. In this case the T coincidence will register one count and should one of the

muons scatter in the target, the event will be vetoed by the other muon(s) going through the K counter. To ensure that the beam and triggers are being scaled accurately all r.f. buckets that contain more than one muon must be rejected. This is effected by demanding that each of the beam hodoscopes BH2, BH3, BH4, BH5 and BH6 do not have two or more elements hit. This condition also helps reject beam muons that have interacted in the material in the beam line. The second effect arises when two muons come down the beam line in successive r.f. buckets. The problem occurs if the first muon showers in the 240 cm steel wall, thereby producing large pulses in the K counters. These large pulses might disable either the photo-tube bases or their associated discriminators such that the K-veto cannot produce a pulse when, 18 nsec later, the second muon passes through it. The logic will then say that the second muon has satisfied condition (b) above. In these cases random coincidences between the G and M hodoscopes or halo particles going through the G and M hodoscopes can produce damagingly large numbers of spurious triggers. To avoid this situation, the coincidence T1.T3 in one r.f. bucket vetoes the next r.f. bucket. So defining:

$$T = T1.T1A.T2.T3$$

$$V = V1 + V2 + V3 + V4 + V5 + \sum_{i=1}^{20} HV_i \quad HV = \text{Halo Veto hodoscope}$$

$$BH = \sum_{J=2}^6 \left[\left(\sum_{i=1}^8 BHJ_i \right) > 1 \right]$$

$$RF = (T1.T3) \text{ in previous r.f. bucket}$$

then it is seen that

$$B = (T.\overline{BH}.\overline{RF}).\overline{V}$$

One can comment that the reason why one needs both G and M in coincidence in the B. \bar{K} .M.G trigger is to avoid triggering on those muons that scatter

in the three walls - 5 cm steel, 40 cm lead and 240 cm steel - and hit the M counter hodoscopes.

Electronics - Figure 3.3 is the complete diagram of the fast electronics.

The apparatus is triggered on the B. \bar{K} .M.G coincidences described above and on every 4 millionth beam muon, the latter being labelled as beam events. These "imbedded" beam triggers provide an unbiased sample of the beam well dispersed within the data, with which to calculate the efficiency for tagging the incoming muon beam. These triggers also turn out to be extremely useful in the data analysis for calculating counter positions and for determining various inefficiencies in the apparatus. In addition to this basic trigger, B. \bar{K} .M.G + imbedded Beam, the apparatus may be triggered by various other coincidences - such as B, B. \bar{K} .M, B. \bar{K} .M.H, V.G.H. The most useful of these proved to be the beam trigger, B, and the halo trigger, V.G.H, and a few runs were taken with each of these triggers. These runs are mainly useful for checks on the beam apparatus and for aligning the wire chambers of the experiment. The beam hodoscope elements and the G, H, M, N, M' hodoscope elements are all latched - i.e. tested to see if they are lit - after a trigger pulse. This latching information is used to determine the timing of tracks found in the spark chambers by the subsequent track-finding analysis. The coincidences marked scalers in Figure 3.3 are all read into CAMAC and in addition the more important ones are displayed on visual scalers at run time. The quantities B, T, V.G.H. (halo) and the number of protons incident on the primary target are displayed on a main ring acceleration pulse to pulse basis. These enable a close watch to be kept on the performance of the muon beam line and are extremely useful when beam tuning. One should also take note of the various

"delayed" coincidences - these may be recognised by the " Δt " symbol in their names in Figure 3.3. These are set up by delaying the relevant signal by an integral number of r.f. buckets - usually three. These delayed coincidences are a direct measure of the various random rates in the experiment. At run time these rates enable one to appraise the quality of the beam and of the data being collected, and in the analysis they are used for calculations of the correction that must be applied to remove the more obvious random losses.

3.C GATING AND EVENT LOGGING

When the fast electronics generates a trigger, the following actions have to be taken to successfully record the event information onto magnetic tape.

- (a) The counters have to be latched and read into CAMAC.
- (b) The MWPC wire information has to be stored.
- (c) The spark chambers have to be fired and their wire information stored.
- (d) The wire information has to be decoded into CAMAC format.
- (e) The event information - i.e. counter latches, scalers, ADCs, wire information - has to be read from CAMAC into the on-line computer.
- (f) The event information has to be re-organised and blocked and written onto tape.

In addition to these tasks, two gating pulses have to be constructed for the fast electronics and CAMAC. The first, Gate 1, disables the trigger and scalers during the time the spark chambers are firing and ensures that the scalers do not pick up spark chamber noise. The second, Gate 2, disables the trigger and scalers during the time taken to record the event information.

Figure 3.4 is a diagram of the logic controlling the timing

The timing sequence is controlled by the RUN box - the master gate of the experiment. The START and STOP pulses are derived from the main ring clock pulse and ensure that data taking occurs during the accelerator extraction only. The $\overline{\text{RUN}}$ input stops data taking and is used to stop event logging when changing runs or checking hardware faults. Figure 3.5 shows the simplified timing sequence produced by the RUN box on receipt of a trigger from the fast electronics. The trigger pulse is fanned out to produce six "prompt" - i.e. within 10 nsec outputs. First the prompt outputs open the gates on the scintillation counter latches and on the MWPC read-outs. The spark chambers fire within 100 nsec of receiving a prompt signal to do so. When the spark chamber noise has died down, the various chamber read-out systems set to work on decoding the wire information into CAMAC output format. To get some idea of the time scales involved in these operations, one may comment that the spark chamber noise dies down in typically a few microseconds and that it takes a few milliseconds for a magnetostrictive pulse to travel along its spark chamber wand. 3 μsec after receiving an input trigger, the RUN box triggers the on-line computer. The latter reads the event information in the following order:- the latches and scalers, the MWPCs, the shift register chambers, and the magnetostrictive chambers. When this reading is completed, the computer sends a signal back to the RUN box. The whole reading-out process takes on average 44 msec. to complete from the time a trigger pulse goes into the RUN box. The RUN box also has a fixed delay which was set to 30 msec during data-taking. If the computer reset comes in before this time, the RUN box waits until the end of this fixed delay before accepting any more triggers. If the reset comes in after the end of the fixed delay, the

RUN box may accept triggers immediately. This means that the dead-time of the apparatus is at least this fixed delay for every trigger and ensures that the magnetostrictive spark chamber power supplies have sufficient time to recover and thus be sparked efficiently again.

Figure 3.6 is a schematic diagram of how the two experimental gates are constructed. Gate 1 is necessitated by the fact that the magnetostrictive spark chambers generate a large amount of r.f. noise when being sparked. This can cause counting errors if it is picked up by the scalers. Gate 1 gates off scalers for 5 μ sec after a trigger goes into the RUN box. Any scaler that is said to be "ungated" is in fact gated by Gate 1. Gate 2 is used to gate off the scalers while the event information is being read into the computer - i.e. from the time the trigger goes into the run box to the time the latter is ready to accept more triggers. Any scaler that is gated by Gate 2 is said to be "gated". Both Gates 1 and 2 are of course off outside of the main ring beam spill or when $\overline{\text{RUN}}$ is holding the event taking. It is apparent that the ungated scaler numbers derive from the total available beam and the gated scaler numbers from the beam actually used by the experiment. Comparison of gated coincidences to the corresponding ungated coincidences give a monitor of the experimental dead-time.

Table 3.1 contains a list of all the gated and ungated scalers accumulated in the experiment together with their values from some typical runs. Table 3.2 lists some rates calculated from these numbers.

3.D ON-LINE CONTROL AND MONITORING

The on-line data acquisition system is centred on an XDS $\Sigma 3$ computer. This has 64K of 16-bit core memory and $\frac{1}{2}$ megabyte disk. Its peripherals include a card reader, a teletype, two 9-track 800 bpi tape drives, a line printer and a Tektronix 613 storage scope.

It is also attached to the CAMAC system of the experiment.

On-Line Program - The on-line program has two major functions.

Firstly, it has to control the hardware and log the event information. Secondly, it has to calculate, accumulate and display various quantities that indicate how well the apparatus is performing. Obviously these functions must be ordered such that the system collects data in preference to displaying information. To this end, the computer has a series of interrupts to which various tasks may be assigned. These define an order of priority such that if the computer receives an interrupt higher than the one it is on, it will stop the task it is doing and proceed on to the task associated with the higher interrupt. On completion of this task, it goes back to the task associated with the lower interrupt.

Figure 3.7 is a simplified flow diagram of the on-line program.

The event information is read out from the CAMAC. It is then organised and blocked into 600 word records. The number of records per event depends on the complexity of the event - i.e. the total number of sparks. It is typically 2 and can be up to a maximum of 4 records per event. The information in these records is in the order:- scaler and counter latching information first, the MWPCs, Muon and downstream momentum measuring planes second, and the Photon and Neutron chambers last. As the latter are associated with by far the largest number of sparks - generated by the various showers - the above order ensures that in the rare case that an event overflows the maximum number of records, the most essential information is always written. The records for events within one beam spill are stored in core. There is room for 20 records which sets a limit of about 10 events/pulse in the experiment. At the end of the beam spill all the events collected in that spill are written onto tape.

The tasks above are set on the highest interrupts and are always done first. While the on-line program is not reading and writing data:

- (a) it monitors the beam-line magnet currents and also the current in the CCM. This is done once a machine spill and the information from the CCM and the D4 dipole magnets is recorded so that it can be written into the event records.
- (b) It accumulates various counter and coincidence rates and also the spark distribution patterns of the wire chambers. This information - called a SAGA output - may be printed out at any stage and provides the first indication of any apparatus malfunction.
- (c) It displays events on the storage scope. This display has a simple version of the track finder and gives an indication as to the quality of data being taken. Various wire chamber read-out problems - such as dropping bits in the spark addresses or missing the fiducial sparks - can be diagnosed by looking at the event displays.
- (d) It displays on the storage scope various histograms - such as plane by plane spark distributions and beam phase space histograms - and other information. These are useful for specific hardware debugging.

The choice of the various on-line program options lies with a set of 32 sense switches and two thumbwheels that are linked to specific addresses within the $\Sigma 3$ core memory.

Additional Monitoring - In addition to this monitoring of the apparatus by the on-line program, the experiment also has access to the Neutrino Laboratory's monitoring and control system. This system gives the status

of the accelerator and of the beam-line magnets and enables the experimenters to tune the muon beam. FNAL also has a TV network which provides more or less general information about the running of the entire laboratory and indicates how the experiment stands vis-a-vis the rest of the FNAL experimental program.

Two other monitors should be mentioned at this stage. Firstly, the hydrogen target has its own safety and control system and checks can be made to establish that the target is indeed full or empty. Secondly there is a storage scope display that shows the intensity distribution of the beam within the beam spill. Superimposed on this display is the distribution of triggers within the beam spill. This allows a check to be made to see if events are associated with any time structure - i.e. high intensity spikes - in the muon beam.

3.E TRIGGER SET-UP AND DATA TAKING

One aspect of the experiment for which the author had particular responsibilities was the scintillation counter system. This section starts off with a brief outline of a few techniques in the setting-up of scintillation counters - the operational details of and physics underlying scintillation counters may be found in Ref. (55). It then goes on to describe the trigger set-up and makes a few observations on actual data taking.

Clipping - The technique of clipping is used to shape the output pulses of photomultiplier tubes and of the various logic units used in the electronics. This is done by combining the direct output pulse with its reflection in a short length of cable. A pulse, its reflection in a length of cable open-circuited at the end, and its reflection in a length of cable short-circuited at the end are shown in Fig. 3.8(a).

Two specific uses of clipping are described here. The first uses an almost shorted clipping cable - i.e. a cable with $10-40\Omega$ at its end - to shorten the width of the photomultiplier output pulse - see Figure 3.8(b). Although the tube base has to be run at a higher voltage to produce a given pulse height - giving rise to higher noise rates - it is found that for high pulse rates the discriminator to which these pulses feed works more efficiently for narrower input pulses. All the counters with high rates - i.e. those in or near the beam - are so clipped. The second mode of clipping is illustrated in Figure 3.8(c). An open clipping cable is used to double the width of an output pulse from a discriminator. This has the advantage that in the second half of the clipped output pulse the discriminator is actually ready to accept another input pulse, thereby reducing the discriminator dead-time for a given width output.

Plateauing - It is obviously important to ensure that the scintillation counters in the experiment are highly - i.e. $>99\%$ - efficient in detecting particles that go through them. Plateauing a counter determines the lowest voltage - and hence the lowest noise rate in the counter - that is required for the phototube base consistent with this high efficiency. The set-up used to plateau the counter C2 is schematically illustrated in Figure 3.9(a). A coincidence of the counters C1 and C3 are used to define particles that go through C2. Using the above circuit the rate $C1.C3.C2/C1.C3$ is obtained as a function of the voltage on the C2 phototube base. Figure 3.9(b) shows a typical plot of the variation of this rate with the base voltage. The flat portion of the curve - called a plateau - corresponds to where C2 begins to register

all the particles going through it. The C2 phototube base voltage is set 50-100 volts - this being a good safety margin - above the shoulder of the plateau, thereby ensuring a high efficiency and a low noise rate for the counter. Two additional comments may be made. Firstly the transit time across a photomultiplier tube varies as a function of the voltage on the tube - typically 0.5 nsec per 100 volts, total transit times being approximately 30-40 nsec for most of the tubes used in the experiment. Because of this the C1.C3 coincidence is made quite wide ensuring that the C2 signal is still in time over its entire voltage range. Secondly, if C2 is a large counter, care has to be exercised to ensure that it is plateaued over its entire area. This is most easily done by overlapping C1 and C3 with that part of C2 that is furthest from the C2 photomultiplier tube.

Timing - Having determined and set the plateau voltages on all of the counters, the next stage in the electronics set up process is to ensure the counter pulses associated with any particular event arrive at the various coincidence units of the fast electronics at the same time. Looking back to the electronics diagram, Figure 3.3, it is seen that this may be achieved by timing in the beam counters - both trigger and veto counters - relative to each other and by making the outputs of the B, K, G, H and M fanouts to be in time with each other. The basic circuit used for timing, Figure 3.10(a), is essentially the same as that used to plateau counters. This time however the C1.C3 coincidence is made as narrow as possible and the rate $C1.C3.C2/C1.C3$ is plotted as a function of the delay in the C2 signal, this rate being a maximum at the timed position. In practice the timing

of all the counters in the experiment is done relative to the T3 signal. T3 is a small counter approximately 9 cm in diameter. Its discriminator output is set to give a very narrow - 3nsec - output pulse. Using an oscilloscope, the coincidence C1.T3 is roughly timed by ensuring that the T3 signal lies within the C1 signal. The output from this coincidence is a pulse whose width is the same as T3 and whose timing depends only on T3. A plot of the rate $C1.T3.C2/C1.T3$ against the delay in the C2 signal will then give the timing of C2 relative to T3 independent of the exact timing of C1. Figure 3.10(b) shows a typical timing curve. For a counter or set of counters that are to be used in veto, a plot of the rate $C1.T3.\bar{V}/C1.T3$ as a function of the delay on V is made, this rate being a minimum at the timed position.

The timing of the large hodoscope elements requires a little more effort. These elements are made of type NE110 scintillator which has a refractive index of 1.5. This means that for a counter of length ℓ , there is a slop in the timing of the output pulses of approximately $2.2 \ell/C$ - C = speed of light and allowing for reflections in the scintillator - depending on exactly where the particle goes through the counter. Because of this, care has to be taken to ensure that the signal from a long counter is in time regardless of exactly where the associated particle goes through it. To demonstrate how this is effected, the timing of the G-hodoscope is specifically described. Figure 3.11(a) shows the electronics associated with the G-hodoscope. An undeflected beam - i.e. with the CCM off - is defined by a coincidence of T3 and a small counter X set-up at the back of the apparatus. The beam so defined passes principally through the G10

element at its end furthest from the photomultiplier tube - this corresponds to the latest G signal. The output of the G discriminator is clipped so that its total output width is approximately $2.2 \ell/C + 10$ nsec. This corresponds to about 30 nsec for the 3 metre long G hodoscope elements. A T3.X coincidence is made at the T coincidence unit - see the fast electronics, Figure 3.3 - and fed through the logic to the B fan-out. The delay on the G signal is then fixed by triggering an oscilloscope on the G fan-out signal and arranging for the B fan-out signal to arrive 5 nsec after the G signal - see Figure 3.11(b). This ensures that the latest possible G signal is still in time with B and the width of the G signal ensures that all other G signals will also be in time. This process is repeated for the other hodoscopes and the B signal is placed inside the hodoscope depending on exactly where the beam intersects with the hodoscope elements.

Counter Geometry - Having cabled up and timed in all the electronics, the next stage of setting-up is to determine the optimum positions of the beam veto counters and the Triggering configuration of the M, N, M' counter elements - see Sections 2.C and 2.D. The holes in the veto counters V1, V2, V3 and V4 are set so as to be smaller than the aperture of the D4 dipole magnets. This helps to reject beam that is degraded in energy by scraping the insides of the D4 magnets. The V5 hole is set so that the beam, after it has been deflected and dispersed by the CCM, still lies within the K-counter. Horizontal and vertical scans of the K-counter are made. Plotting the $B.\bar{K}/B$ and $B.\bar{K}.M.G/B$ rates as a function of the X and Y co-ordinates of the K-counter gives the optimum position for the K. Next various combinations of elements of the M, N, M' hodoscopes are tried in the trigger and various trigger rates determined. Ultimately the geometry

of the muon hodoscope elements used in the trigger is that which gives a data taking dead-time of 20-30% - i.e. approximately 5 triggers per beam spill - and which also triggers on the most physically interesting events. In going from a 147 GeV/c incident beam to a 96 GeV/c incident beam, the magnetic field of the CCM is likewise scaled - i.e. 15 kilogauss for the 147 GeV/c data and 9.45 kilogauss for the 96 GeV/c data. Because of this the position of the K-veto and the configuration of the muon-hodoscopes does not have to be changed, and indeed checks are made to ensure that this is in fact the case.

Data-Taking - Finally to end this section the following few observations may be made. When everything is running smoothly, the whole experiment can be operated by two persons. During the course of an eight-hour shift, a continuous watch is kept on the various monitors and on the beam-line. Various parameters in the experiment itself - such as counter voltages, the chamber voltages and gas systems, and the status of the read-out system - are checked once a shift. The SAGA outputs are printed out and checked every 1500 or so triggers. When the beam intensity is 10^6 muons/machine pulse, data tapes are written at the rate of approximately one every two hours and contain 5000-6000 triggers. In all about 140 data tapes were written during the course of the three-month running period on which this thesis is based, split 65/75 between the 147 GeV/c and the 96 GeV/c datasets.

3.F PION CONTAMINATION OF THE MUON BEAM (56)

A pion in the muon beam can cause an apparent muon scatter if firstly it interacts in the target and secondly one of the secondaries of this interaction decays in flight into a muon before reaching the 240 cm steel wall. Crude assumptions about the interaction cross-section of pions and about the energies and numbers of the various products from pion interactions suggest that this effect will give of the order of 0.01 event triggers per incident pion in our experimental configuration. An experimental estimate of this pion contribution to the trigger rate was made by measuring various coincidence rates for different lengths of the high density polyethylene absorber in the D3 - see Section 2.B - dipole magnets. The results of these measurements are given in Table 3.3.

The coincidence $B \cdot \bar{N} \cdot \bar{M}$ represents the number of particles in the beam that do not appear at the muon hodoscope plane. Figure 3.12 is a graph of the $B \cdot \bar{N} \cdot \bar{M} / B$ rate as a function of ℓ , the length of high density polyethylene absorber. An exponential drop in this rate - associated with the removal of pions from the beam - followed by a flattening off in the rate - consistent with the estimated number of positrons from muon decays after the polythene absorber - may be discerned from this graph.

The π/μ ratio in the beam is expected to vary exponentially as a function of the length of polyethylene absorber.

$$\frac{N_{\pi}(\ell)}{N_{\mu}} = \frac{N_{\pi}(0)}{N_{\mu}} \left[\exp\left(\frac{-\ell}{L_0}\right) \right] \quad \text{where } L_0 = \begin{array}{l} \text{pion absorption} \\ \text{length in the high} \\ \text{density polythene} \\ \text{and } N_{\pi}, N_{\mu} \text{ are the} \\ \text{numbers of pions and} \\ \text{muons.} \end{array}$$

If it is assumed that the measured $B.\bar{N}.\bar{M}/B$ rate at $\ell = 63$ ft is predominantly due to positrons in the beam, then

$$\frac{N_{\pi}(\ell)}{N_{\mu}} = \frac{B.\bar{N}.\bar{M}}{B}(\ell) - \frac{B.\bar{N}.\bar{M}}{B}\left(63 \text{ ft}\right) \quad \text{for small pion contaminations.}$$

From the π/μ ratios for $\ell = 40$ ft and $\ell = 50$ ft of absorber, it is trivial to calculate L_0 is approximately 4 ft and that

$$\frac{N_{\pi}(63 \text{ ft})}{N_{\mu}} \approx 1.6 \times 10^{-6}$$

This ratio indicates an event rate due to pions of the order of 1.6×10^{-8} per incident muon for an absorber length of 63 ft.

Looking directly at the event trigger rates - i.e. $B.\bar{N}.M.G/B$ rates - and assuming that the measured rate at $\ell = 63$ ft is predominantly due to muon interactions, it is seen that

$$\begin{aligned} \frac{B.\bar{N}.M.G}{B} \left(\begin{array}{c} 63 \text{ ft;} \\ \text{due to} \\ \text{pions} \end{array} \right) &= \left[\frac{B.\bar{N}.M.G}{B} \left(\begin{array}{c} 40 \text{ ft;} \\ \text{measured} \end{array} \right) - \frac{B.\bar{N}.M.G}{B} \left(\begin{array}{c} 63 \text{ ft;} \\ \text{measured} \end{array} \right) \right] * \exp \left(-\frac{23}{4} \right) \\ &\approx 5 \times 10^{-8} \end{aligned}$$

This estimate of the contribution to the trigger rate from a pion contamination in the beam is in substantial agreement with the above order of magnitude estimate of 1.6×10^{-8} for this rate.

In the end a total length of 76 ft - 23 metres - of high density polythene absorber was used in the D3 dipole magnets. This reduces the pion contamination to approximately 10^{-7} per muon and the pion induced event rate to the order of 10^{-9} per incident muon. At this level, the pion contamination of the muon beam is quite negligible.

3.G THE MAGNETIC FIELD OF THE CCM

This Section gives a brief description of the measurement of the magnetic field of the CCM and the use of the CCM as a spectrometer magnet. A more complete account of the field mapping may be found in Reference (57).

Field Measurement - Hall probes⁽⁵⁸⁾ are used to measure the magnetic field of the CCM in preference to the more accurate NMR method for two major reasons. Firstly, the NMR method requires a uniform magnetic field and measures only the magnitude of this field. The CCM field varies both in magnitude and direction as function of position. Secondly, Hall probes are considerably easier and quicker to set up and use.

In view of the cylindrical symmetry of the CCM, two Hall probes were used to measure respectively the vertical, B_y , and the radial, B_r - components of the CCM magnetic field at a series of grid points in a cylindrical co-ordinate system whose origin lay at the centre of the CCM. These grid points are listed in Table 3.4 and their extent is indicated in Figure 3.13. No attempt was made to measure the angular component, B_θ , of the magnetic field. The Hall probe mount was attached to a rigid vertical bar fixed on a pneumatic crawler, the latter running on a horizontal railway 190 inches long. The details of this arrangement are illustrated in Figure 3.14 and a complete description of the entire device may be found in Reference (59). The railway bar sat on the lower pole-face of the CCM. It could be arranged for either its middle or one of its ends to coincide with the centre of this pole-face. Rotations of the railway bar, in the horizontal plane, about this centre generated the θ -values of the grid-points. The pneumatic crawler moved between machined notches on the

railway bar, this movement generating the radial co-ordinate. The Hall probe mount could be moved up and down to fixed points on the vertical bar, thereby generating the vertical, Y , co-ordinate of the grid points. The whole system was aligned to ensure that the origin of the cylindrical co-ordinate system coincided with the origin of the experimental system.

The two Hall probes were maintained at a constant temperature inside a protective jacket. The control current was fixed at (100 ± 0.3) mA by the use of a very stable power supply. They were both calibrated relative to NMR readings at the centre of the CCM for the full range of the central field. The outputs of the Hall probes and the various control voltages were displayed on a scanning DVM that could be read out into the on-line computer. Once the vertical height of the Hall probe mount and the angular position of the railway bar were set, the pneumatic crawler traversed the length of the railway under computer control, stopping long enough at every notched position for the outputs of the Hall probes and their positions to be read and logged onto magnetic tape. In this way entire field maps were constructed for currents in the CCM corresponding to 15.0 and 11.5 Kilogauss. In addition, scans were made in the central plane for other values of the CCM current.

Using the calibration data the magnetic field is fitted as a polynomial function of the Hall voltage, V . The function is predominantly linear but terms up to V^5 are retained. The field maps are checked and corrected for possible alignment and positioning errors and the magnetic field is then calculated. Figure 3.15(a) is a plot of the central field of the CCM versus the CCM current. This is called the

"excitation" curve of the magnet. Figure 3.15(b) is a plot of B_y in the central horizontal plane - i.e. the $Y = 0$ plane - as a function of the radial co-ordinate.

Spectrometer Magnet - There are three major advantages in using the CCM as the momentum analysing magnet for the experiment. Firstly it has a large X, Y aperture and hence good acceptance for the forward-going particles from interactions in the target. Secondly, the large value of its field integral ensures good dispersion of - and hence also good momentum resolution for - the charged, forward-going, interaction products in the downstream spectrometer. Lastly, the CCM magnetic field is cylindrically symmetric about the Y -axis. Figure 3.16 shows a charged particle, in the central X - Z plane, bending in the CCM magnetic field. It is easy to show that for a cylindrically symmetric magnetic field $OE = OF = b$. This distance b is known as the impact parameter of the particle track. The equality of the impact parameters of the upstream and downstream tracks in the bending plane of the CCM affords an extremely simple method of associating tracks that belong to the same particle trajectory. Linking upstream and downstream tracks in the non-bending Y - Z plane is even simpler. The particle trajectories are essentially straight lines - two very small corrections, called vertical focussing, and the helix correction, to this assumption are described in Ref. (54). The linking data itself is shown in the event reconstruction description in Section 4.B.

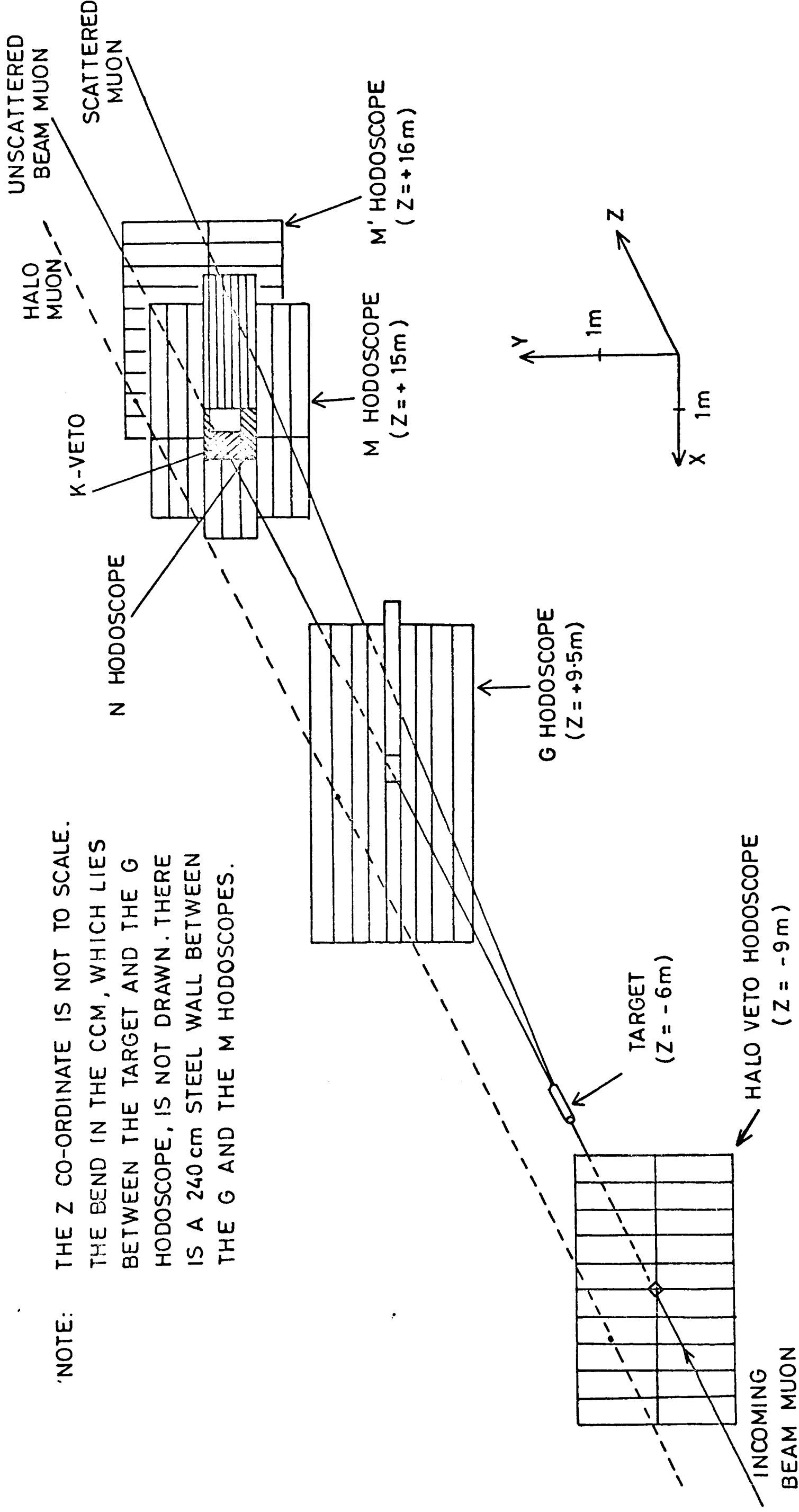
From the measured field map, the parameters B_0 and R of the equivalent hard edge field model are calculated - i.e. the actual field is approximated by one which is equal to a constant B_0 inside of a

cylinder of radius R and is equal to zero outside of this region. This is done by tracking a set of trajectories through the magnet using the measured field and comparing the tracks so obtained with those obtained by applying the hard edge field to the same set of trajectories. Minimizing the differences between the tracks given by these two methods gives B_0 and R . For the 15 kilogauss field map $B_0 = 15$ kilogauss $R = 2.4709$ metres. The momenta of particles going through the magnet are easily calculated from these parameters, B_0 and R , of the hard edge field and the bend of the projection of the particle trajectory on the X-Z plane - see Fig. 3.16.

Finally, two negative aspects of the CCM should be mentioned. Firstly the high residual radio-activity of the pole-tips causes a large number of extra sparks in the 2m x 4m Shift Register chambers immediately downstream of the CCM. These spurious sparks cause confusion in the determination of the event-associated tracks in these chambers. Secondly the CCM has a large fringe field. Certain apparatus - i.e. photomultiplier tubes and magnetostrictive chambers - cannot work in a large magnetic field and have to be shielded and kept well away from the CCM. Also low energy particles in the upstream MWPCs will bend in the fringe field causing possible losses in the detection efficiency in this region.

FIG. 3-1

NOTE: THE Z CO-ORDINATE IS NOT TO SCALE.
 THE BEND IN THE CCM, WHICH LIES
 BETWEEN THE TARGET AND THE G
 HODOSCOPE, IS NOT DRAWN. THERE
 IS A 240 cm STEEL WALL BETWEEN
 THE G AND THE M HODOSCOPES.



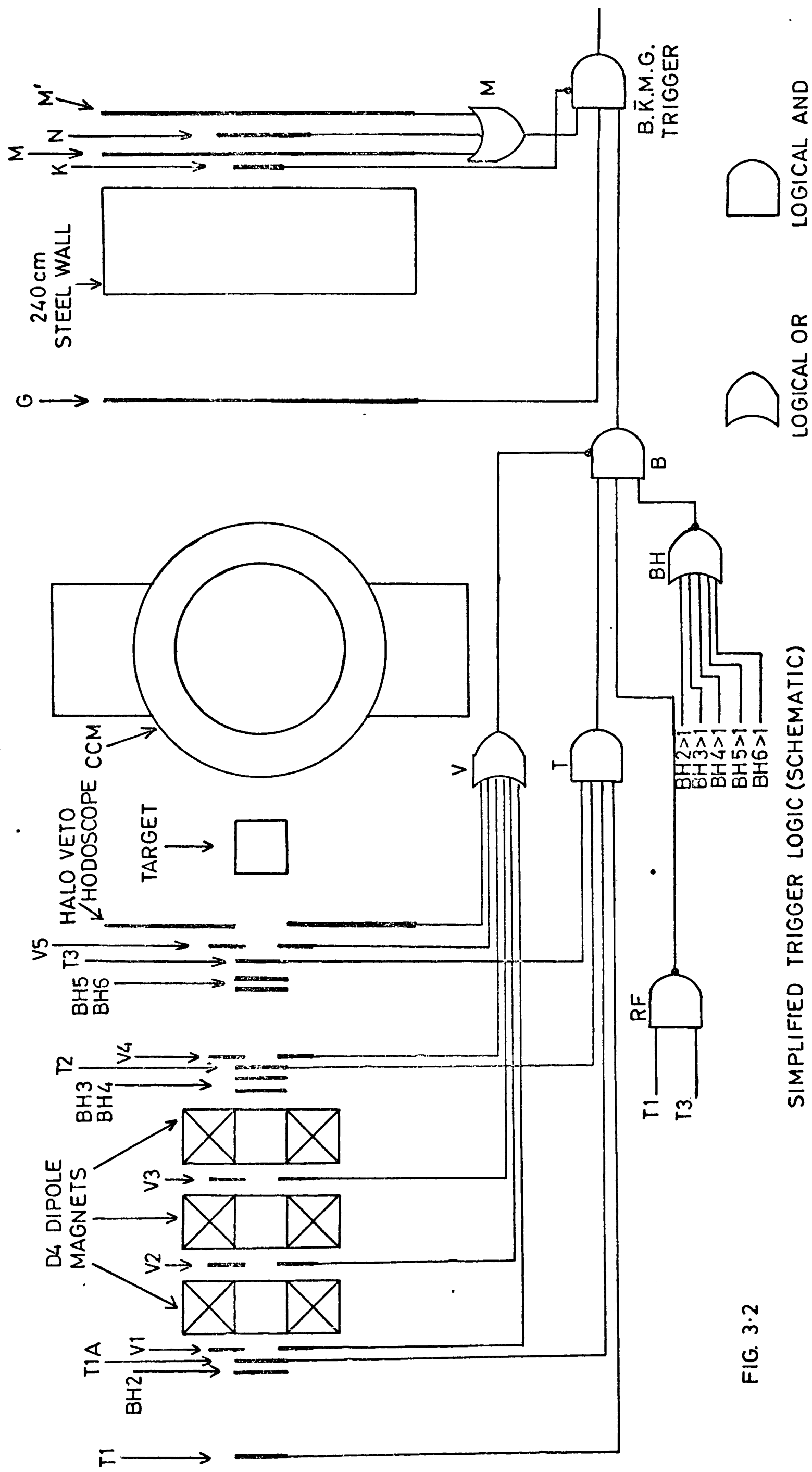
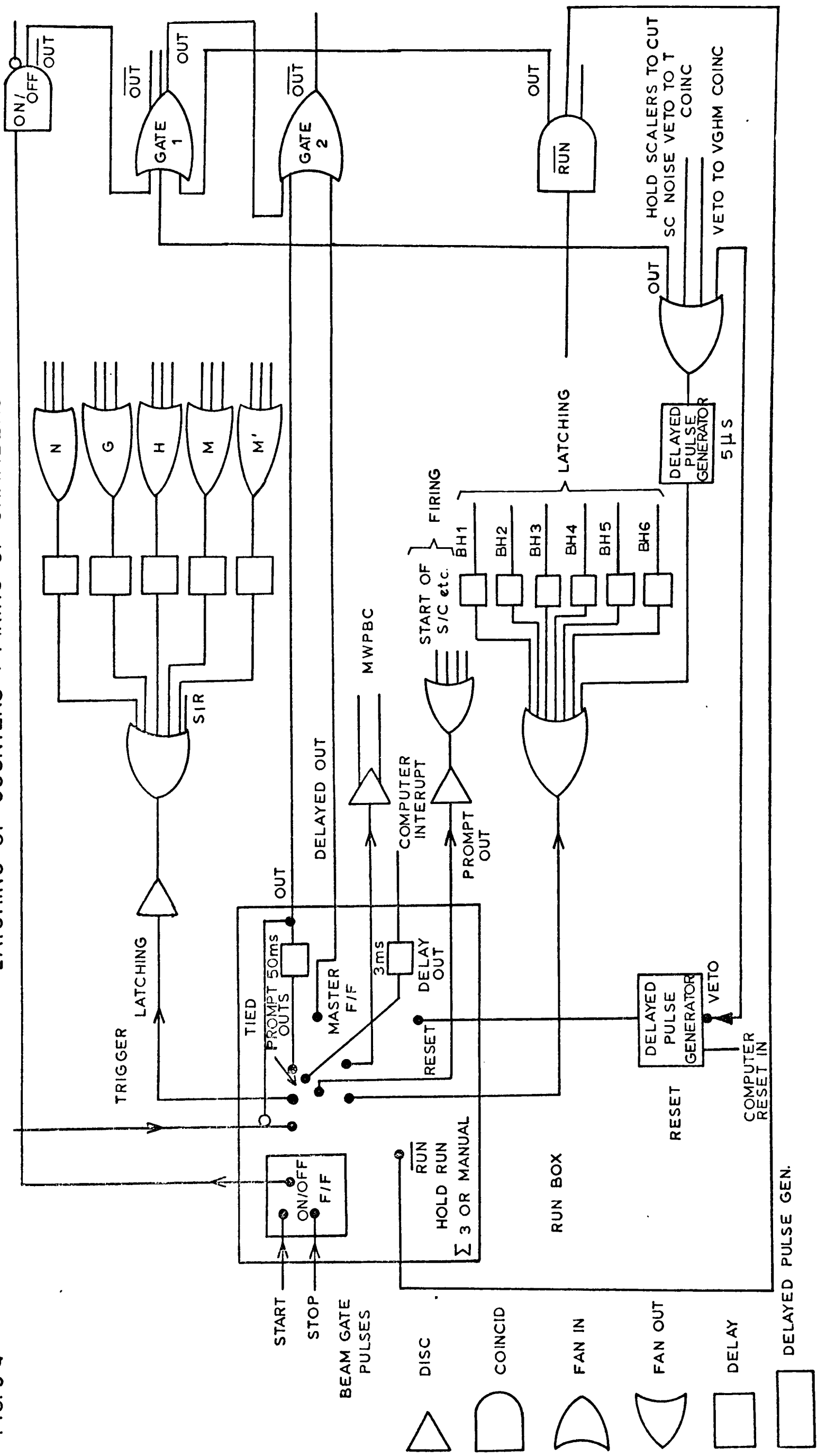


FIG. 3.2

SIMPLIFIED TRIGGER LOGIC (SCHEMATIC)

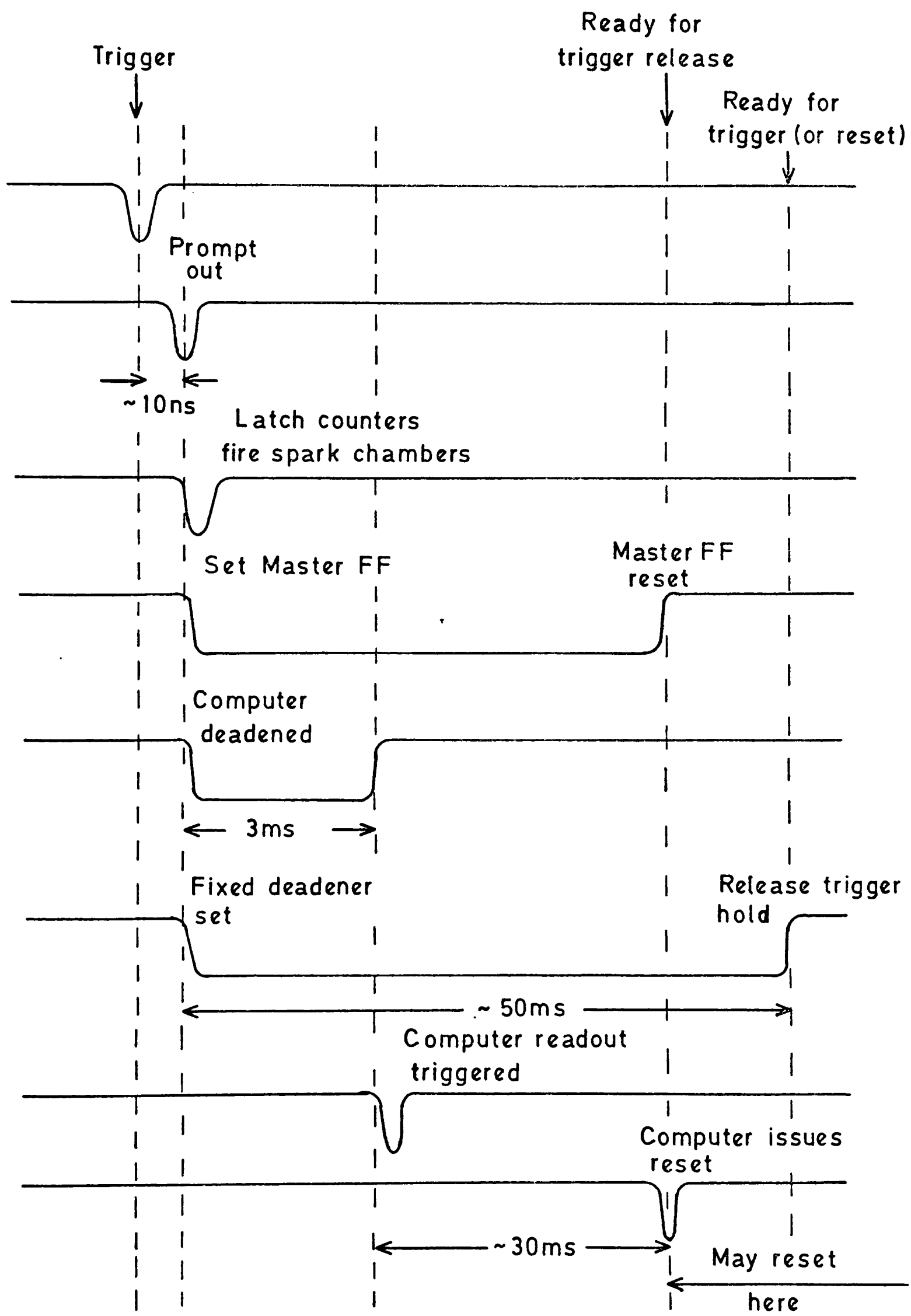
FIG. 3-4

LATCHING OF COUNTERS + FIRING OF CHAMBERS



TRIGGER AND INTERRUPT SEQUENCE

FIG. 3-5

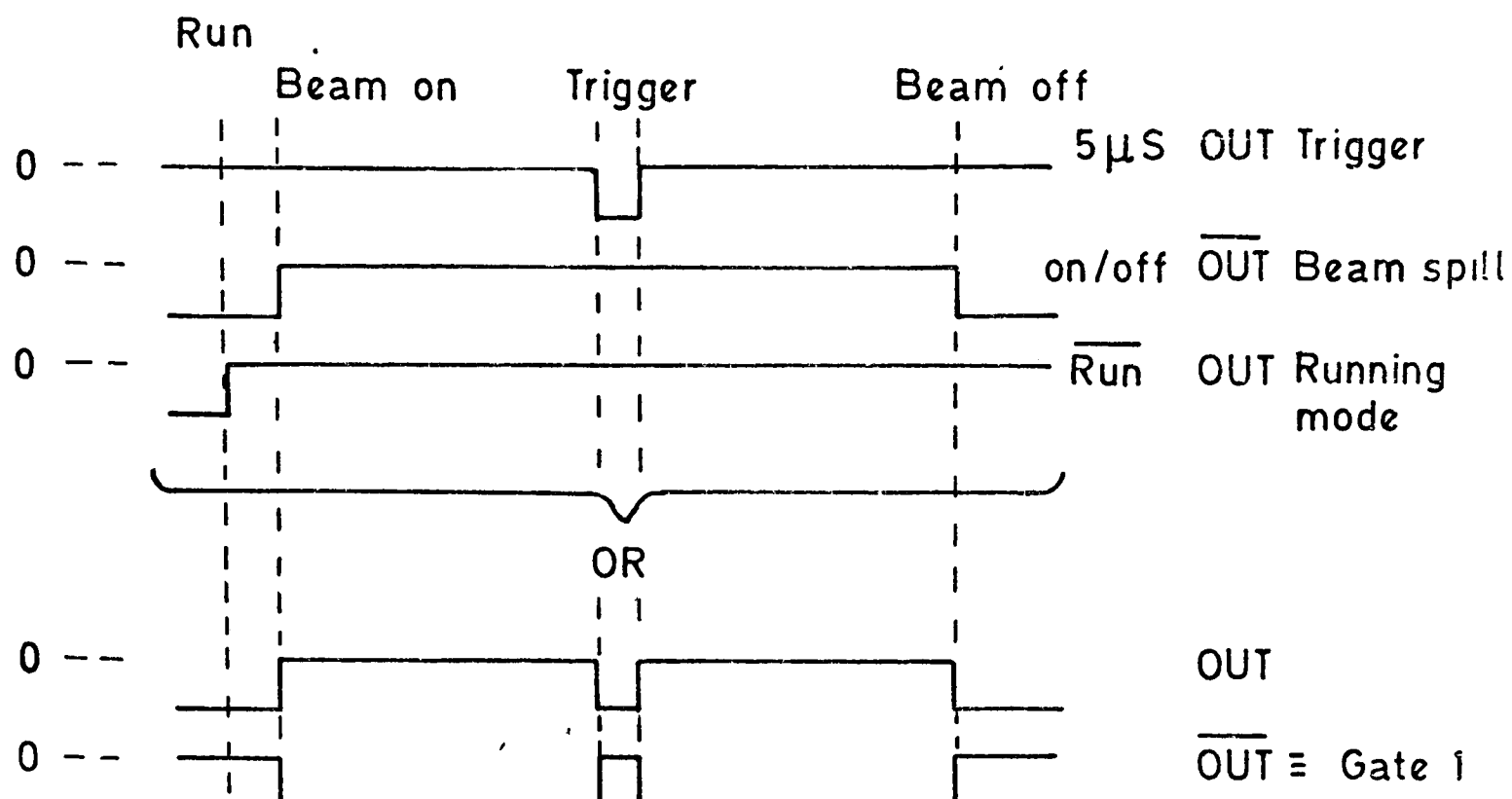


GATING LOGIC

FIG. 3-6

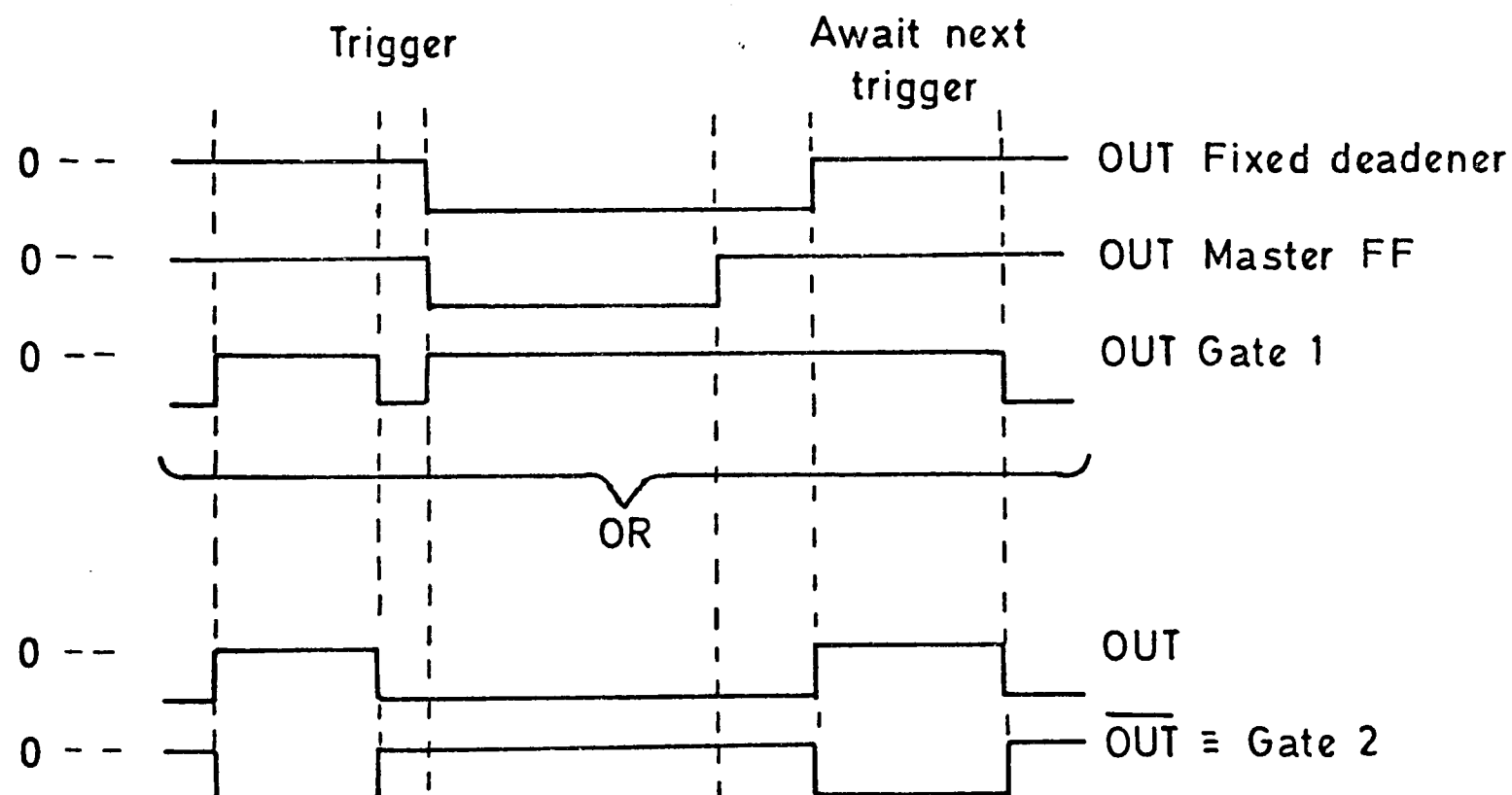
a) Ungated scalers

Gate 1



b) Gated scalers

Gate 2



c) Trigger hold in run box (schematic)

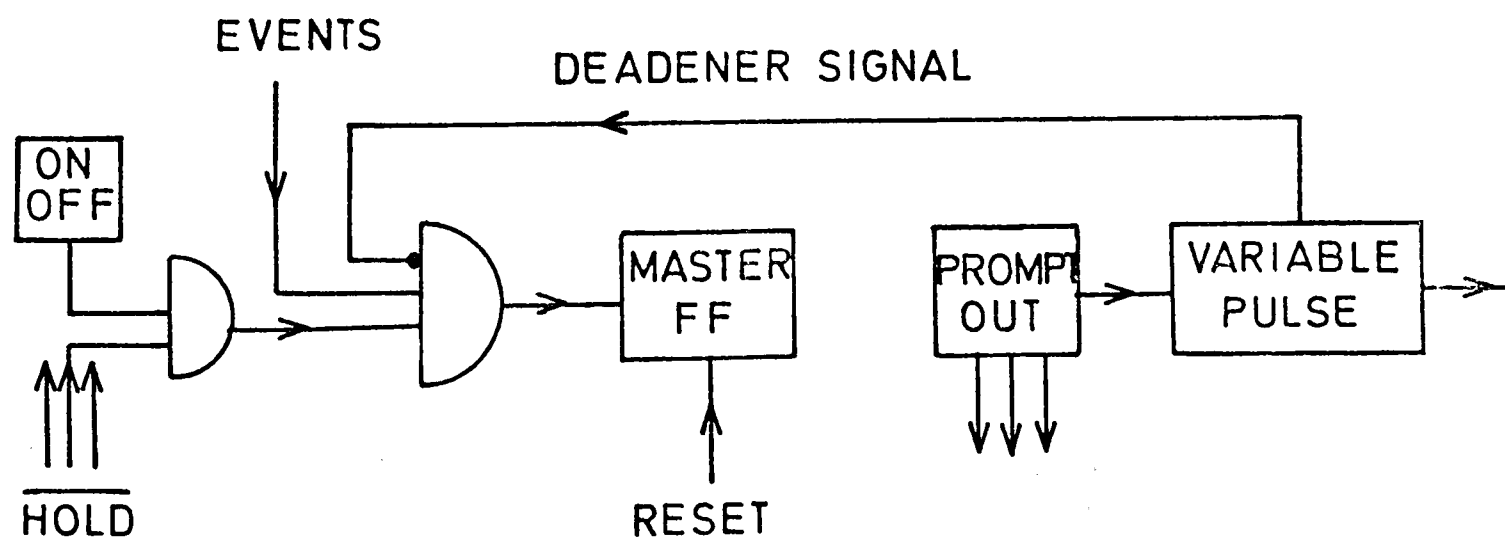


TABLE 3.1

SCALER OUTPUTS FOR A FEW TYPICAL RUNS

	<u>147 GeV/c Incident Beam</u>		<u>96 GeV/c Incident Beam</u>	
	<u>Run 886</u> <u>Target Full</u>	<u>Run 897</u> <u>Target Empty</u>	<u>Run 1005</u> <u>Target Full</u>	<u>Run 930</u> <u>Target Empty</u>
<u>Ungated Scalers</u>				
Beam	708983813	1047827438	537712203	827187423
V.G.H. Halo	1025701107	1432897211	1699160537	2169624275
B. \bar{K}	76884	102315	90717	127506
B.K.M.G.	7861	5665	7709	6017
T ₁ .T ₂ .(T ₃) Δt	125098774	119737318	72499214	118858156
T.(\bar{V}) Δt	1225946483	1754445164	944100387	1543378729
B.(\bar{K}) Δt	584413288	904329250	470927348	719756746
B. \bar{K} .(M.G. \bar{V}) Δt	583	752	621	1144
<u>Gated Scalers</u>				
T	949610999	1637040582	789389089	1487527129
T. \bar{V}	581228531	1025614149	458760883	805180697
T.(\bar{V}) Δt	812236418	1451362129	684973565	1282528176
Beam	463933698	866215609	385060859	686986085
B.(\bar{K}) Δt	387138080	755346731	341543881	604536916
V.G.H Halo	681125156	1200614121	1234895849	1732309585
T ₁ .T ₂ .(T ₃) Δt	82685570	100074191	52705960	99958670
B. \bar{K}	50796	85414	65505	106966
B. \bar{K} .M	13582	19910	16014	23867
B. \bar{K} .M.G	5235	4703	5576	5005
B. \bar{K} .(M.G. \bar{V}) Δt	371	600	437	955
B. \bar{K} .M.(G. \bar{V}) Δt	714	868	955	1140
B. \bar{K} .G.(M. \bar{V}) Δt	1374	1846	2711	2010
Imbedded Beam Trigger	220	376	192	324

TABLE 3.2

SCALER RATES FOR A FEW TYPICAL RUNS

	<u>147 GeV/c Incident Beam</u>		<u>96 GeV/c Incident Beam</u>	
	<u>Run 886</u> <u>Target Full</u>	<u>Run 897</u> <u>Target Empty</u>	<u>Run 1005</u> <u>Target Full</u>	<u>Run 930</u> <u>Target Empty</u>
T. \bar{V} /T	0.612	0.626	0.581	0.541
B/T	0.488	0.529	0.487	0.462
B/T. \bar{V}	0.789	0.844	0.839	0.853
T.(\bar{V}) Δt /T	0.855	0.886	0.867	0.862
T1.T2.(T3) Δt /T	0.087	0.061	0.066	0.067
V.G.H/B	1.468	1.386	3.207	2.521
B. \bar{K} /B	1.09E-4	0.99E-4	1.70E-4	1.55E-4
B. \bar{K} .M/B	2.92E-5	2.29E-5	4.15E-5	3.47E-5
B. \bar{K} M.G/B	11.28E-6	5.42E-6	14.48E-6	7.28E-6
B.(\bar{K}) Δt /B	0.834	0.876	0.886	0.880
B. \bar{K} . (M.G. \bar{V}) Δt /B	0.80E-6	0.69E-6	1.13E-6	1.39E-6
(B Gated)/(B Ungated)	0.654	0.826	0.716	0.830
B. \bar{K} .M.G / B. \bar{K} M.G Gated / Ungated	0.665	0.830	0.723	0.831

B ~ 10⁶ muon/pulse

Protons ~ 8 x 10¹² proton/pulse

Spil 800 ms. Pulse rep rate 1 every 7.2 seconds.

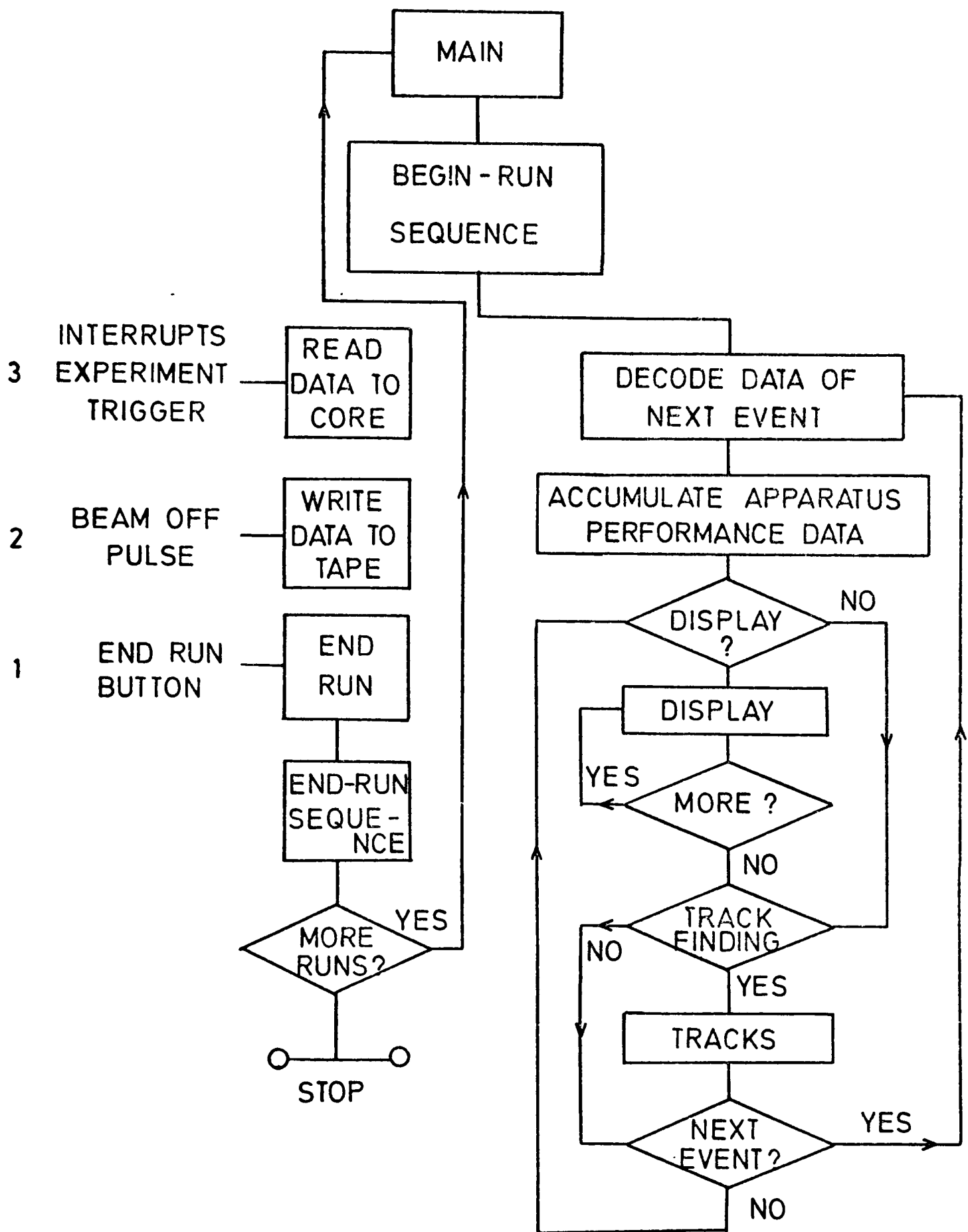
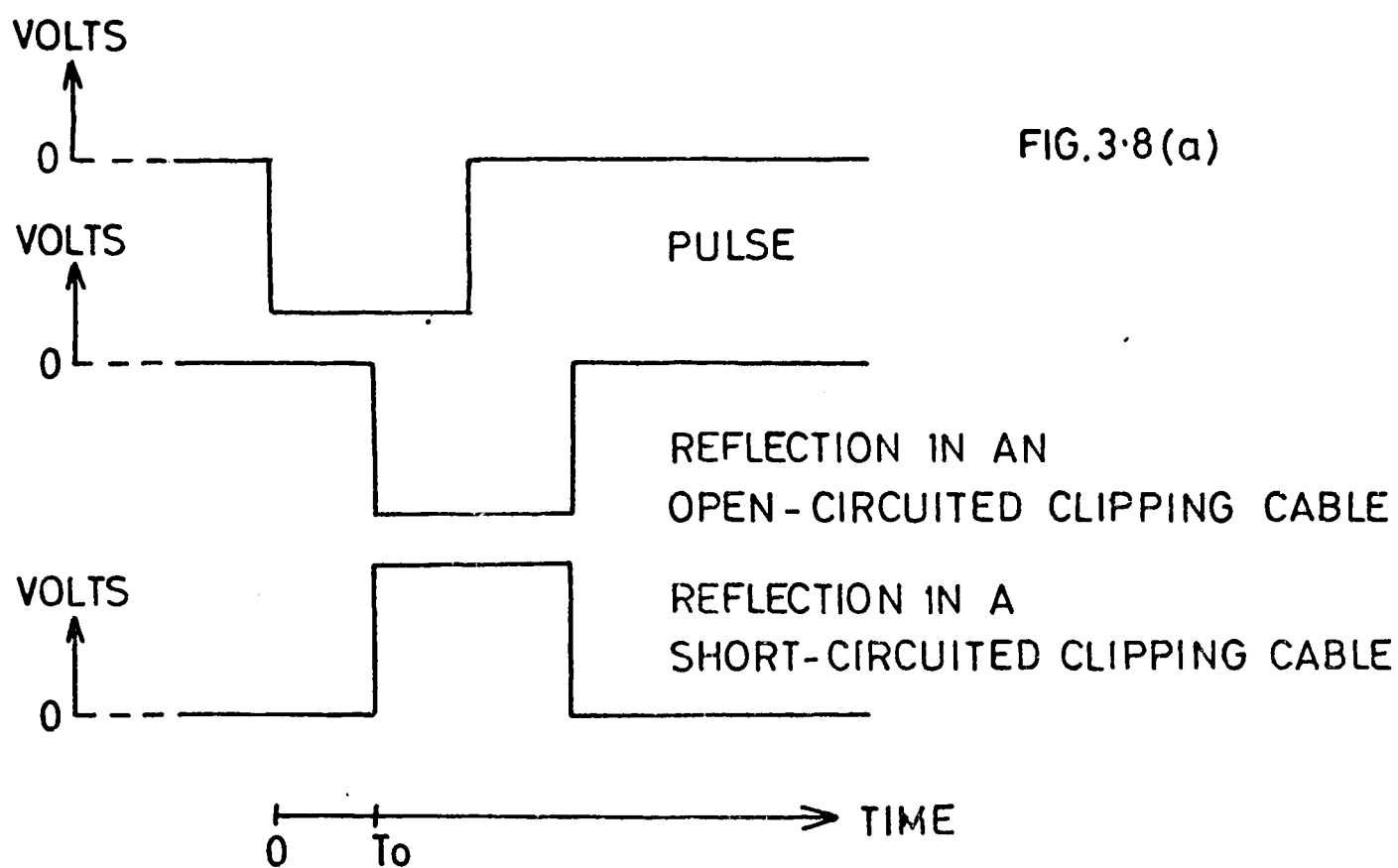
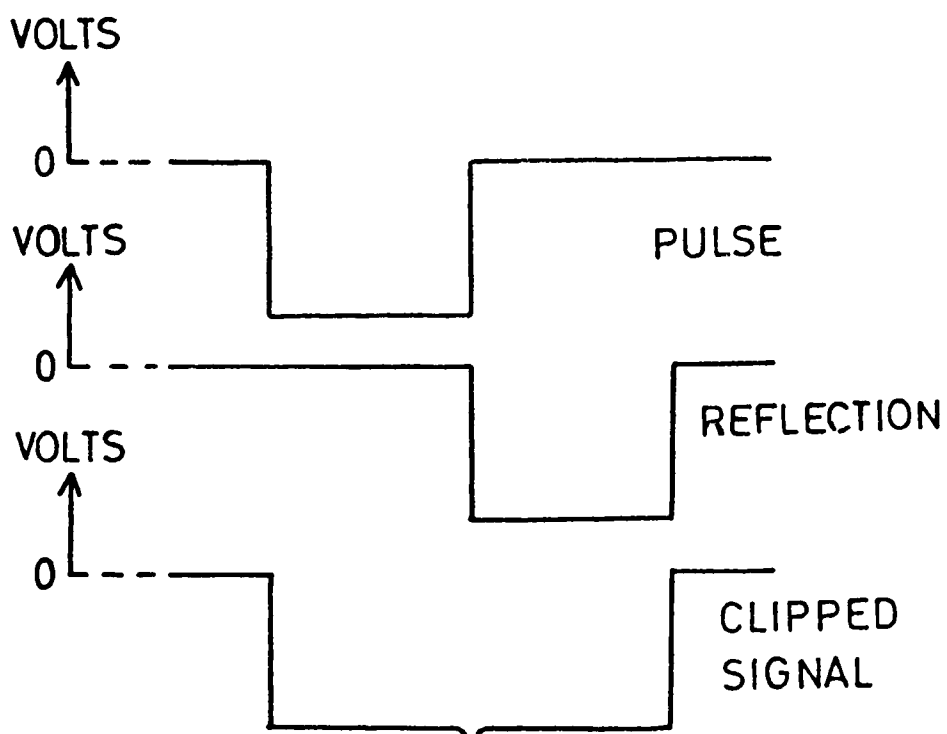
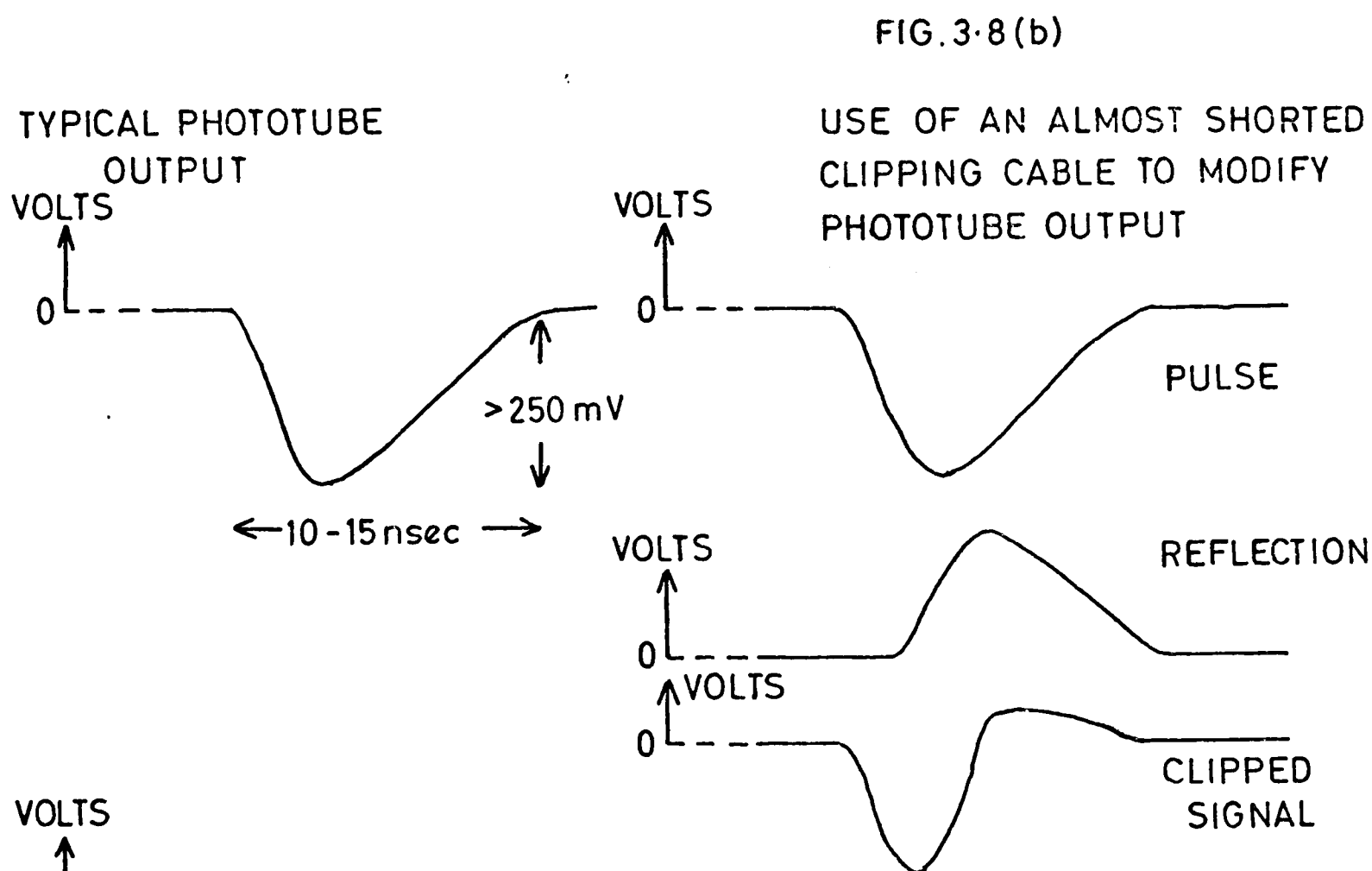


FIG. 3.7

ON - LINE PROGRAM



$$T_0 = 2 * (\text{LENGTH OF CLIPPING CABLE}) * (\text{VELOCITY OF LIGHT IN CABLE})$$



USE OF AN OPEN CLIPPING CABLE TO WIDEN A PULSE

FIG 3.9(a)

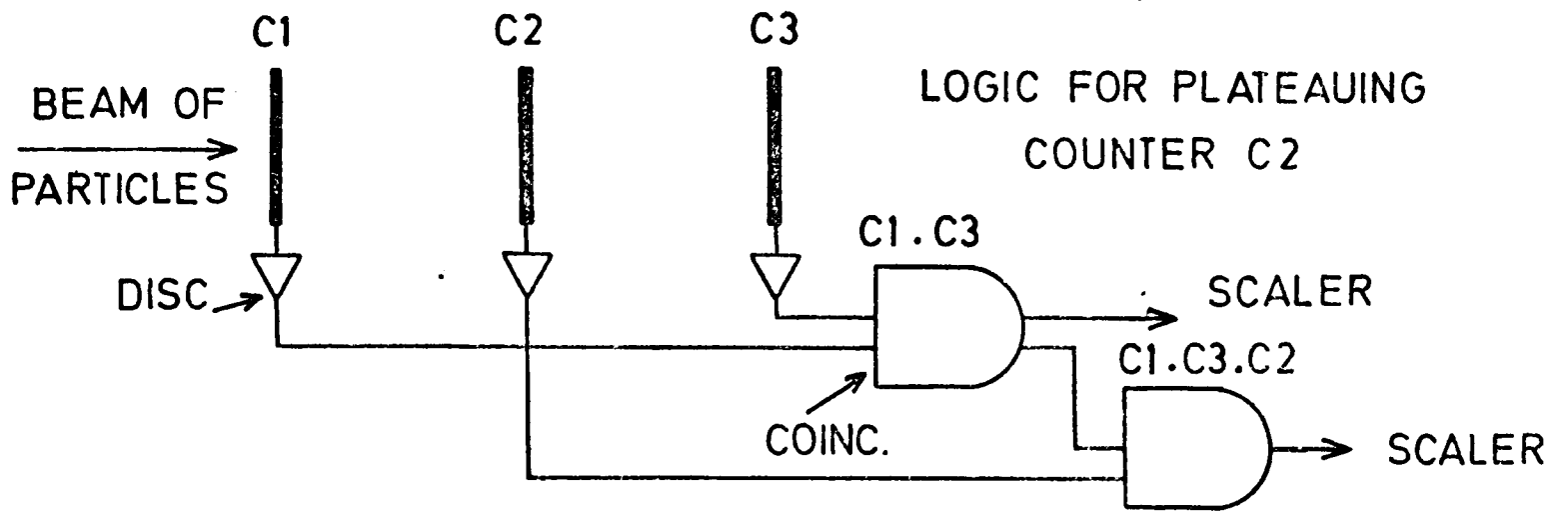


FIG 3.9 (b)

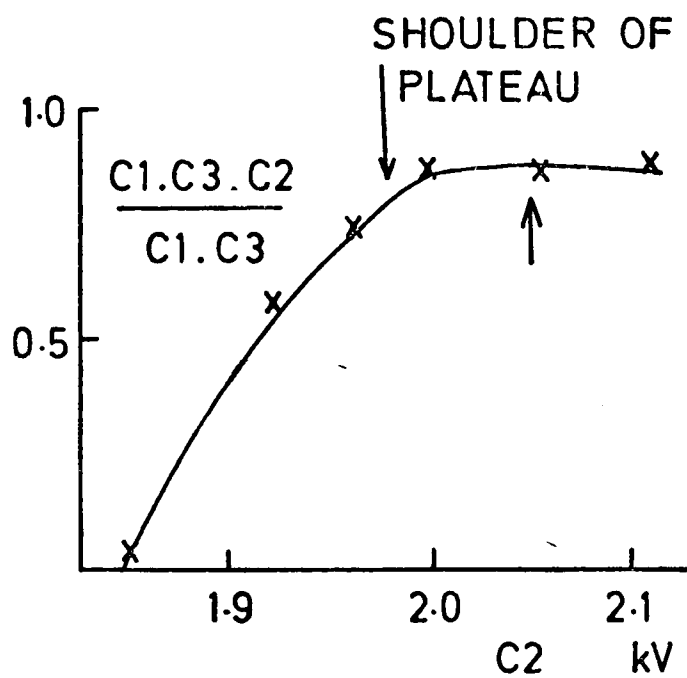


FIG 3.10 (a)

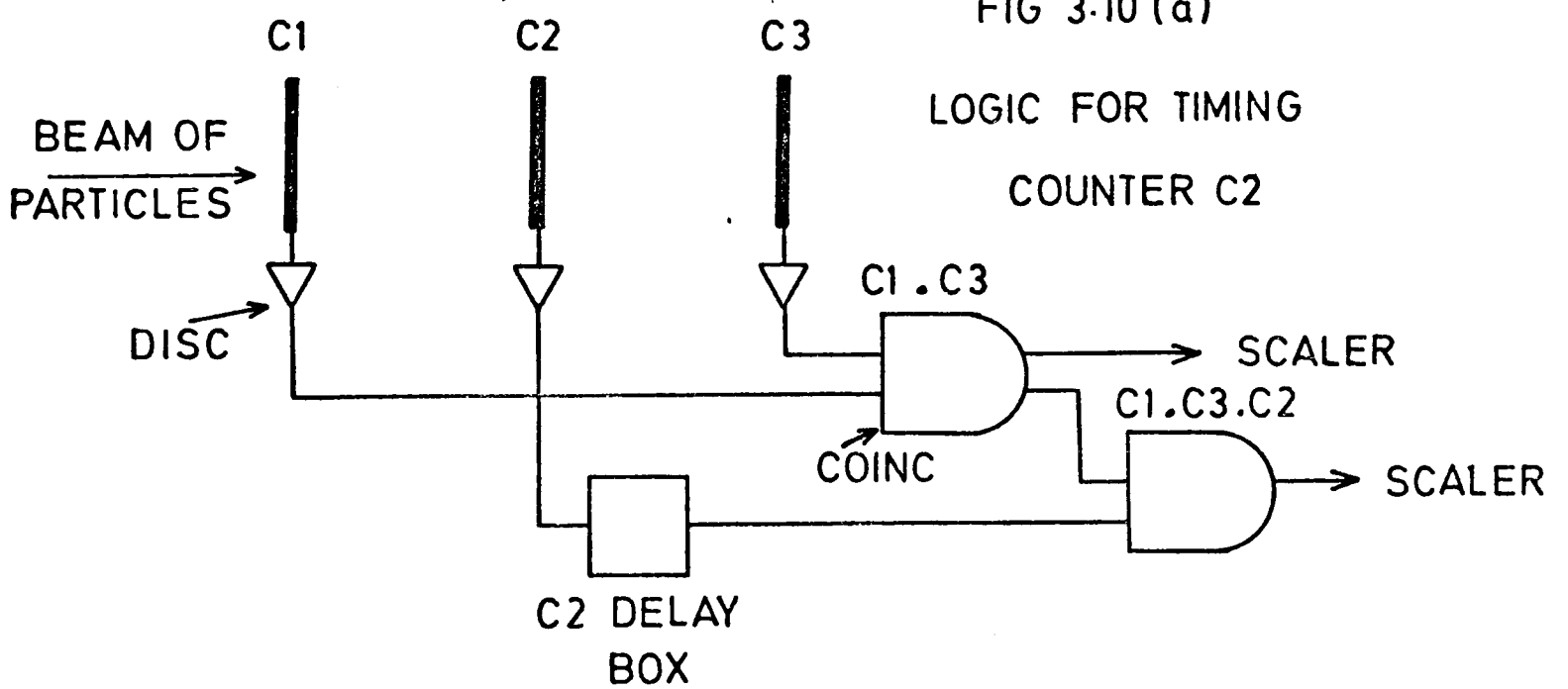
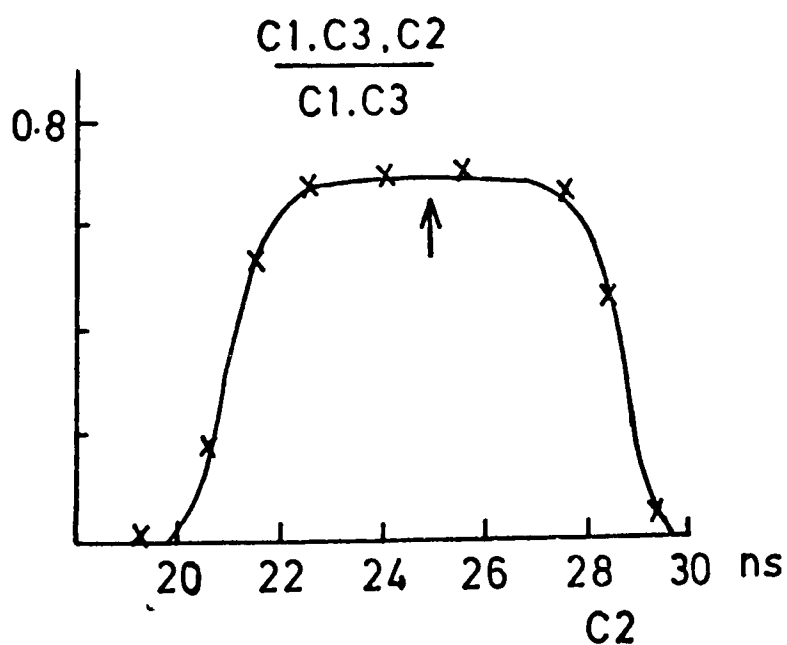


FIG 3.10 (b)



G - HODOSCOPE TIMING

FIG. 3-11(a)

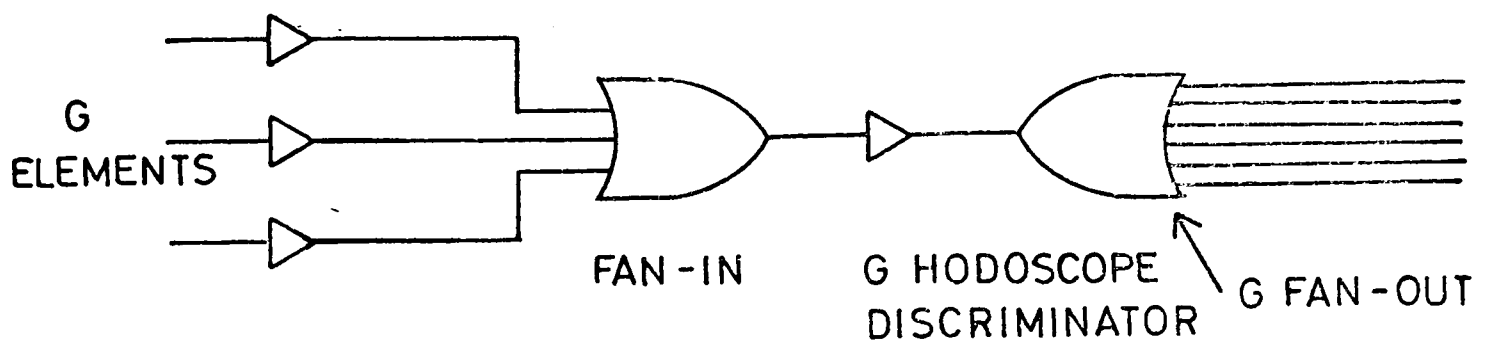


FIG. 3-11(b)

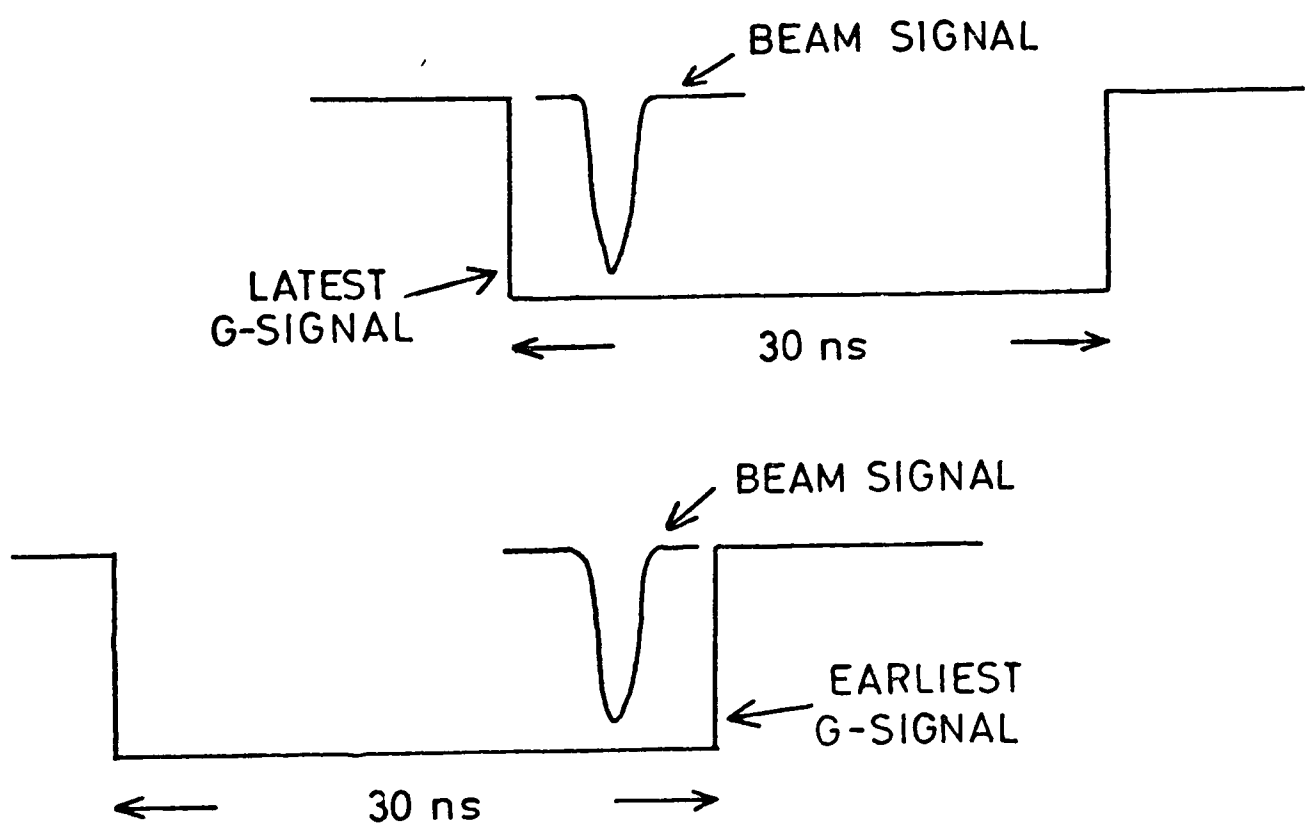
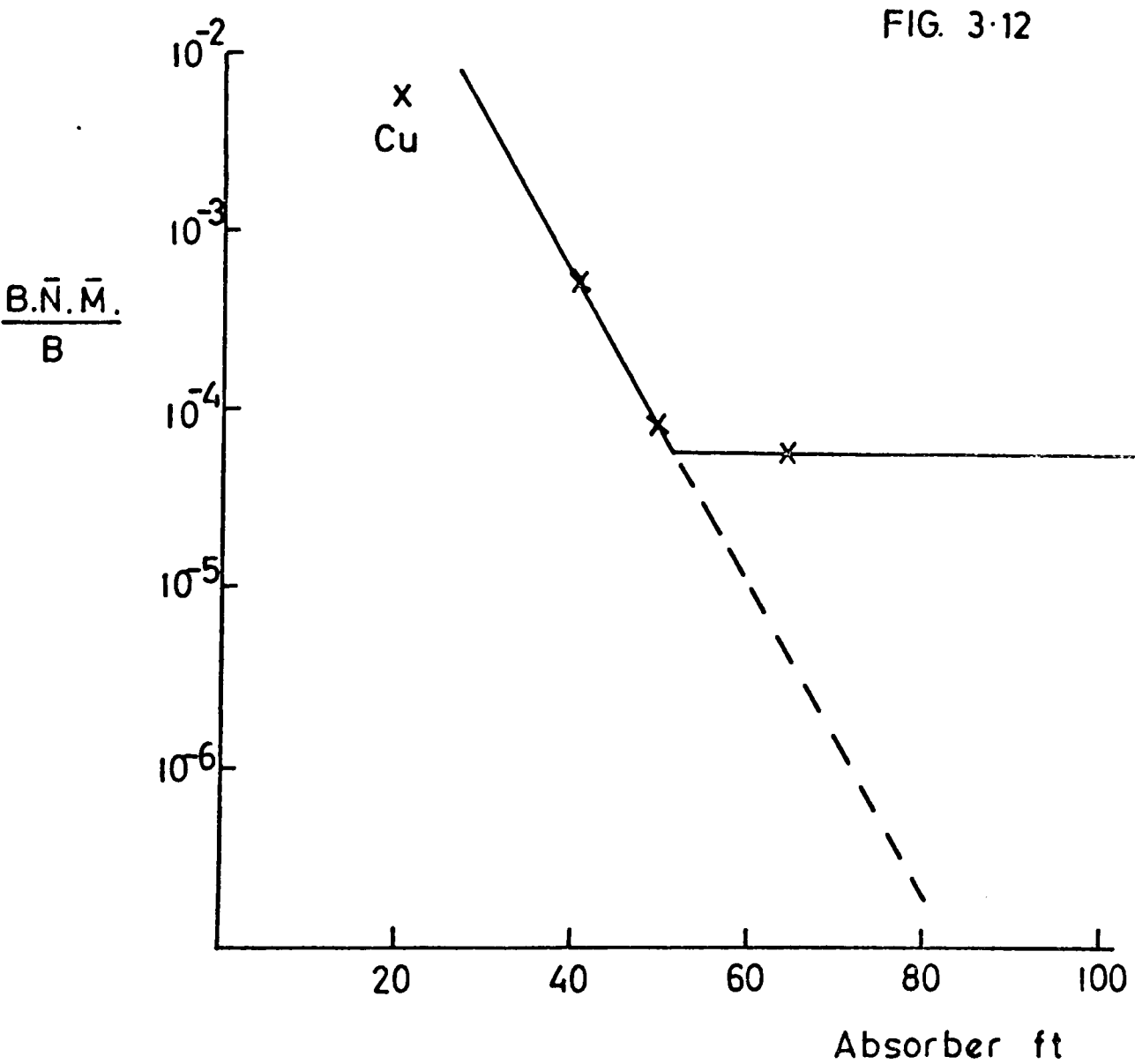


Table 3.3

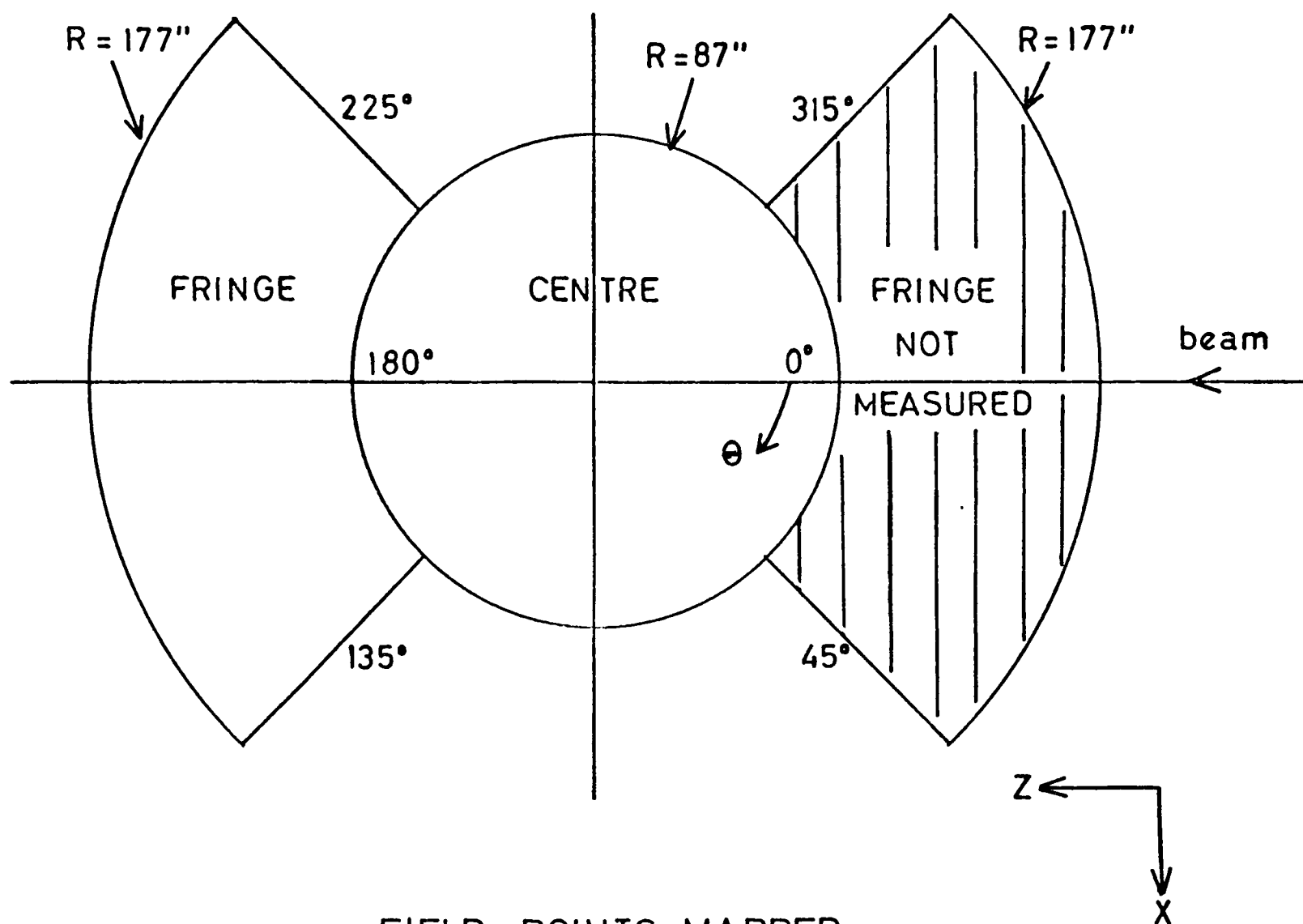
LH₂ target, Triplet train, 150 GeV beam tune.

Absorber Thickness	$\frac{B.\bar{N}}{B}$	$\frac{B.\bar{N}.M}{B}$	$\frac{B.\bar{N}.\bar{M}}{B}$	$\frac{B.\bar{N}.M.G}{B}$
20' (Cu targ)			5.75E-3	
40'	5.70E-4	7.14E-5	4.90E-4	22.60E-6
50'	1.10E-4	1.49E-5	0.95E-4	10.00E-6
63'	0.70E-4	1.04E-5	0.60E-4	9.50E-6 (low Q ² N)
63'	0.68E-4	0.90E-5	0.60E-4	6.50E-6

NOTE: Data taken in April 1974. At this time the N hodoscope was being used instead of the K-counter as the beam veto.



PION ABSORPTION.



FIELD POINTS MAPPED.

FIG. 3.13

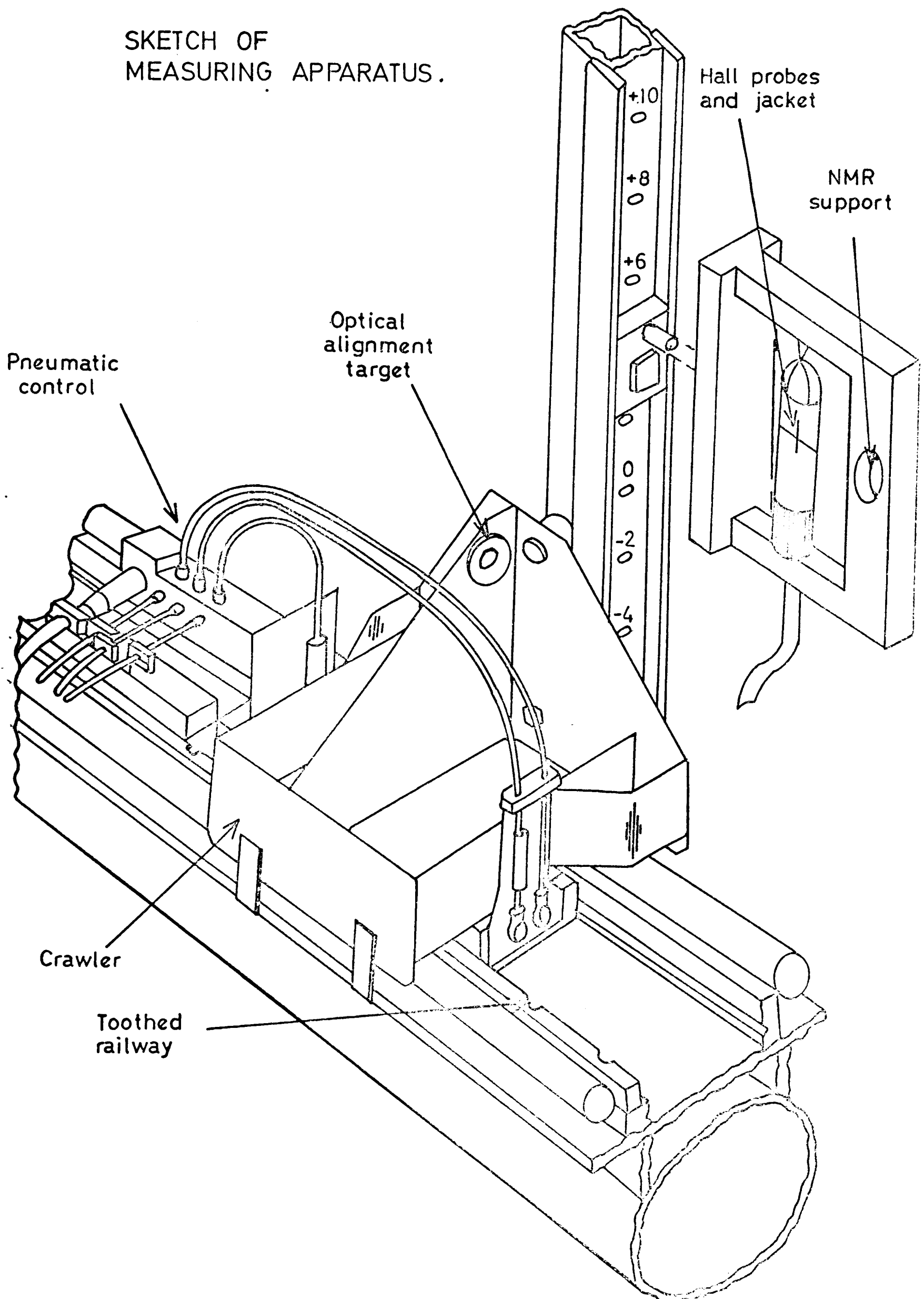
Table 3.4

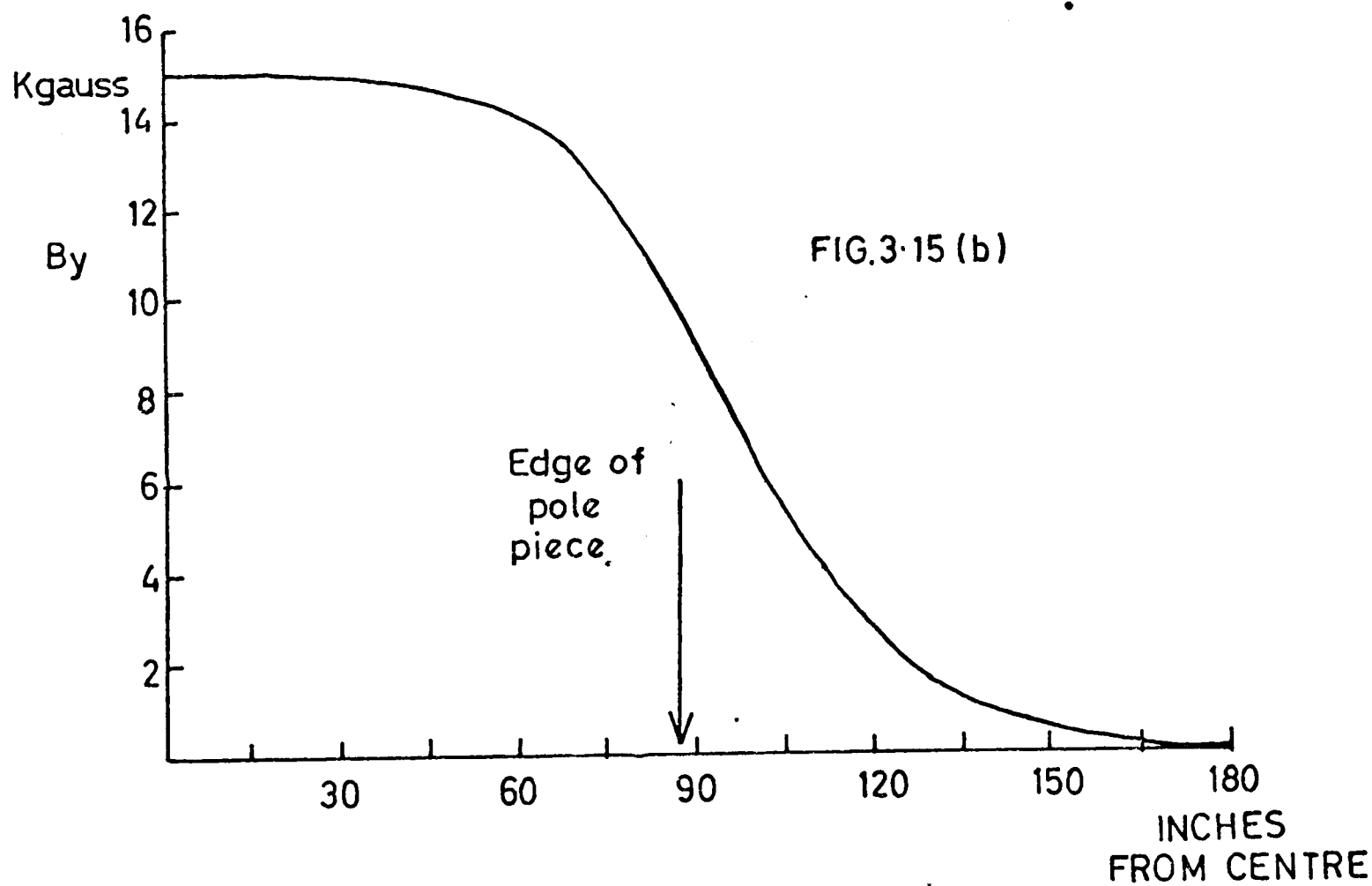
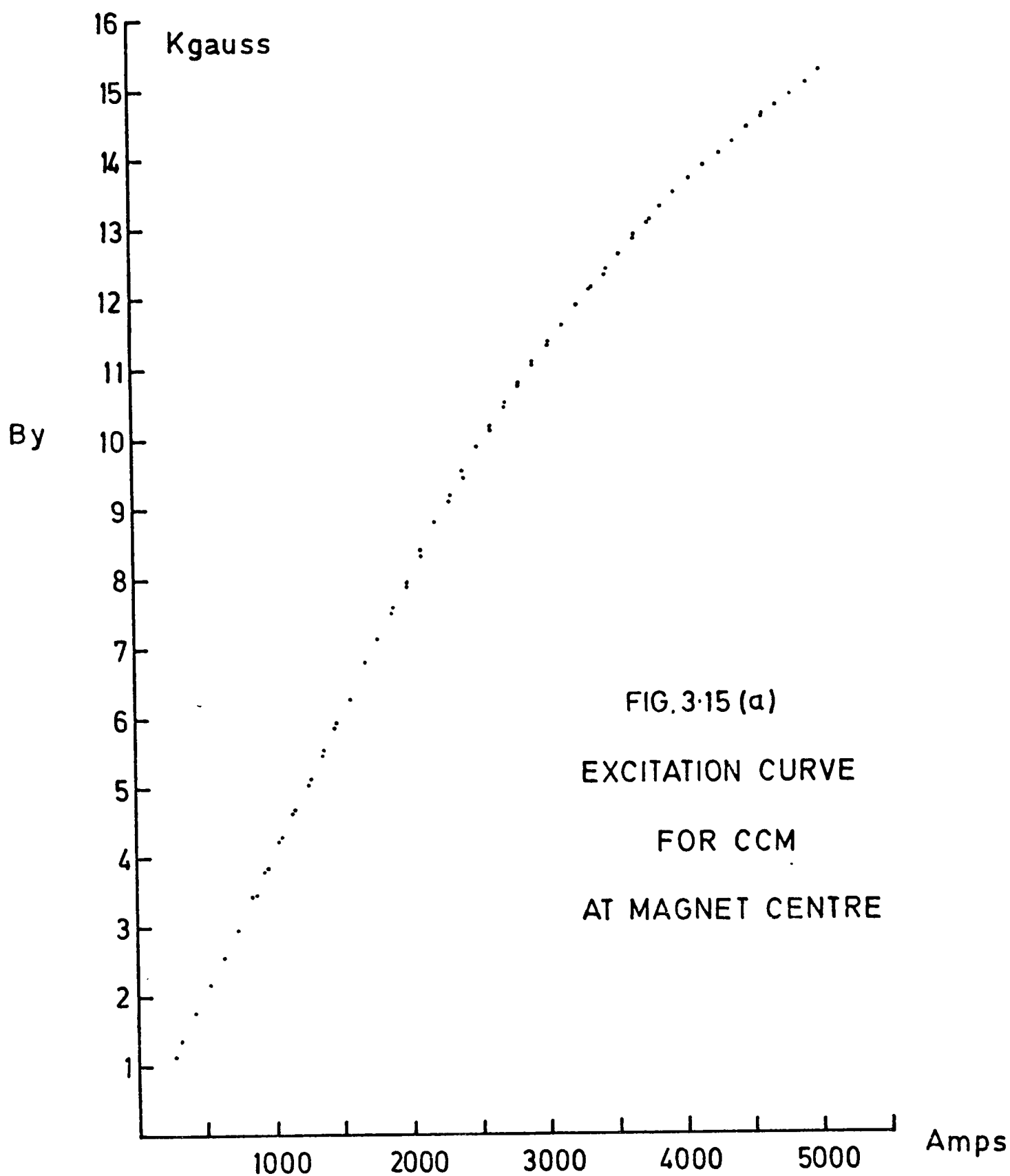
Position of the grid points at which the CCM magnetic field was measured. The grid points lie on a cylindrical co-ordinate system (y, r, θ) .

	Angular Position θ	Radial Position r	Vertical Height y
Steps	$\Delta\theta = 15^\circ$	$\Delta r = 3''$	$\Delta y = 5''$
Extent	$\theta = 0^\circ$ to 360°	$r = 0''$ to $87''$	$y = -15''$ to $+15''$
Extent	$\theta = 135^\circ$ to 225°	$r = 0''$ to $177''$	$y = -15''$ to $+15''$

FIG. 3-14

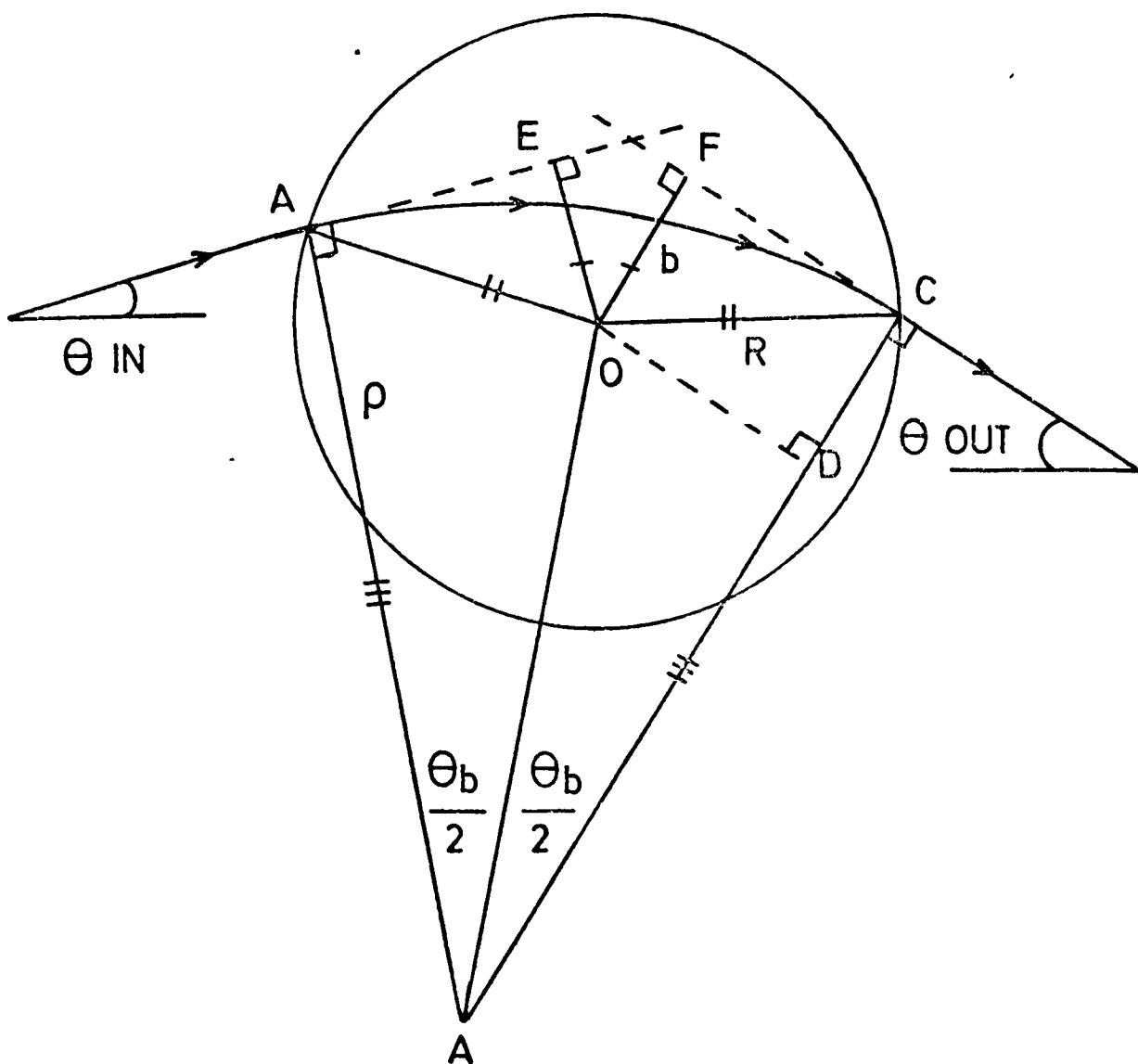
SKETCH OF
MEASURING APPARATUS.





By ALONG CENTRAL PLANE.

FIG. 3.16



O is the centre of the magnetic field

A is the centre of the path taken by the particle

θ_b is the total bend in the field

b is the impact parameter

ρ is the radius of curvature of the particle track

FOR A HARD EDGE FIELD IN WHICH

B_0 is the effective field in kilogauss

R is the effective field radius in metres

$$\rho = AD + DC = (R^2 - b^2)^{1/2} \cot\left(\frac{\theta_b}{2}\right) + b$$

$$P = \frac{c B_0 \rho}{10^{10}} \approx 0.03 B_0 \rho \text{ where } P = \text{momentum in GeV/c}$$

c = velocity of light in metres/sec

CHAPTER 4

DATA ANALYSIS - I

4.A INTRODUCTION

The description of the data analysis for this experiment is rather arbitrarily divided into two parts. This Chapter describes the sequence of operations necessary to obtain the distributions of raw events from the data runs. The next Chapter describes how the cross-sections for muon-proton scattering and the structure functions of the proton are calculated from these raw numbers.

- This Chapter has five sections. Section 4.B describes the pattern recognition programs of the analysis. In these the raw event information as logged onto tape at run time is converted into particle trajectories and momenta. Section 4.C looks at the calculation of the positions and efficiencies of the downstream counter hodoscopes. The process of muon selection in the events is described in Section 4.D and finally Section 4.E describes the cuts made to the data to obtain the raw event distributions.

Two additional comments may be made at this stage. The first concerns the units of length. In writing the on-line program and the raw data tapes it was found convenient to use $\frac{1}{4}$ mm units in the X-Y plane and $\frac{1}{4}$ cm units for the Z co-ordinate. These units were also adopted for the off-line analysis and hence the reader should not be too surprised to find some lengths quoted in $\frac{1}{4}$ mm and $\frac{1}{4}$ cm. The second comment is that the data analysis is by no means as easy or as straightforward as this description suggests and that one often had to loop back and re-program previous steps at various stages of the analysis.

4.B EVENT RECONSTRUCTION - TAPE SEQUENCING

The raw data as logged onto tape by the on-line computer presents far too complex a task for a single program to decode and correct the raw data and to produce particle trajectories from it. It is found convenient to divide the problem into three stages, tapes being written at the end of each stage. These tapes are all written at 6250 bpi and it may be commented that the resulting concentration of the data makes the physical problems of tape handling much easier. No cuts are made to the data in these three stages of the analysis and every trigger that is read off the raw data tapes is processed.

Primary Tapes - The first stage of the event reconstruction process is by far the simplest. The raw data tapes are read and checked for simple tape-writing errors that might have occurred during data logging. Bad records are removed and the corrected data is written onto the primary tapes in exactly the same format as that of the raw data tapes. The latter then act as back-up copies of the data.

Secondary Tapes - A few words about the structure of the raw data are appropriate at this point. At the beginning of every run there is a set of header records - unimaginatively called the "begin run records" - which contain information about the spatial configuration of the apparatus and also information necessary to decode the event data. The event data records contain the packed counter latching and scaler information and the chamber sparks written essentially as the scanner addresses corresponding to the wires that fired in the various chambers.

The purpose of the secondary stage of the event reconstruction is threefold. The first is to correct any of the begin run information

that was incorrectly entered at run time. The second is to unpack the counter latching bits and the scalers. Lastly, the program has to convert the spark addresses of the raw data into spark positions and spreads in real - i.e. X, Y, U, V - co-ordinate space. As one might expect the first two operations are straightforward and the real effort of this program is expended on the third. The entire process is called "scaling" the raw data and is executed one run at a time.

To obtain real space sparks from the raw data, the alignment of the chambers has first to be checked and corrected. During the data taking, a few alignment runs - i.e. runs with a beam trigger and no CCM field - were logged onto tape. In these runs the beam muons provide straight lines through the apparatus, lines which may be used to check the relative alignment of the chambers. First the spark addresses of the raw data are converted into spark positions using the existing begin run information as input. The MWPCs in the beam apparatus - see Section 2.C - were accurately surveyed in by FNAL. Because of this the proportional chambers at the beam stations 3 and 4 are used to define the co-ordinate system, their separation - approximately 31 metres - being quite adequate to define the muon trajectory to better than $\frac{1}{2}$ mm in the X-Y plane throughout the apparatus. The differences between the actual spark positions on a particular chamber plane and the positions predicted from the muon trajectory given by the beam chambers then give the shift that has to be applied to align the plane in question. The horizontal and vertical alignments of the 1m x 1m MWPCs upstream of the CCM fall out fairly readily from this procedure. For the twenty momentum measuring planes downstream of the CCM, additional investigations have to be initiated to check quantities such

as the angles of the wires to the vertical, the Z positions of the chambers and the fiducials of the magnetostrictive spark chambers. The Muon chambers are first aligned relative to each other and then the system as a whole is aligned relative to the downstream measuring planes. Little effort is expended in accurately aligning the Photon and Neutron chambers as these are used principally as shower counters. The MWPCs at the beam stations 1 and 2 are aligned by comparing the impact parameters of the beam trajectories upstream and downstream of the D4 dipole magnets at the centre of the latter magnets. This alignment correction affects only the incident beam momentum and the problem of the momentum calibration of the experiment is further discussed in Section 4.D. Next the data runs are used to look for any nonlinearities in the magnetostrictive chambers. Non-linear effects are schematically illustrated in Figure 4.1 and were found in two of the Muon chamber read-out planes. With all of the above corrections the chamber read-out planes demonstrate their theoretical resolutions of about $\frac{1}{2}$ mm.

Using the alignments so generated to correct the begin run information, the run by run scaling of the raw data is carried out. It is necessary to further check and correct the X, Y alignments on a run by run basis, principally because the properties of the magnetostrictive read-out wires vary with time and temperature. These extra alignments - which may be as much as ± 2 mm - are calculated by an automatic four-pass procedure that uses the first few hundred events of the run. The procedure uses a simple track-finder on the events and then minimises the differences between the actual values of spark positions and those calculated from the tracks found. The previous sets of data had a problem in the MWPC read-out - the noise

from the spark chambers firing caused this read-out to lose bits, see Ref. (54). It is found that for the data on which this thesis is based this problem has been effectively overcome in the hardware. The final alignments obtained are used to generate the real space spark positions and spreads. The corrected begin run information followed by the scaled event data is then written onto the secondary tape. The processing for this secondary stage of the event reconstruction takes about 40 msec per trigger.

Tertiary Tapes - This stage is the pattern recognition stage of the event reconstruction and uses the secondary tapes as input. The program concerns itself principally with finding tracks in the various sets of chambers and linking those tracks in the different sections of the apparatus that belong to the same particle trajectories. Before writing the tertiary tape, the program also makes a first attempt at vertex finding and muon selection. All the information required to carry out the latter is written onto the tertiary event buffer and indeed better attempts at muon selection and vertex finding are later made using the tertiary tape as input.

In order to find the particle trajectories from the real space sparks, the procedure employed looks separately at four regions of the apparatus. These regions are the beam, the 1m x 1m MWPCs, the Muon planes and the 20 momentum measuring planes. The second and fourth of these are also known as the upstream and downstream - relative to the CCM - regions of the apparatus.

Beam Reconstruction - It is self-evident that a successful beam reconstruction - i.e. an unambiguous calculation of the beam momentum and its trajectory incident upon the experimental target - is a prerequisite condition for the successful analysis of an event. For this reason a systematic study of the performance of the beam apparatus - see Section 2.B and 2.C - is made with a view to maximising the beam reconstruction efficiency. Looking back at Figure 2.3, it is seen that six points are needed to totally define the incident muon trajectory - i.e. one X point at each of the four beam stations and one Y point at each of the beam stations 3 and 4. These points are independently produced and the overall efficiency of producing all six points is derived from six independent probabilities. Looking at the data in the beam chambers and hodoscopes it was decided that to have any chance of defining a point at each of the six positions of interest, one of the following four conditions must be satisfied for the appropriate MWPC and beam hodoscope. These are in order of decreasing quality:-

- (a) a single hit in the beam MWPC masked by a lit counter element in the matching beam hodoscope.
- (b) a single hit in the MWPC and no lit elements in the hodoscope.
- (c) a single lit element in the hodoscope and no MWPC hits.
- (d) a single lit hodoscope element and an arbitrary number of MWPC hits.

In addition for the two points at beam station 4 - which has a pair of X and a pair of Y chambers - matching hits from the pair are preferentially used, failing which the chamber which provides the better quality information is used alone. For a perfect beam apparatus, condition (a) would be satisfied at each of the six points. In practice however the

imposition of condition (a) only on each of the six points gives an overall efficiency of less than 50%. Efforts to improve this figure are helped by the large distances between the beam stations. This allows the use of counter information to provide adequate spatial resolution at beam stations 1, 2 and 3. Using this fact, the conditions for obtaining a good beam trajectory may be stated as follows:

- (1) The X and Y points at beam station 4 must satisfy the above conditions (a) or (b). Beam station 4 is too near the experimental target to allow the use of spatial information from the hodoscopes alone.
- (2) The X and Y points at beam station 3 must satisfy the above conditions (a) or (b) or (c).
- (3) The two X points at beam stations 1 and 2 must satisfy the above conditions (a) or (b) or (c) or (d).
- (4) The beam trajectory generated from the six points so obtained must link to within 1 cm in X at the centre of the D4 dipole magnets. Figure 4.2 shows a histogram of this X-linking.
- (5) The beam trajectory must lie inside the apertures of the D4 dipoles at their entrance, centre and exit.

Table 4.1 summarises some reconstruction efficiencies and beam statistics.

Upstream Tracks - For the upstream region of the apparatus, track-finding is carried out separately in the X and Y views. Each view is searched for three or four point tracks that point back either to the incident muon or the target region. A chisquared cut eliminates tracks that are less than 2% probable. In cases where two tracks share two or more common sparks, the track with the worse chisquared is eliminated.

Muon Chamber Tracks - The approach used to find tracks in the Muon chambers utilises the fact that these chambers lie close together relative to their distances from the centre of the CCM and the target. In this method X, Y points are generated from the X, U, V sparks in the read-out planes. The program first looks in the X view, starting with the most negative spark - this may be in any spark gap. It then searches to see if there are at least two sparks in other gaps within a variable X road of the initial spark. Failing this it moves onto the next most negative spark and searches again, the process being repeated until the above spark criterion is satisfied. The sparks thus found, together with the spark being tested, are least-squares fitted for a straight line. A simple chisqrd cut corresponding to an error of $5 \times 1/4$ mm is imposed on the track - it should be borne in mind that the resolution of each plane is better than $2 \times 1/4$ mm and that the typical double spark separation is over $70 \times 1/4$ mm. If the track fails this cut, each of the additional sparks are dropped in turn and another from the same gap is tried to see if the resultant track passes the chisqrd cut. Having found a good X track, the corresponding Y values are searched for a track. The Y resolution of the Muon chambers, and indeed all the spark chambers in the experiment, is much poorer because the Y co-ordinate is derived from U and V read-out planes that have almost vertical wires. Because of this poorer resolution, a chisqrd cut corresponding to an error of $60 \times 1/4$ mm per Y point is employed to weed out the bad tracks. Having found a good X, Y track, the program drops the sparks associated with this track - great care is taken not to introduce any potential biases with this dropping of sparks - and carries on its search through the remaining sparks for further tracks. Figure 4.3 shows schematically how the above track-finding operates on a simple spark pattern.

Downstream Tracks - The situation in the downstream region of the apparatus is complicated by the large number of read-out planes and by the even larger number of sparks in these planes that are not event associated. The extra sparks arise because of the long spark chamber memory times - approximately 2 μ sec for the magnetostrictive chambers and 2 to 9 μ sec for the shift register chambers - and because of muon halo and γ -rays from the pole-faces of the CCM. The twelve shift register chambers suffer more severely from this effect than do the 6-metre chambers - they are nearer the CCM, have longer memory times and are not deadened in the beam region as are the 6-metre chambers.

• Because of this, the downstream track-finder first generates all the tracks in the 6-metre chambers using exactly the same method as is used in the Muon chambers. Each of these tracks is then projected into the shift register planes to pick up extra contributing sparks. The tracks from the 6-metre chambers point well in X - better than 0.7 cm at the furthest shift register plane - and in Y they may be constrained to point back to the incident muon at the centre of the target. These two facts enable a road of up to 3 cm at the most upstream shift register plane to be set for the track projection. Having found the extra sparks the entire track is re-fitted separately in the X, U and V co-ordinates. A χ^2 cut corresponding to $5 \times 1/4$ mm is again applied to weed out any bad tracks. A minimum of three shift register sparks and a minimum of eleven for the total number of sparks is set for the entire downstream track. If the track fails these two requirements, the road is widened by 1.5 cm and a further search for contributing sparks in the shift register planes is made. Good X, Y tracks are then re-constituted from the fitted X, U, V projections of the tracks.

No attempt is made to find tracks in the Photon and Neutron chambers, but the number of sparks in a 1cm road associated with each downstream track is recorded for both sets of chambers. This spark counting is of some use in particle identification.

Track Linking - Having found tracks in all four regions of the apparatus, the next step is to correlate tracks in the various regions that belong to the same particle trajectories. Track linking between the upstream and downstream tracks is effected by the method discussed in Section 3.G - i.e. upstream and downstream tracks that belong to the same particle trajectories have matching impact parameters in the X-Z plane and matching slopes and intercepts in the Y-Z plane. Figure 4.4(a) shows a histogram of the differences between the impact parameters of upstream and downstream tracks at the CCM centre. One can comment that approximately $3/4$ of the width of the distribution comes from the resolution of the upstream track. In X a downstream track is said to have linked to an upstream track if their impact parameters differ by less than $35 \times 1/4$ mm. Histograms of the differences in the Y-slopes and Y-intercepts at $Z = 0$ of upstream and downstream tracks are shown in Figure 4.4(b) and 4.4(c). In these cases most of the width of the distributions come from the poor Y resolution of the downstream track. Upstream and downstream tracks are said to have linked in Y if the following inequality is satisfied

$$\left[\left(\frac{\delta(\text{slope})}{6\text{mr}} \right)^2 + \left(\frac{\delta(\text{intercept at } Z = 0)}{2\text{cm}} \right)^2 \right] < 1$$

The effects of vertical focussing and the helix correction are ignored as far as track-linking is concerned. Every downstream track is allowed to link to up to four upstream tracks, and every upstream track can link to an arbitrary number of downstream tracks.

At this point two separate methods of track recovery are attempted using any upstream and downstream tracks that do not link in the above manner. Firstly, the un-linked downstream tracks are projected back into the upstream chambers - by allowing for the CCM magnetic field and by constraining the projected line to intersect the incident muon trajectory at the centre of the target. The upstream MWPCs are then further searched for two point tracks about this line. For both the 96 GeV/c and 147 GeV/c data approximately 14% of the X-tracks and 16% of the Y tracks in the upstream MWPCs are such two point tracks. Approximately 2.5% of the upstream tracks are two-point in both the X and Y views. The second recovery process searches for extra downstream tracks using the unlinked upstream tracks. The latter are used in combination with a single spark in the 6-metre chambers masked by lit G and H hodoscope elements to define a tight road of 0.5 cm to look for extra tracks in the shift register chambers. This recovery process rescues approximately 16% extra downstream tracks in the 96 GeV/c data and approximately 9% extra tracks in the 147 GeV/c data. It effectively removes any dependence of the track-finding on the 6-metre chambers.

The next step is to link the downstream tracks with those found in the Muon chambers. In theory the downstream and Muon chamber tracks corresponding to the same particle trajectory should have the same slopes and intercepts in both X and Y. In practice the situation is much complicated by both the multiple scattering in the lead and steel walls in between the downstream and Muon chambers and the poor pointing of the Muon chamber tracks especially in Y. In X the slopes and intercepts of the downstream and Muon chamber tracks are compared at a Z corresponding to the weighted multiple scattering centre of the lead and steel walls.

For tracks close to the beam the slope difference of linked tracks is required to be less than 12.5 mr and the intercept difference to be less than $150 \times 1/4$ mm. For tracks further away from the beam these cuts are relaxed by a multiple scattering factor - up to 9 in size - to allow for differences in the amount of material traversed and the different particle energies. Figure 4.5 shows histograms of the X-slope differences of downstream and Muon chamber tracks for different regions of X. Figure 4.6 shows the equivalent histograms for the X-intercept differences. In both plots the multiple-scattered factor mentioned above has been divided out of the differences. In Y the intercepts of downstream and Muon chamber tracks are compared at the Z position of the Muon chambers and are required to be within $750 \times 1/4$ mm of each other for a successful link. In general this Y condition helps only to resolve cases of confusion and ultimately the smallest X-intercept difference is used to decide in cases of ambiguous linking.

Tertiary Output Buffer - The linking information as obtained above can now be used to construct the trajectory of particles in the event and a first attempt at a physics reconstruction may be made. The average values of the currents in the CCM and D4 magnets - these currents were recorded once every beam spill - are input into the tertiary tape program on a run by run basis. These along with the bends of particles in the respective magnets are used to calculate the particle momenta. An attempt at vertex finding is made by looking at the upstream tracks to see if they project back to a point in the target. The ν , Q^2 and angle of scatter are calculated for the possible muon candidates. But as stated before the emphasis of this tertiary stage of the event

reconstruction is in the track-finding and track-linking and the process of muon selection is described in Section 4.D.

The event buffer that is written onto the tertiary tape contains basically the track-finding, track-linking and vertex data and the particle momenta. In addition the scaler and counter latching information is transferred over from the secondary tapes intact. The complete format of the tertiary event buffer may be found in Reference (60). This tertiary stage of the event reconstruction is by far the most time-consuming and takes on average 150-200 msec per trigger. To end this section, it may be commented that the tertiary tapes have two main functions, firstly to be used as input for various debugging and efficiency programs and secondly as input for the various physics programs.

4.C COUNTER POSITIONS AND EFFICIENCIES

As an example of the first use of the tertiary tapes, this section describes how the data is used to check the positions of the elements of the downstream and Muon hodoscopes and to calculate their efficiencies.

Positions - There are two reasons for wanting to know the X, Y positions of the elements of the G, H, M, M' and N - see Section 2.D - counter hodoscopes as accurately as possible and these are related to the two separate functions of these hodoscopes. Firstly, those hodoscope elements that trigger the apparatus define the geometric acceptance of the experiment and a knowledge of the sizes and positions of the active triggering areas is necessary for the calculation of this

acceptance. Secondly, all the hodoscopes, with their 30 nsec time resolution, are used to time the spark chamber tracks - i.e. determine which of these tracks are event associated and which are not. An accurate knowledge of the elemental positions within the hodoscopes will minimise the confusion remaining after track timing.

The positions of the counter elements were measured prior to run time and in general the measurements determine the relative positions of the elements within the hodoscopes very well. However as absolute spatial measurements, they prove less trustworthy and the event data is used both to obtain the absolute shifts in X and Y needed to correct the positions of the hodoscopes and to check the relative positions within the hodoscopes. In principle it would appear to be a straightforward matter to obtain the positions of all the counter elements. This would be done by first selecting all the events in which the counter element of interest is lit. Then by making an X-Y scatter plot of the intersection points of tracks in these events with the hodoscope plane containing the element, the X-Y extent of the element would immediately be seen. In practice this proposition is greatly complicated by three factors. Firstly, there are a large number of spark chamber tracks that are not event associated, secondly, the distribution of tracks is non-uniform in the X-Y plane, falling extremely rapidly with distance from the beam region and lastly the tracks have finite spatial resolution. All three factors serve to complicate and bias the above scatter-plot picture. A more profitable approach is to attempt to define the edges of counters and to calculate positions where two counters touch or overlap. With this in mind, three separate methods are employed to obtain spatial information about the counter elements and the results combined with the positions directly measured to generate the most accurate and consistent geometry for the hodoscopes.

The first method uses the imbedded beam triggers - see Section 3.B - to look at the Y positions of the central N counters. In the data sample there are approximately 8000 reconstructed imbedded beam events in each of the 96 GeV/c and 147 GeV/c data sets. The beam tracks from these events are projected to the N hodoscope, each track being given the appropriate X-bend and the small Y-corrections due to the CCM magnetic field. The distribution of beam events in the X-Y plane is shown in Figure 4.7. For the imbedded beam triggers, the counter latching information shows that the elements N6, N7, N8, N9 and N10 are lit for substantial numbers of events. For each of these elements a histogram is constructed of the Y-distribution of the projected beam tracks at the N hodoscope for events in which the element being considered is lit. These histograms are then normalised to overall Y-distribution of beam events at the N hodoscope and plotted. Figure 4.8 shows the plots so generated and it is seen that the N7/N9, N6/N8 and N8/N10 edges may be determined to $10 \times 1/4$ mm. In an attempt to improve the track resolution at the N hodoscope, the process is repeated using both the beam track and the track in the upstream MWPCs to define the beam trajectory before projecting it through the CCM. It is found that using either method of defining the beam trajectory on either of the 96 GeV/c or 147 GeV/c data gave similar and consistent results. The use of the imbedded beam triggers for finding the positions of counters has two obvious advantages. Firstly, there is only one particle per event and secondly the use of MWPCs - which have timing resolution of approximately 100 nsec - means that there is no confusion due to stale tracks in obtaining its trajectory. Equally obvious is the major disadvantage of this method, namely that the limited spatial extent of the beam gives the Y positions of a few of the N hodoscope elements.

To avoid the latter limitation, the second method used to find counter positions employs a similar histogramming technique using the spark chamber tracks of the real data as input. Firstly, the timing of the downstream tracks - i.e. whether these are event associated or not - is established by demanding that they link in X and in Y to three or four point upstream MWPC tracks. The Muon chamber tracks are timed by demanding that they link to upstream linked downstream tracks. A sample of events with only one such linked muon is selected in order to further reduce any confusion resulting from stale, out-of-time tracks. Next an attempt is made to improve the pointing of the spark chamber tracks. For the downstream tracks, the Y pointing is improved by demanding that the tracks go through the centre of the target at beam height. Each Muon chamber track is re-calculated by taking a line between the point on the Muon chamber track at the centre of the Muon chambers and the point on the corresponding downstream track at the centre of the 6-metre chambers. Then as before the in-time tracks in the chosen sample of events are used to construct normalised histograms that look at the edges of single counters or of groups of counters. Great care is exercised in interpreting the data for those counter edges that lie on the boundaries of the K-veto or of the magnetostrictive chamber deadners as these boundaries cause drastic changes in the track distributions. Figure 4.9 shows a few of the normalised plots obtained using this method.

The last method of position finding employs a Monte-Carlo technique to define the edges of the inner acceptance hole in the Muon trigger plane - i.e. the inner non-triggering area of the M, M' and N hodoscopes. It would be appropriate to say a few words at this point about the Monte-Carlo program that is used. The purpose of the program is to generate muon scatters and to track the scattered muons through

the apparatus simulating the experiment as realistically as possible. To take into account the beam phase space, the program uses the beam tracks from the imbedded beam triggers. To generate a scattered muon, the program first takes a beam track and randomly selects a vertex on this trajectory inside the experimental target volume. It then chooses values of v and Q^2 weighted according to the cross-section and randomly selects the azimuthal angle of scatter. These parameters define the scattered muon track as it leaves the target. This trajectory is then tracked through the CCM magnetic field and is multiply scattered in the lead and steel walls. The scattered muon is then tested to see if it satisfies the experimental triggering requirement and to ensure that it misses the deadeners of the magnetostrictive spark chambers. A scattered muon trajectory that passes the above tests is then modified to take into account the effects of the resolution of the chambers. The process is repeated starting with beam tracks randomly selected from the imbedded beam triggers to generate as large a sample of scattered muons as is necessary. This sample may then be used to construct the various required histograms and scatter-plots. Comparisons of the real data with that which is generated by the Monte-Carlo program prove extremely useful in understanding the apparatus and debugging the analysis, although great care should be taken to ensure that any results of such comparisons are not sensitive to the exact cross-sectional form input into the program. In the particular application considered in this paragraph, various different positions of the inner acceptance hole are input into the Monte-Carlo program and the resulting muon event distributions at the Muon hodoscope plane are compared with the corresponding distribution from the real data. Figure 4.10 is a diagram of this comparison in Y . Using this method, the edges of the hole may be defined to better than 0.5 cm.

The three methods above are used on both the 96 GeV/c and 147 GeV/c datasets. It is found that both give consistent results for the counter positions, as indeed they should given that none of the counter elements were moved in going from one incident momentum to the other. The results for these three methods together with the positions from the pre-run survey give all the elemental positions with errors which are at worst 0.5 cm.

Efficiencies - Once the best set of counter positions is established the performance of the individual counter elements during the data runs may be determined. First a sample of tracks is chosen from the real data in exactly the same way as in the second position finding method - i.e. in-time relative to the upstream tracks, only one such in-time muon track in the event, and re-calculated track parameters for improved pointing. As long as the conditions imposed to obtain a clean and unconfused sample of tracks are independent of the counter information, they may be as stringent as is necessary without fear of biasing the counter efficiency measurement. With the chosen sample of tracks, the counter efficiencies are easily obtained. The tracks are first tested to see if they point to the counter element of interest. To take into account the resolution of the tracks and possible errors in defining the exact position of the element, the tracks are required to lie $50 \times 1/4$ mm inside of any edge of the element in order to satisfy the pointing criterion. This ensures that the track in question definitely points to the element. If the track points to the element in this way, the latter is tested to see if it is lit. As the G hodoscope stands alone in the experimental trigger, it is further insisted that there be at least two tracks per event pointing to different elements of this hodoscope. The efficiency of the element is

then simply

$$\frac{(\text{the number of times the element is pointed at and lit})}{(\text{the number of times the element is pointed at})}$$

Table 4.2 is a list of the efficiencies obtained in this way for both the 96 GeV/c and 147 GeV/c data sets. It is seen that any inefficiencies are in general less than 0.5%, although some of the M' elements give slightly higher inefficiencies. One can comment that the G hodoscope stands alone in the experimental trigger and for it the efficiencies are the efficiencies for latching the counter information once the trigger requirement is satisfied. The counter efficiencies are also generated on a run by run basis and this information is used to see if any particular runs have any counter efficiency problems. This last method did indeed show that a few of the runs in the 96 GeV/c dataset had some bad counter data.

4.D EVENT RECONSTRUCTION - MUON SELECTION AND KINEMATICS

In this step the timing of the spark chamber tracks is established using the counter hodoscopes. Then the muon candidates amongst the in-time tracks of an event are established. The best muon is selected and the interaction vertex of the event is then re-calculated. Some pictures of events are shown and the momentum calibration of the experiment and the calculation of the kinematics of the event are discussed.

Timing - The requirement that downstream tracks link to upstream MWPC tracks and that Muon chamber tracks link to upstream linked downstream tracks does not in general filter out all of the stale halo tracks. If these halo tracks were to be accepted as genuine they would confuse the process of muon selection and bias the resulting particle distributions.

In view of this, the elements of the downstream and Muon hodoscopes - which have a time resolution of typically 30 nsec - are used to define the in-time status of the spark chamber tracks. First these tracks are timed relative to the nearest hodoscopes to their chambers - i.e. the G and H hodoscopes for the downstream tracks and the M', M' and N hodoscopes for the Muon chamber tracks. Every track is tested to see if it passes through the hodoscope being looked at. For this purpose the N hodoscope is considered to contain a hole corresponding to those of its elements that are not in the experimental trigger. If the track does pass through the hodoscope it is further tested to see if it points to a lit element within that hodoscope. To allow for the spatial resolution of the tracks and possible errors in the counter positions, each element is expanded by $150 \times \frac{1}{4}$ mm in X and $300 \times \frac{1}{4}$ mm in Y before being tested to see if the track passes through it. This ensures that good tracks that actually did go through the element being considered, but appear to point just outside its exact edges, are flagged as having hit it.

Extreme care is exercised if the track points near the edges of the holes in the various hodoscopes to ensure that possible in-time tracks - i.e. those that did go through the hodoscope but appear to point into the hole - are not lost. It can be commented that for the Muon chamber tracks, this latter task is not made any easier by the complicated geometry of the K-veto and the holes in the M, M' and N hodoscopes. For every track the success rate ℓ/h is determined - where h is the number of hodoscopes pointed at and ℓ is the number of these in which the track points to a lit element. Downstream tracks are considered in-time if this success rate is $\frac{2}{2}$ or $\frac{1}{1}$ or $\frac{1}{2}$. Likewise, Muon chamber tracks are considered in-time if their success rate is $\frac{3}{3}$ or $\frac{2}{3}$ or $\frac{2}{2}$ or $\frac{1}{2}$ or $\frac{1}{1}$. The downstream tracks are

further timed by being projected past the 240 cm steel muon filter and being tested against the Muon hodoscopes. Allowances for multiple scattering in the lead and steel walls are made by further expansions in size of the counter elements according to the particle trajectory.

Muon Selection - In-time downstream tracks that link to upstream tracks are defined to be event-associated. Possible muon candidates are selected from these tracks by using one of two criteria. Firstly, an in-time downstream track that links to an in-time Muon chamber track gives rise to what is called a track-linked muon. Secondly, an in-time downstream track that points to lit elements in the Muon hodoscopes and also points to a cluster of sparks in the Muon chambers gives rise to what is called a counter labelled muon. Any trajectory that is out-of-time with more than one hodoscope in its path is removed from the list of possible muon candidates. Next the muon candidates are tested against counters N5-N11 which were not in the experimental trigger. If the muon trajectory points $75 \times 1/4$ mm inside the inner acceptance hole in X and points to a lit N5-N11 element in Y, it is removed from the list of possible muon candidates. This helps reject those muons that did not go through the triggering area of the Muon hodoscopes. In the majority - approximately 85% for the 96 GeV/c data and 92% in the 147 GeV/c data - of events in which any muon is found, there is one track-linked muon only and as such the muon selection is trivial. Most of the rest of the events with muons found contain one counter labelled muon only or contain two track linked muons that link to the same downstream track. Of those events that contain two or more genuine muon candidates - approximately 1.5% of the events with muons found in each of the two data-sets - the best muon is chosen. In this choice preference is given to track-linked muons as opposed to counter labelled muons and failing this the muon candidates with the better upstream linking and counter timing

Vertex Finding - Next the vertex of the interaction is re-calculated. This is done by taking the upstream track that corresponds to the downstream scattered muon and looking for its intersection point with the incident beam track. The upstream track buffer is then further searched for tracks that pass close to this intersection point and that are linked to in-time downstream tracks. These extra tracks are used in addition to the upstream scattered muon and beam muon tracks to calculate the interaction vertex. Figure 4.11 shows the distribution of event vertices along the Z-axis for the 96 GeV/c data for events with $Q^2 > 0.5$. Both the target full and target empty data are shown, the target empty distribution being normalised to the same incident flux as for the target full distribution. The target is clearly seen. In addition the Z-positions of the target flask material and the most downstream beam hodoscopes may be discerned.

Event Pictures - An extremely useful method of checking the track-finding, muon selection and other programs consists of drawing out events and visually scanning samples of these to ensure that the various programs are working as well as expected and possible. A program, using both the secondary and tertiary tapes as input, exists to draw out the spark, counter and track information of events. The pictures highlight the complexity of events and help explain why in practice the event reconstruction required a large amount of effort although in theory - and its description - this reconstruction appears fairly straightforward.

Figures 4.12(b) to 4.12(g) are sample pictures of the various types of event triggers. Before describing the events, a few words about the layout of the pictures is necessary. Each picture is divided

into four views - i.e. X upstream, Y upstream, X downstream and Y downstream. Figure 4.12(a) details the apparatus that is drawn in these four views - see Figure 2.7 for the complete diagram of the spectrometer apparatus. Looking at the event pictures themselves, the crosses represent the sparks in the spark chambers and the hits in the MWPCs - the sparks are not drawn in the Y downstream view. The solid and broken lines represent the tracks found, the solid lines being in-time and the broken lines being out of time with respect to the counters. The lit counter elements are also drawn. In the two upstream views the projections of the downstream tracks at the centre of the CCM are drawn and one can see the linking of downstream tracks to upstream tracks. The interaction vertex is indicated by the letter "O".

Figure 4.12(b), 4.12(c) and 4.12(d) are examples of events that the experiment is concerned with - i.e. the inelastic nuclear scatters. Figure 4.12(d) has two downstream muons, one of them probably from a decay in flight of a pion or kaon from the interaction. The next two pictures illustrate the two major sources of background scatters in this experiment. Figure 4.12(e) shows a muon-electron scatter. Such an event is characterised by having two oppositely charged tracks. These have a small opening angle in the upstream MWPCs and the negative particle showers in the 5 cm steel wall to produce a large number of sparks in the Photon chambers. It is seen that the signature of a muon-electron scatter is quite easily distinguishable. Figure 4.12(f) shows a muon bremsstrahlung event. Here there is one positively charged track only and a shower of sparks in the central region of the Photon chambers corresponding to the bremsstrahlung photon. Lastly, Figure 4.12(g) shows an example of a spurious trigger. One can comment that this is the type of trigger that occurs most

Momentum Calibration - Before the kinematic variables - such as ν , Q^2 , W^2 etc. - of events can be calculated and the event data binned to obtain cross-sections and the structure functions, it is necessary to check the momentum calibration of the experiment. This is done in two stages. Firstly, the spectrometer momenta which are derived from the CCM are calibrated relative to the beam momenta which are derived from the D4 dipole magnets. Secondly, the absolute momentum calibration is calculated. In theory these calibrations are easily obtained by looking at the energy balance and Q^2 in the large sample of elastic muon-electron scatters that exist in the data.

• The danger in using the muon-electron scatters to calculate the relative calibration is that the effects of a genuine miscalibration between the CCM and the D4 dipole magnets - which affects positive and negative particles in the spectrometer in the same way - are confused with the effects of a possible angular alignment error of the downstream part of the spectrometer relative to the upstream part - this affecting the positive and negative particles oppositely. To get some idea of the numbers involved, it may be shown that a 0.2 mr error in the alignment produces roughly the same effect as a 1% relative miscalibration on a 110 GeV/c particle in the 147 GeV/c data. For the CCM the relationship between p , the magnitude of the particle momentum and θ , the magnitude of the angular bend in the CCM field may be written as

$$p\theta = K$$

where K is a constant for a particular setting of the magnetic field. If p is in GeV/c and θ is in radians, then $K = 2.23$ for the 147 GeV/c data and $K = 1.404$ for the 96 GeV/c data.

If the angular alignment error of the downstream part of the spectrometer relative to the upstream part is ϵ and the miscalibration of the CCM relative to the D4 dipole magnets is δ , then the following relationships between the measured momentum, p^{seen} and the actual momentum p can be written

$$p_+^{\text{seen}} = (1 + \delta) \frac{(\theta_+ - \epsilon)}{\theta_+} p_+$$

$$p_-^{\text{seen}} = (1 + \delta) \frac{(\theta_- + \epsilon)}{\theta_-} p_-$$

where the +, - subscripts refer to positive and negative particles. For muon-electron scatters the total energy seen in the spectrometer is

$$p_\mu^{\text{seen}} + p_e^{\text{seen}} = (1 + \delta) \left[\frac{(\theta_\mu - \epsilon)}{\theta_\mu} p_\mu + \frac{(\theta_e + \epsilon)}{\theta_e} p_e \right]$$

Using the relationships $p\theta = K$ and $p_\mu + p_e = p_{\text{beam}}$, this simplifies to

$$p_{\text{total}}^{\text{seen}} = (1 + \delta) \left[1 - \frac{\epsilon}{K} (p_\mu - p_e) \right] p_{\text{beam}}$$

Assuming that δ and ϵ are small and that $\delta \times \epsilon$ is negligible, this equation further reduces to

$$\Delta E = p_{\text{beam}} - p_{\text{total}}^{\text{seen}} = -\delta p_{\text{beam}} + \frac{\epsilon}{K} p_{\text{beam}} (p_\mu - p_e)$$

It is seen that a plot of ΔE against $(p_\mu - p_e)$ will generate both δ and ϵ .

The acceptance of the apparatus for muon-electron scatters limits the scattered muon energies in these events to be less than about 45 GeV. Given this, these events are divided into three 10 GeV wide bands of ν and the distribution of events as a function of ΔE is

plotted for each band. This plot is also made for the imbedded beam triggers, these being considered to have $v = p_e = 0$. Figures 4.13(a)-4.13(d) show these plots for the 96 GeV/c data and Figures 4.14(a)-4.14(d) show the equivalent plots for the 147 GeV/c data. The plots are used to generate ΔE values for the $\langle p_\mu - p_e \rangle$ in the various bands of data. Figure 4.13(e) and 4.14(e) show the plots of ΔE versus $\langle p_\mu - p_e \rangle$ for the 96 GeV/c and 147 GeV/c data. From these plots, it may be calculated that

for the 96 GeV/c data, $\delta = -0.0657 \pm 0.0004$, $\epsilon = -0.277 \pm 0.005$ mr
and for the 147 GeV/c data, $\delta = -0.0010 \pm 0.0004$, $\epsilon = -0.141 \pm 0.010$ mr.

• Having corrected the spectrometer momenta by using these values of δ and ϵ , the absolute momentum calibration factor β - i.e. $p_{\text{real}} = \beta p_{\text{calc}}$ for both the beam and spectrometer momenta - is determined. One can comment that the data is far less sensitive to this absolute calibration than it is to the relative calibration - i.e. for a 150 GeV/c incident beam, a 2% relative miscalibration changes a v of 5 GeV by ± 3 GeV whereas a 2% absolute miscalibration changes the same v by ± 0.10 GeV.

For the elastic muon-electron scatters

$$2m_e v = Q^2 = 4EE' \sin^2 \theta / 2 + \frac{m_\mu^2 v^2}{EE'} \quad \text{where } m_e, m_\mu \text{ are the electron and muon masses, } E, E' \text{ are the incident and scattered muon energies and } \theta \text{ the angle of scatter.}$$

Using this equation the values of θ calculated from v are compared with the directly measured θ values.

The $\chi^2 = \sum_{\text{events}} \frac{(\theta_{\text{measured}} - \theta_{\text{calculated}})^2}{\sigma^2}$ where, σ is measurement error for θ , - is plotted for a range of values of β and the latter is determined by looking for a minimum in this plot. Figure 4.13(f) and 4.14(f) show the plots for the 96 GeV/c and 147 GeV/c data respectively. From these

plots β is estimated to be 1.008 ± 0.005 for the 96 GeV/c data and 0.993 ± 0.005 for the 147 GeV/c data.

4.E DATA REDUCTION

This section describes the cuts made on the total data sample to generate the raw event distributions for the scattering of 96 GeV/c and 147 GeV/c incident muons off protons in our experimental set-up. The section ends with a few plots of the event distributions so generated.

Inefficiencies - The data is first inspected on a run by run basis to see if any elements of the apparatus were inefficient during the course of that run. In most cases there is sufficient redundancy in the apparatus such that the effects of these inefficiencies can be corrected for. However, certain elements of the apparatus stand alone and should these malfunction, the whole run has to be rejected. Three cases of apparatus inefficiency may specifically be mentioned, these accounting for almost all of the data lost in this step. It is apparent that the beam hodoscopes and the triggering hodoscopes - especially the G - must be highly efficient. The former are necessary for good beam reconstruction efficiency and the latter for efficient triggering. In theory one can always correct for counter inefficiencies providing that these can be measured sufficiently accurately. In practice however it is hard to estimate the systematic errors introduced by these corrections. The last - and indeed the major - cause of data loss arises from the inefficiencies in the downstream shift register and 6-metre chambers, see Section 2.D. In the downstream region, the

trackfinder requires a high efficiency in the 6-metre chambers and at least 11 sparks from the 20 downstream read-out planes for a good track. The spark distribution of downstream tracks is checked on a run by run basis and a run is rejected if the mean of its spark distribution is less than 2 standard deviations above the 11 spark cut.

Good Muon Scatters - The first cut made on the remaining triggers is the obvious. Good events are required to have a reconstructed beam muon, a scattered muon and an event vertex. The beam muon trajectory is checked to ensure that it lies inside the target along the latter's entire length. The scattered muon trajectory is checked to ensure that it lies within the geometric acceptance of the trigger and that it does not point inside the deadener of the 6-metre chambers.

Target Cut - Looking at Figure 4.11, the Z-positions of event vertices is fairly well defined and a target cut between $Z = -7.0$ m and $Z = -4.8$ m can be made. The event vertex and its error are first re-calculated using the track parameters of the beam and scattered muons only - in this way any biases in the vertex finding that depend on the number of upstream tracks are avoided. Any event whose re-calculated vertex position is more than three standard deviations outside the target cut is removed from the data sample.

Q^2 Cut and Explicit Muon-Electron Scattering Cut - The events that go to make up the raw datasets are further required to have a $Q^2 > 0.2$ (GeV/c)². This helps to eliminate almost all of the muon-electron scatters -

$Q^2 = 2m_e \nu \lesssim 0.15 \text{ (GeV/c)}^2$ - and most of the muon bremsstrahlung triggers.

Comparison of the event data at this stage with that predicted from the form of the cross-section from the SLAC data indicated an excess of events in the low Q^2 and high ν kinematic region for the 147 GeV/c data - i.e. for $Q^2 < 0.6 \text{ (GeV/c)}^2$ and $\nu > 80 \text{ GeV}$ or so. Some pictures were drawn of events in this kinematic region and these confirmed suspicions of a possible contamination of the data from muon-electron scatters. In theory the latter should all be eliminated by the $Q^2 > 0.2 \text{ (GeV/c)}^2$ cut. In practice the effects of the resolution of upstream tracks - θ , and hence Q^2 , is derived from these tracks - and possible confusion in linking upstream to downstream tracks make it possible for the measured Q^2 to be larger than 0.2 (GeV/c)^2 . Given the large number of muon-electron scatters, a few events can spill over into the lowest Q^2 regions. In addition one expects this effect to be more pronounced in the 147 GeV/c data because the ν 's - and hence the Q^2 's of the muon-electron scatters - are higher in this data than in the 96 GeV/c data.

A program written to recognise the signature of a muon-electron event - see Figure 4.12(e) - is used to eliminate the extra muon-electron scatters from the data. This program is approximately 80% efficient in flagging muon-electron events. It is estimated that, after applying this program to the data, there is a residual muon-electron contamination in the 147 GeV/c data of approximately 6% - just less than the statistical errors - for $\nu > 80 \text{ GeV}$ and $0.2 \text{ (GeV/c)}^2 < Q^2 < 0.3 \text{ (GeV/c)}^2$ and approximately 3% - about $1/3$ of the statistical error - for $\nu > 80 \text{ GeV}$ and $0.3 \text{ (GeV/c)}^2 < Q^2 < 0.6 \text{ (GeV/c)}^2$. For all other kinematic regions in the 147 GeV/c data and for all of the 96 GeV/c data the residual contamination is less than 0.5%.

Next the $Q^2 > 0.2 \text{ (GeV/c)}^2$ trigger rate of the raw events is calculated on a run by run basis. This rate contains the appropriate factor to make allowances for the different beam reconstruction rates for the different runs - see the next Chapter. The average $Q^2 > 0.2 \text{ (GeV/c)}^2$ is calculated and any run whose rate is more than 3 standard deviations from this average rate is removed from the data sample. This cut helps remove runs where it is possible that the target was not completely full.

The events that are left go to make up the raw event datasets for the two incident energies. Table 4.3 summarises the various cuts made and the triggers lost at the various stages.

Distributions - To end this section and chapter, a few plots of the raw event distributions are shown. Figure 4.15(a) shows the X, Y scatterplot of raw events at the Muon hodoscopes for the 96 GeV/c data. Figure 4.15(b) shows a scatterplot of these events in ν and Q^2 and Figure 4.15(c) histograms the projections of the ν , Q^2 scatterplot. Figure 4.16(a), 4.16(b) and 4.16(c) show the equivalent scatterplots and histograms for the 147 GeV/c data.

FIG 4.1

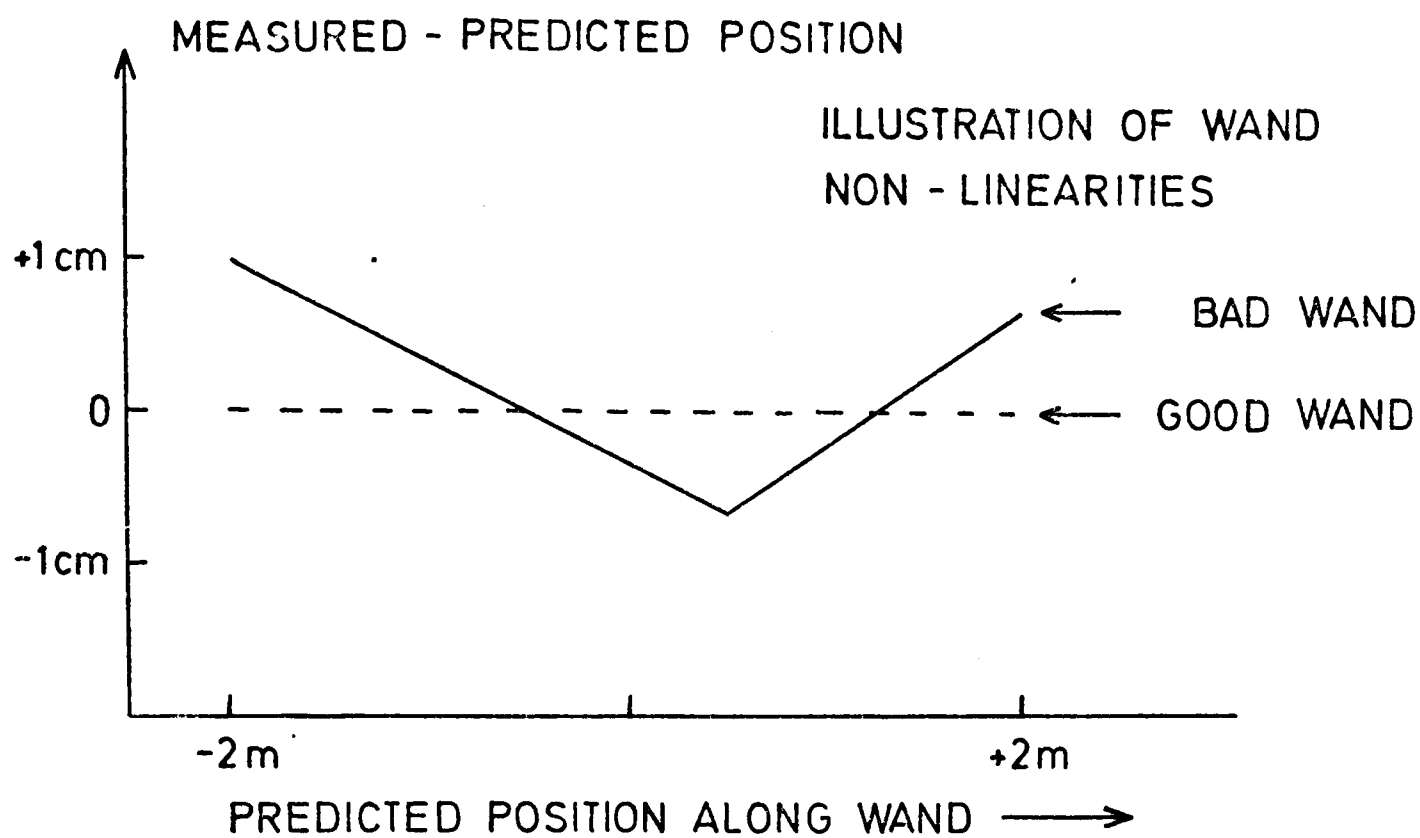


FIG 4.2

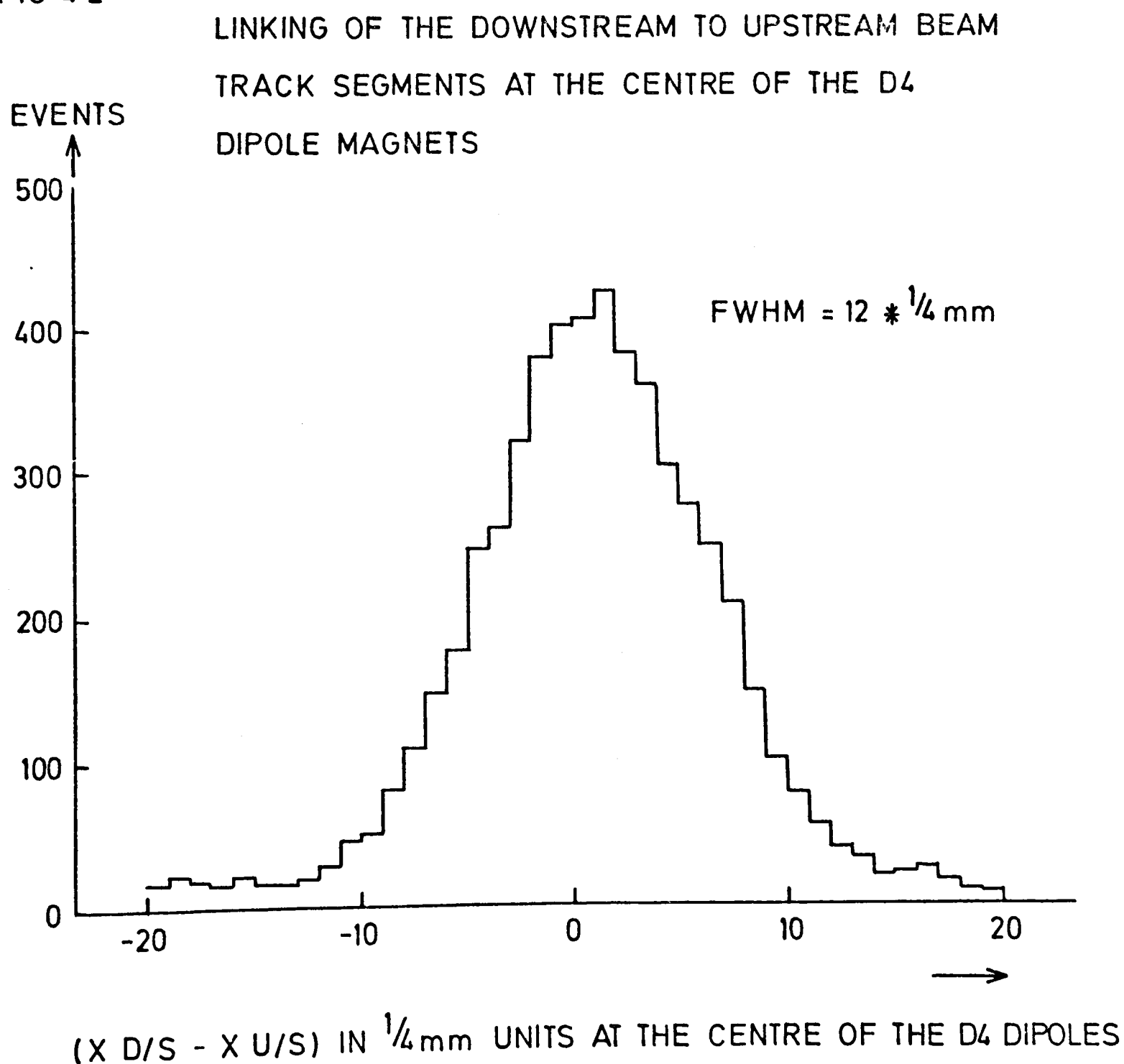


TABLE 4.1
SOME TYPICAL BEAM STATISTICS
(96 GeV/c data)

BINS CONTAIN % OF THE TOTAL NUMBER OF TRIGGERS (= 16504)

Beam Station	Direction	Elements lit in the Hodoscope			Wire Hit in the MWPC			Hit Wires Masked by Lit Elements			Beam Reconstruction Condition as per Description in Section 4.B				
		0	1	>1	0	1	>1	0	1	>1	(a)	(b)	(c)	(d)	
1	X	4.5	91.7	3.8	5.5	68.1	26.4	10.5	83.9	5.6	83.96	2.28	4.04	4.88	
2	X	1.2	98.8	0.0	9.2	66.1	24.8	12.8	78.5	8.7	78.50	0.75	9.08	8.68	
3	X	1.3	98.7	0.1	4.5	65.8	29.7	7.8	86.3	5.8	86.35	0.84	4.44		
4	Y	1.4	98.6	0.0	4.6	66.6	28.8	8.0	85.3	5.8	85.92	0.94	4.55		
	X(a)	1.9	98.1	0.0	5.6	79.4	15.0	8.0	89.4	2.6	95.88	1.19			
	(b)				25.7	67.6	6.7	28.8	69.7	1.5					
	Y(a)	1.7	98.3	0.0	6.8	78.6	14.6	9.1	87.8	3.1	94.47	1.03			
	(b)				6.2	76.8	17.0	8.6	87.7	3.7					
N.B.	In 64.1% of events, MWPCs 4X(a) and 4X(b) have matching hits														
	In 87.3% of events, MWPCs 4Y(a) and 4Y(b) have matching hits														
		Overall										47.88	4.14	17.32	7.61

N.B. Conditions (a)→(b) represent an order of decreasing quality of information. Events are put into bins in order of decreasing quality.

MAGNET FAILURES

Failure to Link in D4 Centre		Type of Trigger	No. of Triggers	Reconstruction Efficiency
Scraping at Entrance of D4	= 3.58%	Imbedded Beam	484	77.5
Scraping at Centre of D4	= 1.07%	Trigger	16020	71.9
Scraping at Exit of D4	= 1.46%	Overall	16504	72.1
Overall D4 Related Failures	= 0.34%			
	= 4.82%			

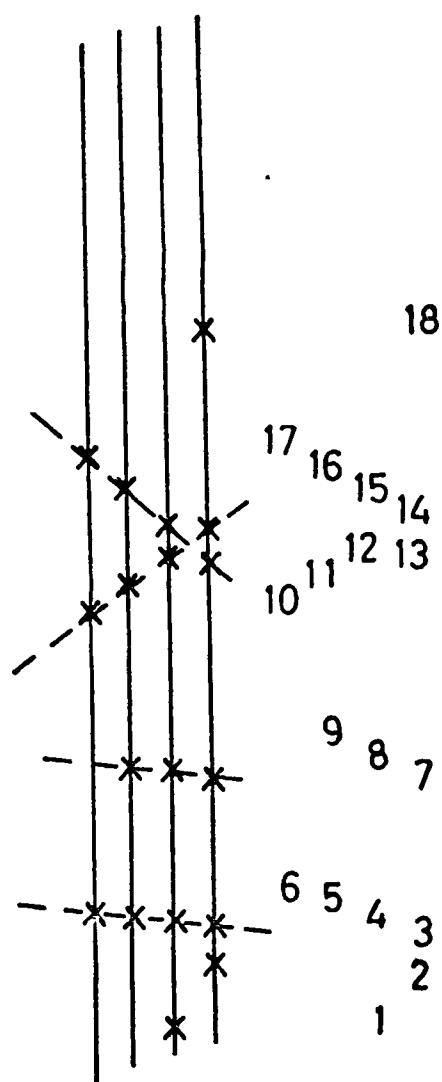


FIG. 4:3
SCHEMATIC EXAMPLE OF
TRACKFINDING IN THE
MUON AND 6 METRE
CHAMBERS.

<u>Pass</u>	<u>Sparks</u>	<u>Result</u> (* indicates most negative spark)
1	6 5 1* 2	Only 2 sparks in road Abandon 1
2	6 5 4 2*	4 sparks, poor chi-square, not allowed to drop 2*. Abandon 2
3	6 5 4 3*	4 sparks, good track. New sparks on each plane
4	10 9 8 7*	10 is outside road, good 3 spark track
5	10* 11 12 13	4 sparks, poor chi-square. Drop 13 find 17, good track New sparks on each plane.
6	17 16 15* 18	18 outside road. Drop 18, good 3 spark track (search for 4th spark only allowed to retrace 1 spark, misses 13).

The compactness of the chambers in which this trackfinder was used and their distance from the centre of the magnet made crossing tracks - as shown on passes 5 and 6 - comparatively rare.

LINKING OF UPSTREAM TRACKS TO DOWNSTREAM TRACKS

147 GeV/c DATA

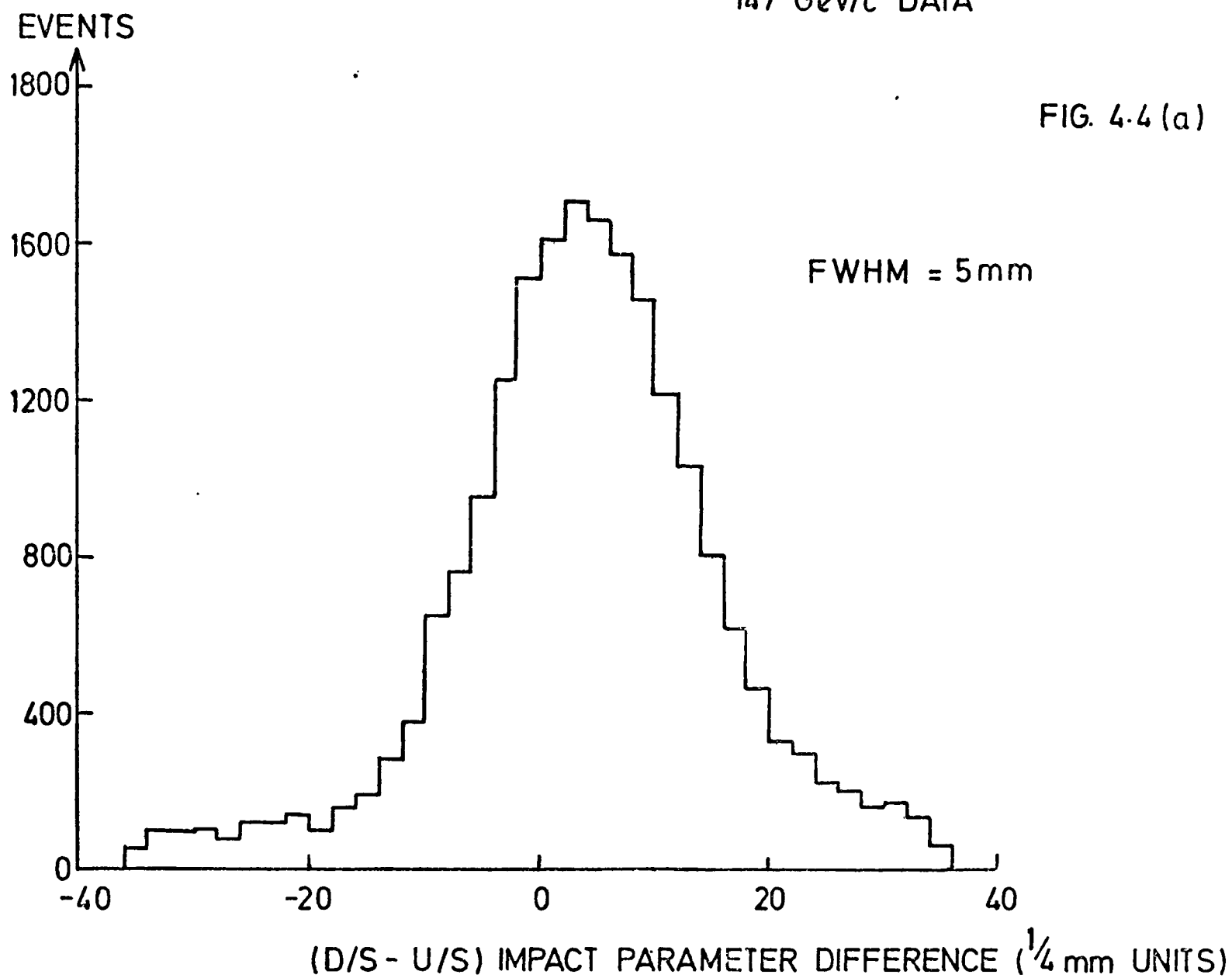


FIG. 4.4 (b)

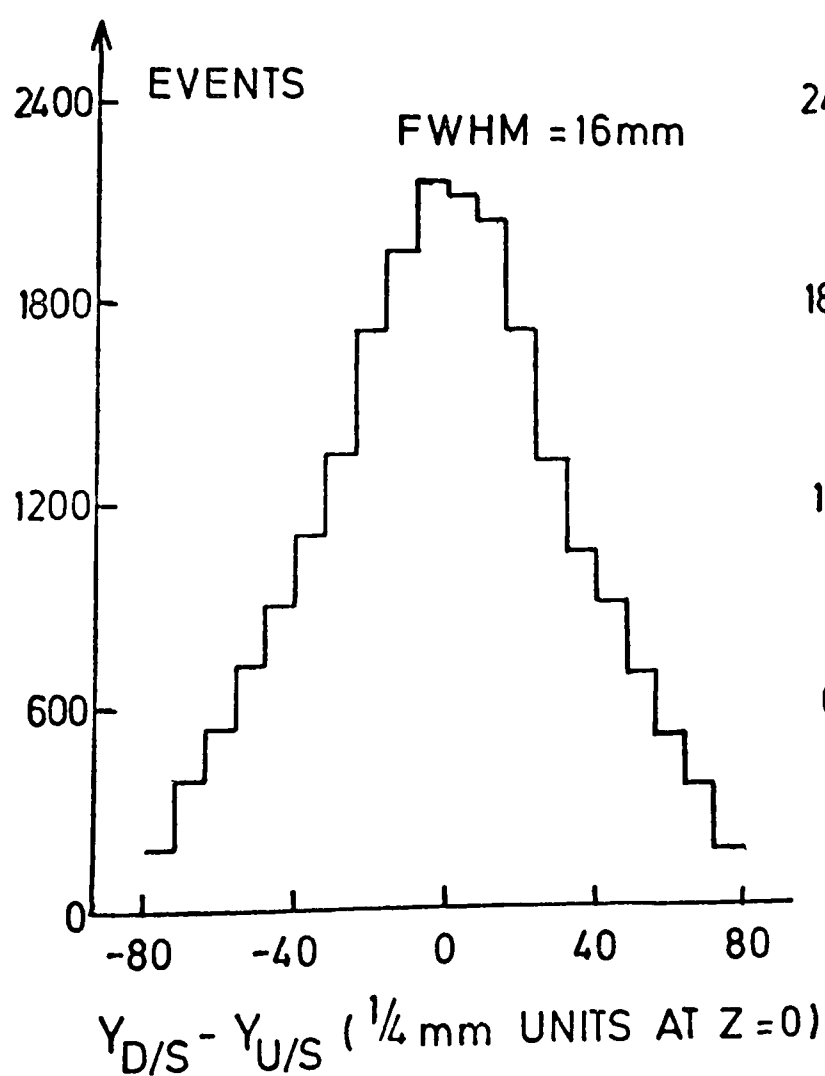


FIG. 4.4 (c)

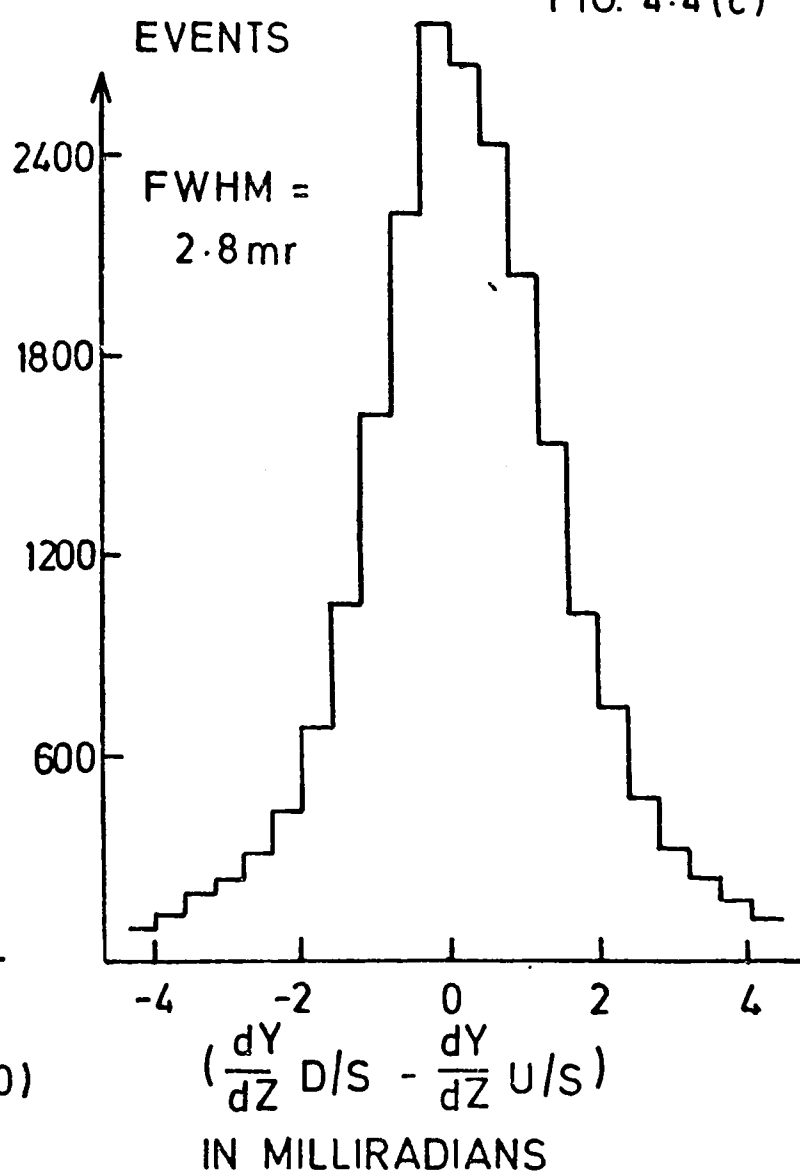


FIG 4.5

MATCHING OF THE X - SLOPES OF D/S TRACKS WITH THOSE OF THE MUON TRACKS

FOR DIFFERENT REGIONS OF X

96 GeV/c DATA

EVENTS

12000

10000

8000

6000

4000

2000

0

A

B

C

D

-10

0

10

-10

0

10

-10

0

10

-10

0

10

$\frac{dX}{dZ}$ OF D/S TRACK - $\frac{dX}{dZ}$ OF MUON TRACK (MILLIRADIANS)

THE DIFFERENCES HAVE BEEN DIVIDED
BY THE FACTOR USED TO COMPENSATE
FOR THE EFFECTS OF MULTIPLE
SCATTERING

- (A) $|X + 30\text{cm}| < 60\text{cm}$
- (B) $60\text{cm} < |X + 30\text{cm}| < 120\text{cm}$
- (C) $120\text{cm} < |X + 30\text{cm}| < 180\text{cm}$
- (D) $180\text{cm} < |X + 30\text{cm}|$

X is calculated for a $Z = 13.5\text{m}$

FIG. 4.6

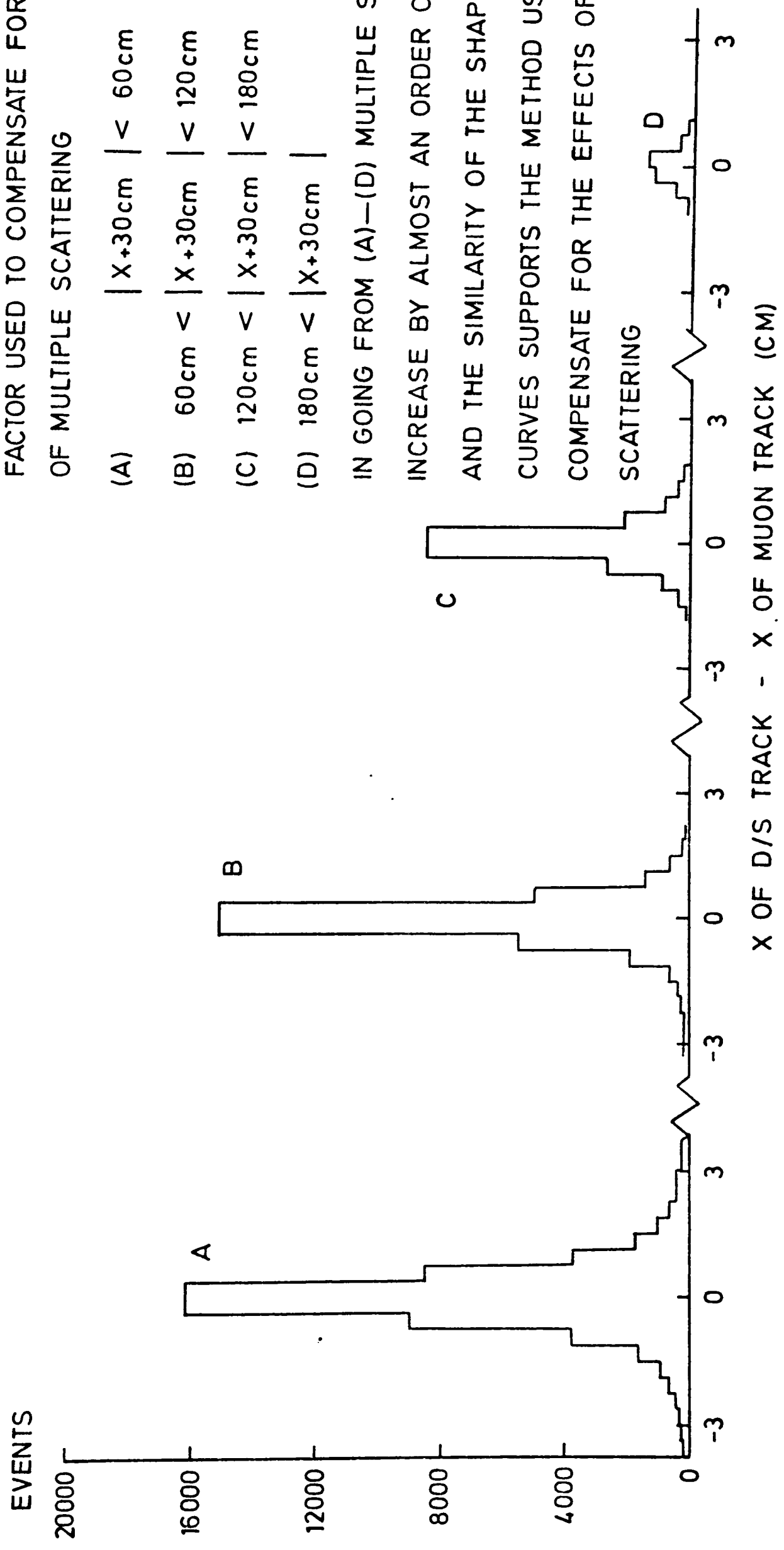
MATCHING OF THE X - INTERCEPTS OF D/S TRACKS WITH THOSE OF THE MUON TRACKS AT $Z = 13.5\text{m}$
FOR DIFFERENT REGION OF X 96 GeV/c DATA

THE DIFFERENCES HAVE BEEN DIVIDED BY THE
FACTOR USED TO COMPENSATE FOR THE EFFECTS
OF MULTIPLE SCATTERING

- (A) $|X + 30\text{cm}| < 60\text{cm}$
- (B) $60\text{cm} < |X + 30\text{cm}| < 120\text{cm}$
- (C) $120\text{cm} < |X + 30\text{cm}| < 180\text{cm}$
- (D) $180\text{cm} < |X + 30\text{cm}|$

IN GOING FROM (A)—(D) MULTIPLE SCATTER EFFECTS
INCREASE BY ALMOST AN ORDER OF MAGNITUDE
AND THE SIMILARITY OF THE SHAPES OF THE
CURVES SUPPORTS THE METHOD USED TO
COMPENSATE FOR THE EFFECTS OF MULTIPLE

SCATTERING



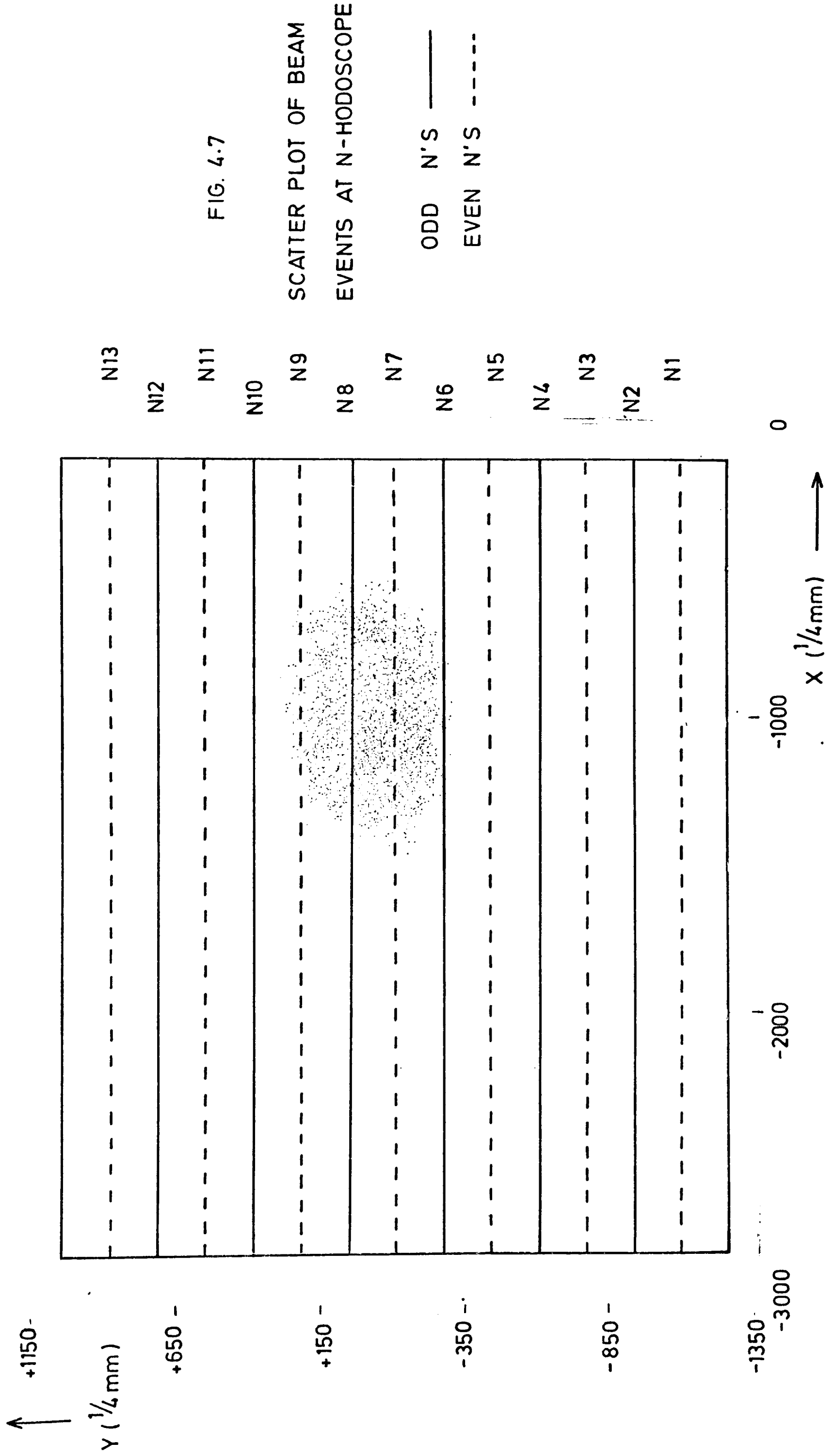


FIG. 4.8 N - COUNTER POSITIONS USING THE IMBEDDED BEAM TRIGGERS

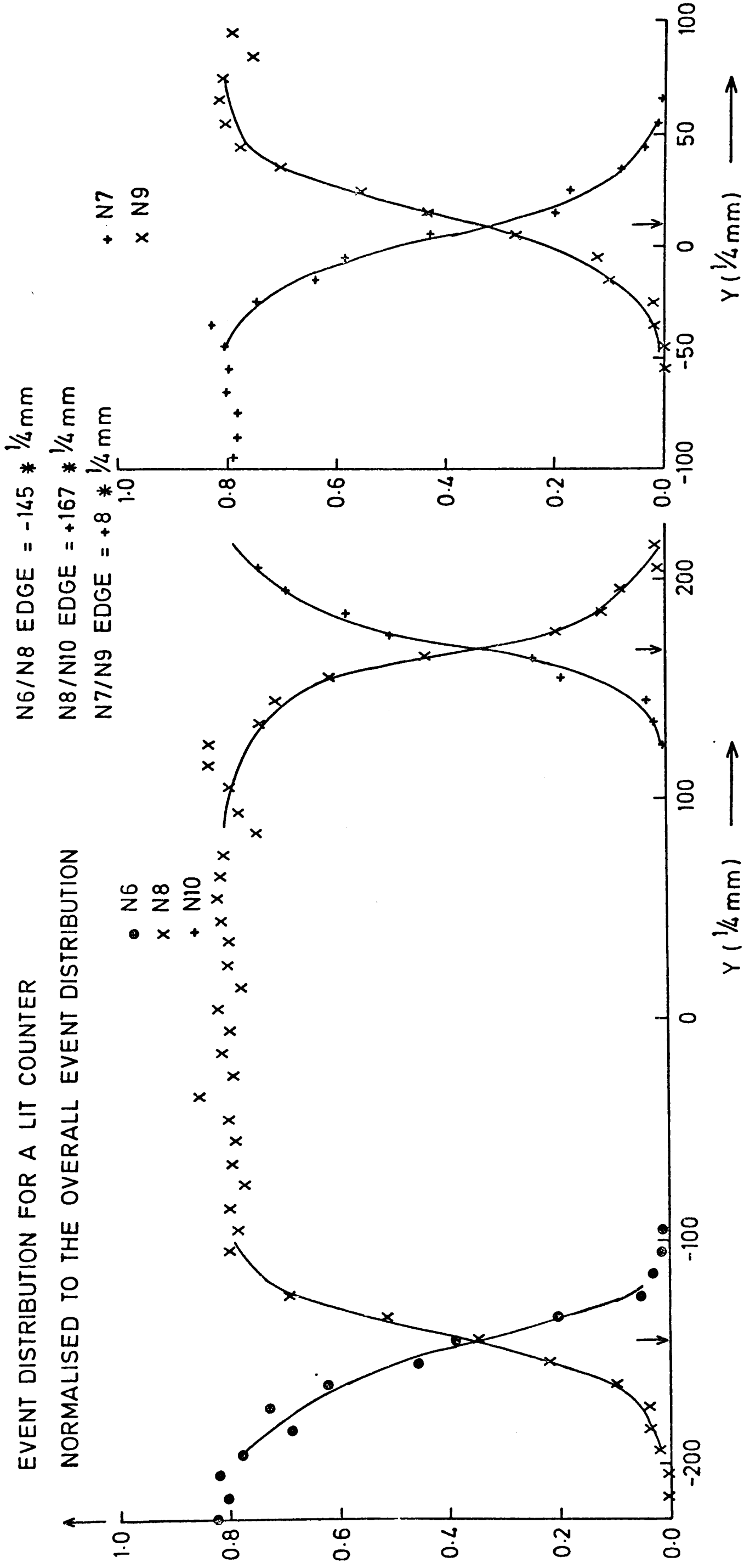


FIG. 4.9 (a) X - POSITIONS OF THE N HODOSCOPE
AND THE M' HOLE.

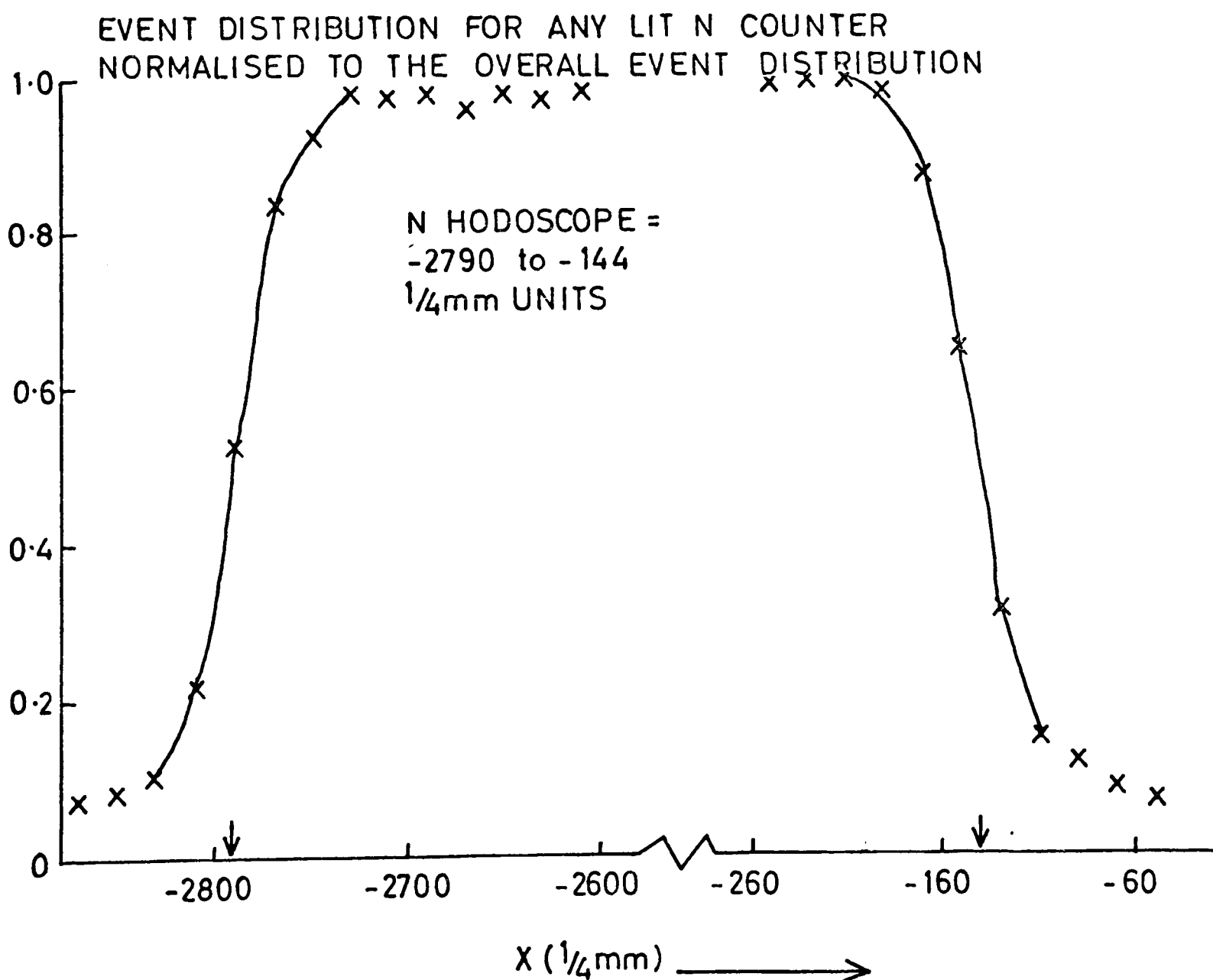
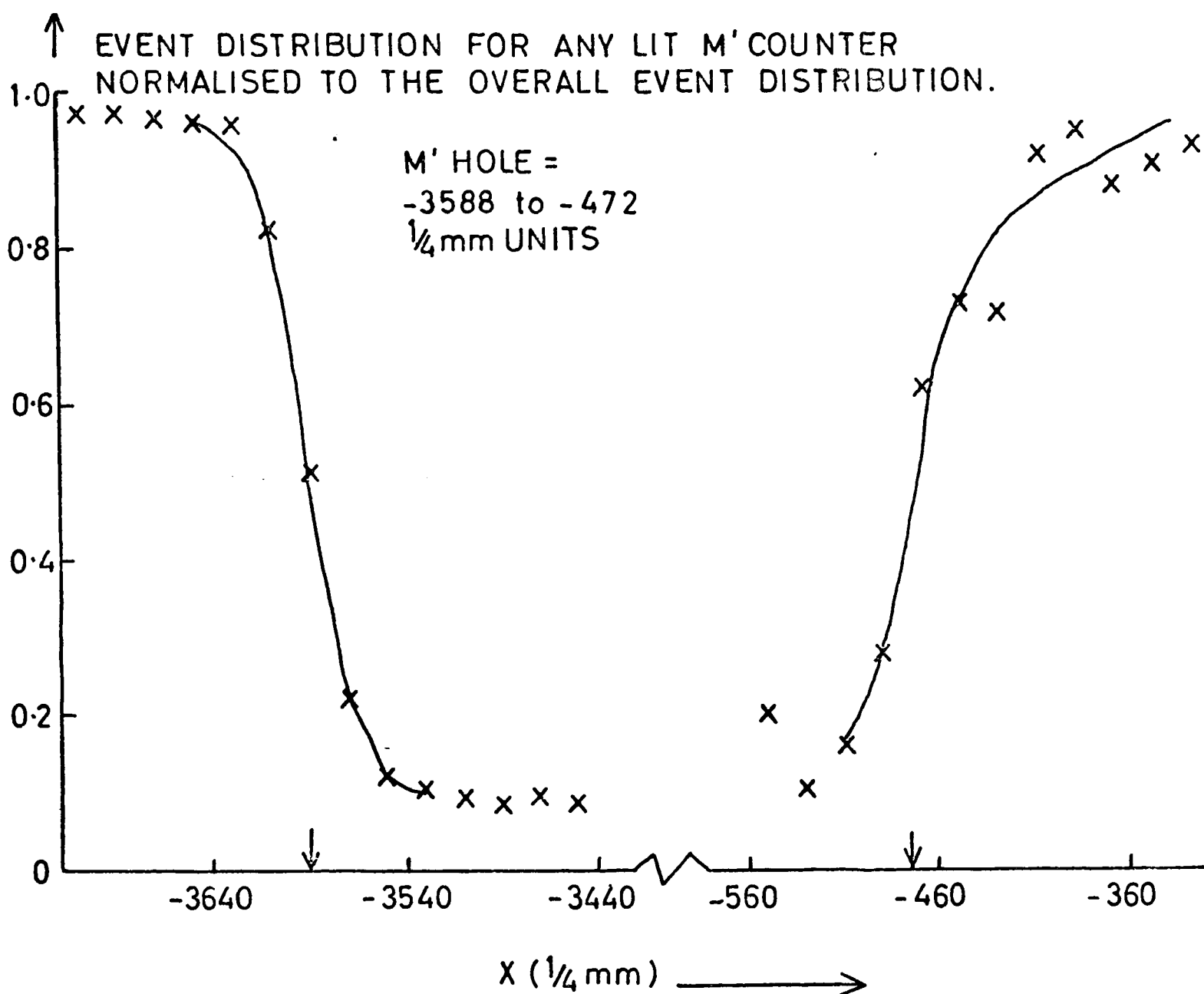


FIG 4.9 (b)

Y - POSITIONS OF M16, M17, M18

EVENT DISTRIBUTION FOR A LIT COUNTER

NORMALISED TO THE OVERALL EVENT DISTRIBUTION

- M16
- x M17
- + M18

M16/M17 EDGE = $+28 \times \frac{1}{4} \text{ mm}$
M17/M18 EDGE = $+352 \times \frac{1}{4} \text{ mm}$

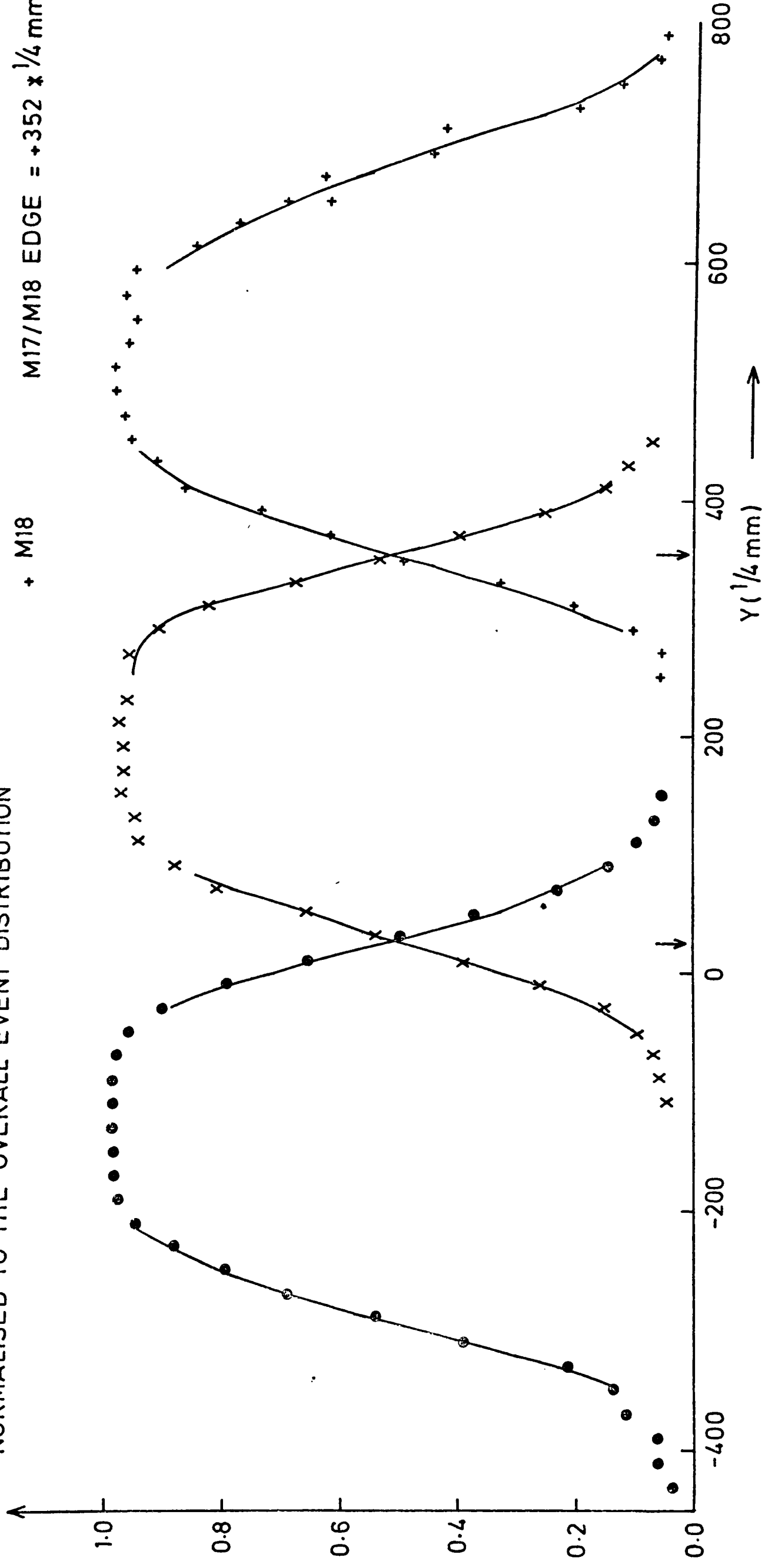
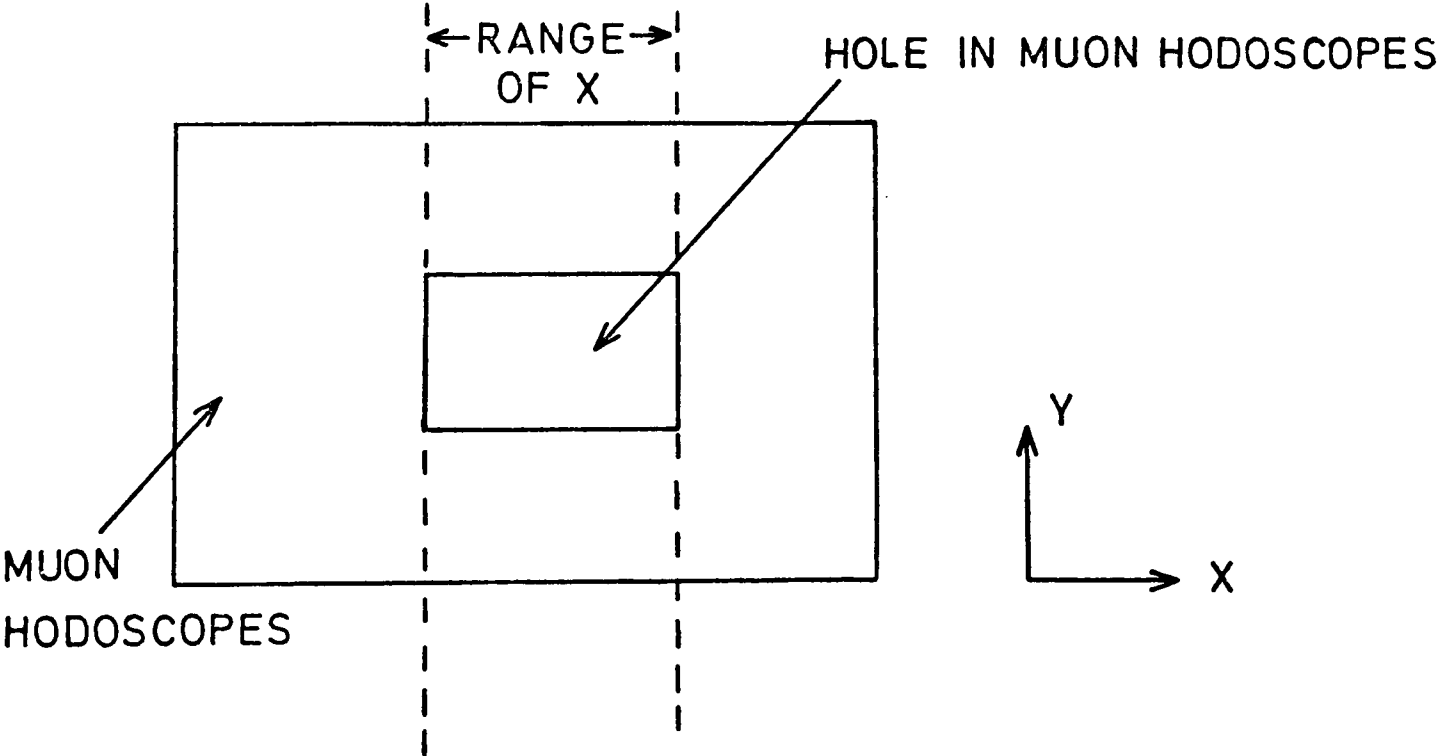
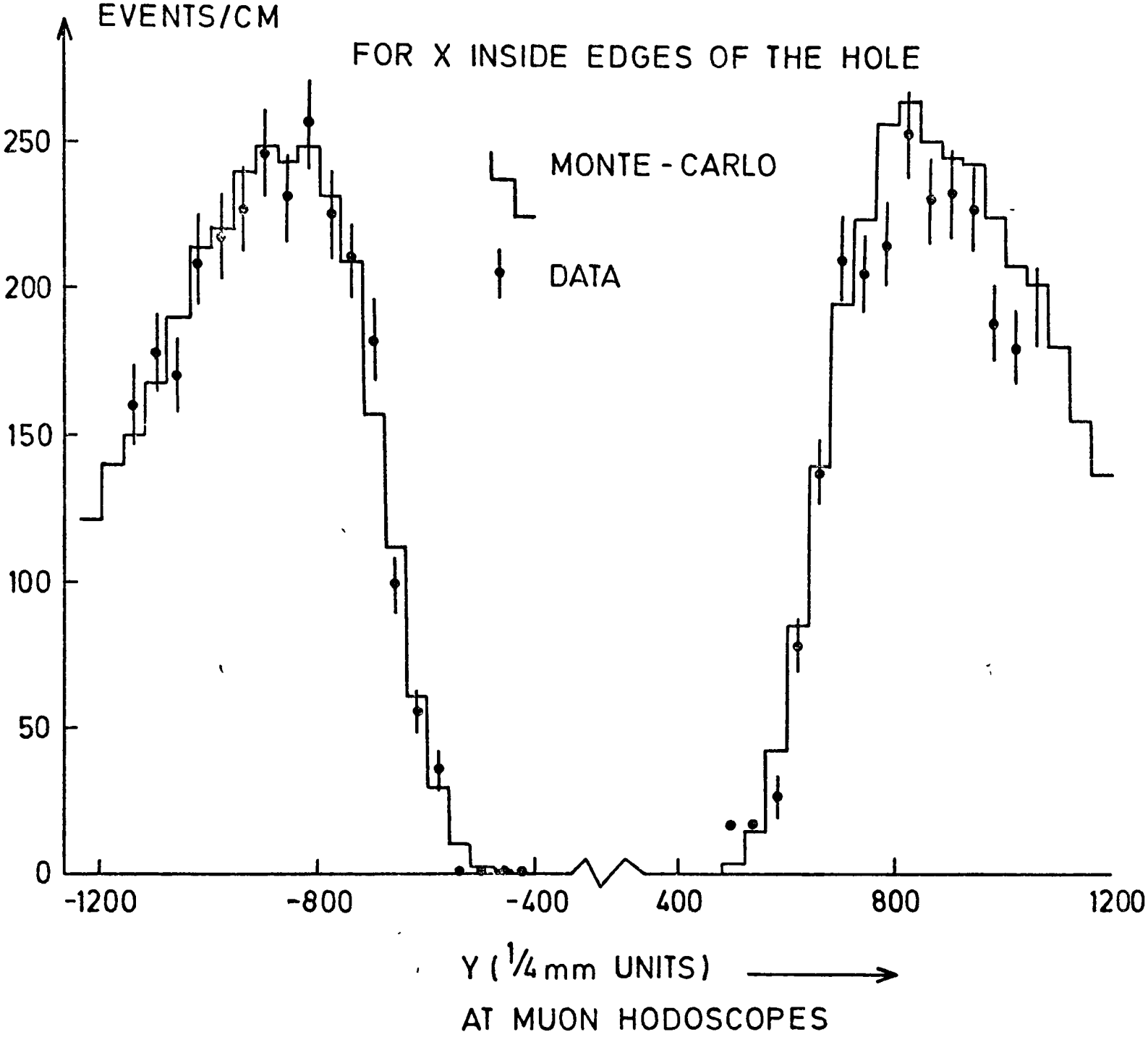


FIG 4.10

COMPARISON OF THE EVENT DATA WITH THE
MONTE - CARLO DATA TO FIND THE LIMITS OF
THE HOLE IN THE MUON HODOSCOPIES



SCHEMATIC ILLUSTRATION OF THE X - CUT FOR
THE ABOVE PLOT

TABLE 4.2
COUNTER EFFICIENCIES

Counter Element	96 GeV/c Data		147 GeV/c Data	
	No. of Tracks Pointing to Element	Efficiencies (%)	No. of Tracks Pointing to Element	Efficiencies (%)
G1	41	97.6 ± 2.4	40	100.0 ± 0.0
G2	27	96.3 ± 3.6	31	100.0 ± 0.0
G3	108	95.4 ± 2.0	108	99.1 ± 0.9
G4	54	100.0 ± 0.0	84	100.0 ± 0.0
G5	126	100.0 ± 0.0	125	100.0 ± 0.0
G6	51	100.0 ± 0.0	65	100.0 ± 0.0
G7	444	99.8 ± 0.2	297	99.3 ± 0.5
G8	143	97.9 ± 1.2	146	98.6 ± 1.0
G9	8614	100.0 ± 0.0	9223	99.9 ± 0.0
G10	7266	100.0 ± 0.0	6948	100.0 ± 0.0
G11	316	100.0 ± 0.0	232	99.6 ± 0.4
G12	114	100.0 ± 0.0	177	99.4 ± 0.6
G13	131	100.0 ± 0.0	123	100.0 ± 0.0
G14	61	100.0 ± 0.0	46	100.0 ± 0.0
G15	120	99.2 ± 0.8	121	100.0 ± 0.0
G16	68	98.5 ± 1.5	78	100.0 ± 0.0
G17	61	98.4 ± 1.6	53	100.0 ± 0.0
G18	46	100.0 ± 0.0	38	100.0 ± 0.0
H1	79	100.0 ± 0.0	185	100.0 ± 0.0
H2	109	100.0 ± 0.0	268	100.0 ± 0.0
H3	201	100.0 ± 0.0	558	100.0 ± 0.0
H4	463	100.0 ± 0.0	752	100.0 ± 0.0
H5	677	100.0 ± 0.0	991	99.1 ± 0.1
H6	1152	100.0 ± 0.0	1381	100.0 ± 0.0
H7	1668	99.9 ± 0.1	2104	100.0 ± 0.0
H8	3073	99.9 ± 0.1	3548	100.0 ± 0.0
H9	6387	99.6 ± 0.1	7084	100.0 ± 0.0
H10	3771	99.5 ± 0.1	4094	99.7 ± 0.1
H11	835	100.0 ± 0.0	495	99.8 ± 0.2
H12	760	100.0 ± 0.0	371	100.0 ± 0.0
H13	2795	98.9 ± 0.2	2333	100.0 ± 0.0
H14	3947	97.4 ± 0.3	2195	99.7 ± 0.1
H15	708	100.0 ± 0.0	649	99.8 ± 0.2
H16	364	100.0 ± 0.0	420	100.0 ± 0.0
H17	288	100.0 ± 0.0	356	100.0 ± 0.0
H18	205	99.5 ± 0.5	319	100.0 ± 0.0
H19	188	100.0 ± 0.0	251	100.0 ± 0.0
H20	126	99.2 ± 0.8	228	100.0 ± 0.0
H21	107	100.0 ± 0.0	197	100.0 ± 0.0
H22	82	100.0 ± 0.0	191	100.0 ± 0.0
H23	55	100.0 ± 0.0	171	100.0 ± 0.0
H24	55	98.2 ± 1.8	154	100.0 ± 0.0

TABLE 4.2 (continued)

Counter Element	96 GeV/c Data		147 GeV/c Data	
	No. of Tracks Pointing to Element	Efficiencies (%)	No. of Tracks Pointing to Element	Efficiencies (%)
M1	23	100.0 \pm 0.0	20	100.0 \pm 0.0
M2	7	100.0 \pm 0.0	3	100.0 \pm 0.0
M3	92	100.0 \pm 0.0	89	98.9 \pm 1.1
M4	45	100.0 \pm 0.0	20	100.0 \pm 0.0
M5	305	100.0 \pm 0.0	178	100.0 \pm 0.0
M6	159	99.7 \pm 0.3	92	98.9 \pm 1.1
M7	424	100.0 \pm 0.0	334	100.0 \pm 0.0
M8	333	99.7 \pm 0.3	157	100.0 \pm 0.0
M9	148	95.6 \pm 1.6	105	93.3 \pm 2.4
M10	85	98.8 \pm 1.2	38	100.0 \pm 0.0
M11	34	97.1 \pm 2.9	31	100.0 \pm 0.0
M12	22	100.0 \pm 0.0	9	100.0 \pm 0.0
M13	68	98.5 \pm 1.5	63	100.0 \pm 0.0
M14	226	98.7 \pm 0.8	177	97.2 \pm 1.2
M15	1084	99.9 \pm 0.1	1285	99.9 \pm 0.1
M16	2139	100.0 \pm 0.0	3154	99.9 \pm 0.1
M17	1831	99.9 \pm 0.1	2585	100.0 \pm 0.0
M18	696	99.7 \pm 0.2	619	100.0 \pm 0.0
M19	134	99.3 \pm 0.7	143	97.9 \pm 1.2
M20	102	100.0 \pm 0.0	91	100.0 \pm 0.0
M21	983	100.0 \pm 0.0	519	100.0 \pm 0.0
M22	212	100.0 \pm 0.0	122	100.0 \pm 0.0
N1	274	98.5 \pm 0.7	163	99.4 \pm 0.6
N2	482	99.8 \pm 0.2	268	100.0 \pm 0.0
N3	265	98.5 \pm 0.7	197	100.0 \pm 0.0
N13	182	94.5 \pm 1.7	74	100.0 \pm 0.0
M'1	16		39	94.9 \pm 3.5
M'2	50		54	96.3 \pm 2.6
M'3	89	100.0 \pm 0.0	55	90.9 \pm 3.5
M'4	110	100.0 \pm 0.0	103	99.0 \pm 1.0
M'5	180	99.4 \pm 0.6	139	97.1 \pm 1.4
M'6	429	99.1 \pm 0.5	287	97.2 \pm 1.0
M'7	1012	99.4 \pm 0.2	554	97.3 \pm 0.7
M'8	155	99.4 \pm 0.2	91	95.6 \pm 2.1
M'9	14	100.0 \pm 0.0	11	90.9 \pm 8.7
M'10	1	100.0 \pm 0.0	1	0.0 \pm 0.0
M'11	74	100.0 \pm 0.0	359	95.0 \pm 1.2
M'12	339	99.7 \pm 0.3	611	96.6 \pm 0.7
M'13	792	100.0 \pm 0.0	1201	97.8 \pm 0.4
M'14	1895	99.9 \pm 0.1	2535	97.2 \pm 0.3
M'15	5236	99.8 \pm 0.1	6484	97.1 \pm 0.2
M'16	313	99.4 \pm 0.5	239	98.3 \pm 0.8
M'17	793	99.9 \pm 0.1	443	98.0 \pm 0.7
M'18	1874	99.3 \pm 0.2	1013	97.0 \pm 0.5
M'19	43	88.4 \pm 4.9	22	72.7 \pm 9.5
M'20	9	100.0 \pm 0.0	4	100.0 \pm 0.0

FIG 4.11

EVENT VERTEX DISTRIBUTION IN Z

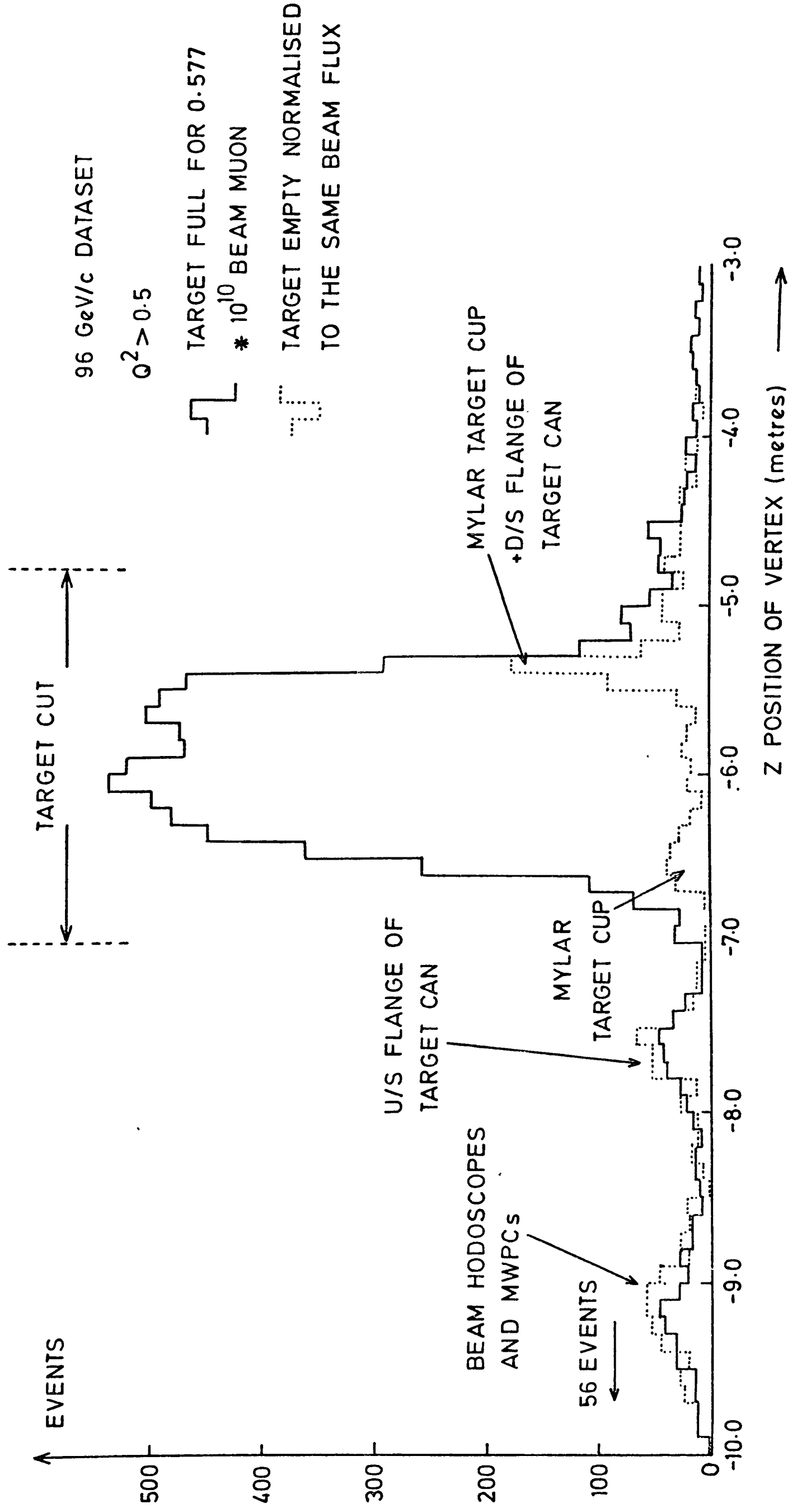


FIG 4.12 (a)

NOT TO SCALE

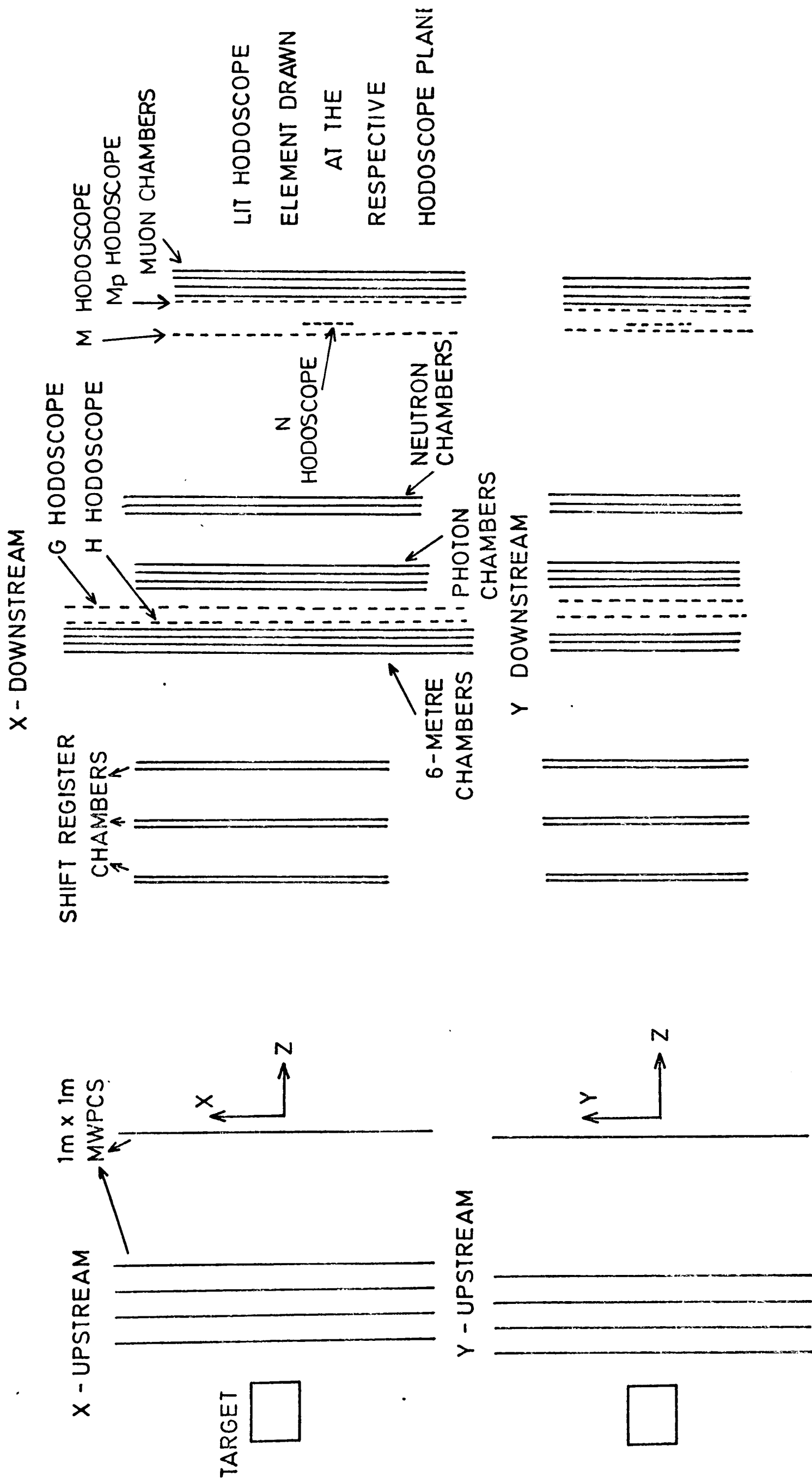
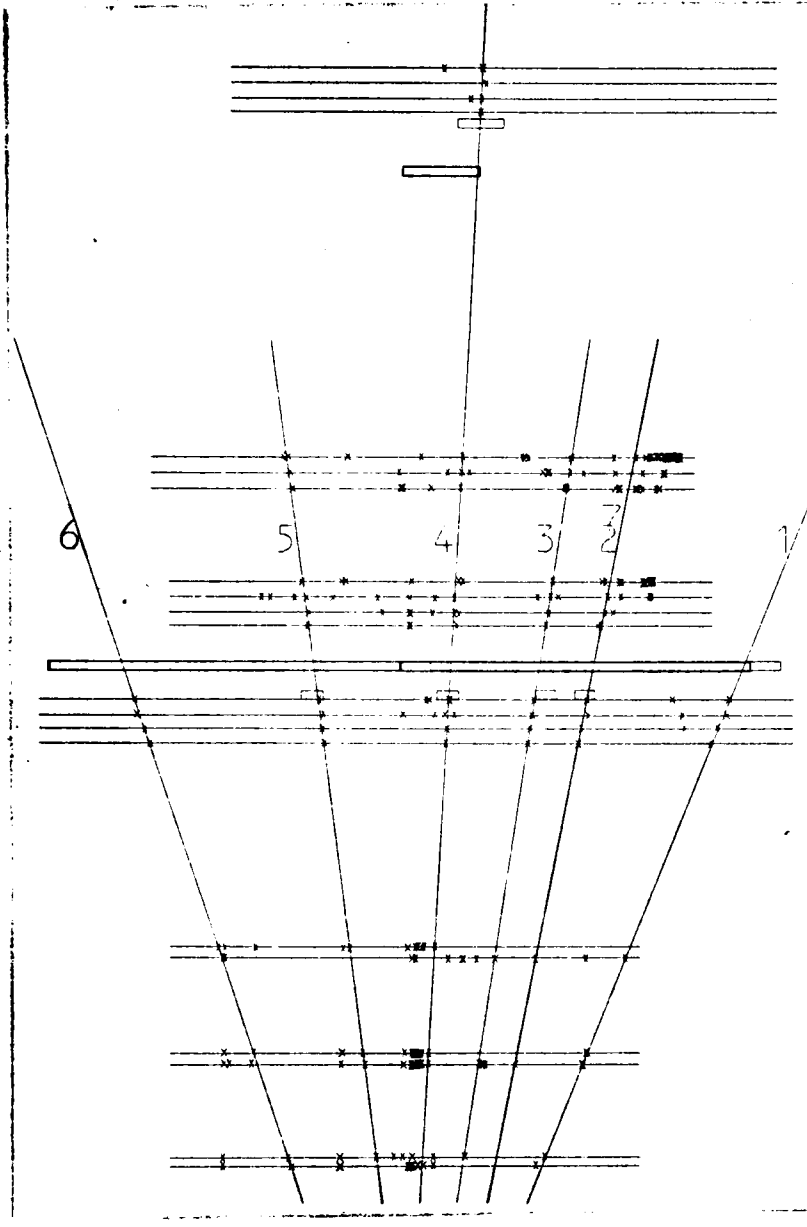


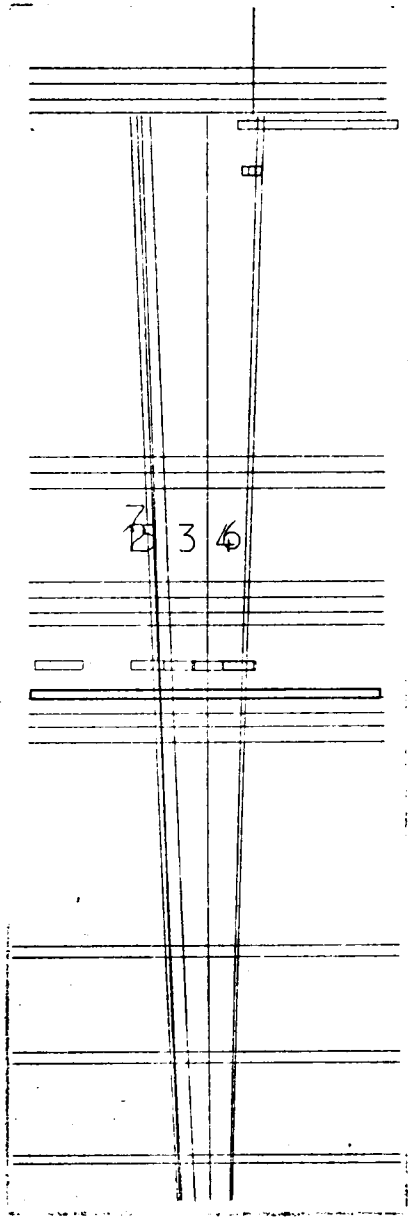
FIG. 4.12 (b)

INELASTIC MUON SCATTER

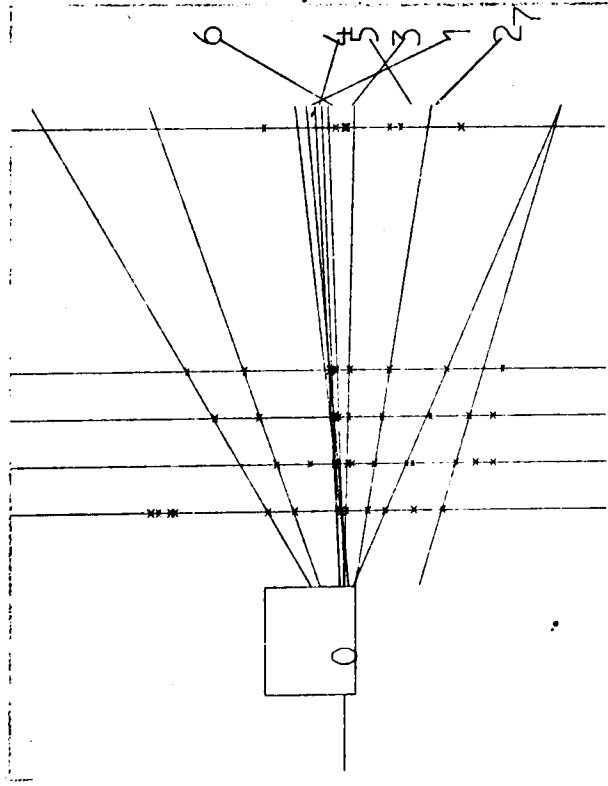
X - DOWNSTREAM



Y - DOWNSTREAM



X - UPSTREAM



Y - UPSTREAM

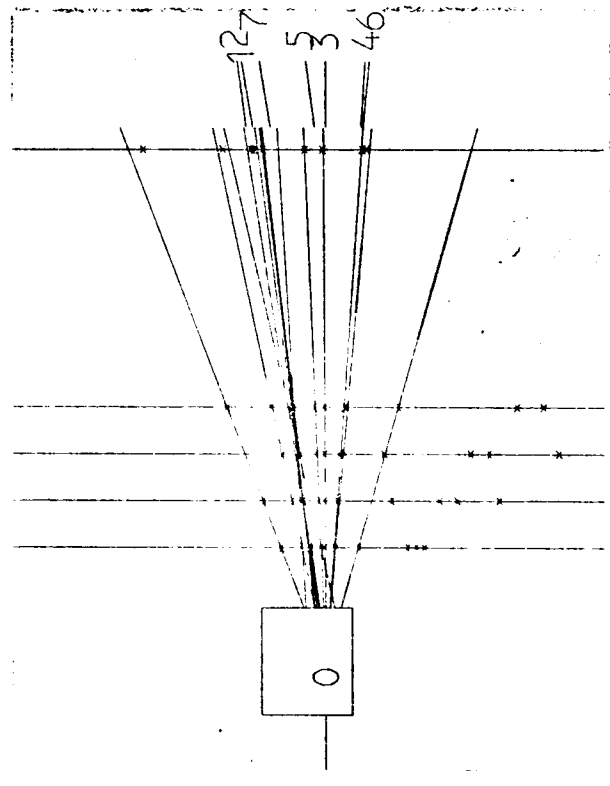
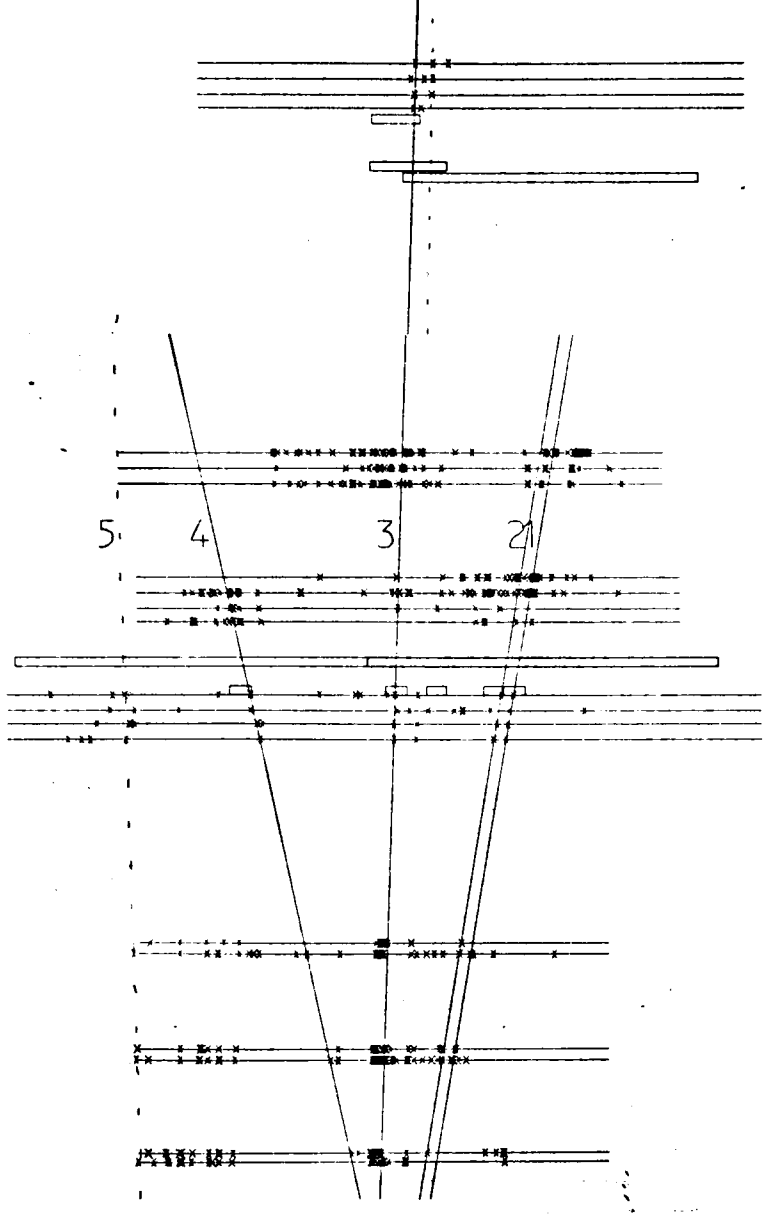
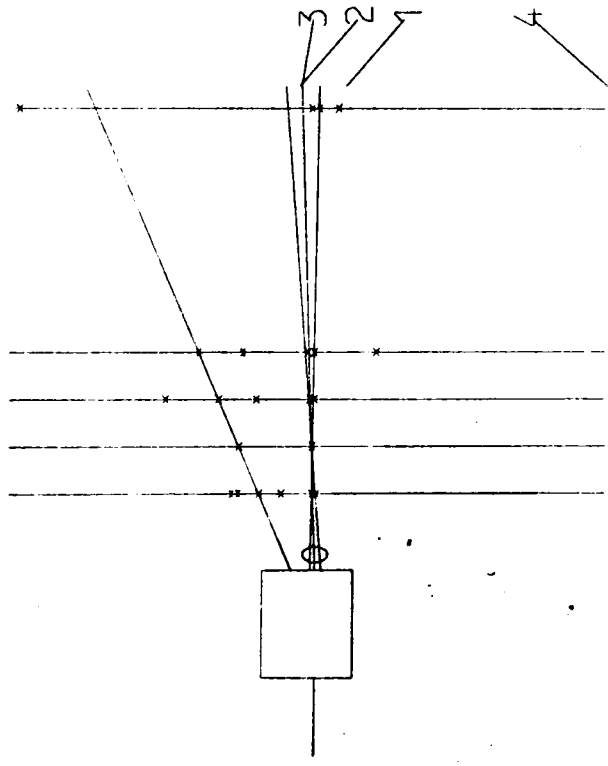


FIG. 4.12 (c)

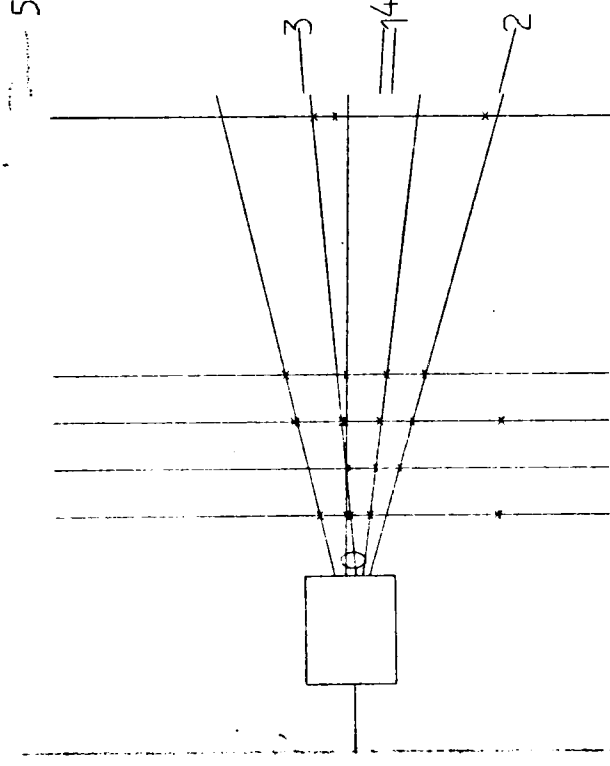
INELASTIC MUON SCATTER

X - DOWNSTREAM

X - UPSTREAM



Y - UPSTREAM



Y - DOWNSTREAM

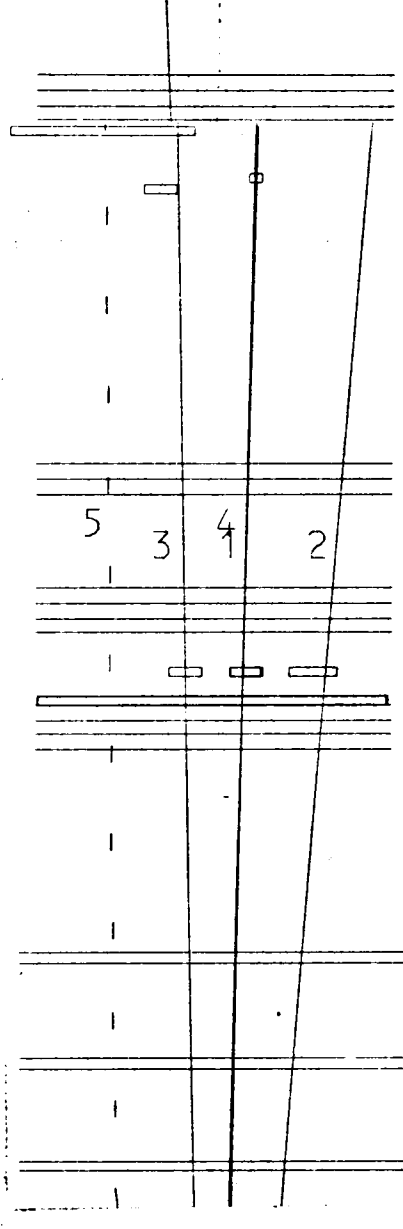
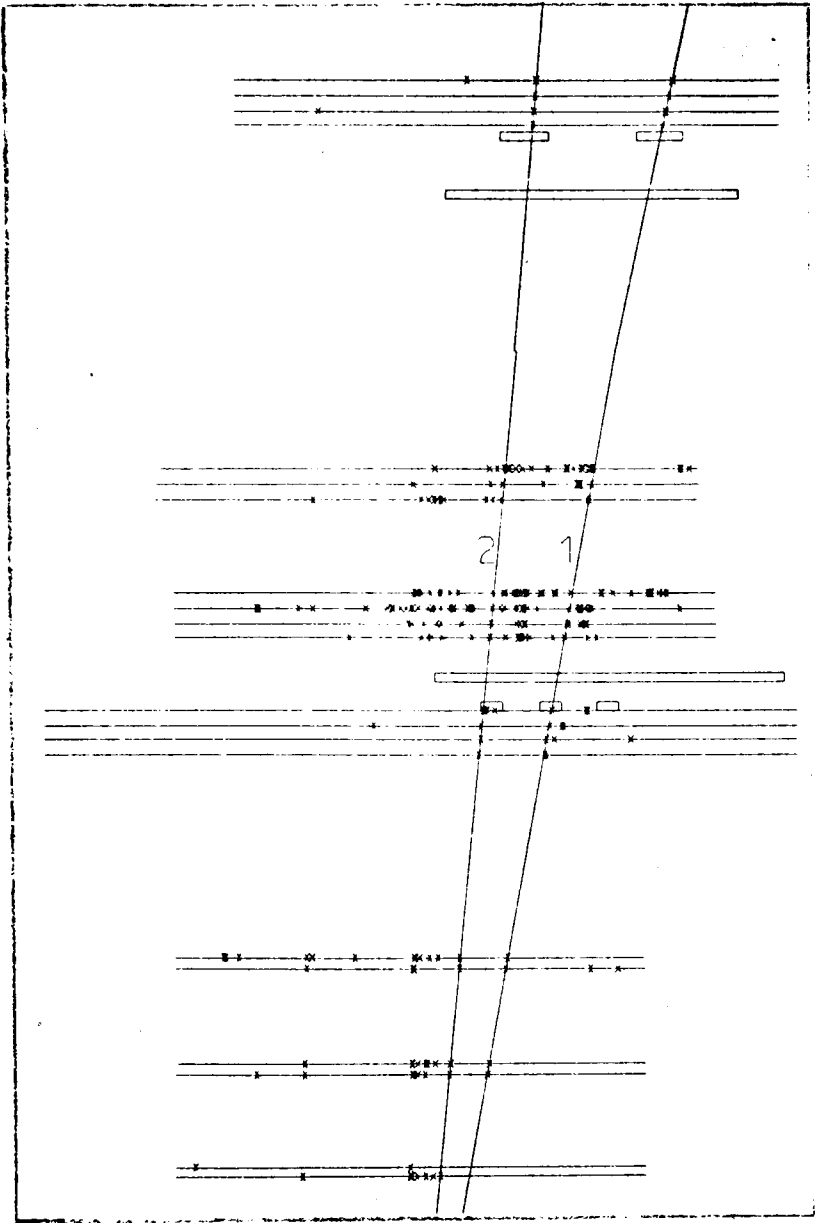


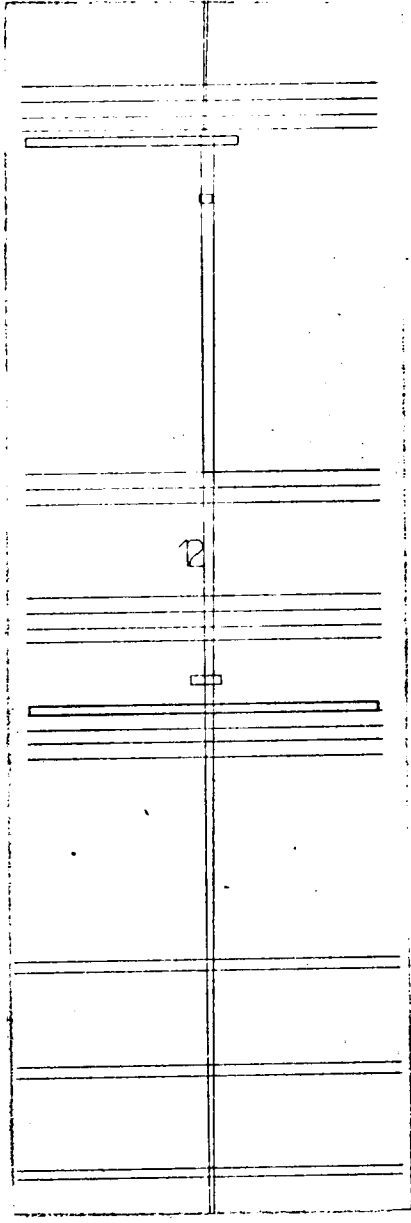
FIG. 4.12 (d)

INELASTIC MUON SCATTER

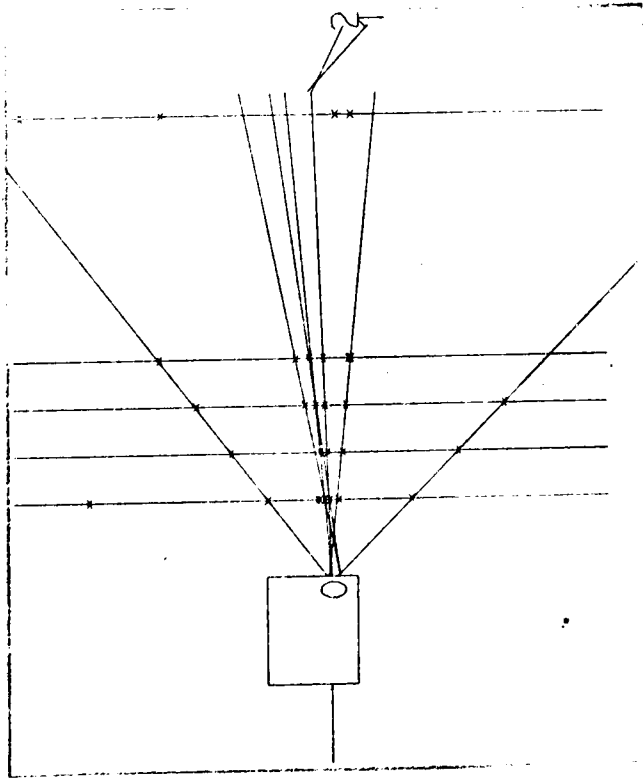
X - DOWNSTREAM



Y - DOWNSTREAM



X - UPSTREAM



Y - UPSTREAM

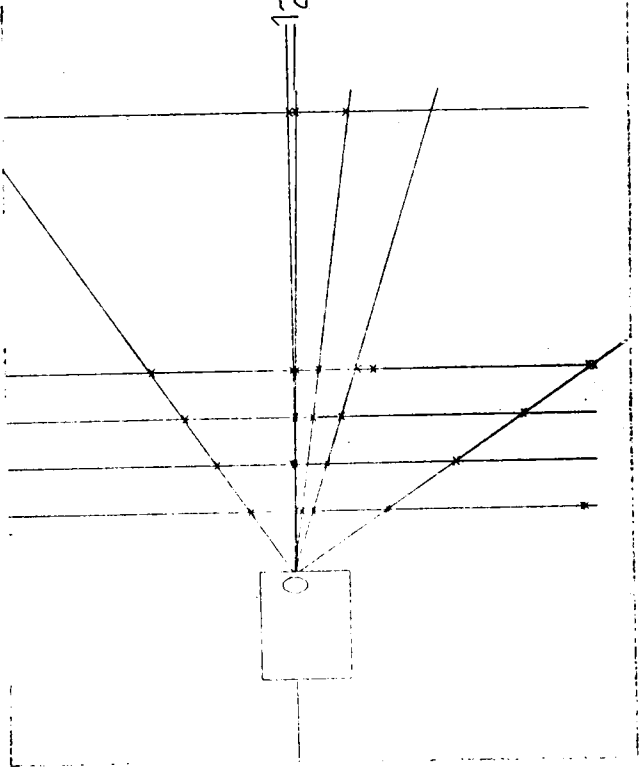
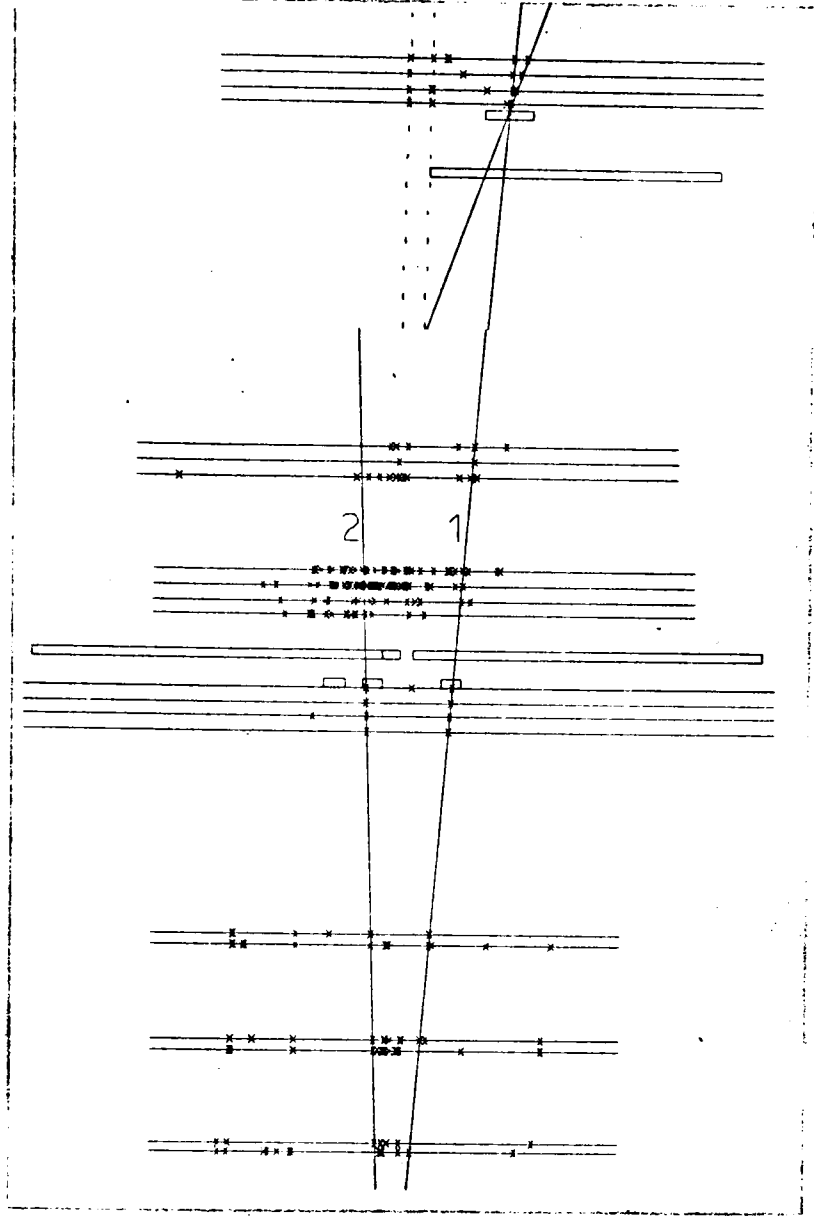


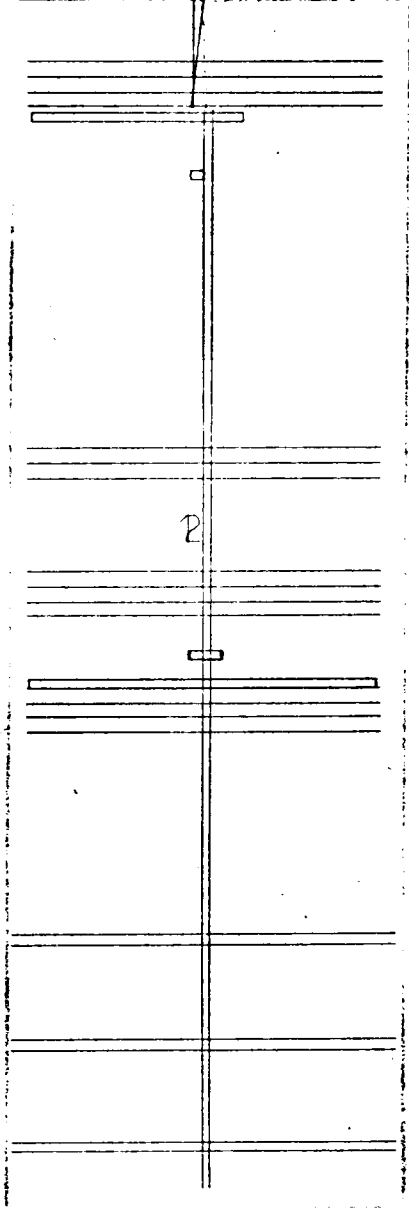
FIG. 4-12 (e)

MUON - ELECTRON SCATTER

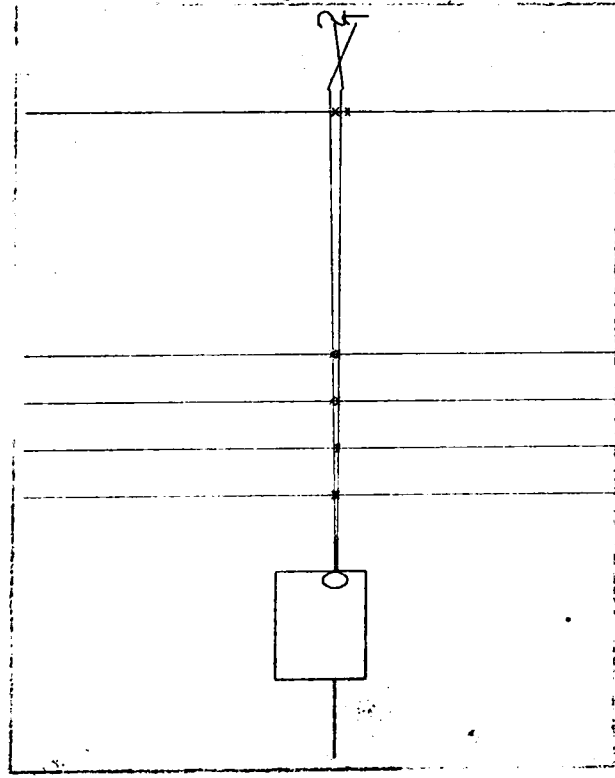
X - DOWNSTREAM



Y - DOWNSTREAM



X - UPSTREAM



Y - UPSTREAM

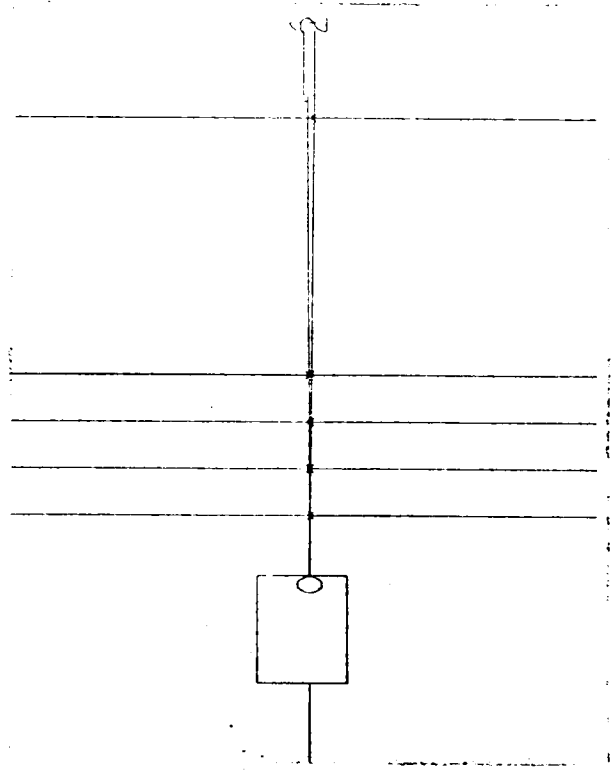
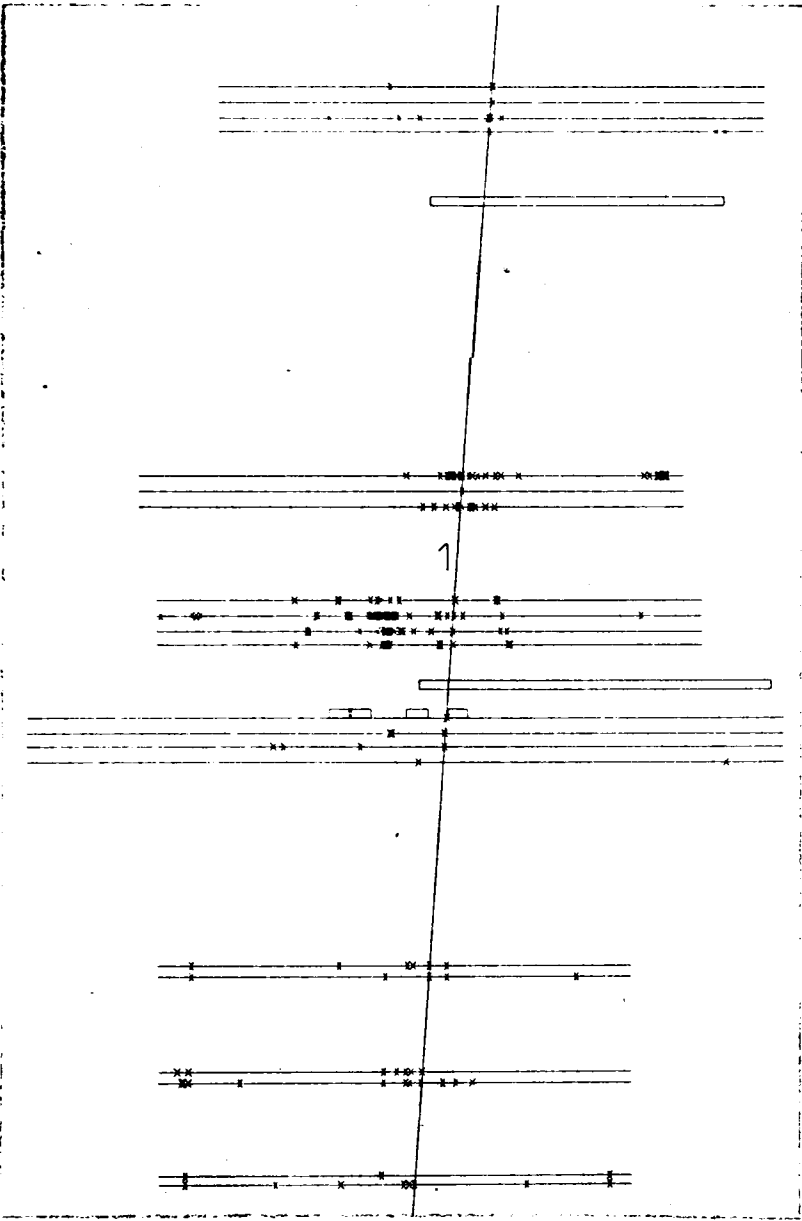


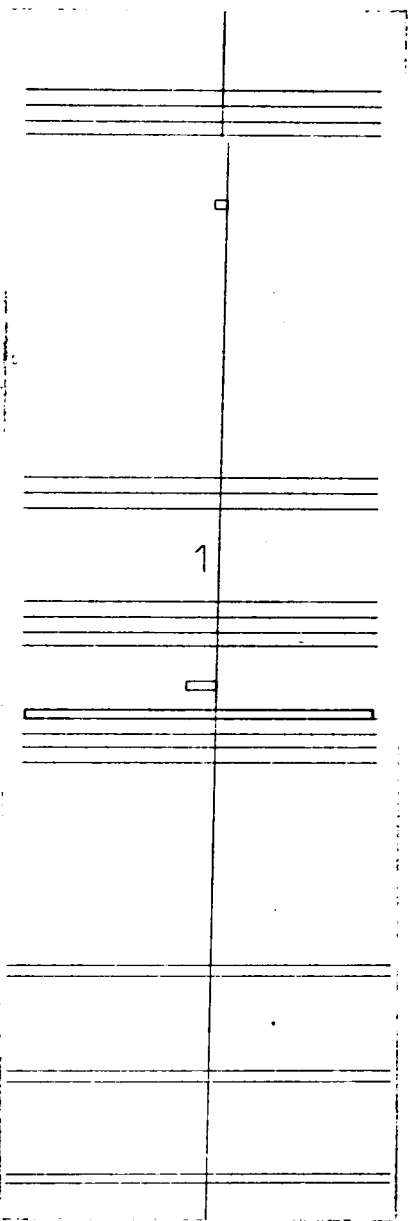
FIG. 4.12(f)

MUON BREMSSTRAHLUNG

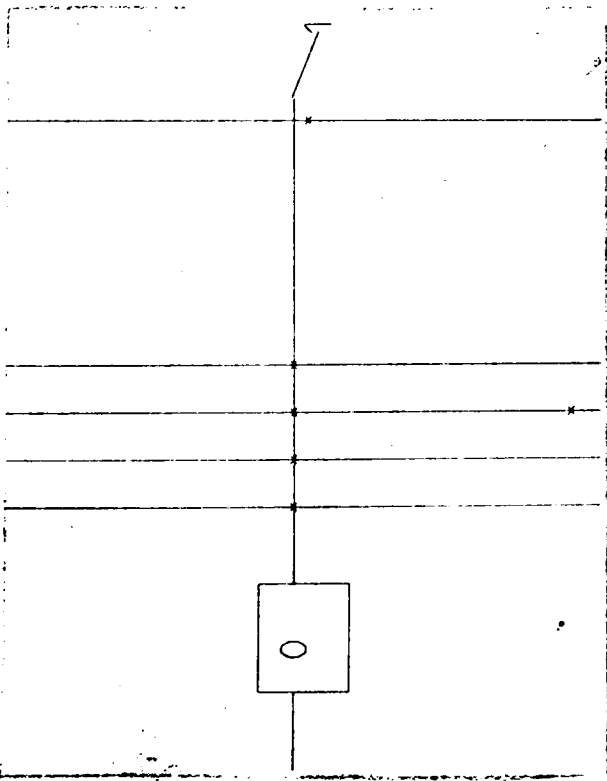
X - DOWNSTREAM



Y - DOWNSTREAM



X - UPSTREAM



Y - UPSTREAM

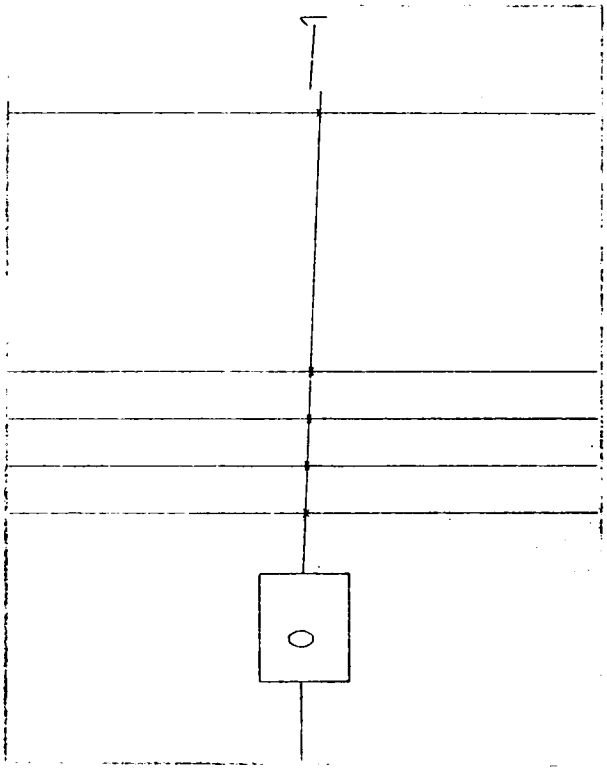
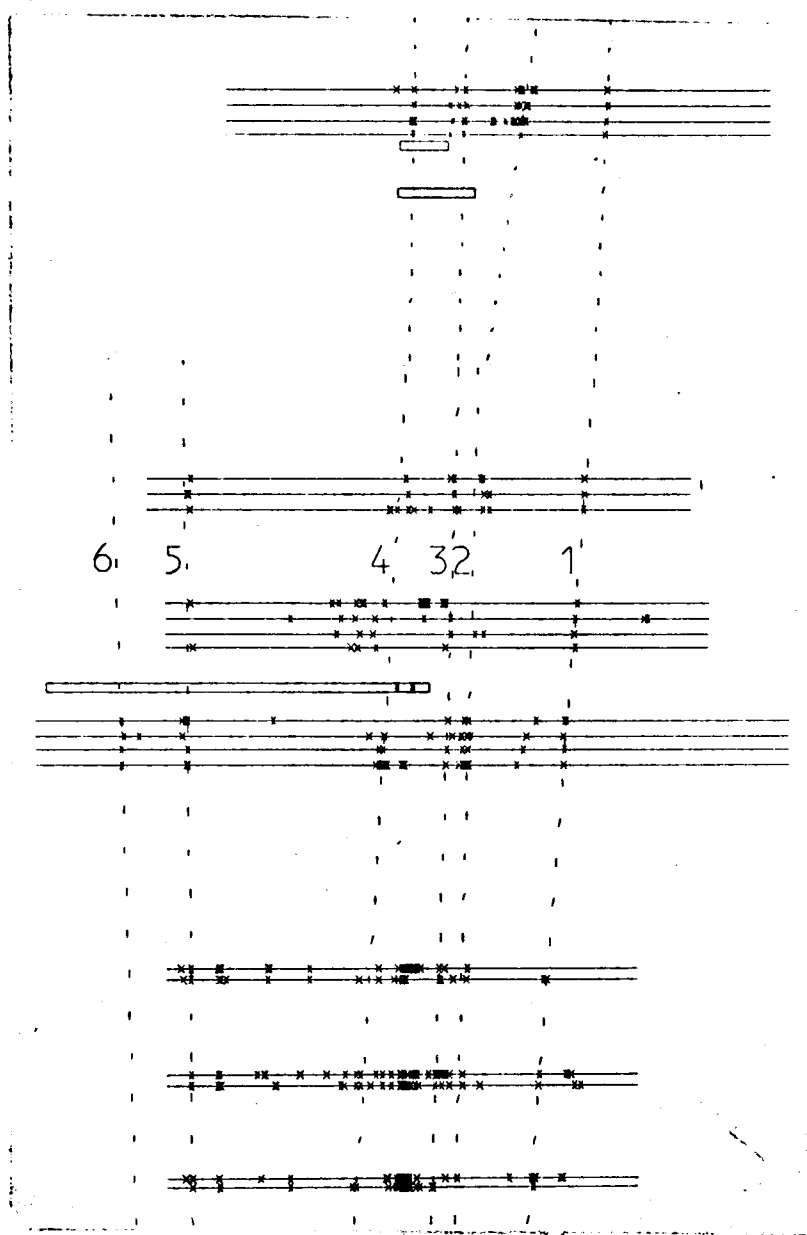


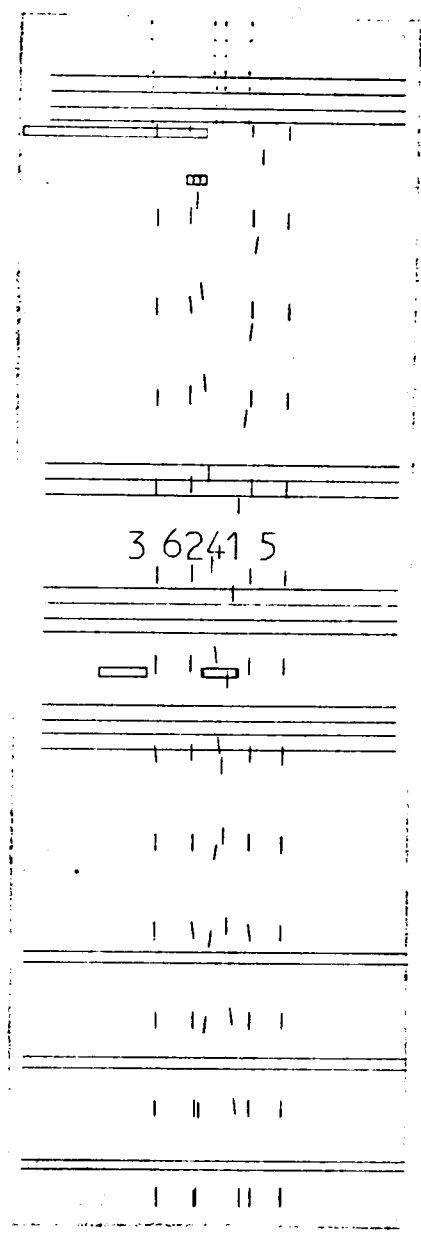
FIG. 4.12 (g)

SPURIOUS TRIGGER

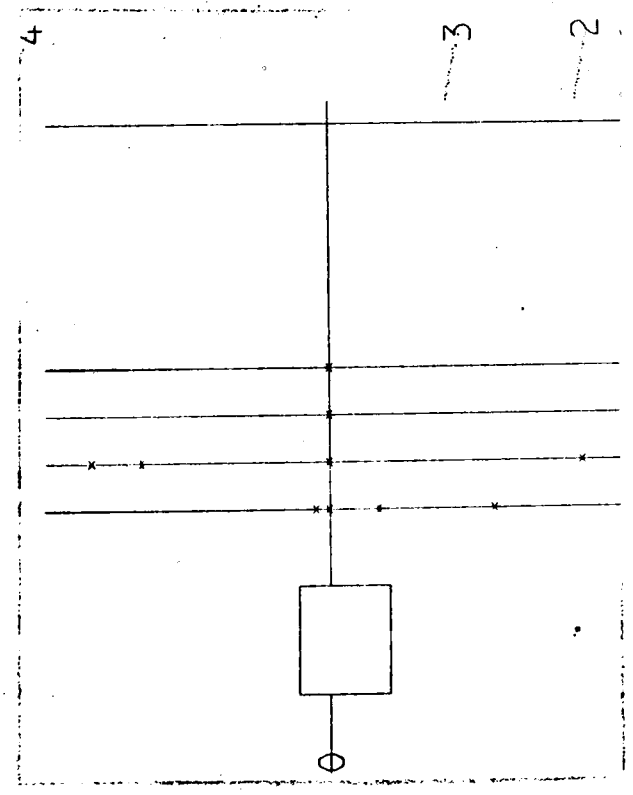
X - DOWNSTREAM



Y - DOWNSTREAM



X - UPSTREAM



Y - UPSTREAM

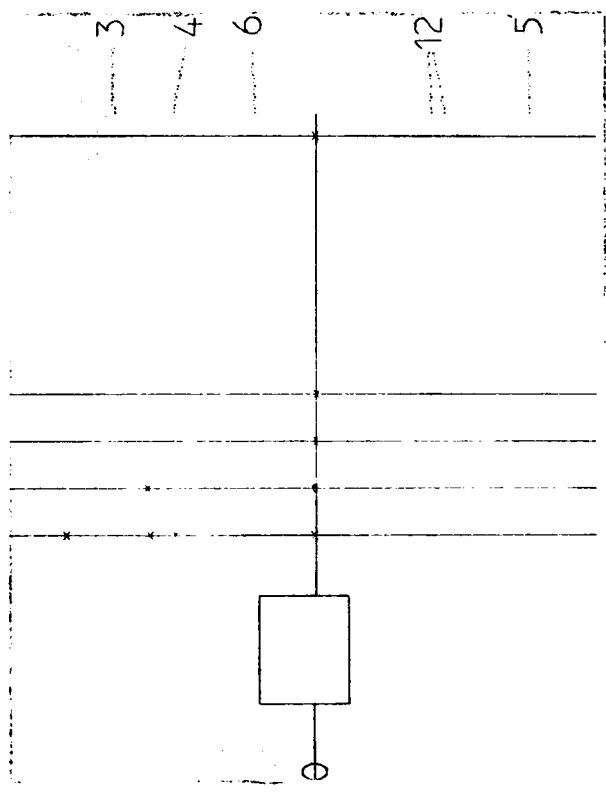


FIG. 4-13 (b)

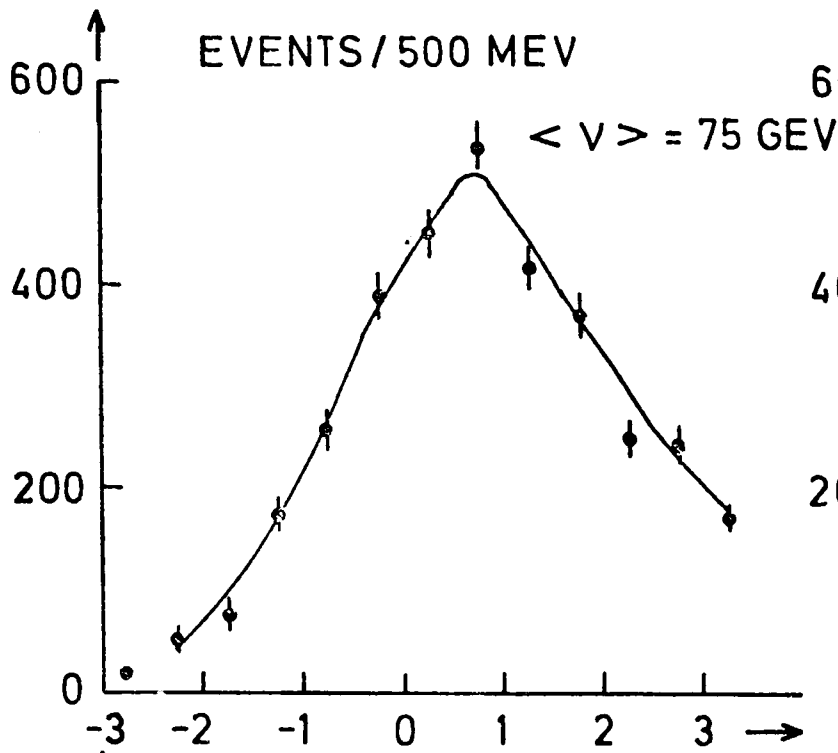
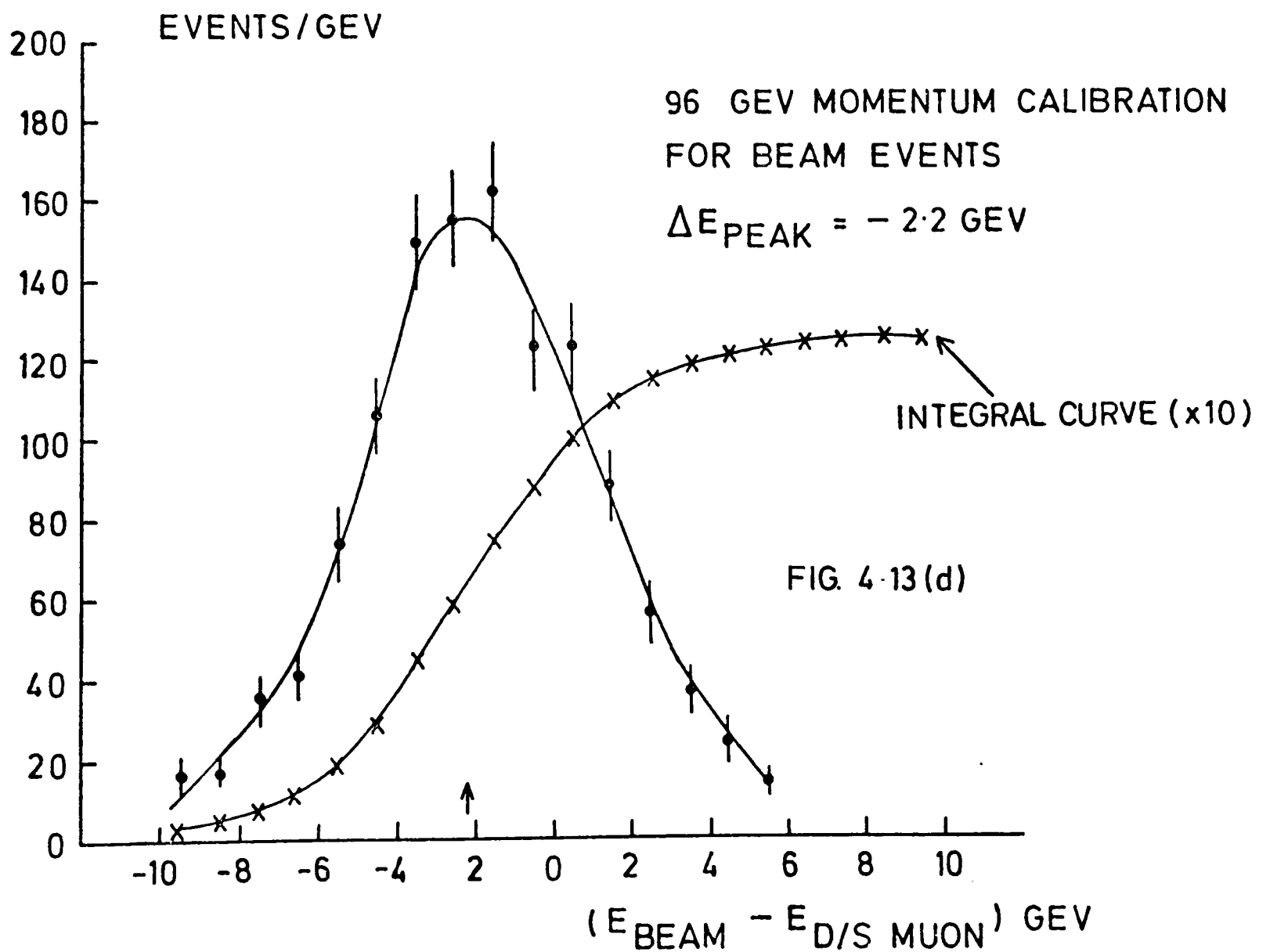
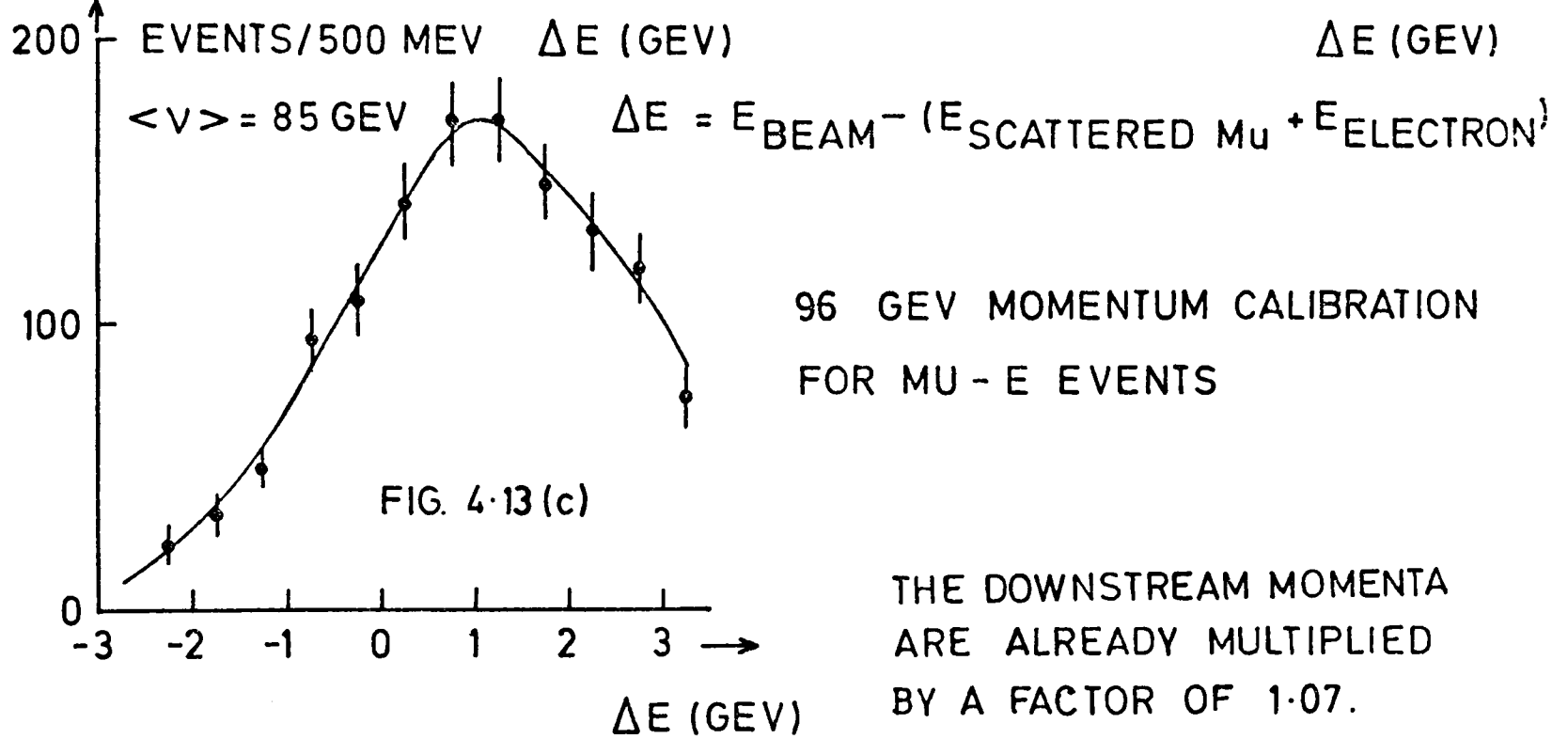
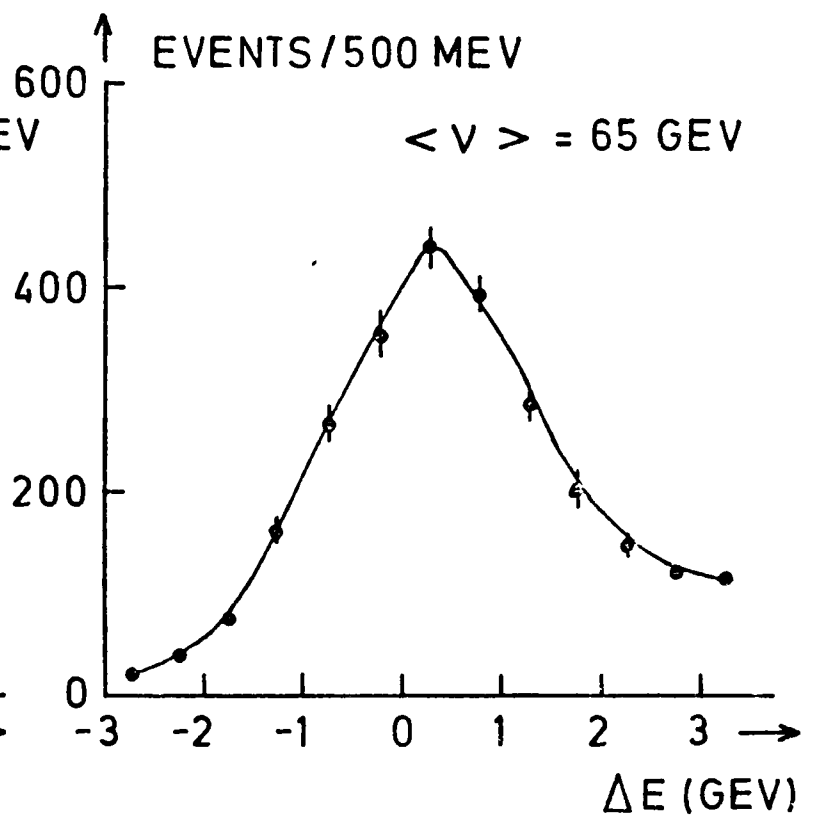


FIG. 4-13(a)



ABSOLUTE MOMENTUM CALIBRATION 96 GEV DATA

χ^2 (for 4800 events)

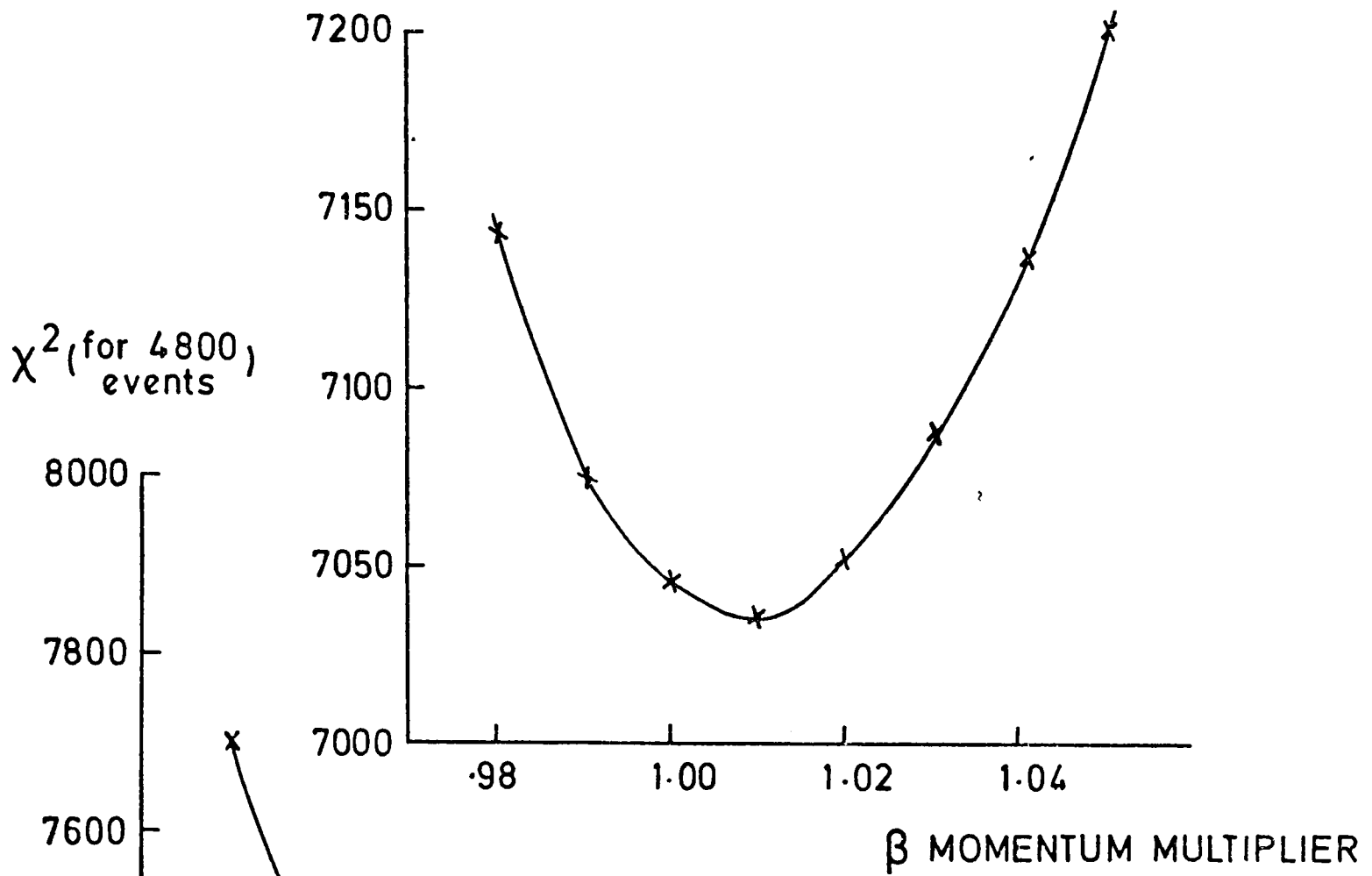
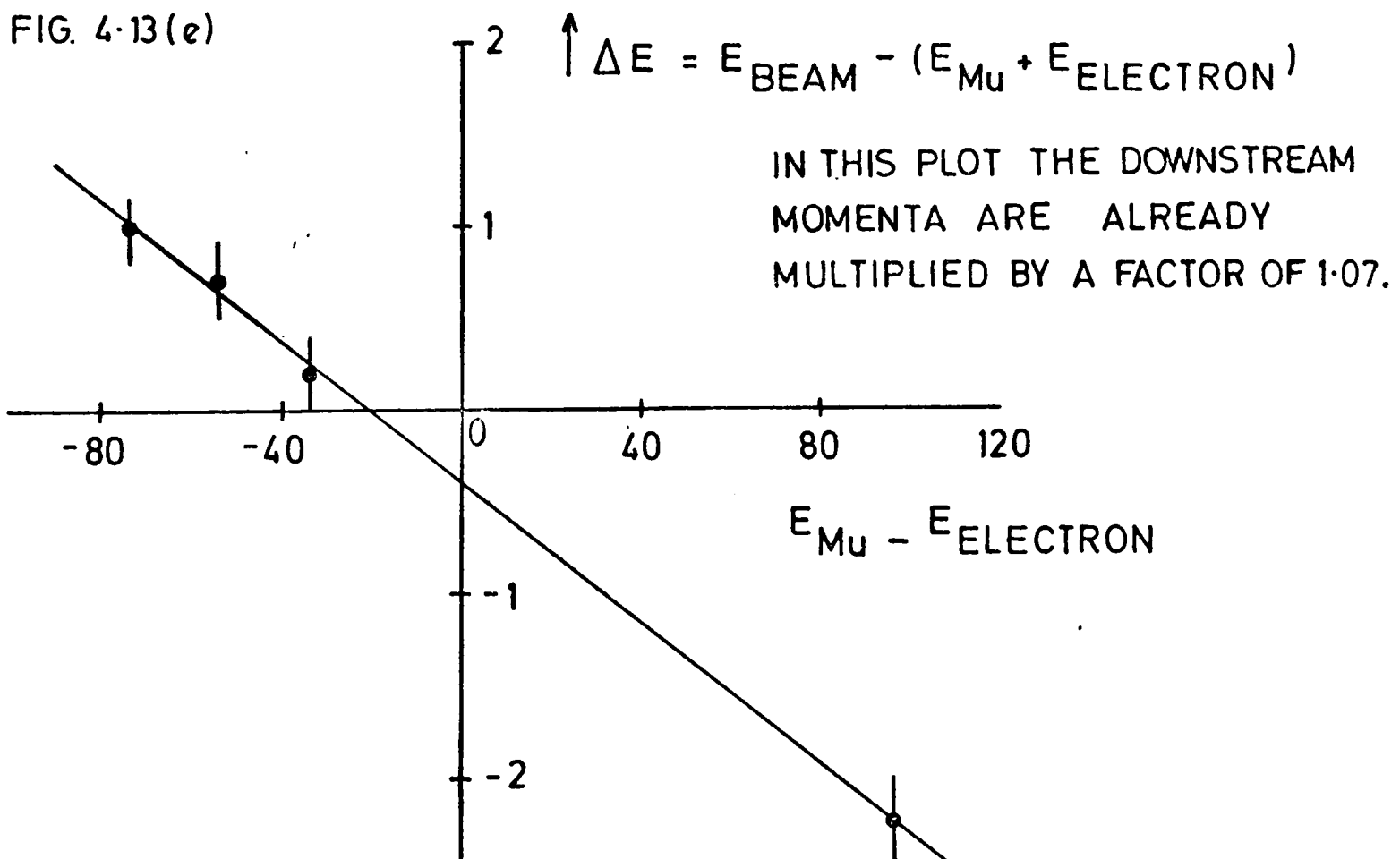
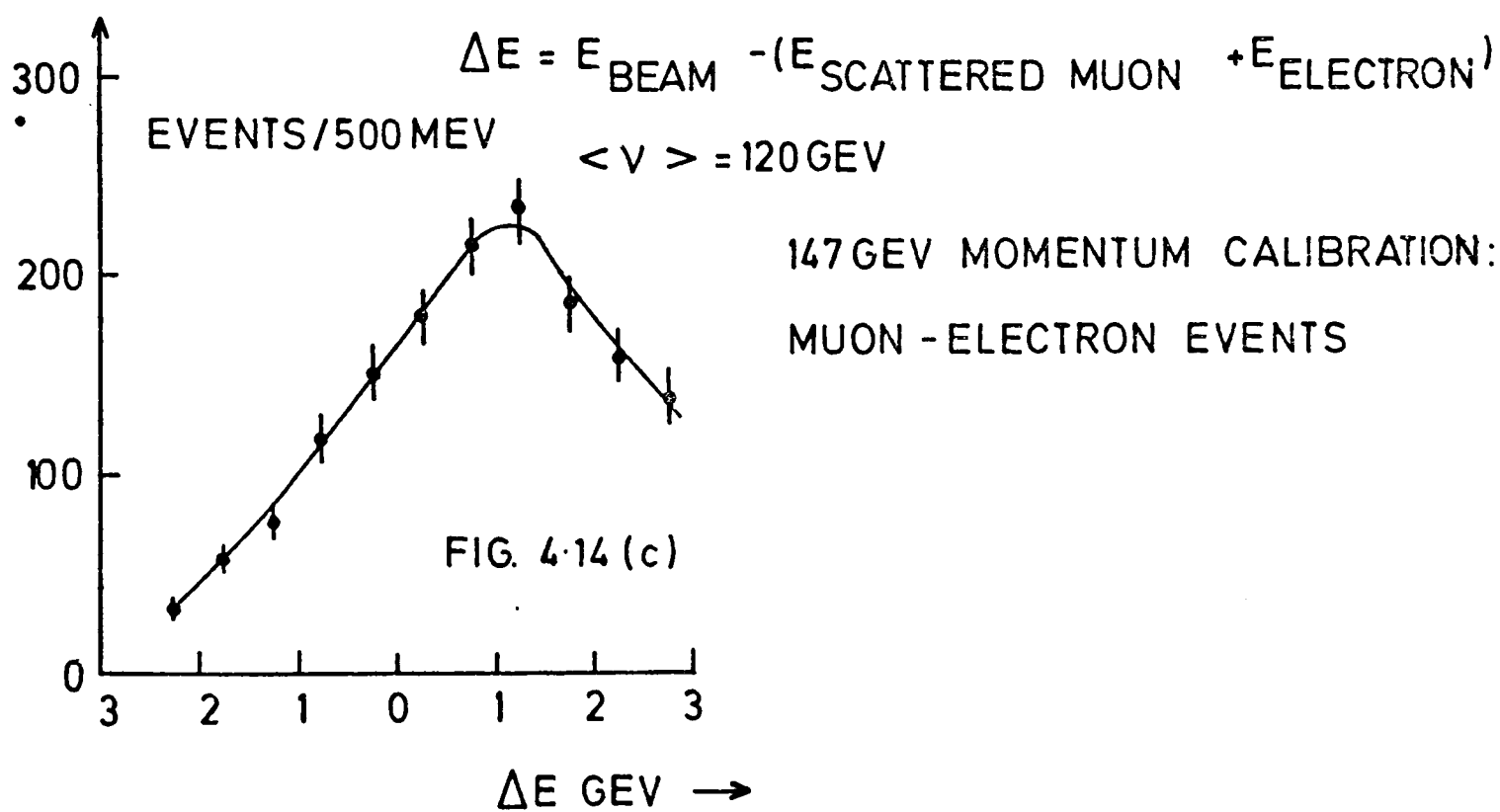
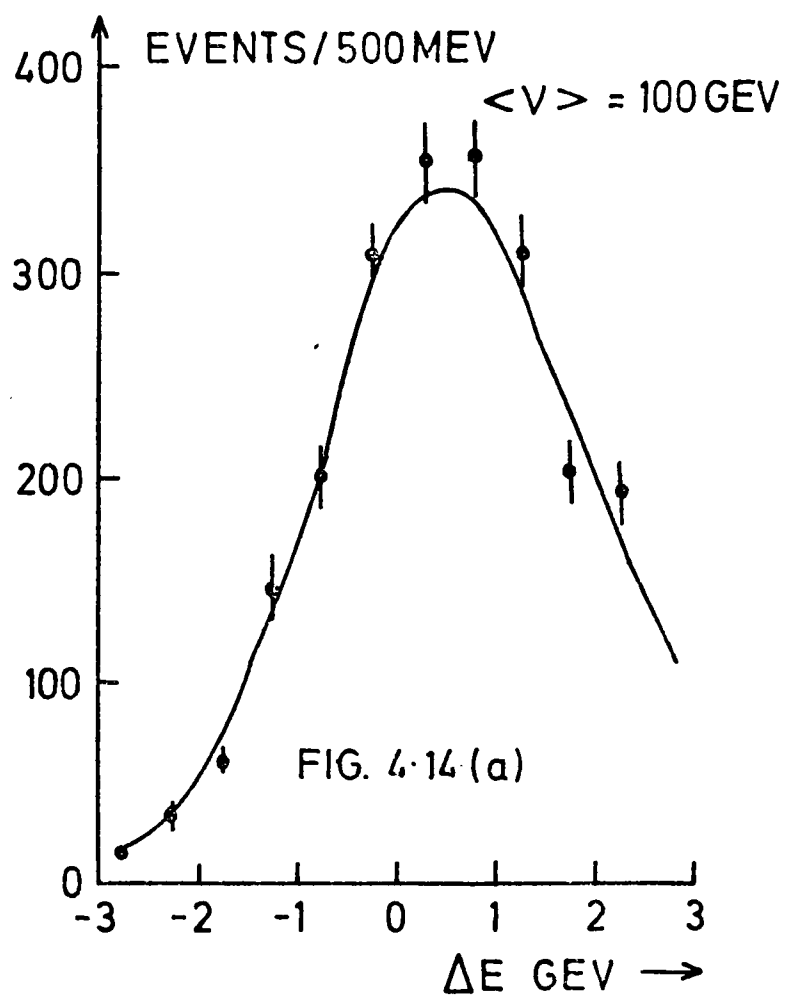
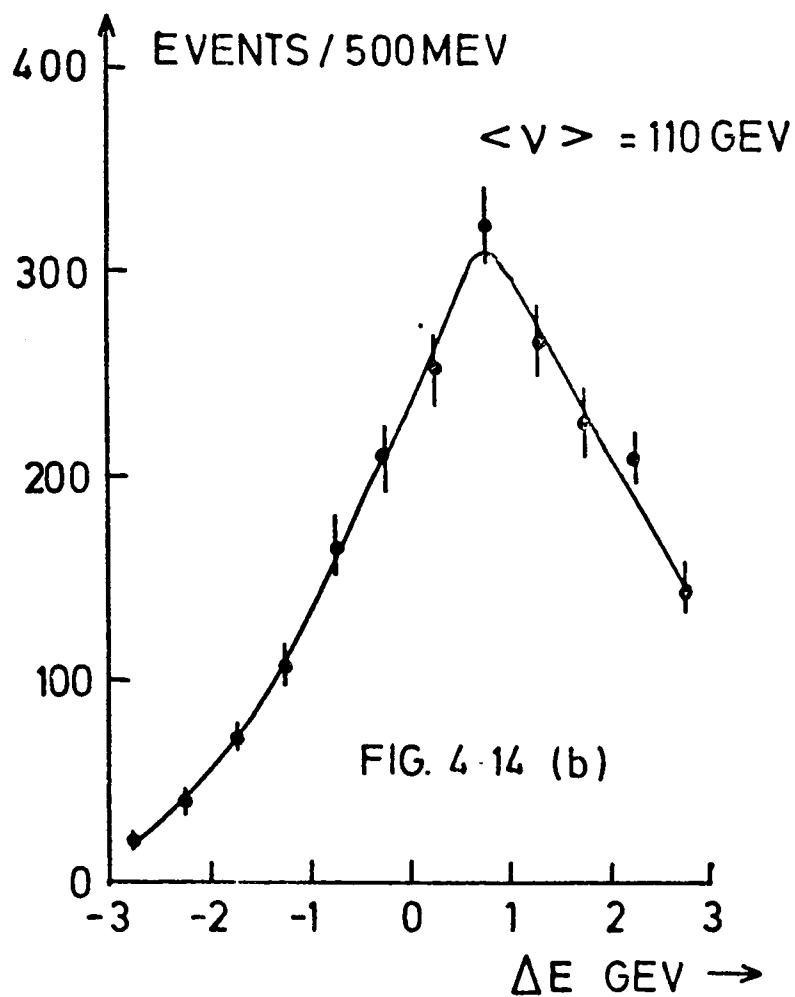


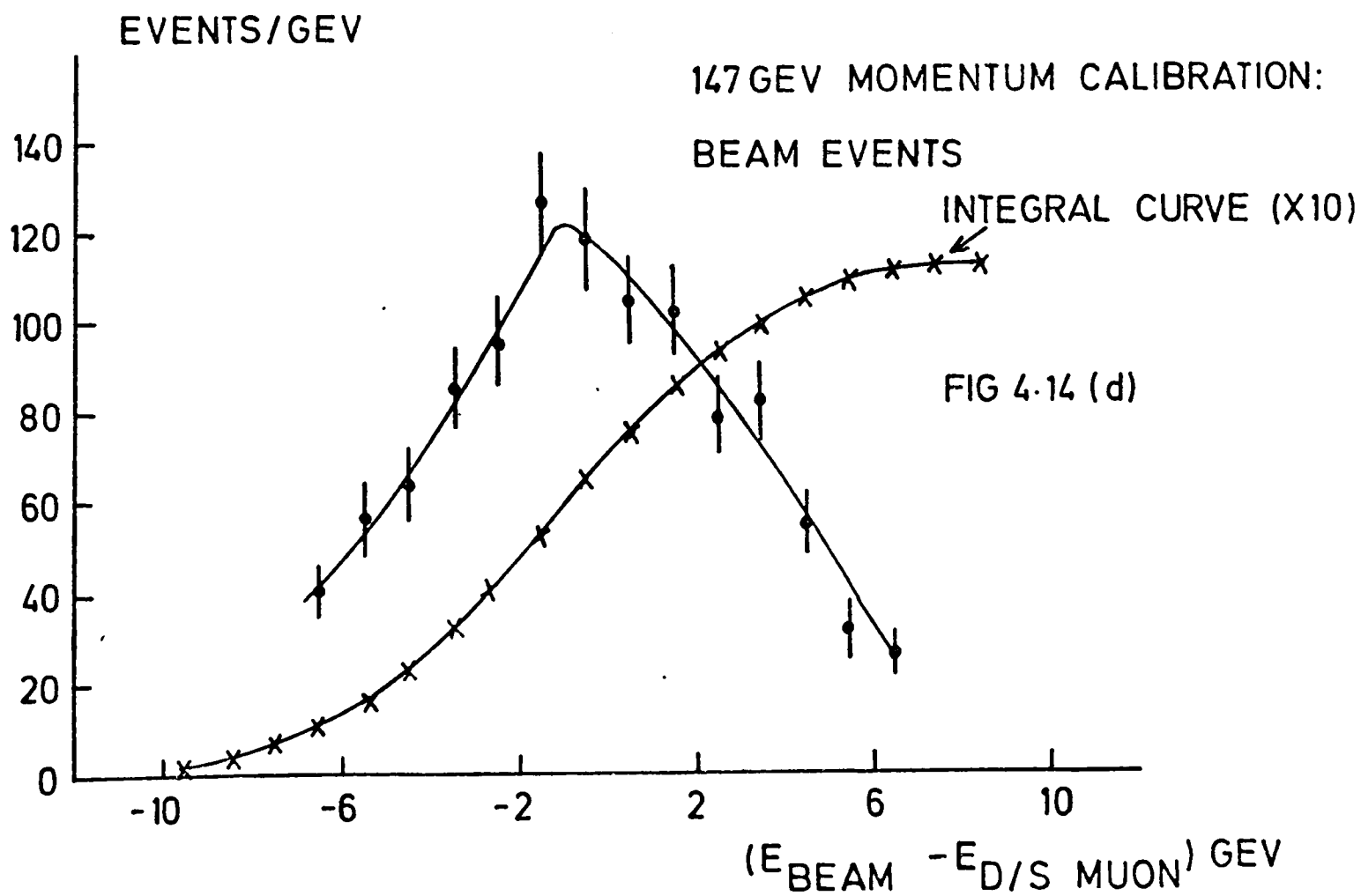
FIG. 4-13(f)

FIG. 4-13(e)





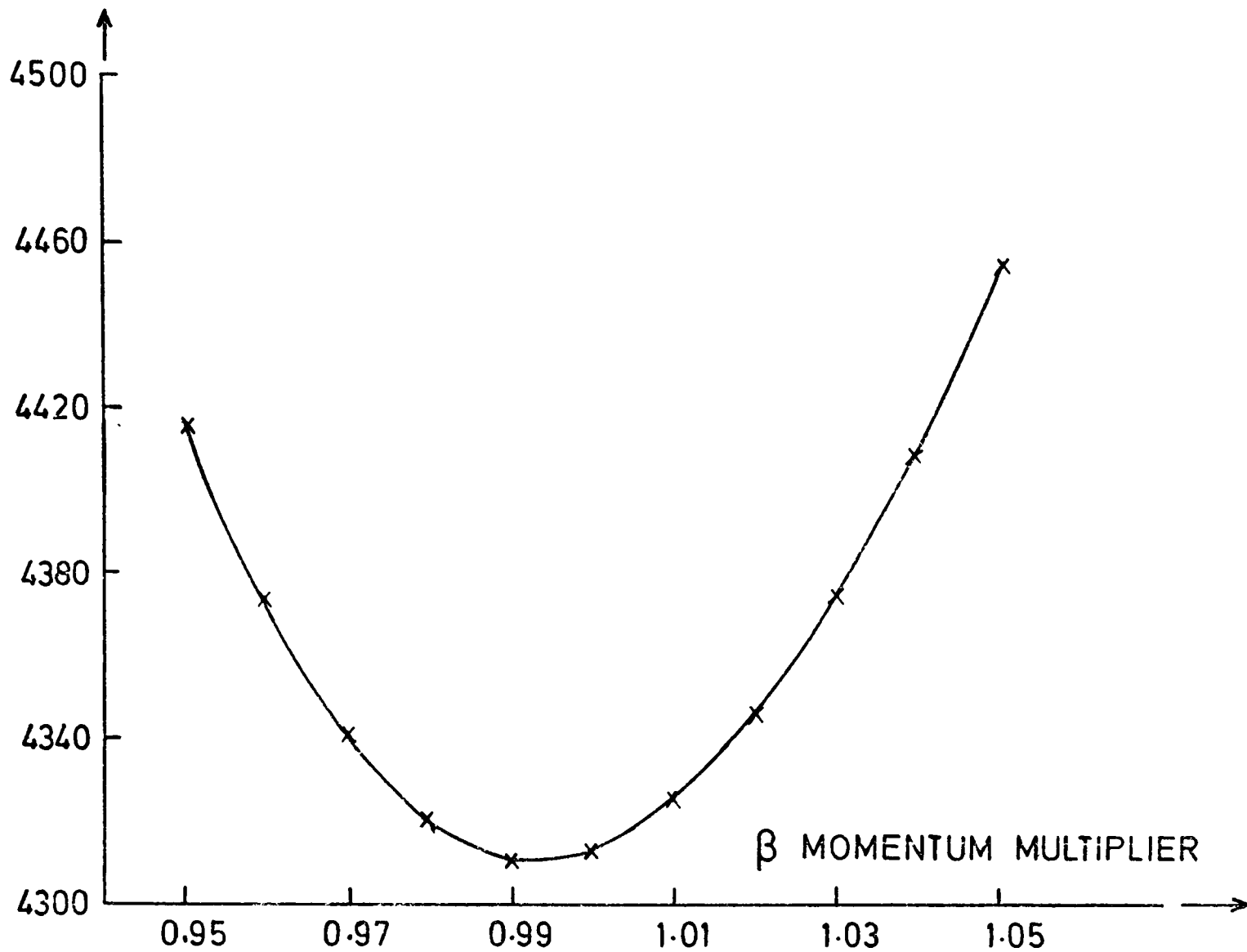
147 GEV MOMENTUM CALIBRATION:
MUON - ELECTRON EVENTS



ABSOLUTE MOMENTUM CALIBRATION
FOR THE 147 GEV DATA

χ^2 (for 5605 events)

FIG. 4-14 (f)



RELATIVE MOMENTUM CALIBRATION FOR THE 147 GEV DATA

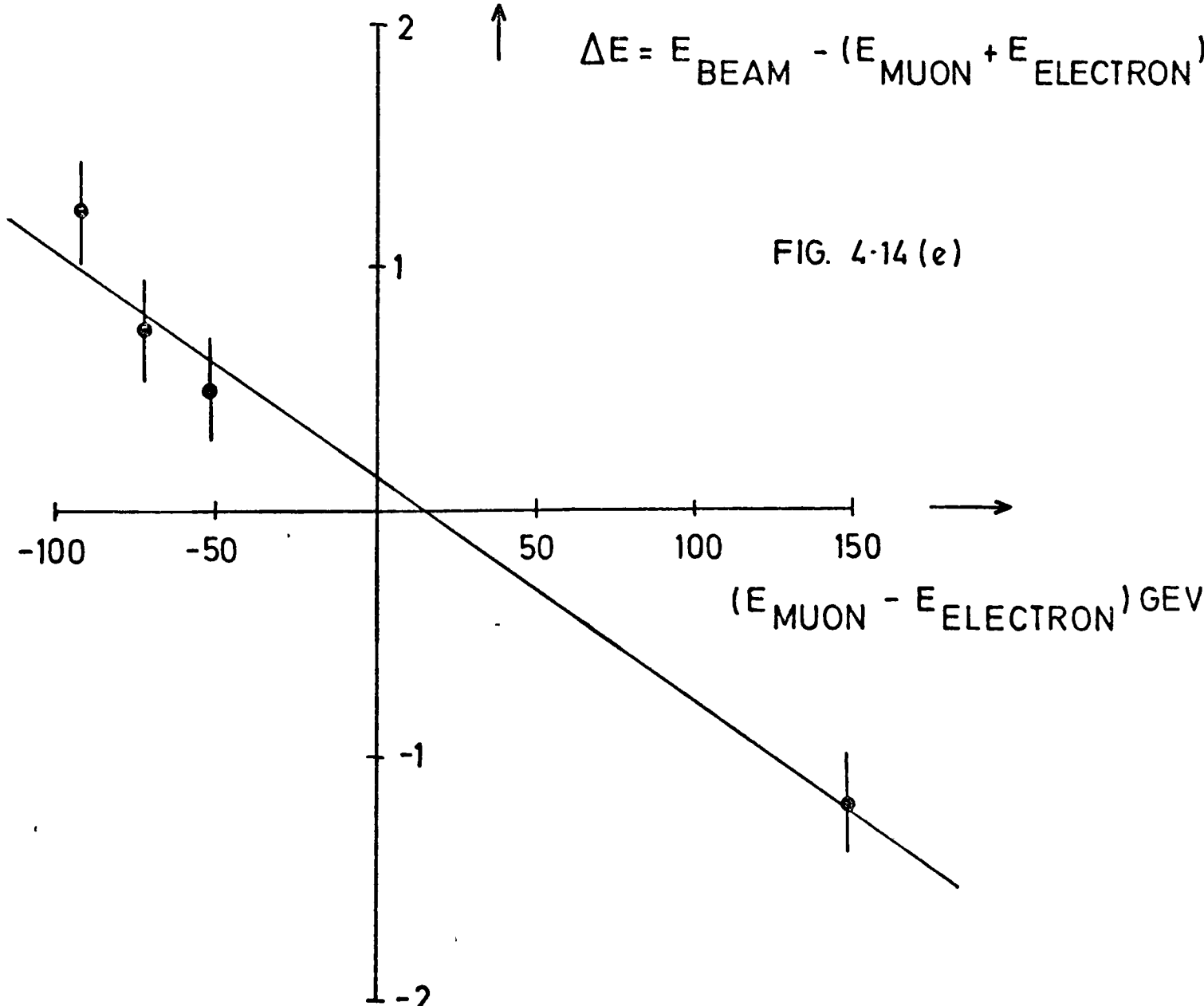


FIG. 4-14 (e)

TABLE 4.3

DATA REDUCTION STATISTICS

Total Data Sample	96 GeV/c Data		147 GeV/c Data	
	Beam Muons	Triggers	Beam Muons	Triggers
Alignment + Halo Runs	0.116E+05	5343	0.133E+04	663
Target Empty Runs	0.245E+10	18726 (+ 1183) (imbedded beam)	0.213E+10	12513 (+1010) (imbedded beam)
Target Full Runs	0.221E+11	337136 (+ 10525) (imbedded beam)	0.205E+11	224720 (+ 9757) (imbedded beam)
All Runs	0.246E+11	372913	0.266E+11	248663
Sample of Good Runs	Target Full	Target Empty	Target Full	Target Empty
Runs	36	4	29	5
Beam Muons	0.987E+10	0.189E+10	1.180E+10	0.213E+10
Triggers	152285	14409	130713	12513
Events with a Scattered Muon and a Vertex	50224	3139	46905	2940
Events with Vertex Inside Target				
Raw Events	42598	1815	39810	1920
(i.e. $Q^2 > 0.2$, Muon-Electron scatters removed, unphysical muons removed)	14165	327	10660	266
Run to Run consistency for the $Q^2 > 0.2$ rate.	$\chi^2 = 1.53$ per degree of freedom		$\chi^2 = 1.18$ per degree of freedom	

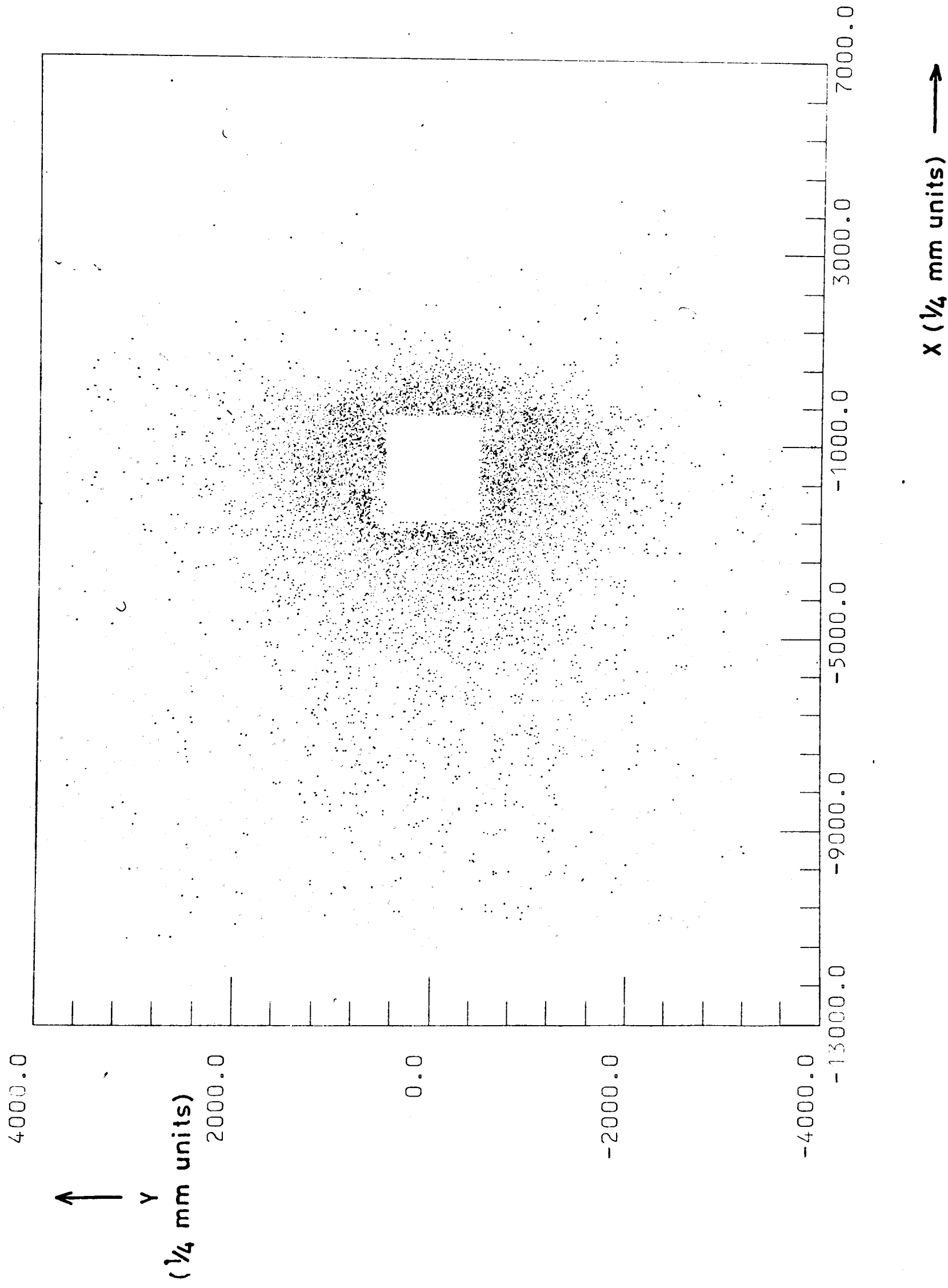


FIG. 4.15(a)
X,Y SCATTER PLOT AT
THE MUON HODOSCOPES
OF RAW EVENTS FOR
THE 96 GeV/c DATASET .

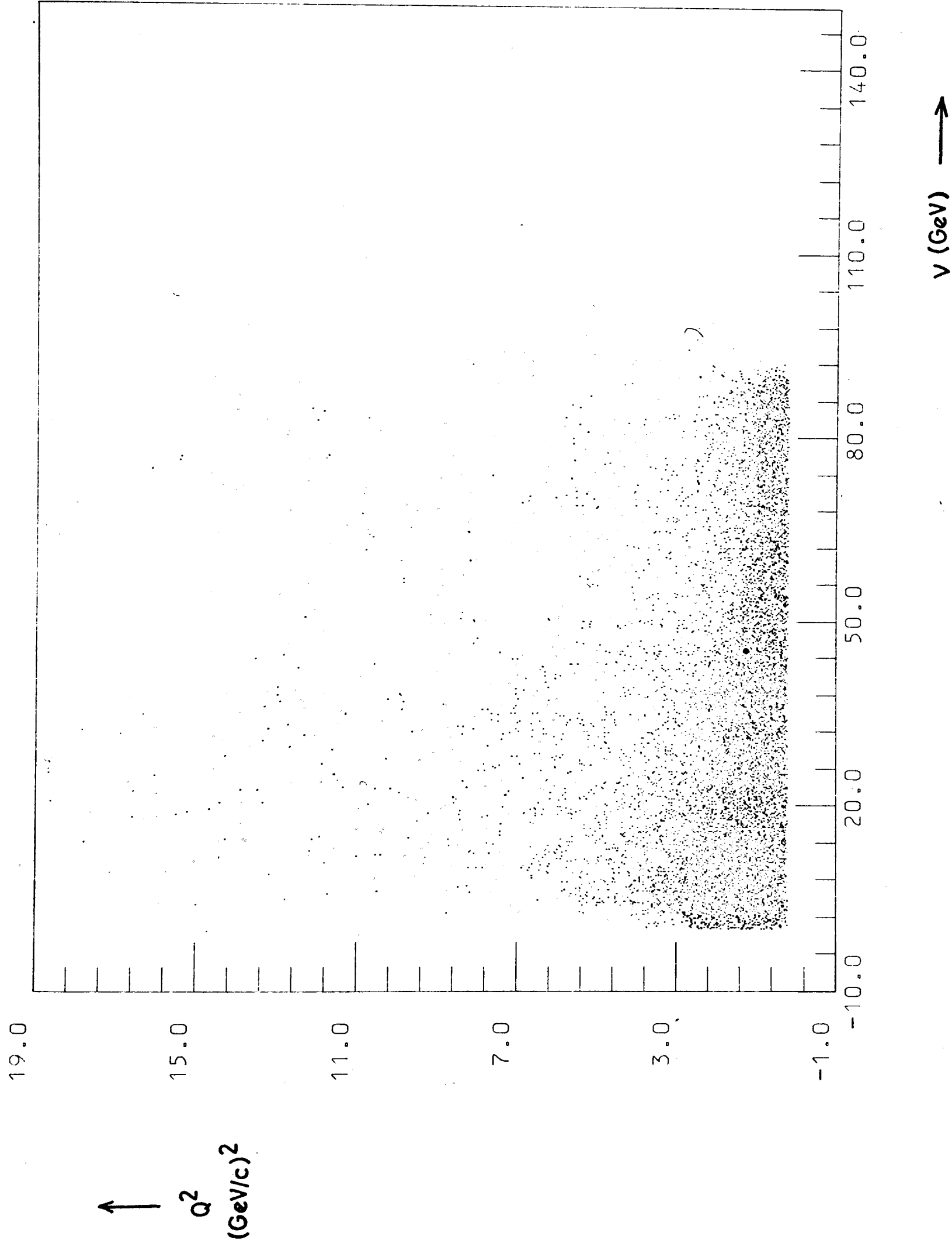
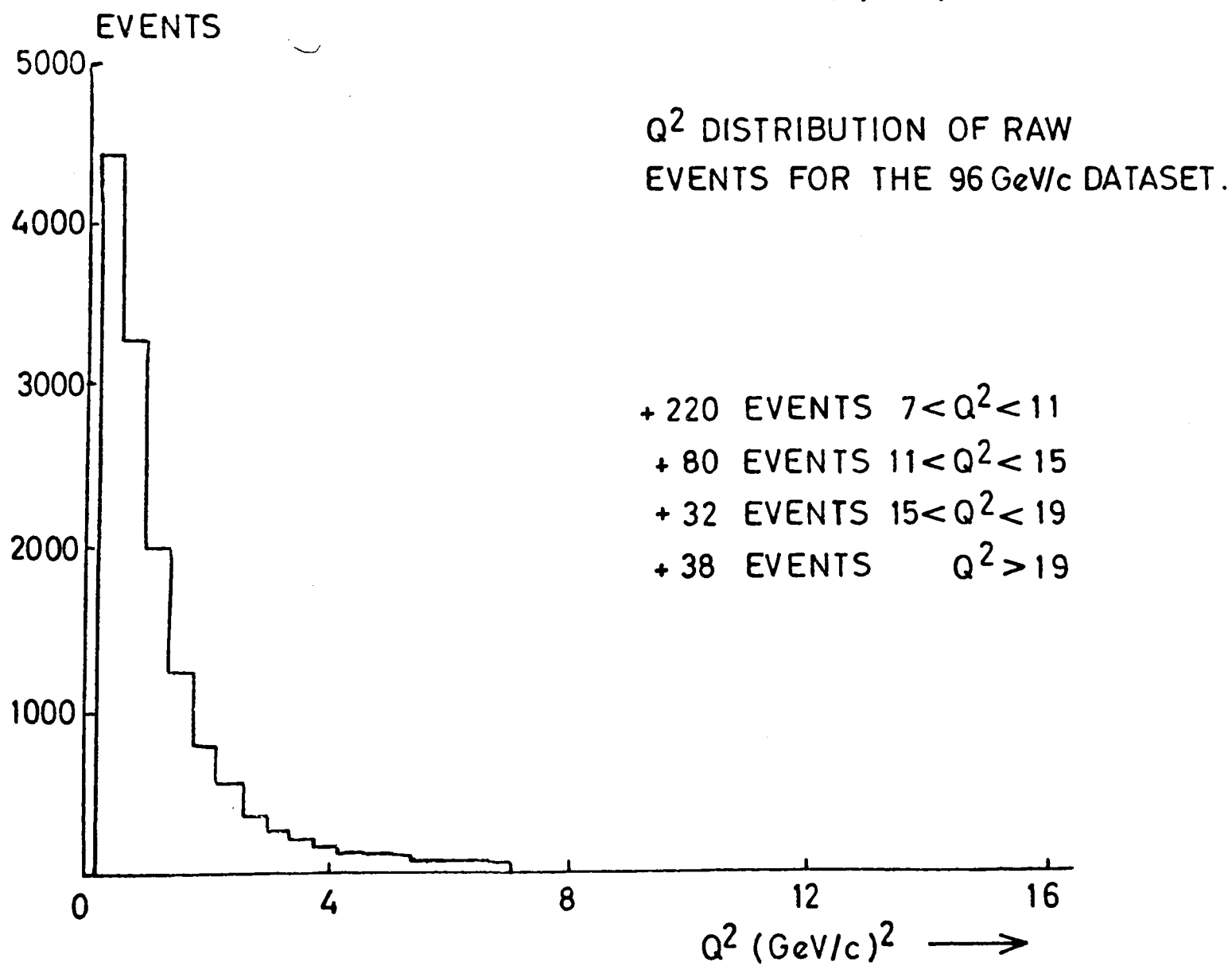
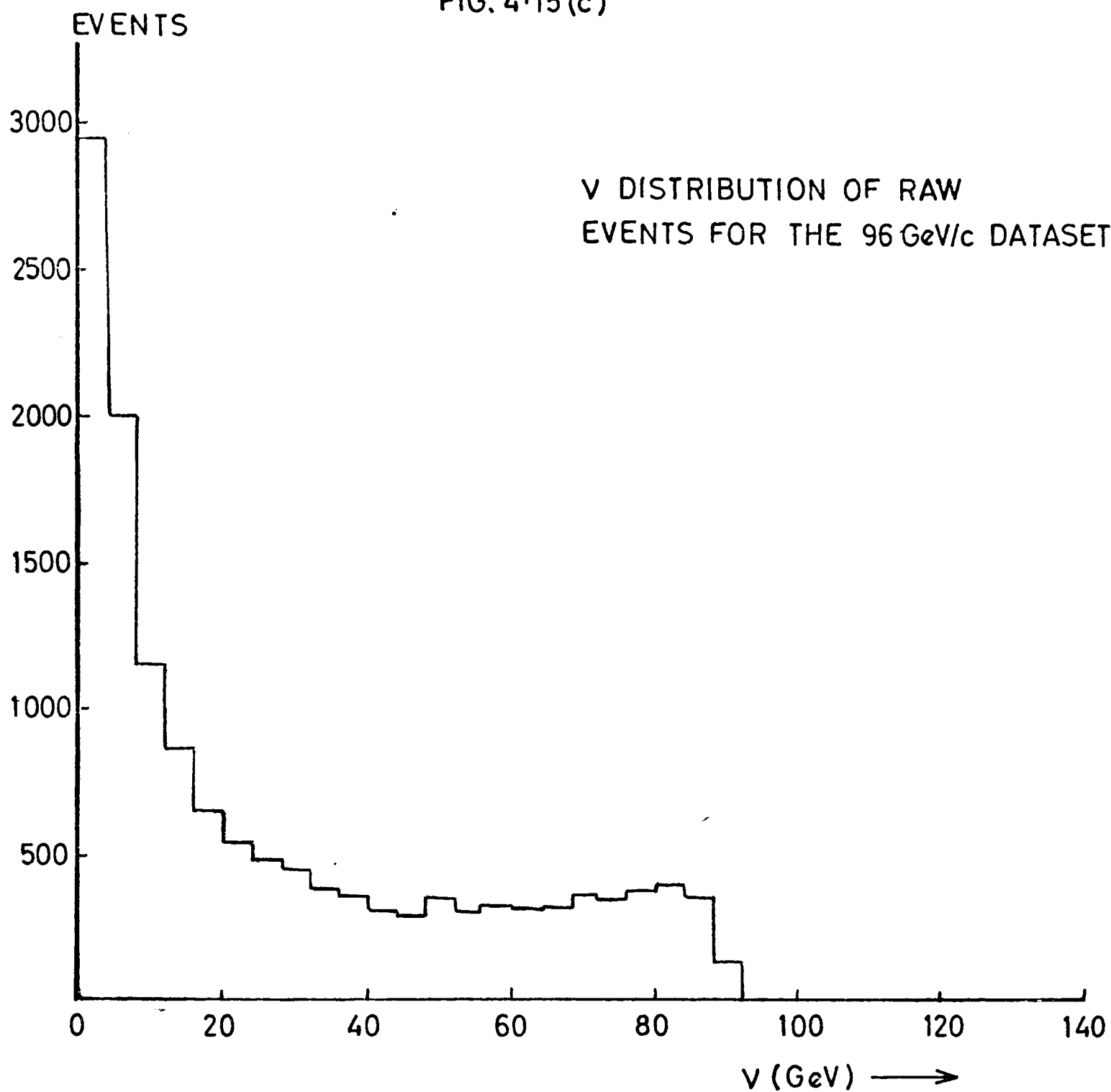


FIG. 4-15 (b)
 ν, Q^2 SCATTER PLOT OF
RAW EVENTS FOR THE
96 GeV/c DATASET.

FIG. 4.15(c)



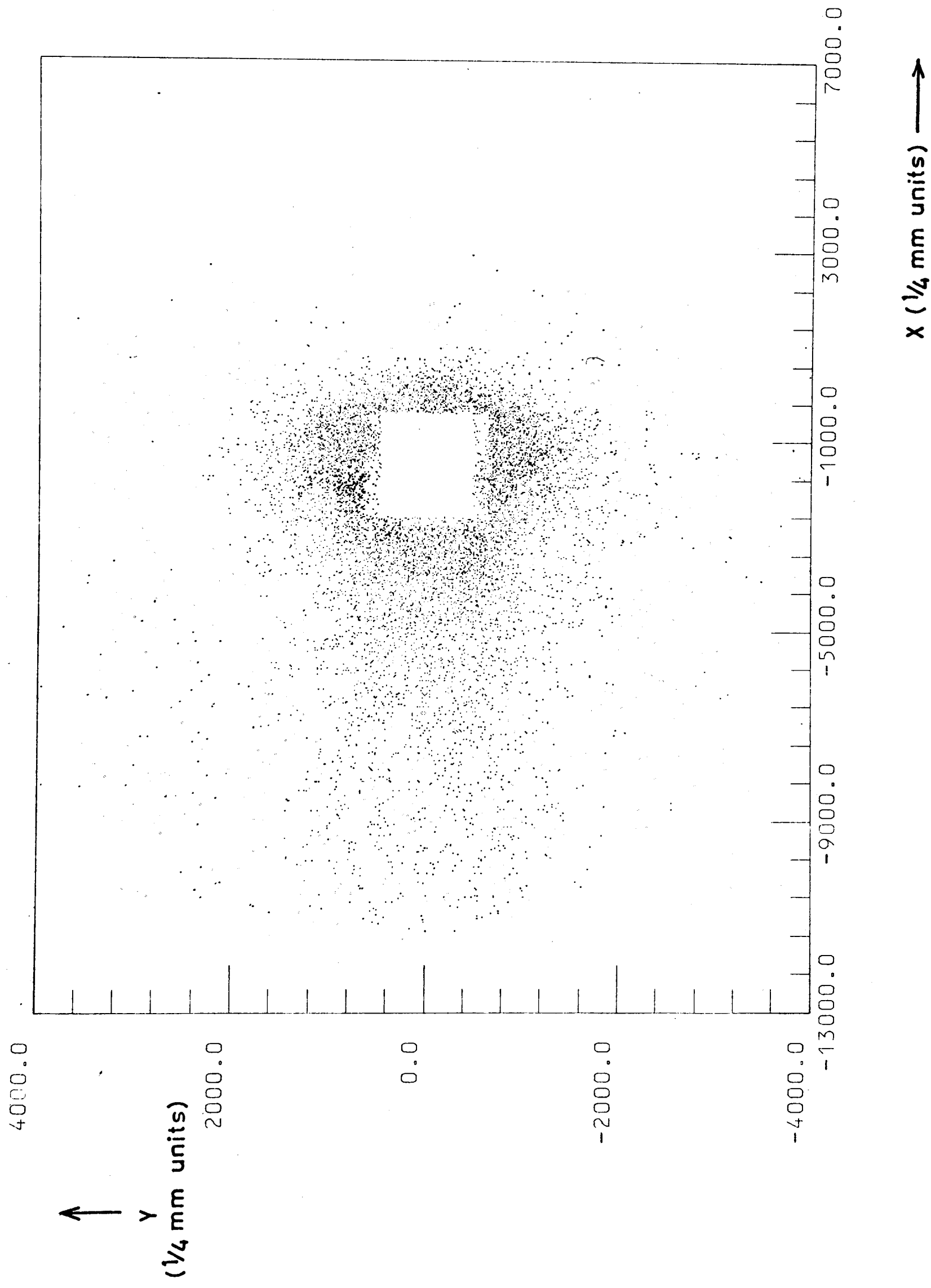


FIG. 4.16 (a)
X,Y SCATTER PLOT AT
THE MUON HODOSCOPES
OF RAW EVENTS FOR
THE 147 GeV/c DATASET.

FIG. 4.16(b)
 ν, Q^2 SCATTER PLOT
OF RAW EVENTS FOR
THE 147 GeV/c DATASET.

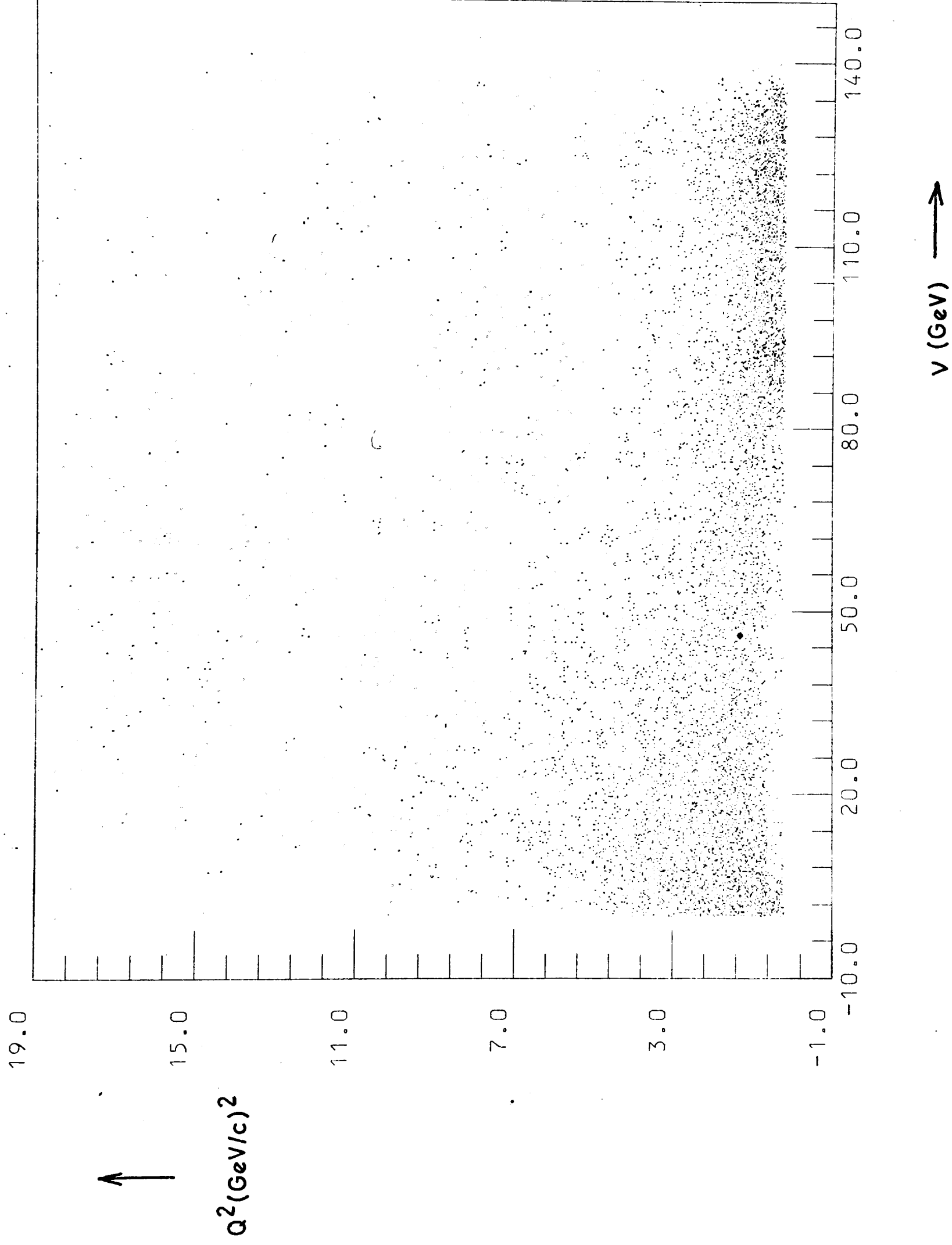
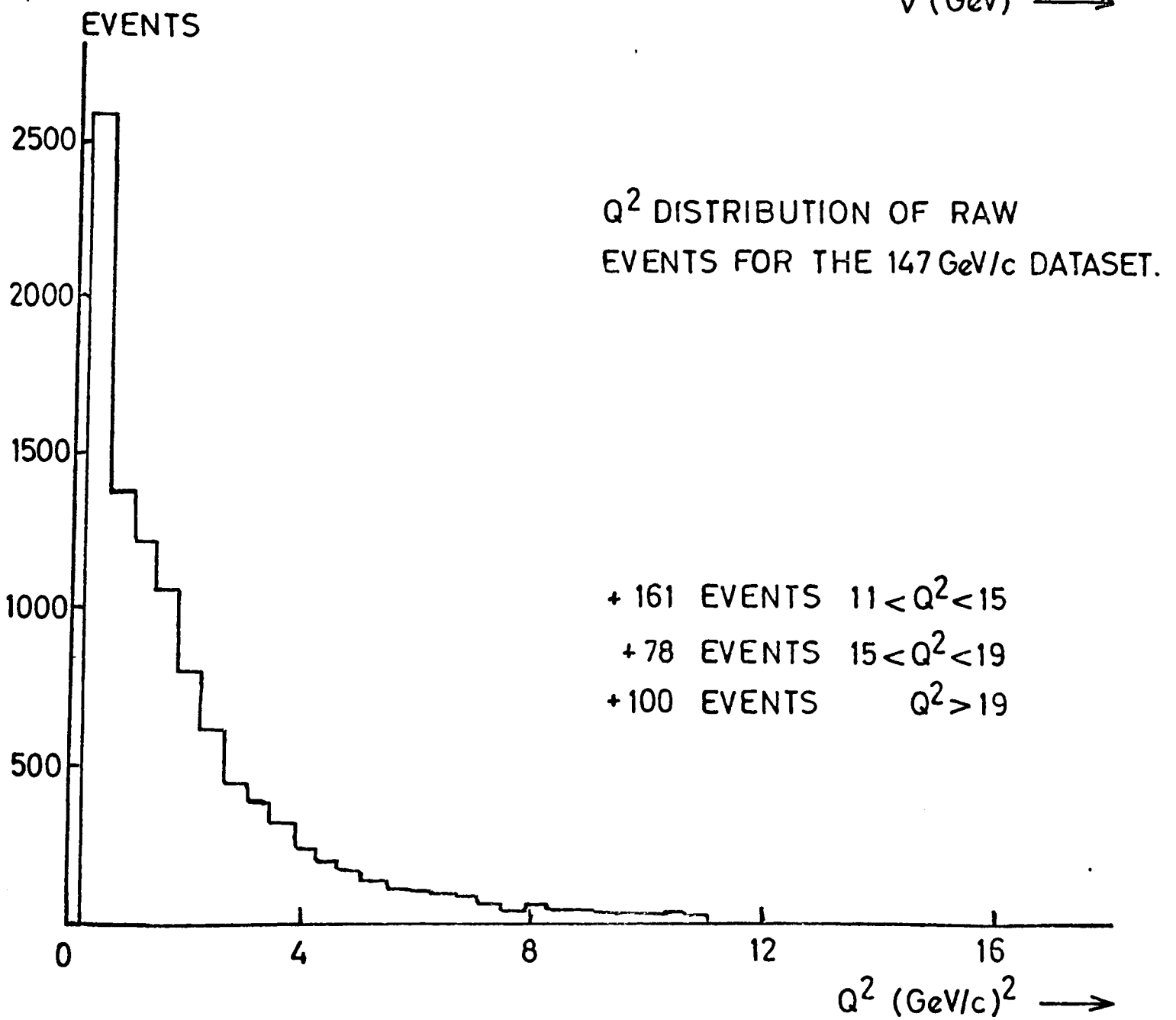
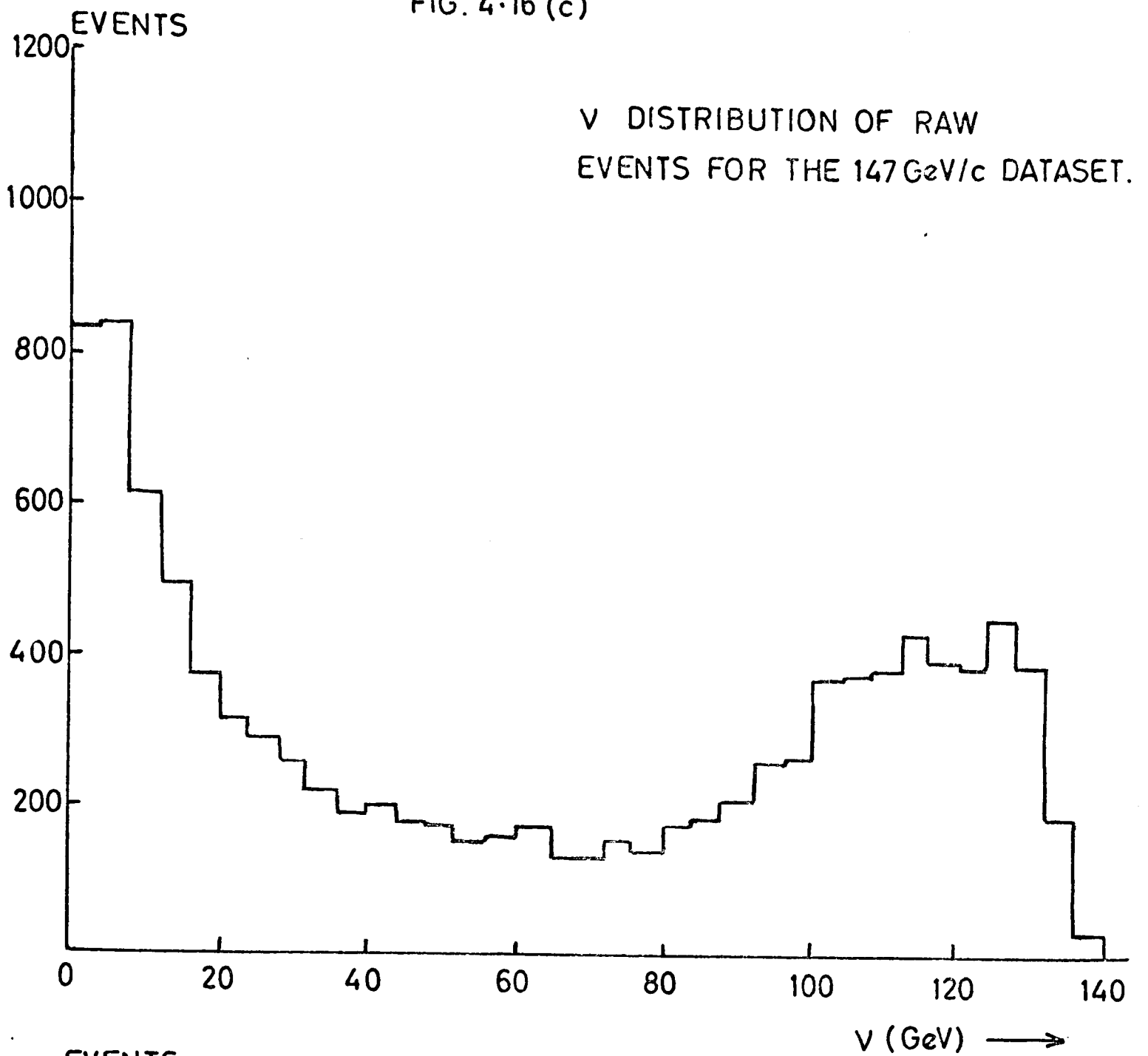


FIG. 4.16 (c)



5.A INTRODUCTION

This chapter describes how the raw event numbers are used to calculate the physical quantities of interest - i.e. cross-sections and structure functions.

In principle this is quite straightforward. The data is first binned in the chosen kinematic variables - i.e. (ν, Q^2) , (ω, Q^2) , (W^2, Q^2) , (x, y) etc. The bin sizes are selected such that there are reasonable numbers of events in most bins. If (α, β) are the chosen kinematic variables, then

$$\begin{aligned}
 N_{\Delta\alpha, \Delta\beta}^{\text{target}} &= N_{\Delta\alpha, \Delta\beta} - E_{\Delta\alpha, \Delta\beta} \\
 &= L\epsilon \int_{\alpha_1}^{\alpha_2} \int_{\beta_1}^{\beta_2} \left[d\alpha d\beta \frac{d^2\sigma}{d\alpha d\beta} \frac{A(\alpha, \beta) B(\alpha, \beta)}{RC(\alpha, \beta) RS(\alpha, \beta)} \right] \quad (\text{eqn. 5.1})
 \end{aligned}$$

where $\Delta\alpha = \alpha_2 - \alpha_1$ define the bin

$\Delta\beta = \beta_2 - \beta_1$ sizes in α and β

$N_{\Delta\alpha, \Delta\beta}^{\text{target}}$ = the number of events that fall in the
bin $\Delta\alpha, \Delta\beta$ from interactions in the
liquid hydrogen.

$N_{\Delta\alpha, \Delta\beta}$ = the number of full target events in the
 $\Delta\alpha, \Delta\beta$ bin

$E_{\Delta\alpha, \Delta\beta}$ = the background subtraction for the $\Delta\alpha, \Delta\beta$
bin

L = total luminosity - i.e. luminosity integrated
over time

ϵ = normalisation corrections. These corrections
include all the efficiency factors that are
independent of the event kinematics.

$A(\alpha, \beta)$	= geometric acceptance of the apparatus
$B(\alpha, \beta)$	= efficiency corrections that depend on the event kinematics
$RC(\alpha, \beta)$	= radiative corrections
$RS(\alpha, \beta)$	= resolution corrections
$\frac{d^2\sigma}{d\alpha d\beta}$	= the cross-section of interest

Section 5.B looks at the calculation of L , ϵ , $A(\alpha, \beta)$ and $B(\alpha, \beta)$. Section 5.C discusses the calculation of the correction factors $RC(\alpha, \beta)$ and $RS(\alpha, \beta)$. Section 5.D presents values of cross-sections, νW_2 and R and lists some of the conclusions drawn from the data.

5.B NORMALISATION CORRECTIONS AND WEIGHTED EVENTS

It is found convenient to modify equation 5.1 as follows. The data is first weighted on an event-by-event basis for the geometric acceptance, $A(\alpha, \beta)$, and the varying efficiency corrections, $B(\alpha, \beta)$. The number of weighted events, $W_{\Delta\alpha, \Delta\beta}$, in a bin $\Delta\alpha, \Delta\beta$ is given by

$$W_{\Delta\alpha, \Delta\beta} = \sum_{i=1}^{N_{\Delta\alpha\Delta\beta}} [A_i(\alpha, \beta) B_i(\alpha, \beta)]^{-1} - EW_{\Delta\alpha, \Delta\beta} \quad (\text{eqn. 5.2})$$

the sum is evaluated for all the raw events in the $\Delta\alpha, \Delta\beta$ bin and $EW_{\Delta\alpha, \Delta\beta}$ is the weighted background subtraction.

Using this, equation 5.1 may be re-written as

$$\frac{W_{\Delta\alpha, \Delta\beta}}{L\epsilon} = \int_{\alpha_1}^{\alpha_2} \int_{\beta_1}^{\beta_2} \left[d\alpha d\beta \frac{d^2\sigma}{d\alpha d\beta} \frac{1}{RC(\alpha, \beta) RS(\alpha, \beta)} \right] \quad (\text{eqn. 5.3})$$

One can comment that weighting procedure may be used to

Historically however, only $A(\alpha,\beta)$ and $B(\alpha,\beta)$ are so factored out and the quantity $\frac{W_{\Delta\alpha,\Delta\beta}}{L\epsilon}$ may be thought of as a raw cross-section for scattering into the $\Delta\alpha,\Delta\beta$ bin. This section describes the calculation of L , ϵ , $A(\alpha,\beta)$ and $B(\alpha,\beta)$ and looks at the distributions of weighted events:

Luminosity - Luminosity is defined as: (the flux of incident particles) \times (the number of scattering centres in the target per unit area). The integrated luminosity is an easy number to calculate given the length and density of the hydrogen target and the total incident flux of muons,

$$\text{i.e. } L = N_{\mu} \ell \rho N_{\text{Avogadro}} \quad \text{where} \quad \begin{aligned} N_{\mu} &= \text{total incident flux of muons} \\ \ell &= \text{length of hydrogen target} \\ \rho &= \text{density of hydrogen target} \\ N_{\text{Avogadro}} &= \text{Avogadro's number} \end{aligned}$$

From the measurement errors in the target thickness and the vapour pressure of the hydrogen in the target, the luminosity is estimated to be accurate to better than 0.5%.

Normalisation Corrections - The factor ϵ is a product of six independent corrections, i.e. $\epsilon = \epsilon_1 \epsilon_2 \epsilon_3 \epsilon_4 \epsilon_5 \epsilon_6$. The first five are efficiency corrections that compensate for the fact that, even if a genuine muon scatter occurs, there is a probability that it will pass undetected by the apparatus and/or the analysis programs. The sixth factor, ϵ_6 , corrects for the effects of the hydrogen gas that remains in the target during the target empty runs.

ϵ_1 is the beam reconstruction efficiency. This gives the probability that the beam reconstruction program - see Section 4.B - can calculate a good incident trajectory for a given beam muon. One

might think it possible to just use the beam reconstruction efficiency for event triggers. In practice however the apparatus is biased towards triggering on bad beam and the efficiency generated from the event triggers is likely to be too low. Instead the sample of imbedded beam triggers is used to calculate ϵ_1 . The fraction of the imbedded beam triggers that reconstruct to give a good incident trajectory is $(68.46 \pm 0.67)\%$ for the 96 GeV/c data and $(72.72 \pm 0.59)\%$ for the 147 GeV/c data.

The second correction, ϵ_2 , is also beam related. $(1-\epsilon_2)$ gives the probability that there is more than one incident muon in an r.f. bucket. As discussed in Section 3.B the overwhelming probability in this case is that if one of the muons scatters, the other(s) will veto the event by hitting the K-counter. The beam hodoscopes are used, as described in Section 3.B, to attempt to reduce this effect. Previous sets of data^(54,57) used double hits in BH5 or BH6 to veto r.f. buckets and $(1-\epsilon_2)$ was found to be of the order of 1%. For the data on which this thesis is based, double hits in BH2 or BH3 or BH4 or BH5 or BH6 are used to veto r.f. buckets and it is found that $(1-\epsilon_2)$ is approximately 0.1% for either incident energy and as such ϵ_2 has a negligible effect on the data.

The remaining three corrections arise from the requirement that the analysis finds the scattered muon. The correction, ϵ_3 , takes into account the downstream spark chamber efficiencies. The latter may be calculated on a plane-by-plane basis. It is estimated that the 11 spark requirement for a downstream track loses less than 0.5% of events.

Any downstream track must link with an upstream track before it can be considered as a muon candidate. The factor, ϵ_4 , is the upstream MWPC efficiency. It is directly estimated taking a set

of 'perfect' downstream muon tracks and asking what fraction link to upstream MWPC tracks. The 'perfect' muon tracks are required to be positively charged, to be intime with respect to the downstream counter hodoscopes and to be linked to intime Muon chamber tracks. In addition they are required to have an impact parameter of less than 16 cm and in the Y-view to be within 5 cm of the incident beam track at the target centre - these two conditions help cut out halo muons. The interaction of beam muons in the material of the upstream MWPCs and the air before the CCM field will give rise to 'perfect' downstream muons that do not have upstream links. Taking this effect into account, it is found that $\epsilon_4 = (99.17 \pm 0.05)\%$ for 96 GeV/c data and that $\epsilon_4 = (98.68 \pm 0.06)\%$ for the 147 GeV/c data.

The factor ϵ_5 , is the counter efficiency correction. $(1-\epsilon_5)$ is the probability that a scattered muon will not be registered intime with respect to the downstream and Muon counter hodoscopes. Section 4.C shows that the downstream counter elements are highly efficient and $(1-\epsilon_5)$ is estimated to be less than 0.1%.

The full target data contains events in which the incident muons interact in the target flask material. To compensate for these interactions a background subtraction is made using the target empty data - this is more fully described under "Background subtraction" later on in this section. The empty target however still contains hydrogen gas and the background subtraction derived from the target empty data will be overestimated because of interactions in the gas.

The factor

$$\epsilon_6 = 1 - \frac{(\text{density of hydrogen gas in the empty target})}{(\text{density of liquid hydrogen in the full target})} = 0.977$$

allows for this overestimation of the background subtraction.

From the six corrections described above, ϵ is calculated to be 0.6586 ± 0.0085 for the 96 GeV/c data and to be 0.6962 ± 0.0079 for the 147 GeV/c data. An instructive way of looking at ϵ is to say that the six corrections reduce the effective flux seen by the experiment. Compounding N_μ and ϵ gives the following total effective fluxes for the two datasets:-

total effective flux for the 96 GeV/c data = 0.652×10^{10} muons

total effective flux for the 147 GeV/c data = 0.822×10^{10} muons

Geometric Acceptance - The geometric acceptance of the apparatus, $A(\alpha, \beta)$, represents the probability that a scattered muon with the given α, β will satisfy the experimental triggering condition and thus allow the event to be recorded on the data tapes. As such it is defined by the triggering areas of the G, M, M' and N hodoscopes.

Before describing the calculation of A, it is instructive to see how the various v 's and Q^2 's relate to the (X,Y) co-ordinates at the M hodoscope plane. A given v and Q^2 corresponds to a given E' and θ . If it is assumed that all the incident muons lie along the beam-line axis and all scatters occur at the target centre, then the scattered muons will lie on a cone of half-angle θ - whose axis is the beam-line - as they leave the target. To a good approximation the half-angle of the cone is unchanged in going through the CCM field. The axis of the cone, however, is bent in X by the angle appropriate to the scattered muon energy, E' . This means that the

locus of events at the M hodoscope for a given ν and Q^2 is a circle whose radius depends on θ and whose central displacement from the origin depends on E' . Figures 5.1 and 5.2 show some of the circles so generated for various ν 's and Q^2 's at the M hodoscope for the two datasets. The scattered muons are equally distributed in the azimuthal angle - i.e. equally distributed on the circumference of the (ν, Q^2) circles. Given this, it is seen that the geometric acceptance for any particular (ν, Q^2) is just the fraction of the circumference of the given (ν, Q^2) circle that is inside the triggering areas of the hodoscope.

In calculating the actual geometric acceptance of the apparatus, there are three complications to the above picture. Firstly, the incident muon trajectories do not all lie along the beam-line axis - see Figures 2.6 for beam phase space plots. Secondly, the interaction points lie along the entire length of the target. Qualitatively these two effects smear the locus of events for a given ν and Q^2 from a circle into an annulus. The third complication results from there being four hodoscopes that define the overall geometric acceptance. In view of this, it is found convenient to employ a Monte-Carlo method to calculate the geometric acceptance. First a table is constructed of the geometric acceptances for a set of points on the ν, Q^2 plane. The Monte Carlo program used is basically the same as that described in Section 4.C. Again the beam phase space is introduced by using the imbedded beam trajectories as input, an interaction point is randomly selected on the beam trajectory inside the target, and an azimuthal angle is randomly selected. This time however, a scattered muon is thrown corresponding to every (ν, Q^2) point for the table being constructed.. The scattered muons are tracked through the apparatus and tested

to see if they satisfy the experimental triggering condition - it is further tested to ensure that the scattered muon does not go through the deadners of the 6-metre chambers. Repeating this process over large number of input trajectories and interaction points will give a table of $A(\nu, Q^2)$.

$$\text{i.e. } A(\nu, Q^2) = \frac{\text{Number of scattered muons accepted at } \nu, Q^2}{\text{Number of scattered muons thrown at } \nu, Q^2}$$

From this table of $A(\nu, Q^2)$ values, the geometric acceptance, $A(\alpha, \beta)$, at any point α, β may be calculated by interpolation. Data tables DT1(a) and DT1(b) are the tables of $A(\nu, Q^2)$ for the two incident energies. It is estimated that the maximum errors in A are ± 0.02 . Furthermore, the geometric acceptances calculated by this Monte-Carlo method are consistent with those calculated by a geometric method described in Ref. (57):

Varying Efficiency Corrections - The term $B(\alpha, \beta)$ is comprised of two specific effects that depend on the kinematics of the scattered muon.

The first of these is the downstream trackfinding efficiency. The technique used to determine this efficiency starts off with the real data. The program generates a fake downstream track and calculates the sparks associated with this track. In doing so, it takes into account the plane-by-plane inefficiencies and track resolutions. The sparks so calculated are put into the spark buffer, allowances being made for spark spreads, and the track-finder is set to work on the modified spark buffer. The process is repeated for sufficiently large numbers of fake tracks and real events. The fraction of the fake tracks found is a measure of the downstream

track-finding efficiency. Figure 5.3 shows a plot of the efficiency as a function of X across the 6-metre chambers. It is seen that there is approximately a 20% dip in the beam region of the chambers. The track-finding efficiency has an overall effect of about 10% on the data, although it affects some of the lower ν bins by as much as 20%. It is estimated that the form of the inefficiency can be parameterised with an error of at worst 30%. Given this the low ν bins could have a systematic error of up to 6% from the downstream track-finding efficiency correction.

The second effect to go into the term $B(\alpha, \beta)$ is called the K-veto showering correction. It reflects the probability that as the scattered muon emerges from the 240 cm steel wall, it is accompanied by an electron shower. Were one of these electrons from the shower to hit the K-counter, the good muon scatter would be vetoed. To calculate the correction for this effect, first the probability distribution, $P(R)$, of there being an electron in the shower with sufficient energy to set a scintillation counter is determined as a function of the distance between the electron and muon, R . This is done by looking at the distribution of multiple hits in the N hodoscope in the sample of imbedded beam events - the beam tracks are used to determine which of the N hits are due to muons and all other N hits are assumed to be due to electrons. Figure 5.4(a) shows the fraction of events with associated electrons as a function of R , the coarse binning in R arising from the widths of the N counters. The overall normalisation - and hence the central bin - is obtained by looking at the total fraction of imbedded beam events with multiple - i.e. greater than 2 - hits in the N hodoscope. The probability that an event is accidentally vetoed by an

electron from a shower is just $P(R)$ integrated over the dimensions of the K-counter. Figure 5.4(b) plots this integrated probability, $Q(R)$, along a horizontal line going through the centre of the K-counter. The overall effect on the data is approximately 2% and any systematic error introduced by this showering correction are less than 1%.

Background Subtraction - As has been stated before the event distributions from the full target runs also contain some scatters where the muons have interacted with the material of the target flask itself. The vertex determination does not have sufficient resolution to reject these events using target cut in Z. Some target empty runs were logged onto tape and are used to calculate the background subtraction. As there are very few target empty events - a few hundred for each of the two datasets, see Table 4.3 - it was decided to fit a function to the ratio of target empty to target full data and use this function to make a smoothed background subtraction. The parameterisation eventually used is

$$C(\alpha, \beta) = \frac{\text{Target empty events in } \Delta\alpha, \Delta\beta \text{ bin}}{\text{Target full events in } \Delta\alpha, \Delta\beta \text{ bin}} ; \quad \begin{array}{l} \text{target empty event} \\ \text{normalised to the} \\ \text{same incident flux} \end{array}$$

$$= 0.023 + (C_1 + C_2 v + C_3 v^2)(1.0 - 0.375x); \quad x = \frac{Q^2}{2Mv}$$

This parameterisation is purely phenomenological. The number 0.023 is the ratio of the weights of the hydrogen gas in the empty target and the liquid hydrogen in the full target and the factor $(1.0 - 0.375x)$ allows for the fact that the target flask material is deuteron-like. C_2 and C_3 are expected to be small and this is indeed found to be the case. Figure 5.5 shows how the actual background data compares with the smoothed background curve for the 96 GeV/c data. It is

estimated that the maximum systematic errors introduced by the smoothed background subtraction are less than 3%.

Weighted Events - Having found $A(\alpha, \beta)$, $B(\alpha, \beta)$ and $C(\alpha, \beta)$, the weighted event distributions, $W_{\Delta\alpha, \Delta\beta}$ may be found by using equation 5.2, i.e.

$$W_{\Delta\alpha, \Delta\beta} = \sum_i [(A_i(\alpha, \beta)B_i(\alpha, \beta))^{-1} - C_i(\alpha, \beta)]$$

where the sum is evaluated over all the raw events, $N_{\Delta\alpha, \Delta\beta}$, in the bin $\Delta\alpha, \Delta\beta$.

Furthermore overall cuts are made in the (ν, Q^2) plane to cut out data where the geometric acceptance is less than 0.1. Figure 5.6(a) shows the boundaries of the weighted data in the (ν, Q^2) plane for the 96 GeV/c dataset. Figures 5.6(b) and 5.6(c) show histograms of weighted events in ν and Q^2 for this dataset. Figures 5.7 show the equivalent plots for the 147 GeV/c dataset.

5.C RADIATIVE AND RESOLUTION CORRECTIONS

The quantities $\frac{W_{\Delta\alpha, \Delta\beta}}{L\epsilon}$ may be thought of as raw cross-sections.

Two further factors have to be unfolded from them to obtain the physical cross-sections. These factors allow for radiative effects and the apparatus resolution and their evaluation is discussed in this section.

Radiative Corrections - The process of interest in the experiment is the inelastic reaction $\mu^+ + N \rightarrow \mu^+ + X$, see Figure 1.1. The muon,

however, can also radiate real photons before, during and after the interaction of interest. The processes involving the emission of a single real photon are illustrated in Figures 5.8. Figure 5.8(a) is ordinary bremsstrahlung in which the muon radiates in the presence of a nucleon, M. In this process the scattering angle, θ , tends to zero and the Q^2 's for these events tend to be near the $Q^2 = Q_{\min}^2$ line. The processes shown in Figures 5.8(b) and 5.8(c) are given the name straggling and in these the muon radiates a real photon in the presence of nucleon M before or after the interaction with the nucleon N. In the processes shown in Figures 5.8(d) and 5.8(e), the muon radiates a photon in the field of the same nucleon, N, from which it scatters. These processes are termed internal bremsstrahlung. In addition further radiative processes involving the emission of two or more photons may also occur. It is apparent that in these radiative events, the measured kinematic quantities, α and β , derived from the muon track before and after the target are not those of the interaction of interest. This means that the measured number of events in any particular bin will differ from the "true" number of events - i.e. the number of events that the bin would contain if the one-photon exchange process, Figure 1.1, were the only process - by the difference in the numbers of events lost to and gained from the rest of the kinematic plane through radiative effects. Specifically this difference can be considered as a sum of two factors. Firstly radiative effects will move some elastic scatters from the $Q^2 = 2M\nu$ line into inelastic bins and secondly they will move inelastic events from bin to bin.

The measured cross-section at the point (α, β) may be written as

$$\frac{d^2\sigma_{\text{meas}}(\alpha,\beta)}{d\alpha d\beta} = \frac{1}{RC_{\text{inel}}(\alpha,\beta)} \frac{d^2\sigma_{\text{inel}}(\alpha,\beta)}{d\alpha d\beta} + \frac{d^2\sigma_{\text{tail}}(\alpha,\beta)}{d\alpha d\beta}$$

where $\sigma_{\text{inel}}(\alpha,\beta)$ is the inelastic cross-section

$\sigma_{\text{tail}}(\alpha,\beta)$ is the cross-section for seeing radiatively degraded elastic events at α,β . This is known as the elastic radiative tail

and $RC_{\text{inel}}(\alpha,\beta)$ is the inelastic radiative correction factor.

The procedure adopted for calculating RC_{inel} and σ_{tail} , and thus obtaining σ_{inel} from σ_{meas} , follows the method of Mo and Tsai⁽⁶¹⁾. It is described in detail in Ref.⁽⁵⁷⁾ and the more important features are presented here.

Given a form for the elastic cross-section - i.e. a form for the elastic form factors - explicit formulae⁽⁶²⁾ exist to calculate the elastic radiative tail. It is found that the most important contribution to the tail comes from the single photon internal bremsstrahlung. Data tables DT2(a) and DT2(b) show the elastic radiative tail cross-sections, $\frac{d^2\sigma_{\text{tail}}}{d\Omega dE'}$, at a series of ν, Q^2 points for the 96 GeV/c and 147 GeV/c data. From these tables any $\frac{d^2\sigma_{\text{tail}}}{d\alpha d\beta}$ may be calculated by interpolation. The elastic radiative tail is only important at low Q^2 and lies in the range 0%-40% of the raw cross-sections. It is estimated that any errors in the elastic radiative tail are less than 5%.

In the continuum region, given a form for the inelastic cross-section, it is relatively easy to calculate the factor $RC_{\text{inel}}(\alpha,\beta)$ and thus obtain estimates of $\left. \frac{d^2\sigma}{d\alpha d\beta} \right|_{\text{meas}}$. Figure 5.9 is a simple illustration of what happens. Region 1 is the data bin of interest. Events will be moved into it by radiative effects from regions A, B and 2. Events move from A into the bin if the scattered muon radiates and move from B into the bin if the incident muon radiates. Region 2 will feed into the bin if both the incident

and scattered muon radiate. In addition some events that would have fallen into the bin will be lost into region C because of radiation by the scattered muon. Two approximations are made when calculating the inelastic radiative corrections. Firstly it is assumed that the emitted photon is radiated along the muon direction - this is called the peaking approximation. Secondly it is assumed the contribution of events into the data bin from region 2 is small and can be ignored. If the "true" cross-sectional form for inelastic scattering and the probability of radiating photons of the appropriate energy is known over the extent of region 1,A and B, then the measured inelastic cross-section for the bin can be calculated by integrating over these regions. RC_{inel} is then simply given by

$$RC_{inel} = \frac{\text{True inelastic cross-section}}{\text{Measured inelastic cross-section}}$$

In practice an iterative procedure is used to construct a table of $RC_{inel}(\nu, Q^2)$ at a set of (ν, Q^2) points. In this an initial "guess" is first made for the form of the inelastic structure functions - this guess is derived from the SLAC data. The inelastic spectrum is then radiatively degraded and RC_{inel} values are calculated. These are used to correct the measured inelastic cross-sections and the corrected data is fitted for the structure functions. The fit so derived is then input back into the program and used to construct another set of RC_{inel} values. The process is repeated until there is no significant difference between the input and output forms of the structure functions. Data tables DT3(a) and DT3(b) are the values of $RC_{inel}(\nu, Q^2)$ so generated for the 96 GeV/c and 147 GeV/c data. These numbers are estimated to be accurate to approximate 2%. Required $RC_{inel}(\alpha, \beta)$ may be calculated from these tables by interpolation.

Looking back to equations 5.1 and 5.3, it is seen that the radiative corrections are lumped into the factor $RC(\alpha, \beta)$ which may be written as

$$RC = \left[1 - \frac{\frac{d^2\sigma_{\text{tail}}}{d\alpha d\beta}}{\frac{d^2\sigma_{\text{meas}}}{d\alpha d\beta}} \right] RC_{\text{inel}}$$

Radiative corrections involve terms containing factors that vary as $\log(m^2)$ where m is the mass of the radiating particle. From this it is seen that the use of muons instead of electrons reduces radiative corrections by a factor of 5 or so.

Resolution Corrections - The factor $RS(\alpha, \beta)$ allows for the fact that the measured (α, β) of an event may be different from the actual (α, β) of an event because of the finite resolution of the apparatus. Again this correction is calculated by first constructing a table of $RS(v, Q^2)$ values at a set of (v, Q^2) points. Any $RS(\alpha, \beta)$ may then be calculated from this table by interpolation.

The quantities used to calculate the v and Q^2 of an event are the incident muon energy, E , the scattered muon energy E' and the muon scattering angle θ . It may be shown that the measurement error on E is less than 0.1% and as such its effect on v and Q^2 is negligible. The effect of the measurement errors of E' and θ on v and Q^2 may be investigated using the muon-electron scatters that exist in the data.

The relationship between a particle momentum p and its angle of bend in the CCM, θ_b , is given by

$$p\theta_b = \text{constant} \quad (\text{see Section 4.D on "Momentum Calibration"})$$

Given this, then

$$\frac{\Delta p}{p} = \frac{\Delta \theta_b}{\theta_b}$$

and furthermore if $\Delta \theta_b$ is assumed to be a constant, then

$$\frac{\Delta p}{p} = kp \text{ where } k \text{ is a constant}$$

Figure 5.10(a) shows the distribution of muon-electron scatters in the 147 GeV/c data as a function of $(E-E'-E_e)$ where E_e is the energy of the electron. The distribution is centred on zero and has a half width of 1.9 GeV. Given the restricted range of muon-electron scatters - i.e. $E' < 50$ GeV and $Q^2 \lesssim 0.15$ (GeV/c)² - it is seen that this width is dominated by the error on E_e . For a 147 GeV/c incident beam the average E_e is approximately 115 GeV. Using this number, it is seen that k is approximately 1.44×10^{-4} if p is in GeV/c. This corresponds to $\Delta \theta_b = 0.32$ mr. The major contribution to $\Delta \theta_b$ comes from the particle trajectory as it enters the CCM and the above figure agrees well with the angular error expected from this track.

Figure 5.10(b) shows the distribution of muon-electron scatters as a function of $(Q^2 - 2m_e v)$. Again the distribution is centred on zero. It has a half-width of 0.014 (GeV/c)² which comes almost entirely from the error in Q^2 . ΔQ^2 may be written as

$$Q^2 = 2EE' \sin \theta \quad \Delta \theta \quad \text{from which } \Delta \theta \text{ is calculated}$$

to be 0.35 mr - the scattering angle is calculated from the muon track upstream of the CCM. If $\Delta \theta$ is assumed constant over the range of Q^2 , it is seen that the error in Q^2 is small and can be neglected in the calculation of the resolution correction.

From the above study of muon-electron scatters, it is seen that to a good approximation only the measurement errors of the scattered muon momenta affect the resolution correction - this is why the correction is also known as the (momentum) smearing correction. If the "true" cross-sectional form is known then the smeared cross-section is given by

$$\left. \frac{d^2\sigma}{d\alpha d\beta} \right|_{\text{smeared}} = \iint \frac{d^2\sigma}{d\alpha' d\beta'} P(\alpha, \alpha'; \beta, \beta') d\alpha' d\beta'$$

where $P(\alpha, \alpha'; \beta, \beta')$ is the probability that the point (α', β') will be considered as (α, β) because of the apparatus resolution. (P depends only on ν).

Then $RS(\alpha, \beta)$ is given by

$$RS(\alpha, \beta) = \frac{\left. \frac{d^2\sigma}{d\alpha d\beta} \right|_{\text{true}}}{\left. \frac{d^2\sigma}{d\alpha d\beta} \right|_{\text{smeared}}}$$

In practice a table of $RS(\nu, Q^2)$ values is constructed for a set of (ν, Q^2) bins. Various input cross-sections were tried and it is found that RS is not very model dependent in the deep inelastic region. Any $RS(\alpha, \beta)$ may be obtained from the table by interpolation.

It is found that the smearing correction only affects the kinematic region $\nu < 20$ GeV. Its maximum effect on the data is approximately 20% and it is estimated that any systematic errors arising from this correction are less than 1%. The region $\nu < 5$ GeV is cut because of poor resolution. Data tables DT4(a) and DT4(b) show the values of $RS(\nu, Q^2)$ for the 96 GeV/c and 147 GeV/c datasets.

5.D RESULTS AND COMMENTS

Having calculated all the various correction and efficiency factors, equation 5.3 may be used to calculate the various physical quantities of interest. If the quantity of interest is $F(\alpha, \beta)$ and its relationship to the cross-section $\frac{d^2\sigma}{d\alpha d\beta}$ can be written as

$$\frac{d^2\sigma}{d\alpha d\beta} = D(\alpha, \beta) F(\alpha, \beta); \quad \text{where } D(\alpha, \beta) \text{ is a known kinematic factor}$$

then equation 5.3 is transformed into

$$\langle F(\alpha, \beta) \rangle_{\Delta\alpha, \Delta\beta} = \frac{W_{\Delta\alpha, \Delta\beta}}{L\epsilon \int_{\alpha_1}^{\alpha_2} \int_{\beta_1}^{\beta_2} [d\alpha d\beta \frac{D(\alpha, \beta)}{RC(\alpha, \beta) RS(\alpha, \beta)}]}$$

where $\langle F(\alpha, \beta) \rangle_{\Delta\alpha, \Delta\beta}$ is the average value of $F(\alpha, \beta)$ in the bin $\Delta\alpha, \Delta\beta$

Furthermore the value of $F(\alpha, \beta)$ at any point α_0, β_0 in the bin may be written as

$$F(\alpha_0, \beta_0) = \frac{W_{\Delta\alpha, \Delta\beta}}{L\epsilon \int_{\alpha_1}^{\alpha_2} \int_{\beta_1}^{\beta_2} \left[d\alpha d\beta \frac{F(\alpha, \beta)}{F(\alpha_0, \beta_0)} \frac{D(\alpha, \beta)}{RC(\alpha, \beta) RS(\alpha, \beta)} \right]}$$

Providing the function $F(\alpha, \beta)$ is reasonably well behaved, this formula forms the basis of an iterative method of generating values of $F(\alpha_0, \beta_0)$ and is used to calculate bin-centred values of F . The calculation of the integrals is effected by using the standard Gaussian quadrature technique. This section presents the results from the analyses for three physical quantities, namely the muon inclusive cross-section $\frac{d^2\sigma}{d\nu dq^2}$, the inelastic structure function νW_2 and the total virtual photoabsorption cross-section.

Muon Inclusive Cross-Section - To obtain average values of $\frac{d^2\sigma}{d\nu dq^2}$, it is apparent that the binning is carried out in ν and Q^2 and that the factor $D(\nu, Q^2)$ in this case is 1. The data for the analysis for $\frac{d^2\sigma}{d\nu dq^2}$ is presented in Data Tables DT5(a)-(d) and DT6(a)-(d) for the 96 GeV/c and 147 GeV/c datasets respectively. The contents of the four separate tables in each set are:

- (a) the raw events seen for the target full and target empty data
- (b) the weighted events, $W_{\Delta\nu, \Delta Q^2}$
- (c) the weighted events after the subtraction of the elastic radiative tail
- (d) the average inclusive cross-sections in picobarns per (GeV)³

The formula for the inclusive cross-section $\frac{d^2\sigma}{d\nu dq^2}$ can be written as

$$\frac{d^2\sigma}{d\nu dq^2} = \frac{2\pi\alpha^2}{E^2} \frac{1}{Q^4} \frac{1}{\nu} \left[2EE' - \frac{Q^2}{2} + \frac{(Q^2 - 2m_\mu^2)(\nu^2 + Q^2)}{Q^2(1+R)} \right] \nu W_2$$

Figure 5.11 shows the variation of $\frac{d^2\sigma}{d\nu dq^2}$ vs. Q^2 at fixed ν and from this it is seen that the major Q^2 dependence of the cross-section comes from the $\frac{1}{Q^4}$ term. Figure 5.12 shows the variation of $\frac{d^2\sigma}{d\nu dq^2}$ vs. ν at fixed Q^2 .

Inelastic Structure Function νW_2 - As will be seen later in this section, the values of R are not determined well enough to enable a complete separation of the two inelastic structure functions, $2MW_1$ and νW_2 , to be carried out. This analysis looks at the extraction of $\nu W_2(\omega, Q^2)$ assuming a value of $R = 0.18$. One may comment that data from this experiment is relatively insensitive to the choice

of the scaling variable - ω , ω' , $\xi^{(31)}$ etc. The data for this analysis is presented in Data Tables DT7(a)-(f) and DT8(a)-(f) for the 96 GeV/c and 147 GeV/c datasets respectively. The contents of the six tables in each set are

- (a) the target full events, $N_{\Delta\omega, \Delta Q^2}$
- (b) the weighted events, $W_{\Delta\omega, \Delta Q^2}$
- (c) the weighted events after the subtraction of the elastic radiative tail
- (d) νW_2 before the inelastic radiative corrections and momentum smearing (bin centred values)
- (e) final values of νW_2 after all corrections (bin centred values)
- (f) average values of the inclusive muon cross-section $\frac{d^2\sigma}{d\omega dq^2}$ in picobarns per $(\text{GeV})^2$

The values of νW_2 are plotted in Figure 5.13-5.17. Figure 5.13 is a plot of νW_2 averaged over all Q^2 as a function of ω for both the 96 GeV/c and 147 GeV/c datasets - the differences between the two datasets reflect the different Q^2 extents of the two sets of data. Figure 5.14 shows the values of νW_2 as a function of Q^2 for various ω bands for the 96 GeV/c data. Figure 5.15 is the equivalent plot for the 147 GeV/c data. The consistency of νW_2 between the two datasets is checked and gives a $\chi^2 = 188.4$ for 185 degree of freedom, a variance ratio of 1.02. Figures 5.16 and 5.17 plot the values of νW_2 obtained by combining the two datasets. Figure 5.16 shows the values of νW_2 vs. Q^2 for various bands of ω . In addition the separated values of νW_2 obtained by the SLAC-MIT group⁽¹⁴⁾ are also plotted in this figure. Finally, Figure 5.17 plots the combined values of νW_2 as a function of ω for various bands of Q^2 . Only the statistical errors are quoted in the tables and

drawings. If the possible systematic errors on the corrections ϵ , A, RC and the background subtraction combine in the worst possible way, this leads to a systematic error of approximately 8% in all the values of νW_2 . Furthermore for $\omega < 15$ there is a further possible systematic error of 6% because of uncertainties arising from the track finding efficiency and smearing corrections at low ν . The systematic error arising from the possible contamination of the data from muon-electron scatters only affects the $\omega > 500$ bins. The immediate observation from the plots shown in Figure 5.13 and 5.17 are firstly that this experiment agrees with SLAC in the regions of overlap, secondly that, although gross scaling holds, violations of scaling are seen and that νW_2 rises with Q^2 at high ω , and lastly that there is insufficient data to make any positive statement about the fall of νW_2 with Q^2 at small ω .

Scaling violations may be investigated by calculating the quantity

$$B = \frac{\partial(\log F_2(x, Q^2))}{\partial(\log Q^2)}$$

as a function of x ($F_2 = \nu W_2$). Figure 5.18 shows the variation of B with x for data from this experiment and from the SLAC-MIT group. Three functional forms are drawn on the plot. The first, $B = 0.12 \log(1/6x)$, is favoured by the other muon scattering experiment at Fermilab⁽¹⁷⁾ and the second is derived from a field theoretical model of Parisi and Petronzio⁽⁶³⁾. It is seen that the $B = 0.12 \log(1/6x)$ form does not do very well at large x . Furthermore one may comment that a simple straight line, $B = 0.66 (0.25-x)$, does as well as any other functional form.

Figure 5.19 compares the values of νW_2 from this experiment and from the SLAC group A⁽⁶⁶⁾ with prediction of the generalised vector meson dominance theory. Two curves are drawn through the data, the first derived from Greco⁽⁶⁴⁾ and the second, which explicitly uses the ψ vector meson, from Close, Scott and Sivers⁽⁶⁵⁾. It is seen that at high ω , the data fits the second curve tolerably well.

Total Virtual Photoabsorption Cross-section and R - The last analysis presented is the extraction of the total virtual photoabsorption cross-section, $\sigma = \sigma_T + \epsilon\sigma_L$ as a function of W^2 and Q^2 . The data is contained in Data Tables DT9(a)-(d) and DT10(a)-(d) for the 96 GeV/c and 147 GeV/c datasets respectively. The contents of the four tables in each set are

- (a) the weighted events $W_{\Delta W^2 \Delta Q^2}$
- (b) the weighted events after the subtraction of the elastic radiative tail
- (c) the total virtual photoabsorption cross-sections before the inelastic radiative corrections and momentum smearing.
- (d) the total virtual photoabsorption cross-sections after all the corrections have been applied.

Figure 5.20 shows the variation of σ vs. Q^2 at fixed W^2 and it is seen that σ falls as a power of Q^2 . Figure 5.21 shows plots of σ vs. W^2 for fixed Q^2 . The variation of σ with W^2 is flat or possibly falling slightly except in the lowest Q^2 bins plotted.

As was discussed in Chapter 1, the values of σ in the same (W^2, Q^2) bins for the two incident energies may be used to extract values of R . Figures 5.22 show plots of $\sigma = \sigma_T + \epsilon \sigma_L$ vs. ϵ for various data bins in two bands of W^2 . In these plots the slope of the straight line gives σ_L and the intercept at $\epsilon = 0$ gives σ_T . It is readily seen how difficult it is to obtain accurate values of R on a bin-by-bin basis. The results for σ_L , σ_T and R in the three W^2 bands in which the difference between ϵ (96 GeV/c) and ϵ (147 GeV/c) is greater than 0.1 are tabulated in Table 5.1 - it may easily be shown that ϵ varies with W^2 and is essentially constant as a function of Q^2 . The data suggests an average value of $R = 0.07 \pm 0.34$ for the kinematic region $64 \text{ (GeV)}^2 < W^2 < 144 \text{ (GeV)}^2$; $1 \text{ (GeV/c)}^2 < Q^2 < 4 \text{ (GeV/c)}^2$.

Fits to the Data - In an attempt to obtain better estimates of R , a program was written to fit the data to various functional forms of νW_2 and R . The principle of this program is quite straightforward, namely that the functional forms of νW_2 and R are used to calculate the number of raw events expected in the various data bins. The quantity

$$\chi^2 = \sum_{\text{bins}} \frac{(\text{measured events} - \text{expected events})^2}{(\text{error in measured events})^2}$$

is calculated. The parameters of the input functions are then varied in an attempt to minimise χ^2 . This method has the additional advantage that systematic effects may be studied by varying the magnitudes of the various corrections.

Two fits to the data are described here, i.e.

$$(1) \quad \nu W_2 = [a_1(1-x)^3 + a_2(1-x)^4 + a_3(1-x)^5] (1 + a_4 \log \frac{Q^2}{3} \log \frac{\omega}{6})$$

$$R = a_5$$

$$(2) \quad \nu W_2 = [a_1(1-x)^3 + a_2(1-x)^4 + a_3(1-x)^5](1+a_4(0.25-x) \log \frac{Q^2}{a_5})$$

$$R = a_6$$

where the a 's are the fitting parameters.

In the first the form for νW_2 is suggested by asymptotically free gauge theories and is used by Chang et al⁽¹⁷⁾. The second form of νW_2 is chosen because it fits the SLAC-MIT data⁽¹⁴⁾ very well, see Figure 5.18. The results from these fits are tabulated in Table 5.2 and the more important features are listed here.

- (1) A cut of $Q^2 > 1.0 \text{ (GeV/c)}^2$ gives much better fits to the data - i.e. better variance ratios - than when all the data is used. This is because there is little overlap in the (ν, Q^2) plane between the two datasets for $Q^2 < 1.0 \text{ (GeV/c)}^2$ and because a possible muon-electron contamination of the data in the low Q^2 , high ν region in the 147 GeV/c data. In addition the $Q^2 < 1.0 \text{ (GeV/c)}^2$ kinematic region is the turn-on of scaling region and the above forms of νW_2 are bad fits to the data in this region.
- (2) The correlations between the coefficients of the $(1-x)^n$ terms is high.
- (3) The correlations between R and the scaling violation parameter a_4 are small.
- (4) For fit 1; $R = 0.15 \pm 0.08$, $a_4 = 0.049 \pm 0.002$
All the data variance ratio = 1.034 per degree of freedom
For fit 1; $R = 0.21 \pm 0.12$, $a_4 = 0.061 \pm 0.015$
 $Q^2 > 1.0 \text{ (GeV/c)}^2$ variance ratio = 0.649 per degree of freedom
data

In both these cases the systematic errors for R are estimated to be approximately ± 0.05 .

(5) For fit 2; $R = 0.51 \pm 0.14$, $a_4 = 0.72 \pm 0.24$
 All the data variance ratio = 0.868 per degree of
 freedom

For fit 2; $R = 0.38 \pm 0.16$, $a_4 = 0.61 \pm 0.20$
 $Q^2 > 1.0 \text{ (GeV/c)}^2$ variance ratio = 0.630 per degree of
 data. freedom

In these cases, the systematic errors for R are estimated
 to be approximately ± 0.08 .

Attempts were made to fit the data for varying functional
 forms for $R^{(14)}$ - various theories suggest $1/Q^2^{(67)}$ or $1/\log Q^2^{(68)}$
 dependences. These fits however suffer from the fact that most of
 the data lies in a limited region of Q^2 and could not be made to
 converge in a sensible manner.

Callan-Gross Sum Rule - Once the data has been fitted for $F_2 = \nu W_2$,
 the values of the $\int F_2 dx$ may be evaluated in various ranges of x and
 Q^2 . In parton models, the integral gives the mean of the squares
 of the parton charges. The results for the integrations are presented
 in Table 5.3. These calculations also include earlier hydrogen data⁽⁵⁴⁾
 from this experiment as well as the SLAC-MIT data and R is set equal
 to 0.18. The form for F_2 used for the fits is

$$F_2 = \left[\sum_{i=1}^n a_i (1-x)^{i+2} \right] \left(1 + b_1 (0.25-x) \log \frac{Q^2}{3} \right)$$

Fits for both $n = 3$ and $n = 4$ are tried and the effects of changing
 the normalisation of this experiment with respect to the SLAC-MIT
 data are investigated.

Table 5.3 may be divided into two parts. First the results
 for the integral from $x = 0$ to $x = 1$ for various bands of Q^2 is
 presented using data from both this experiment and SLAC-MIT group.
 It is seen that the integral is essentially flat as a function of

Q^2 and has a value in the range 0.16-0.19 as compared with 0.33 for a naive three quark model. In addition one can comment that raising the normalisation of this experiment by 5% improves the fits for $Q^2 > 2.0 \text{ (GeV/c)}^2$. The second part of the table evaluates the contribution of the data from this experiment alone to the integral. This contribution is seen to increase with increasing Q^2 and the integral for $0.0 < x < 0.25$ lies in the range 0.06-0.10.

Conclusions - The conclusions drawn from this experiment may be listed as follows:

1. Scaling violations are seen and the inelastic structure function, νW_2 , increases with increasing Q^2 for large ω .
2. The value of R remains small - as in the previous electron experiments - in the extended kinematic region of this experiment although unfortunately there is insufficient data to investigate its variation with the kinematic variables.
3. The Callan-Gross sum rule integral is in the range 0.16-0.19 which suggests that in parton models roughly 50% of the proton momentum is carried by partons and that this fraction does not vary with Q^2 .

In view of these observations, it will be extremely interesting to see the results from the second generation of high energy muon experiments, especially at CERN, which promise greatly improved statistics with which to extract accurate values of R and the inelastic structure functions.

CIRCLES OF CONSTANT V, Q^2 AT THE MUON HODOSCOPE FOR AN INCIDENT ENERGY OF 96 GeV/c (V 's IN GeV AND Q^2 's (GeV/c)²)

FIG. 5.1(a)

$Q^2 = 1.0$

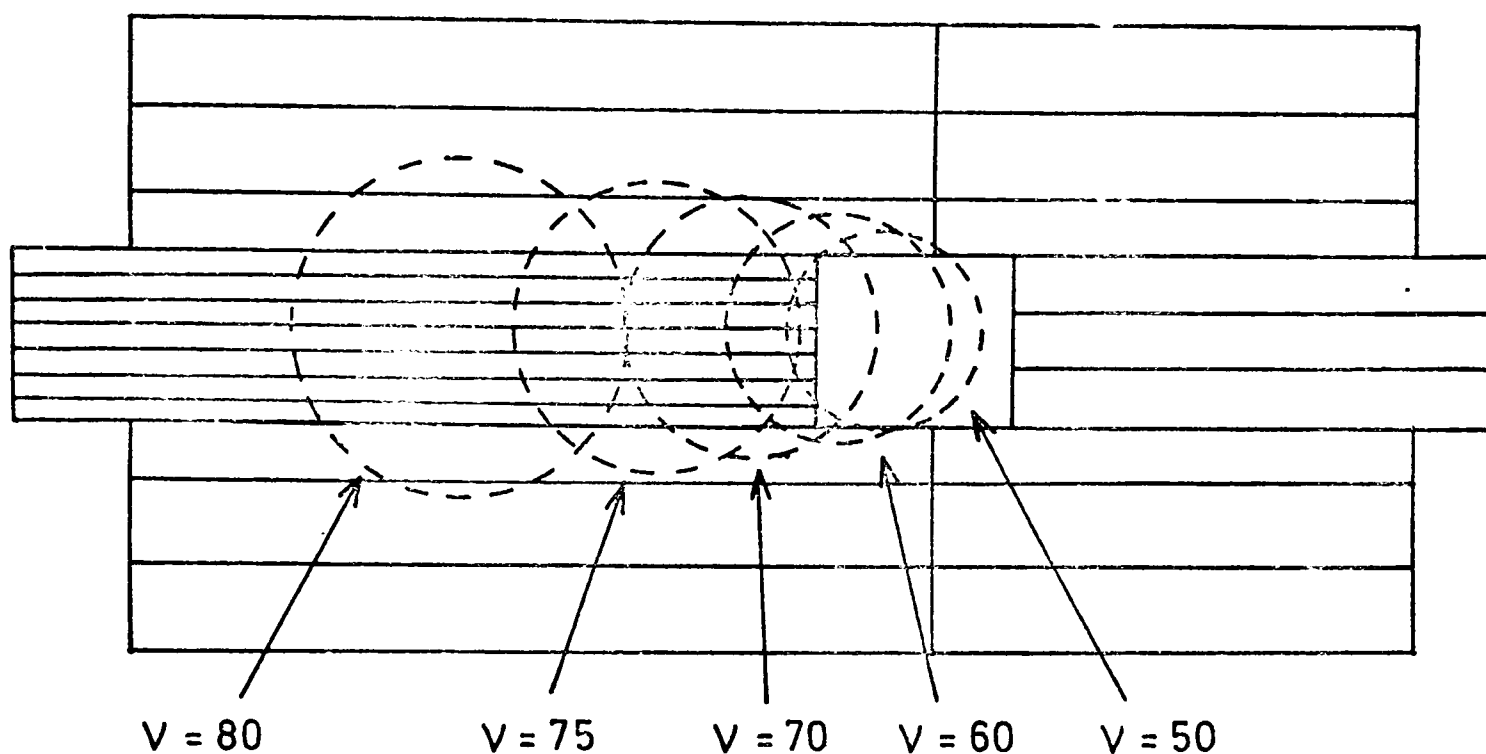


FIG. 5.1(b)

$Q^2 = 2.0$

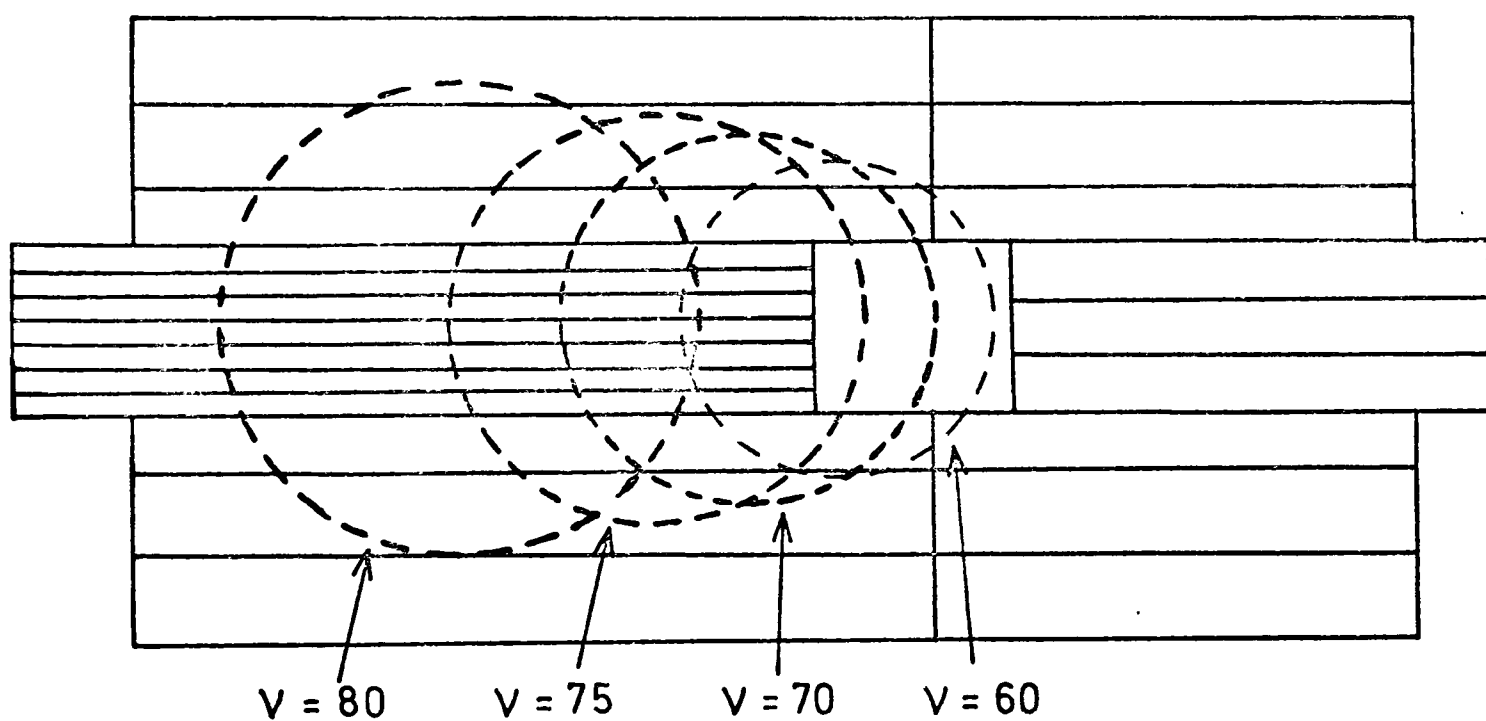
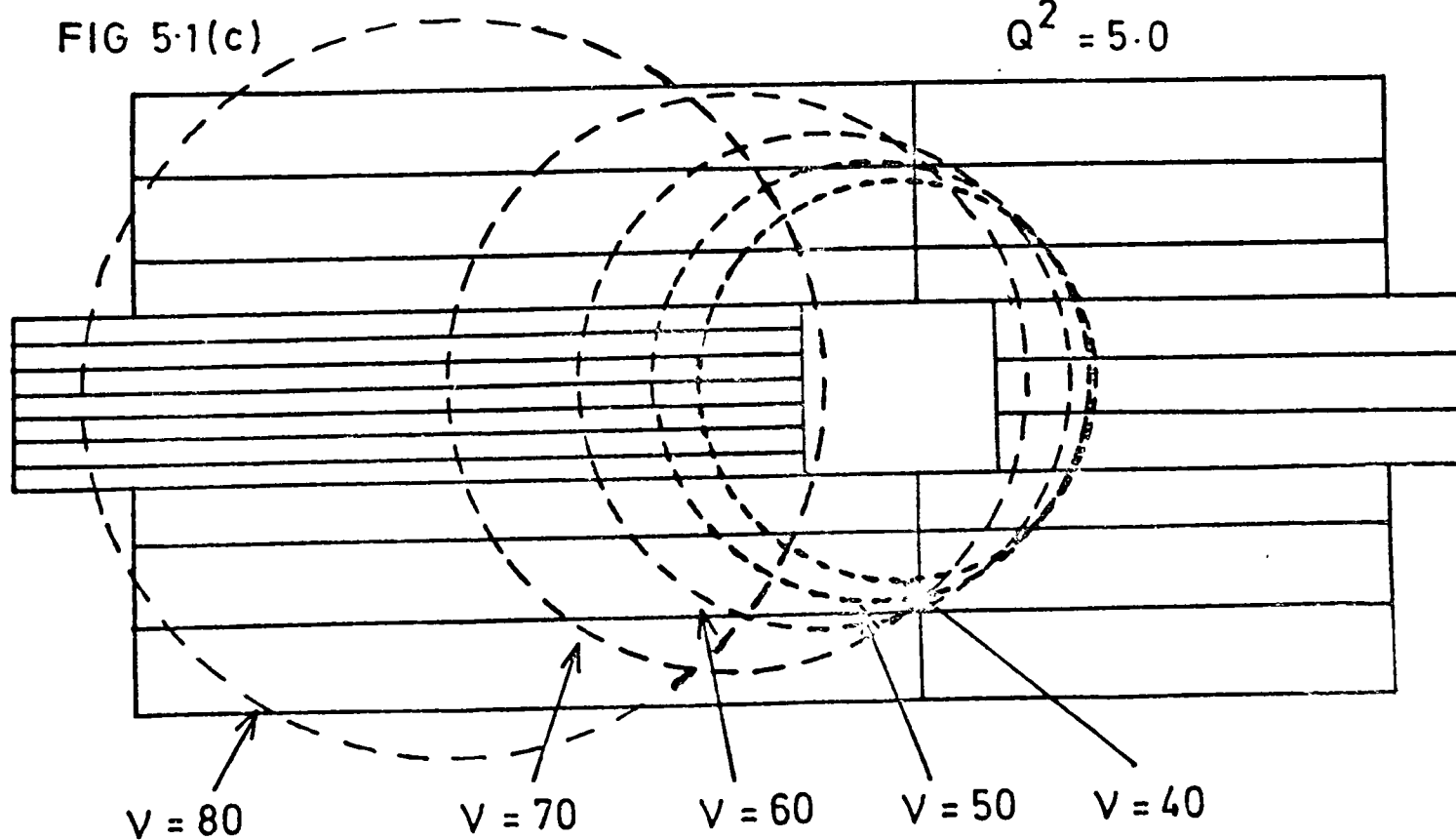


FIG 5.1(c)

$Q^2 = 5.0$



CIRCLES OF CONSTANT ν , Q^2 AT THE MUON HODOSCOPE FOR AN
INCIDENT ENERGY OF 96 GeV/c (ν 's IN GeV AND Q^2 's IN (GeV/c)²)

FIG. 5.1(d)

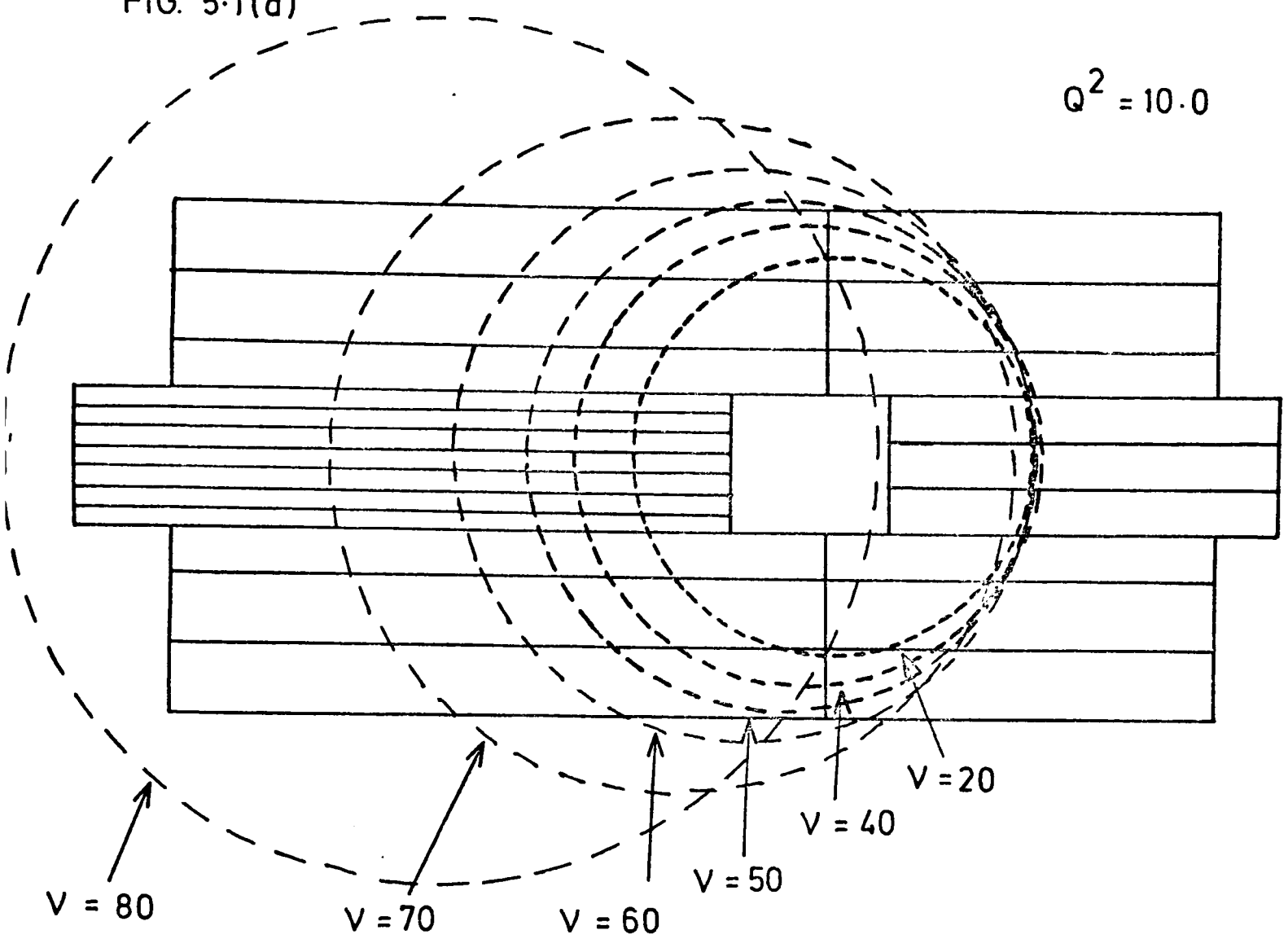
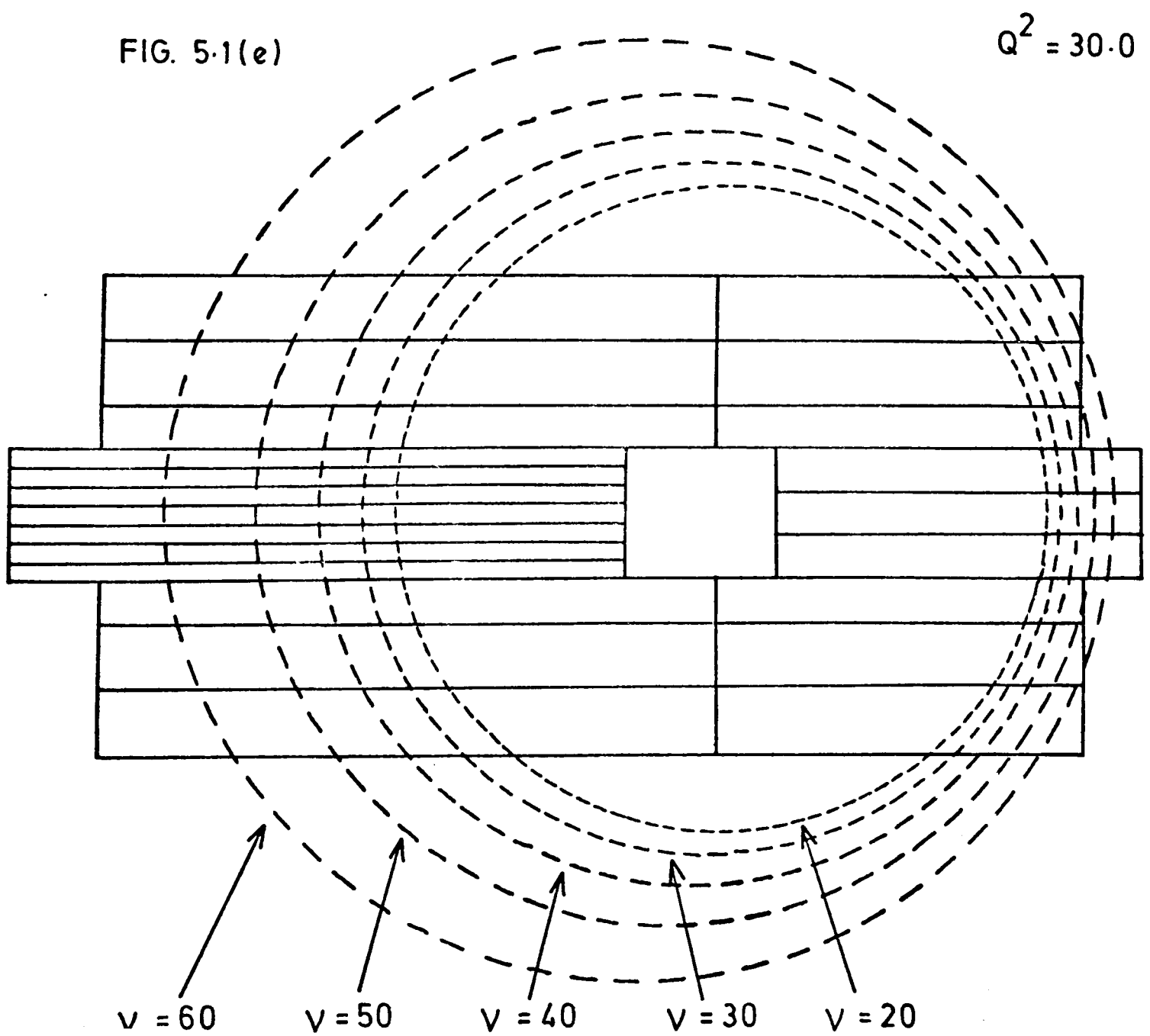


FIG. 5.1(e)



CIRCLES OF CONSTANT ν, Q^2 AT THE MUON HODOSCOPE FOR AN INCIDENT ENERGY OF 147 GeV/c (ν 's IN GeV AND Q^2 's IN $(\text{GeV}/c)^2$)

FIG. 5.2 (a)

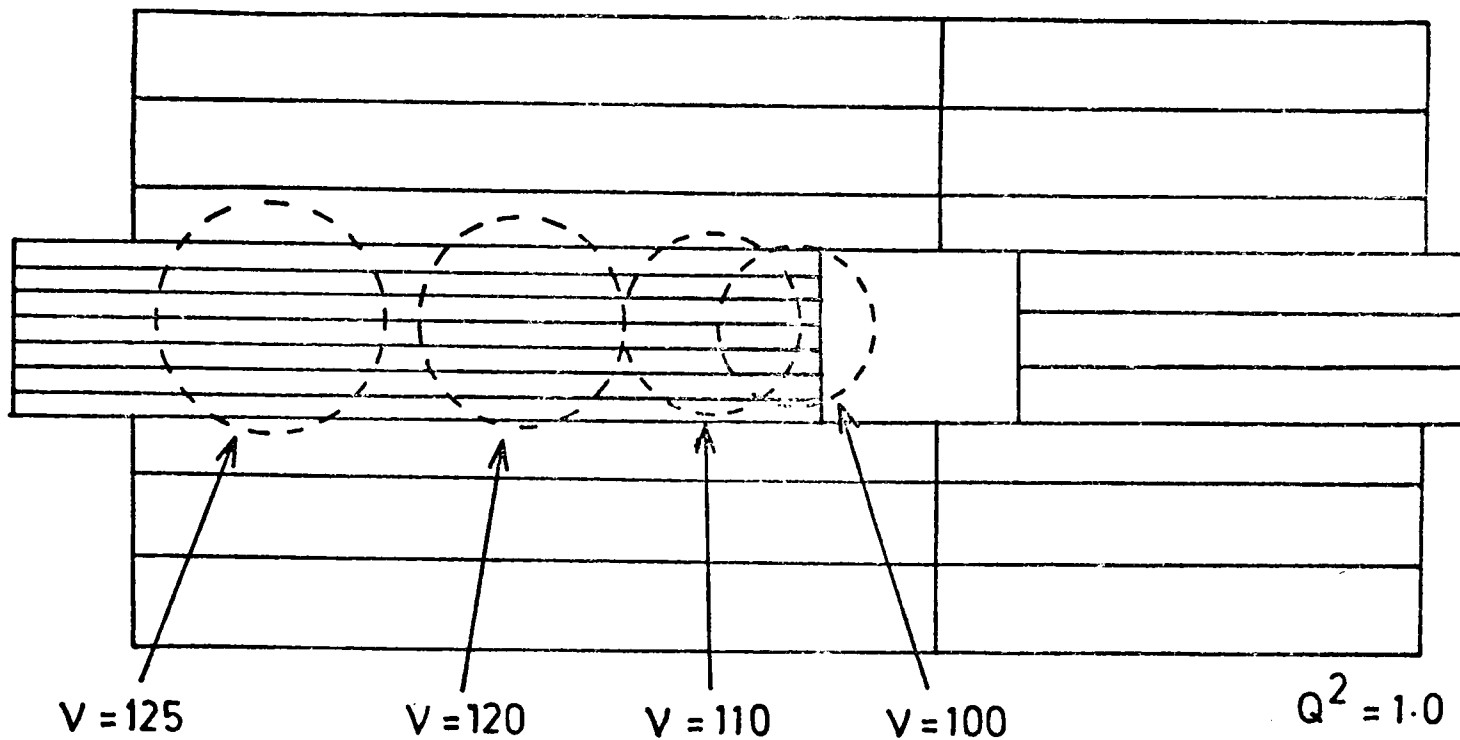


FIG. 5.2 (b)

$Q^2 = 2.0$

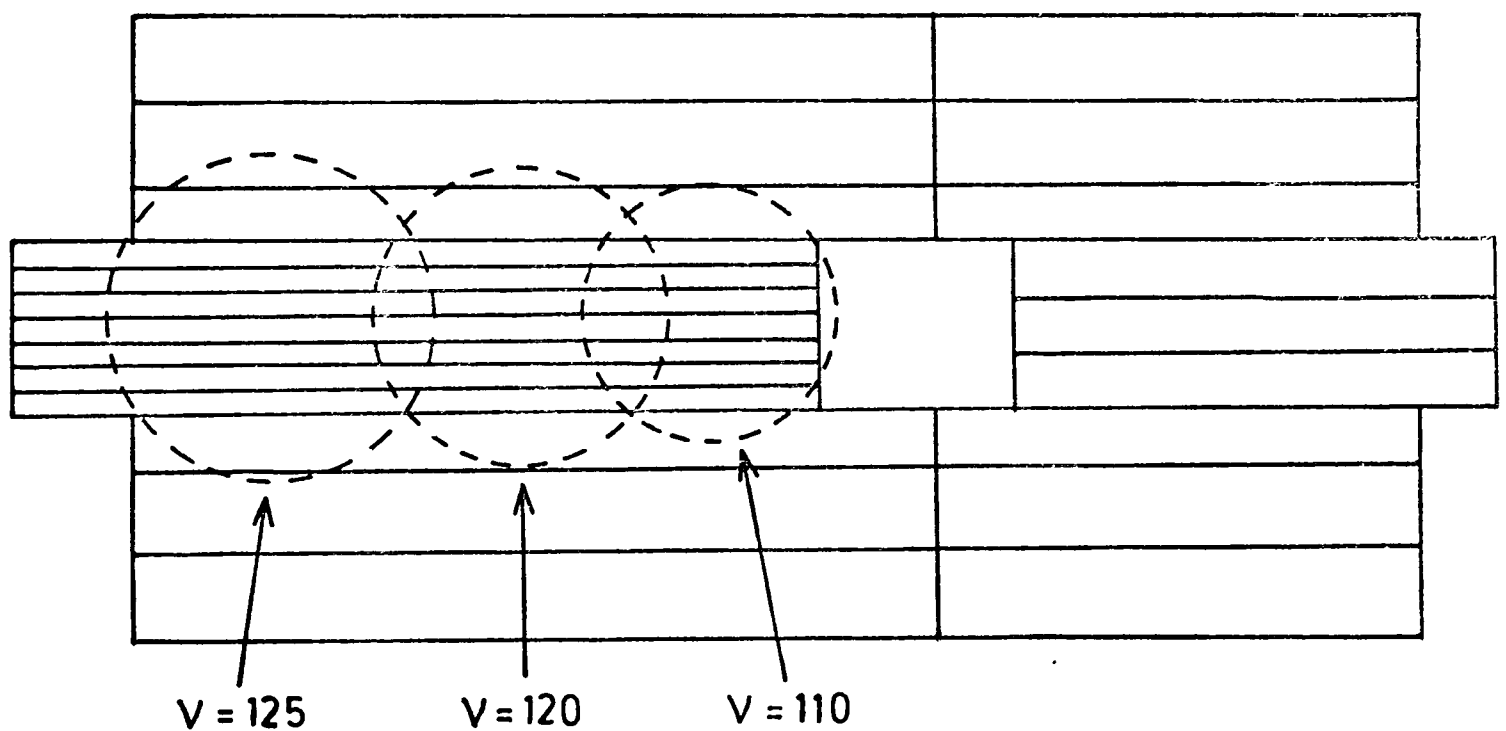
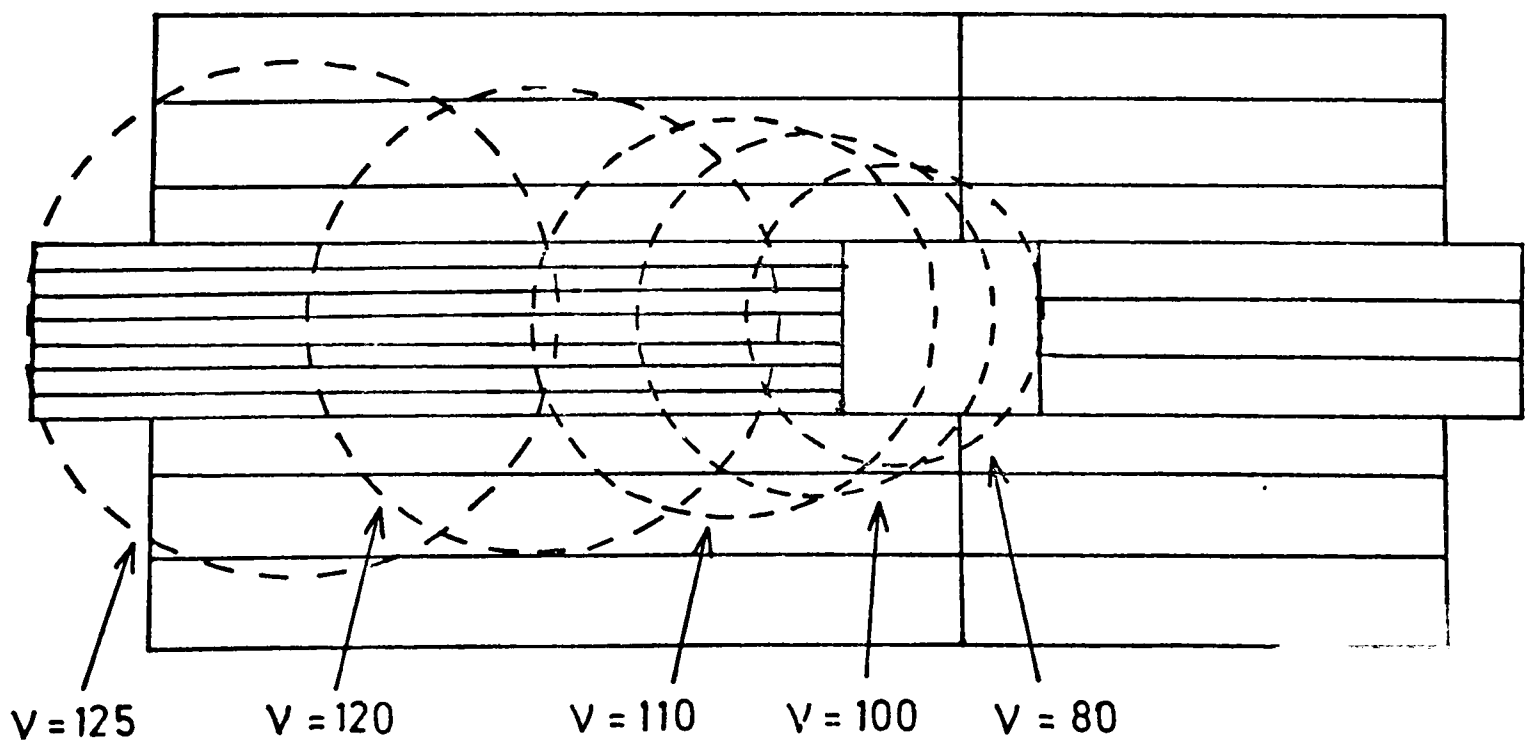


FIG. 5.2 (c)

$Q^2 = 3.0$



CIRCLES OF CONSTANT ν , Q^2 AT THE MUON HODOSCOPE FOR AN INCIDENT ENERGY OF 147 GeV/c (ν 's IN GeV AND Q^2 's IN (GeV/c)²)

FIG. 5-2(d)

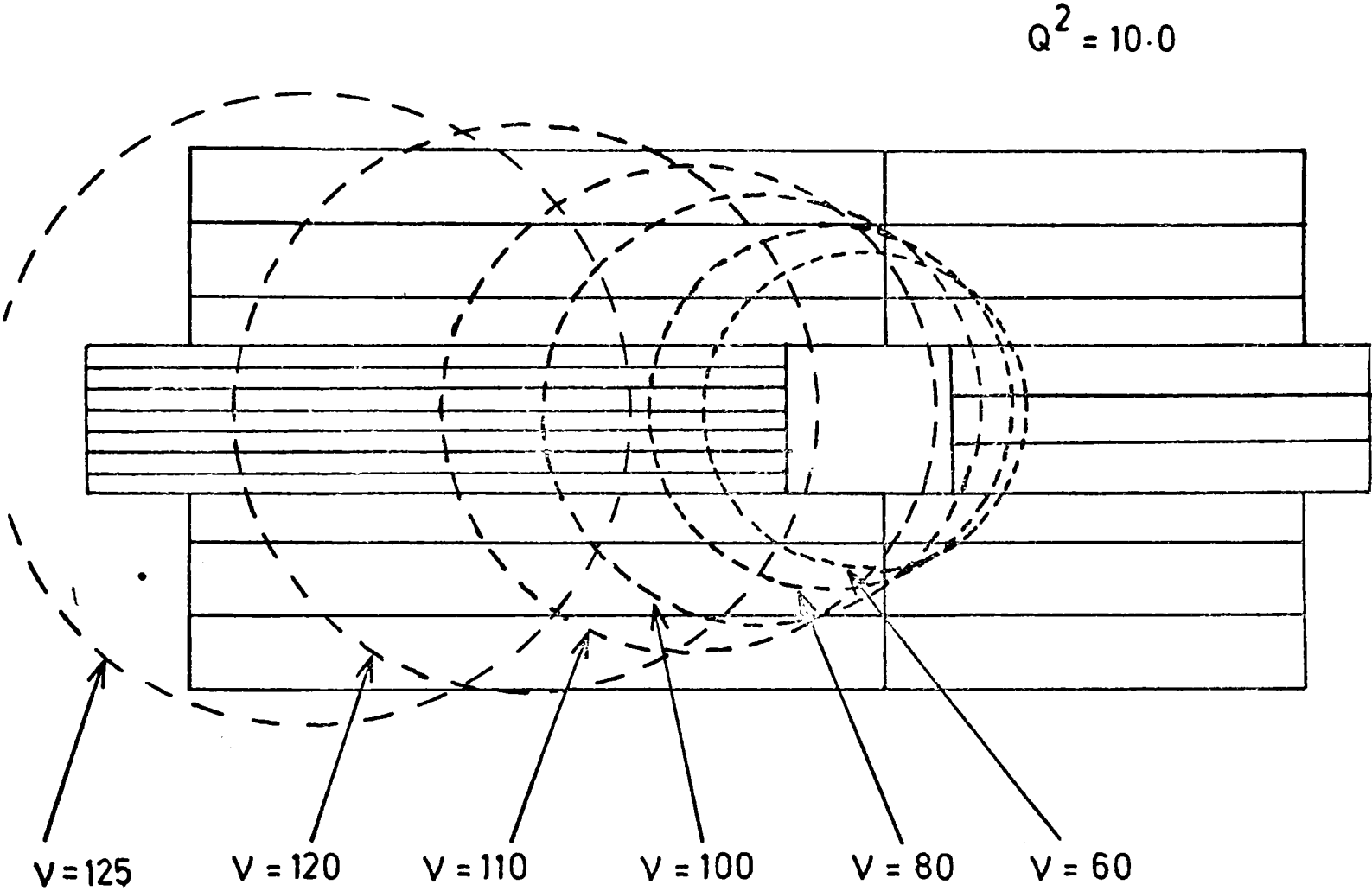


FIG. 5-2(e)

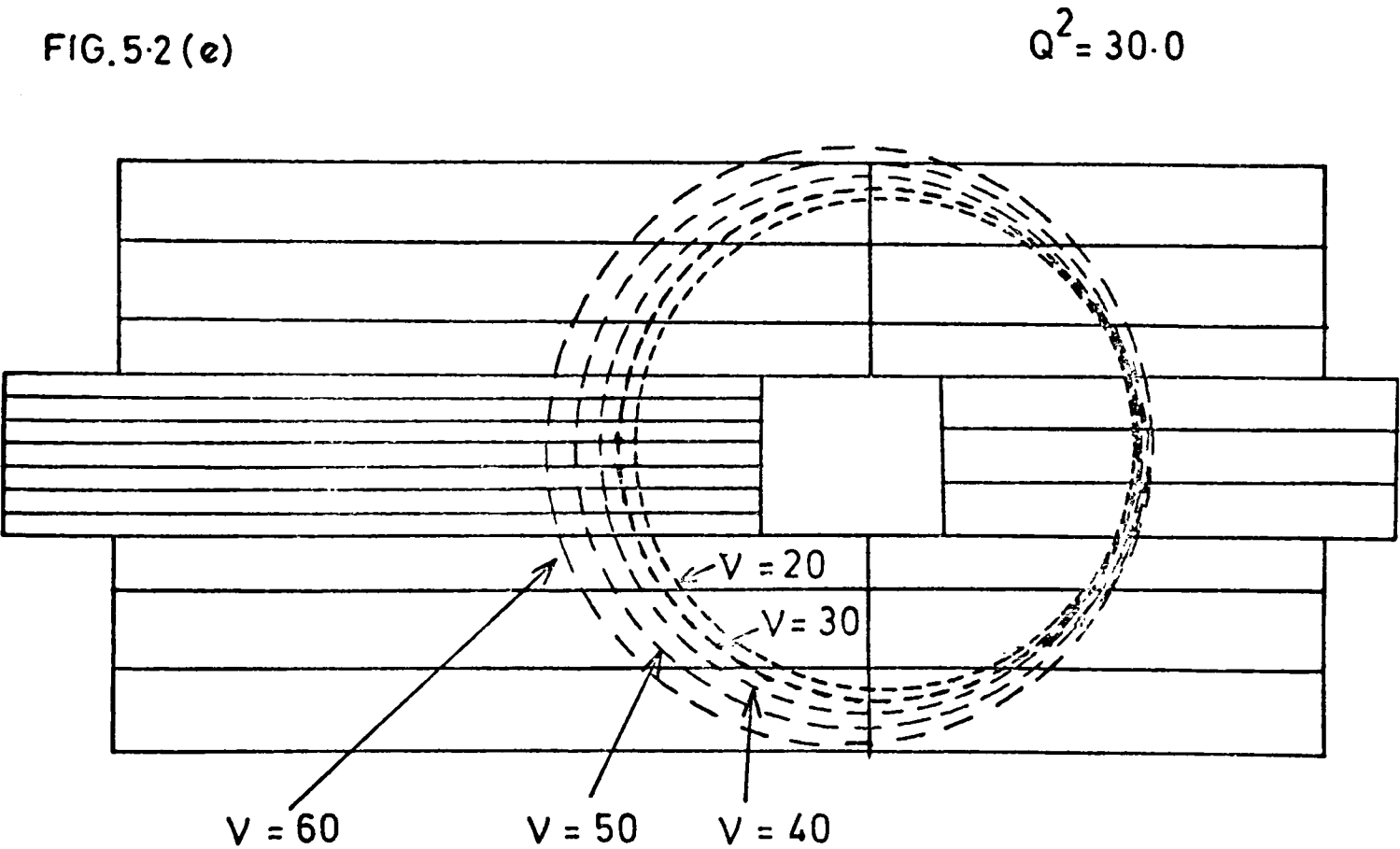
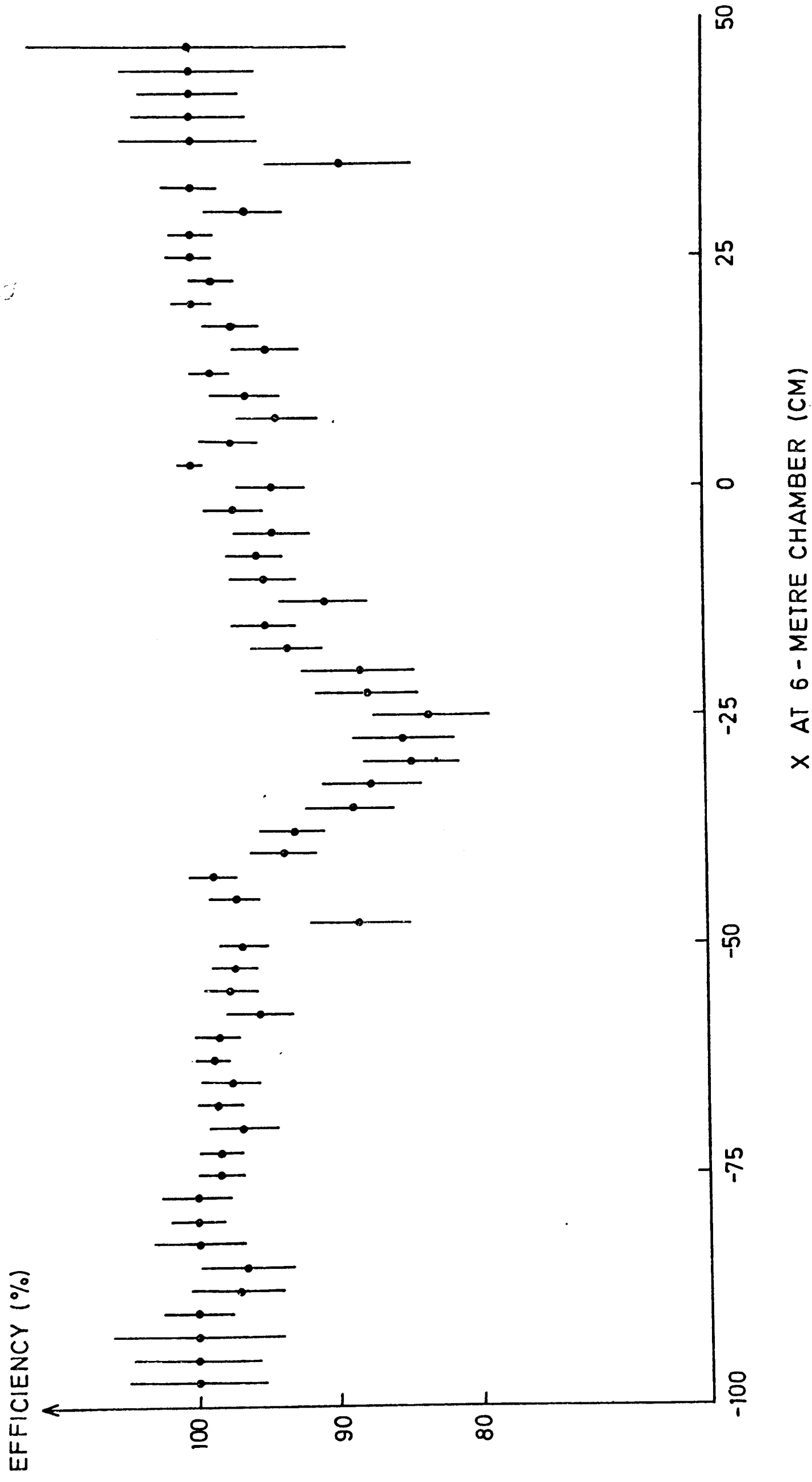


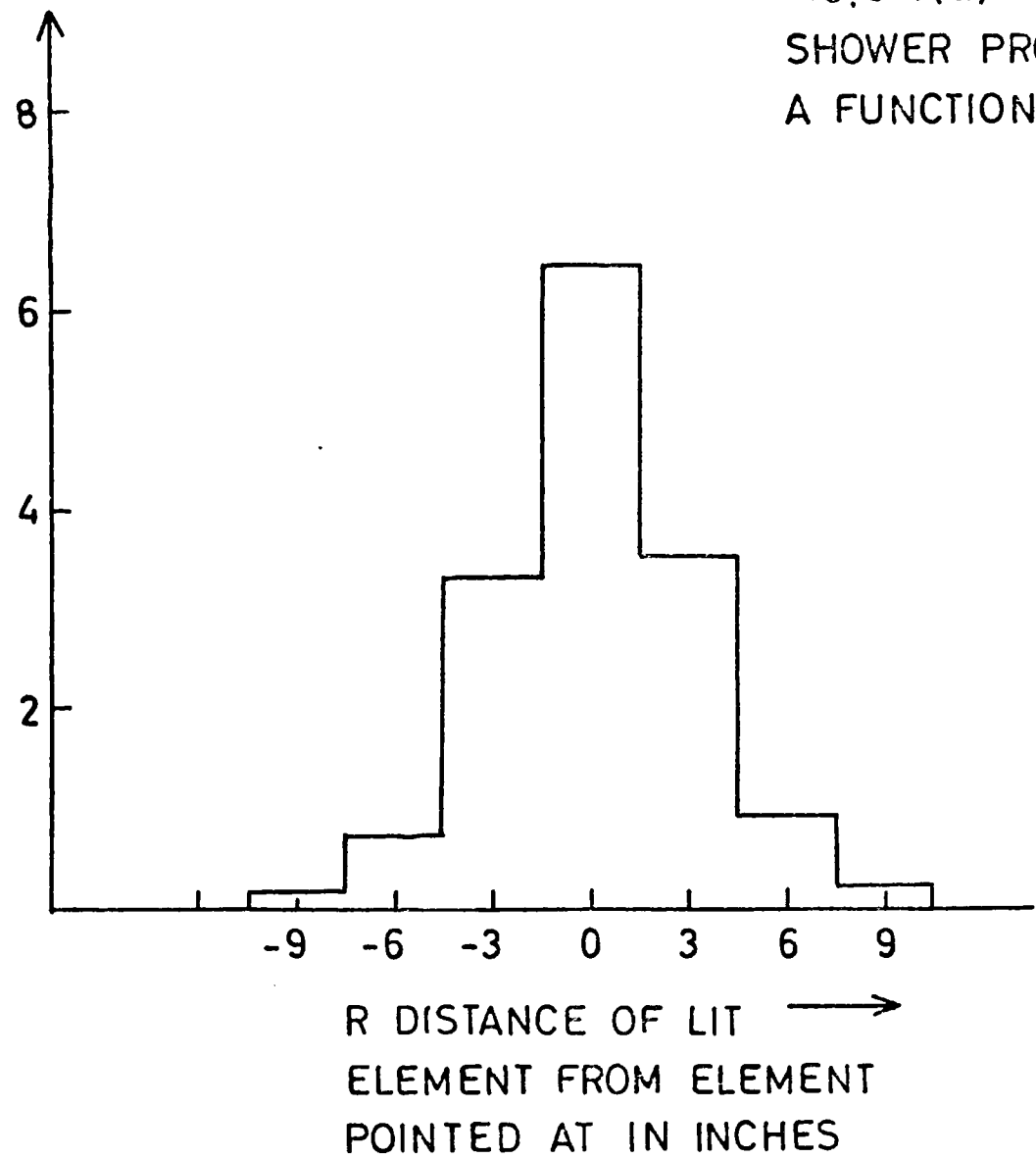
FIG. 5.3

TRACK - FINDING EFFICIENCY IN THE BEAM REGION OF THE D/S CHAMBERS



K-VETO SHOWERING CORRECTION (147 GeV/c DATA).

$P(R)dR$ %



SHOWER
VETO
PROBABILITY
 $Q(R)$

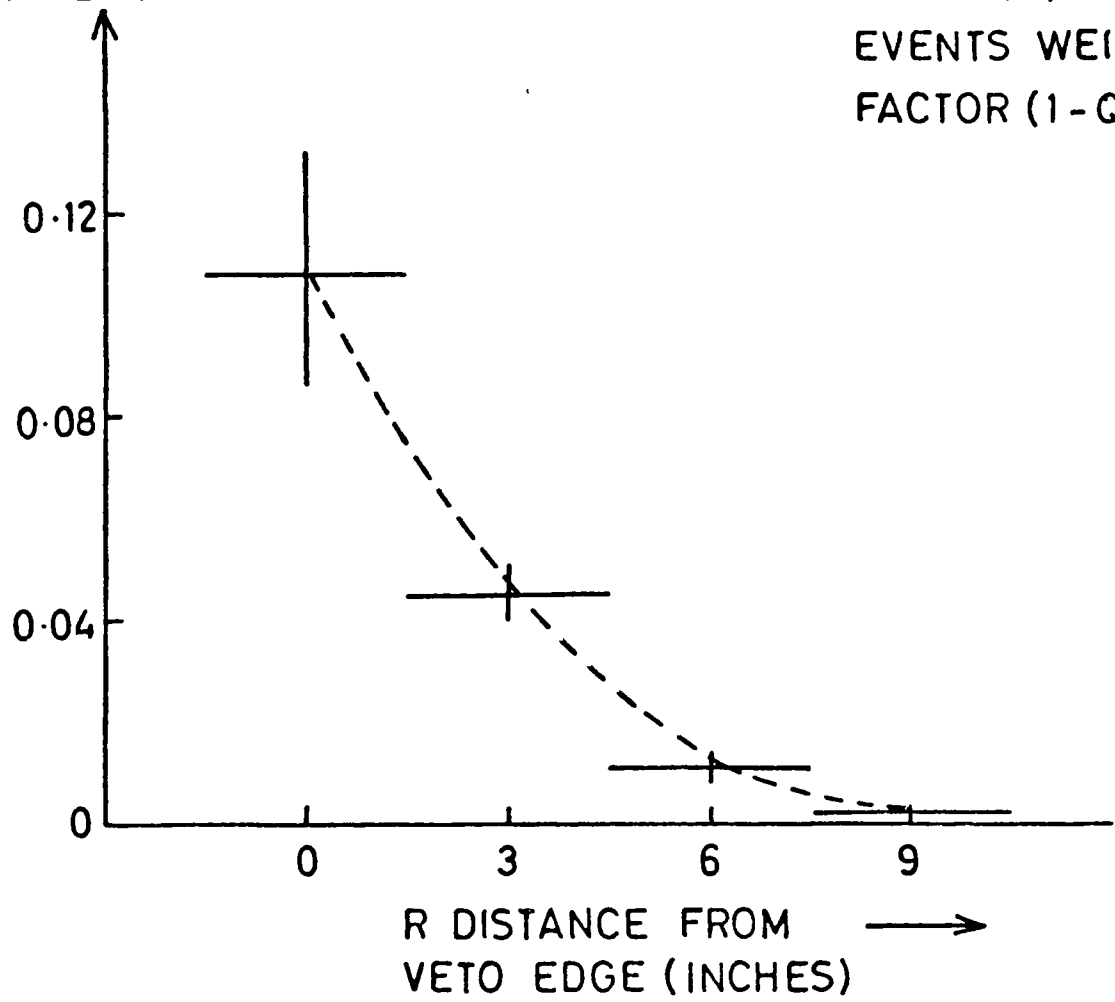
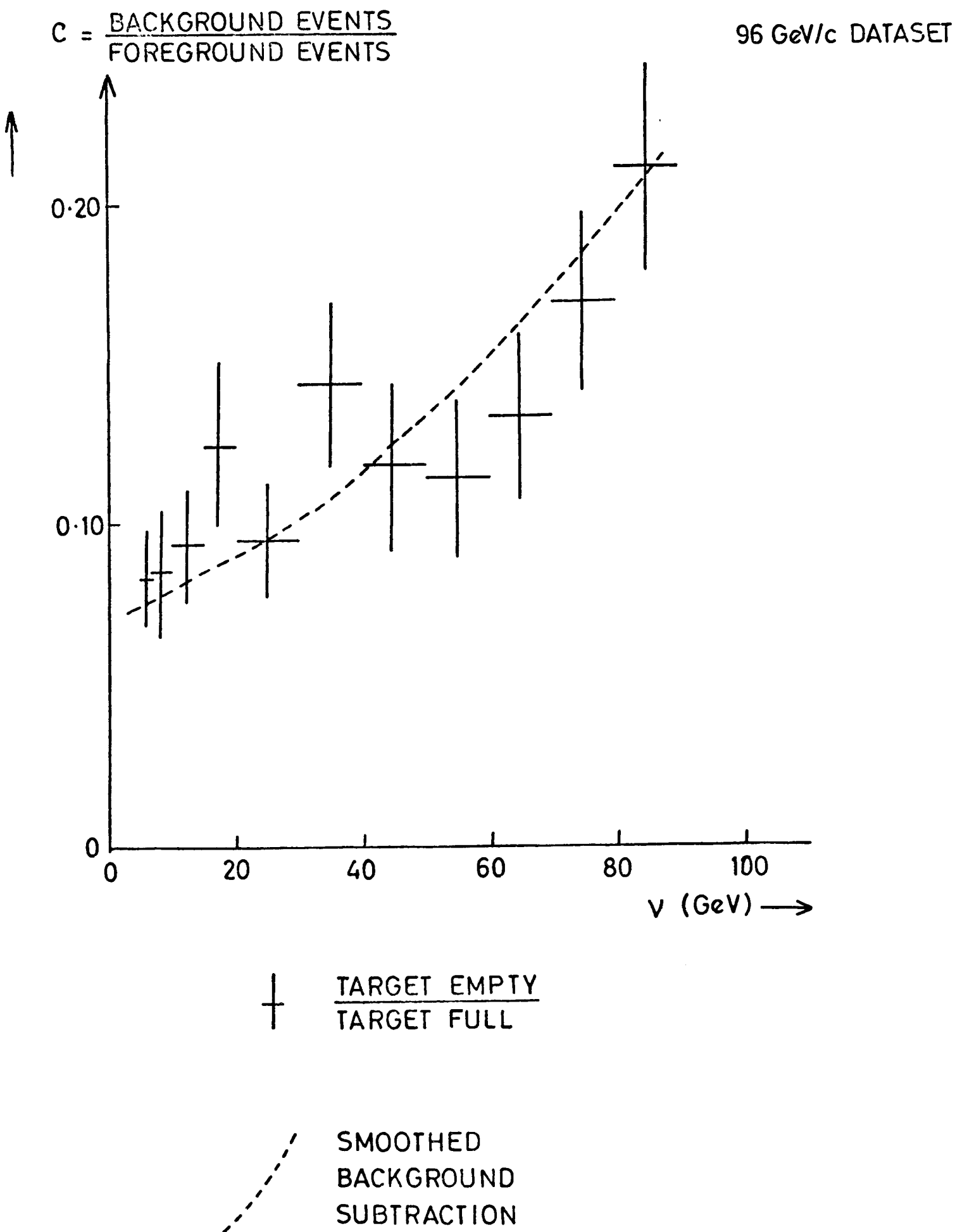
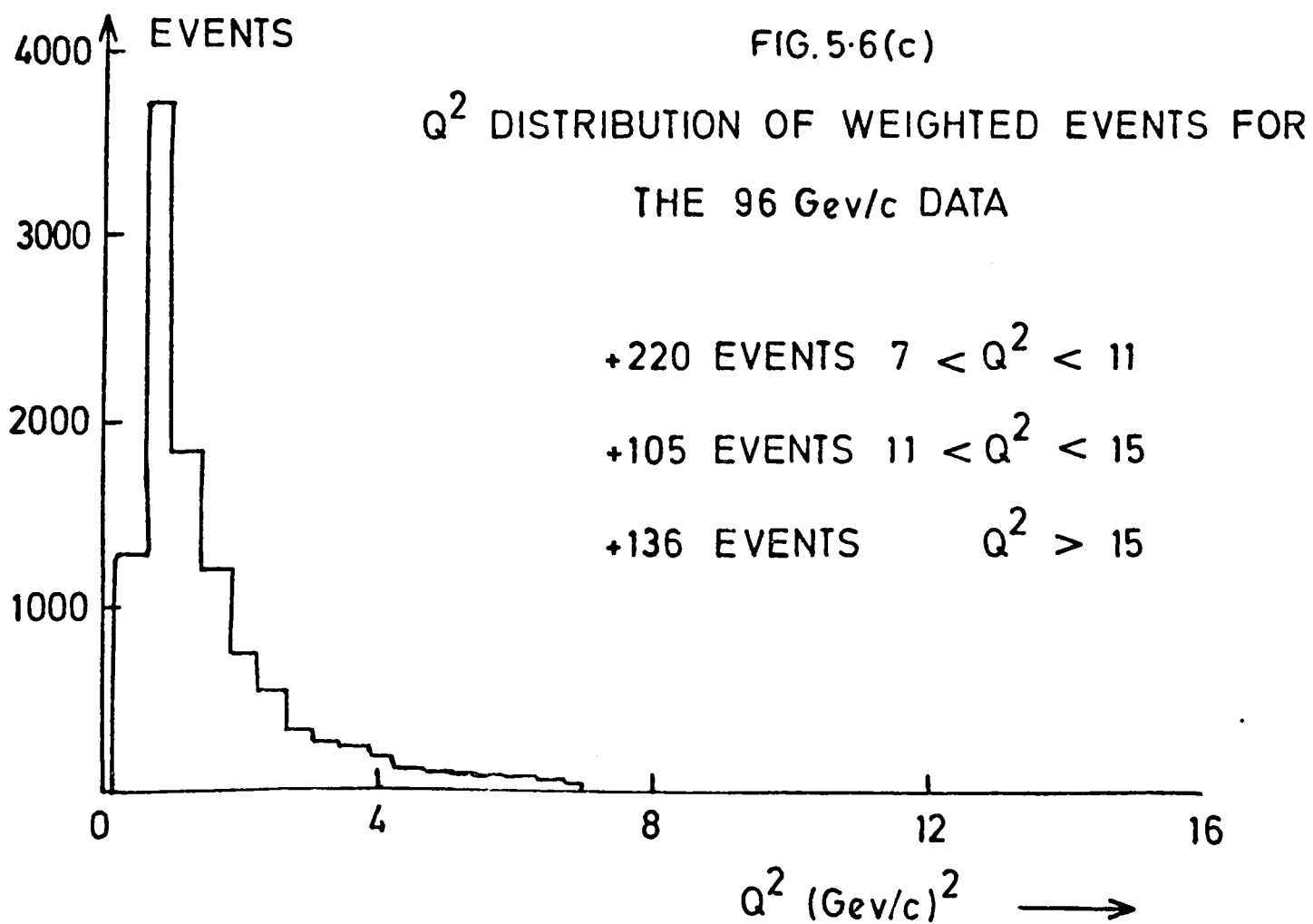
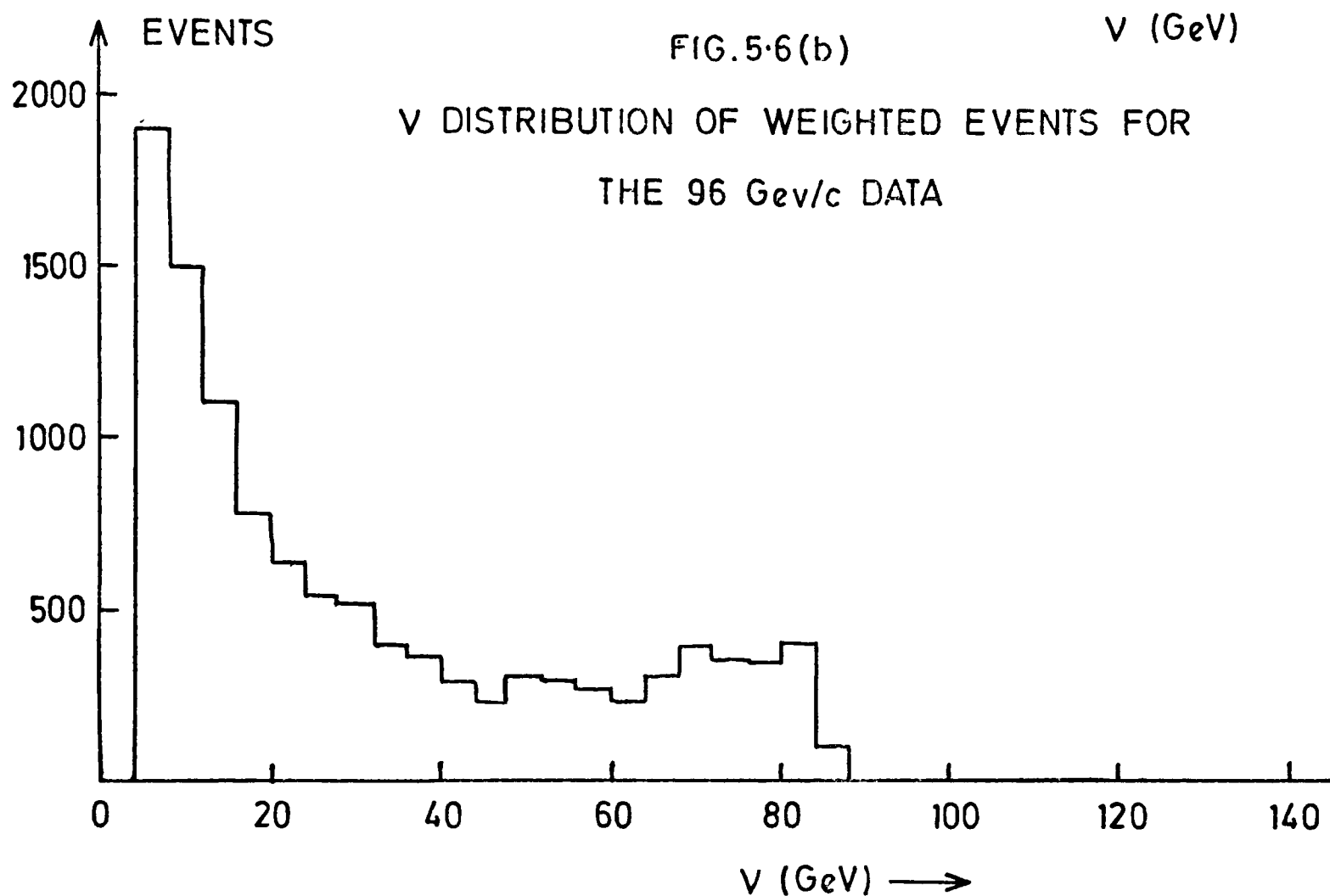
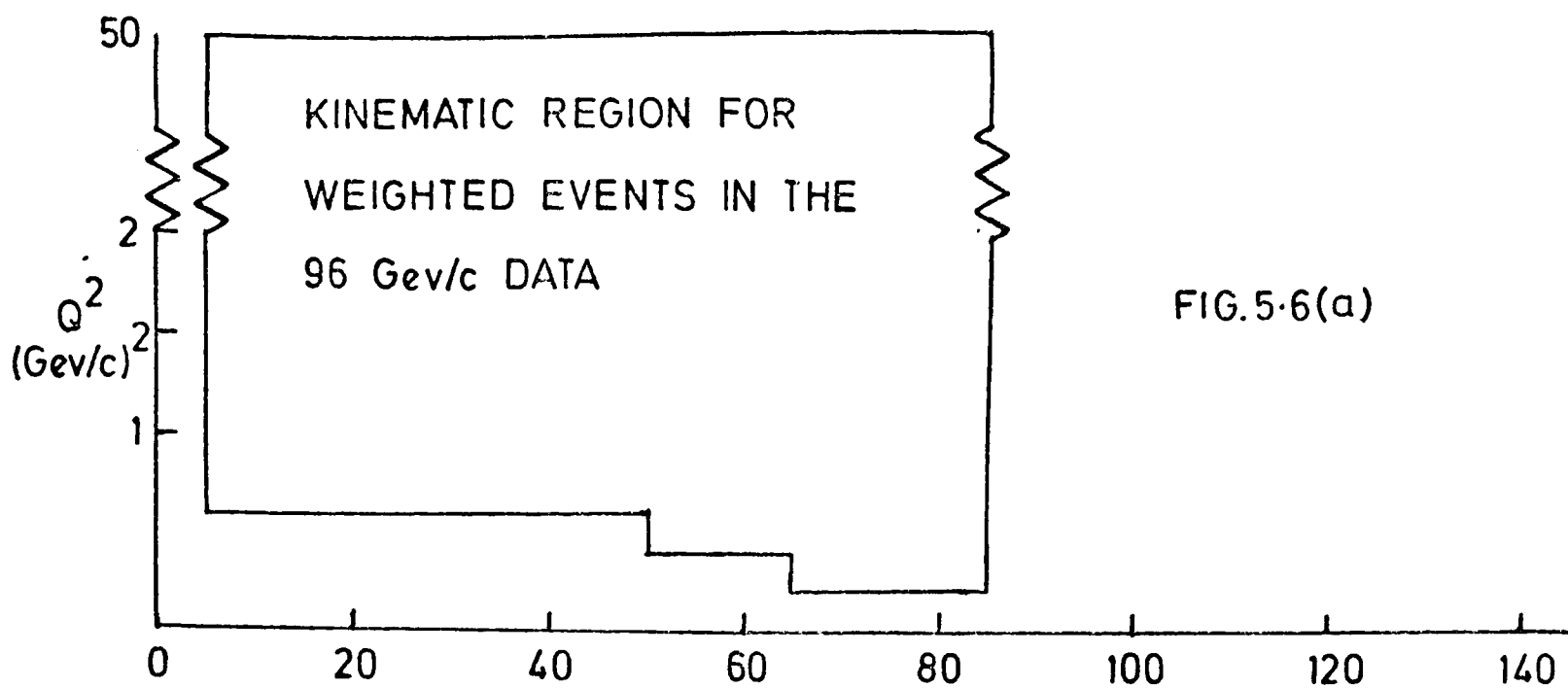
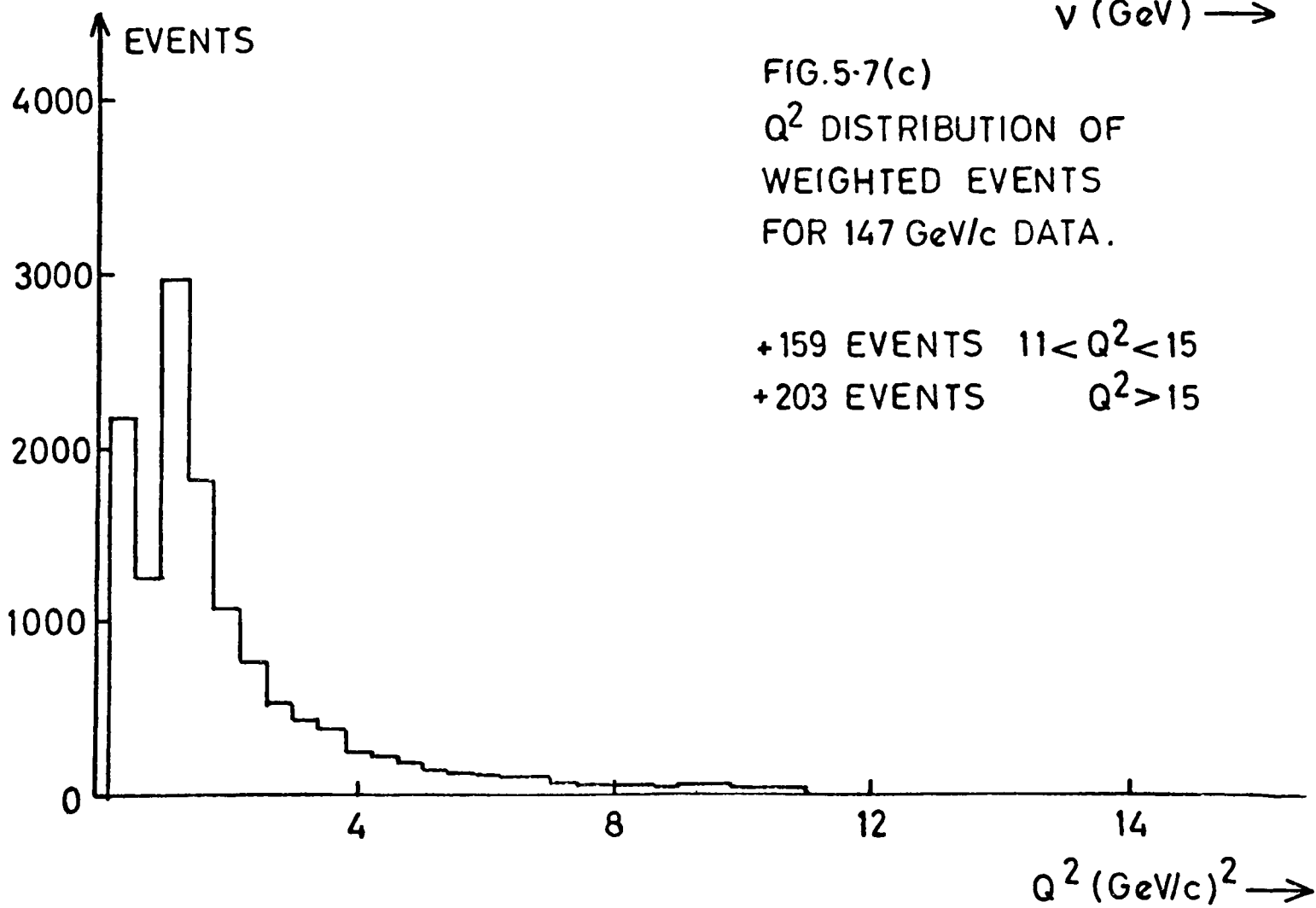
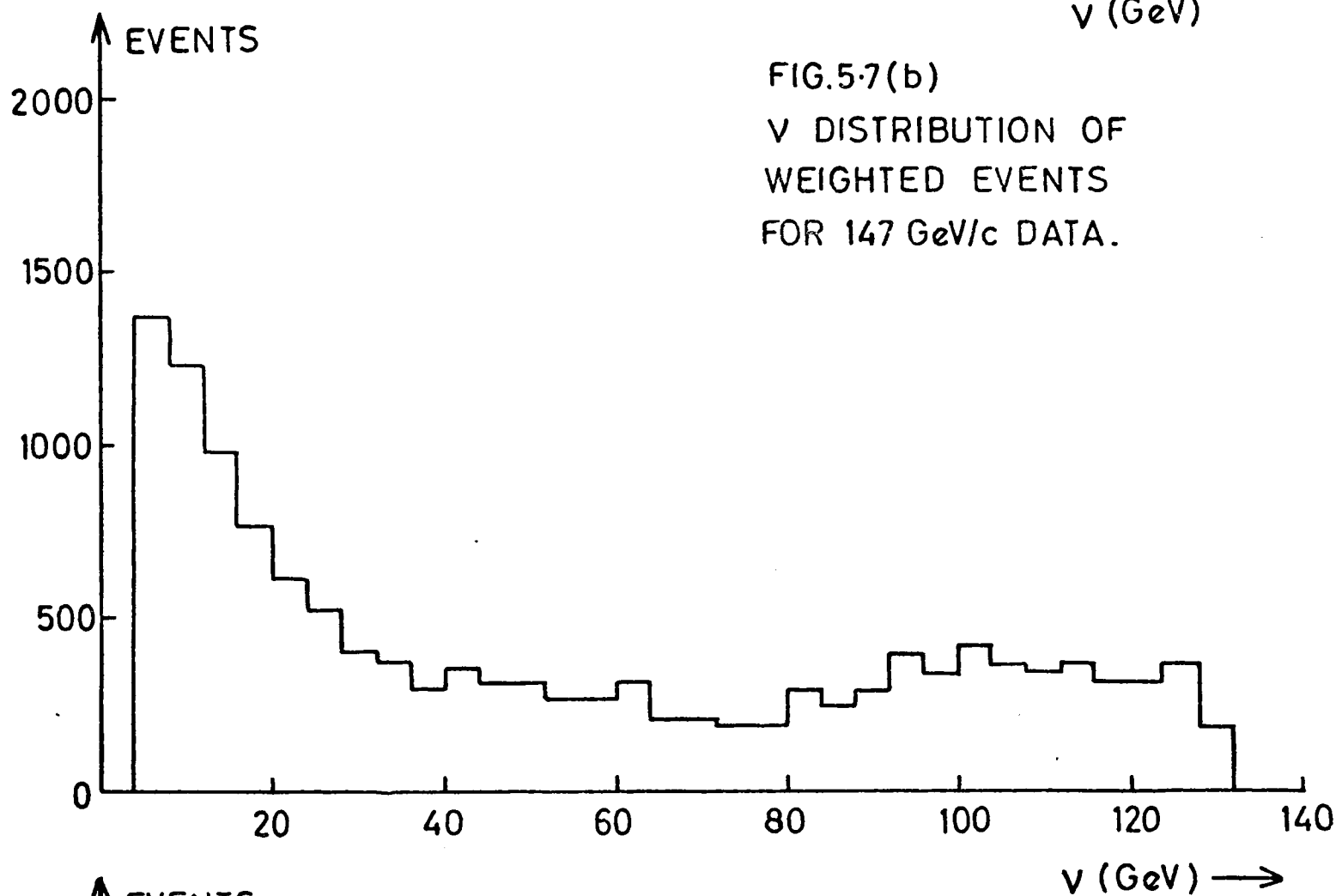
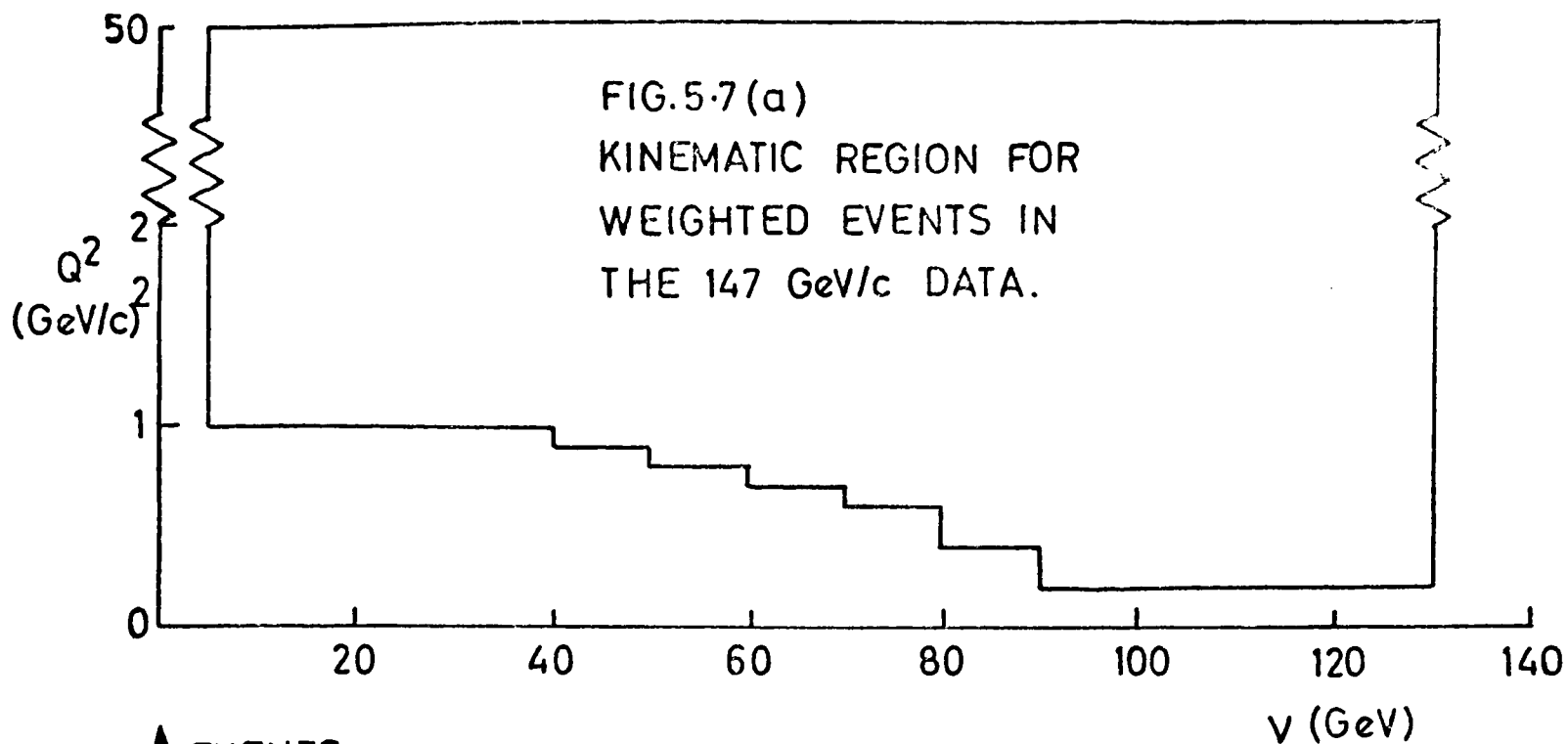


FIG 5.5
BACKGROUND SUBTRACTION.

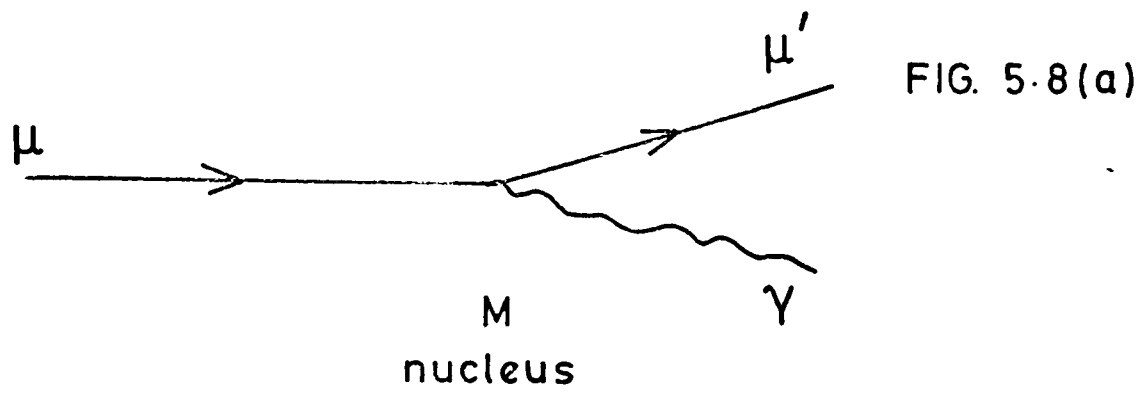




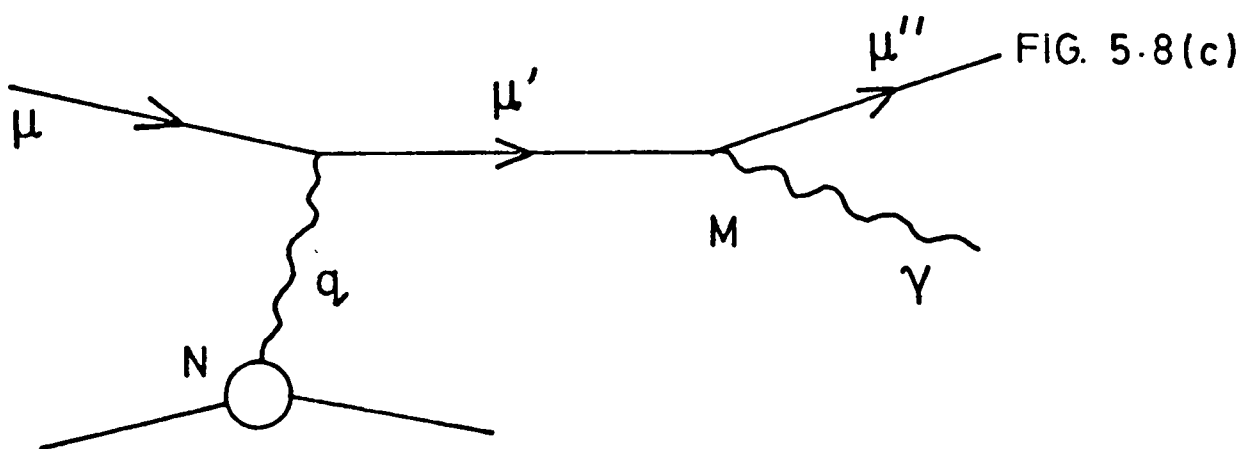
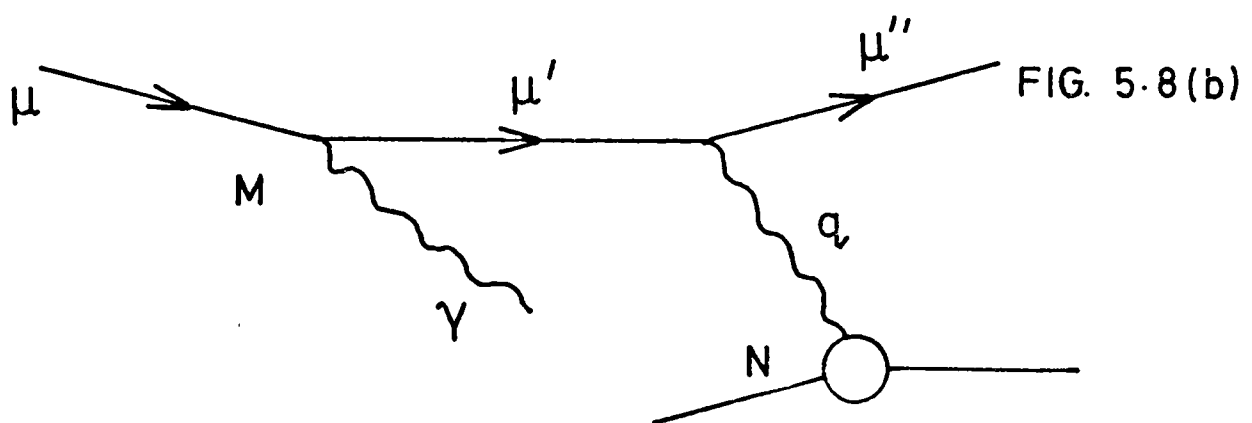


RADIATIVE PROCESSES

Muon Bremsstrahlung



Straggling



Internal Bremsstrahlung

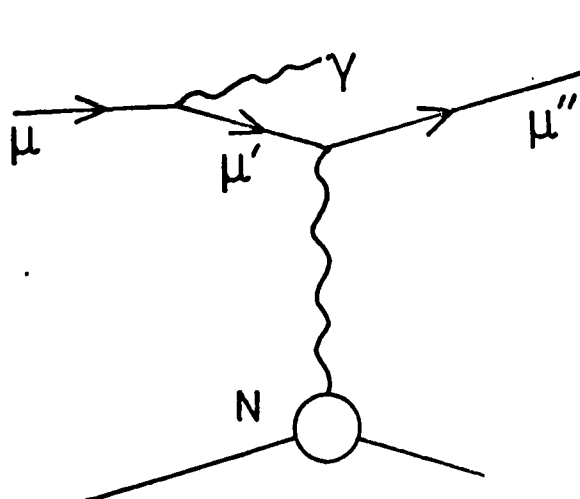


FIG. 5.8(d)

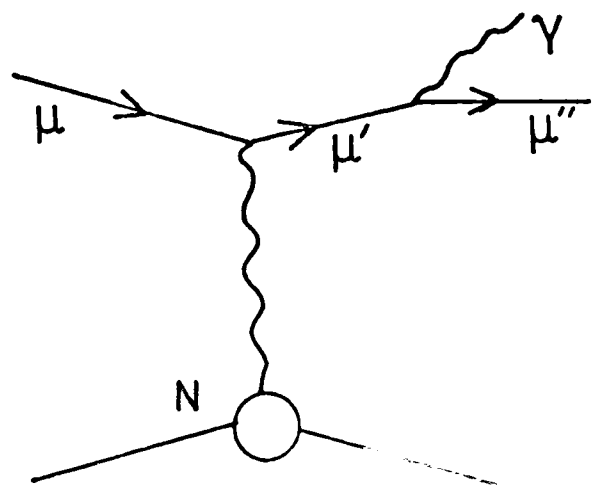


FIG. 5.8(e)

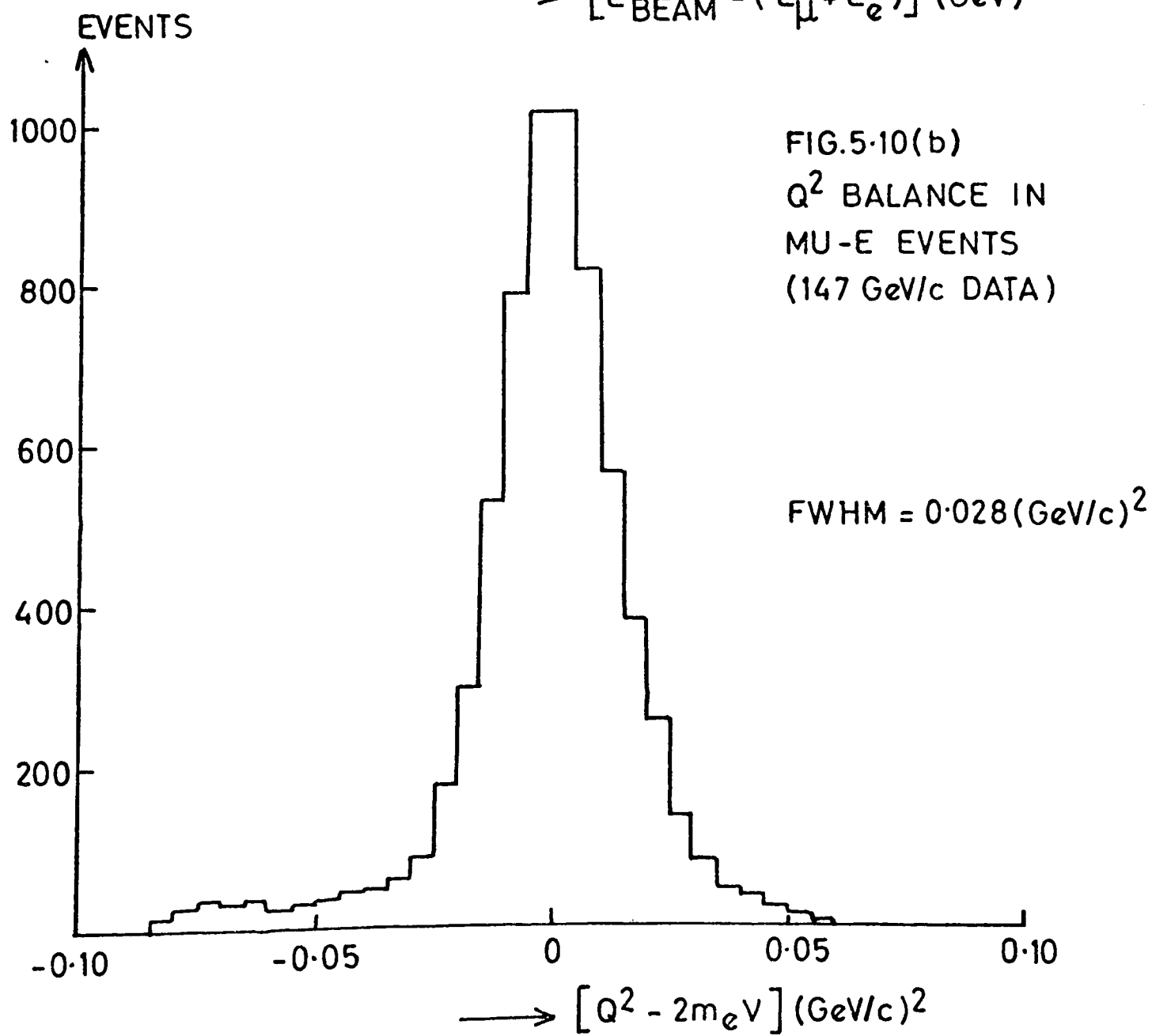
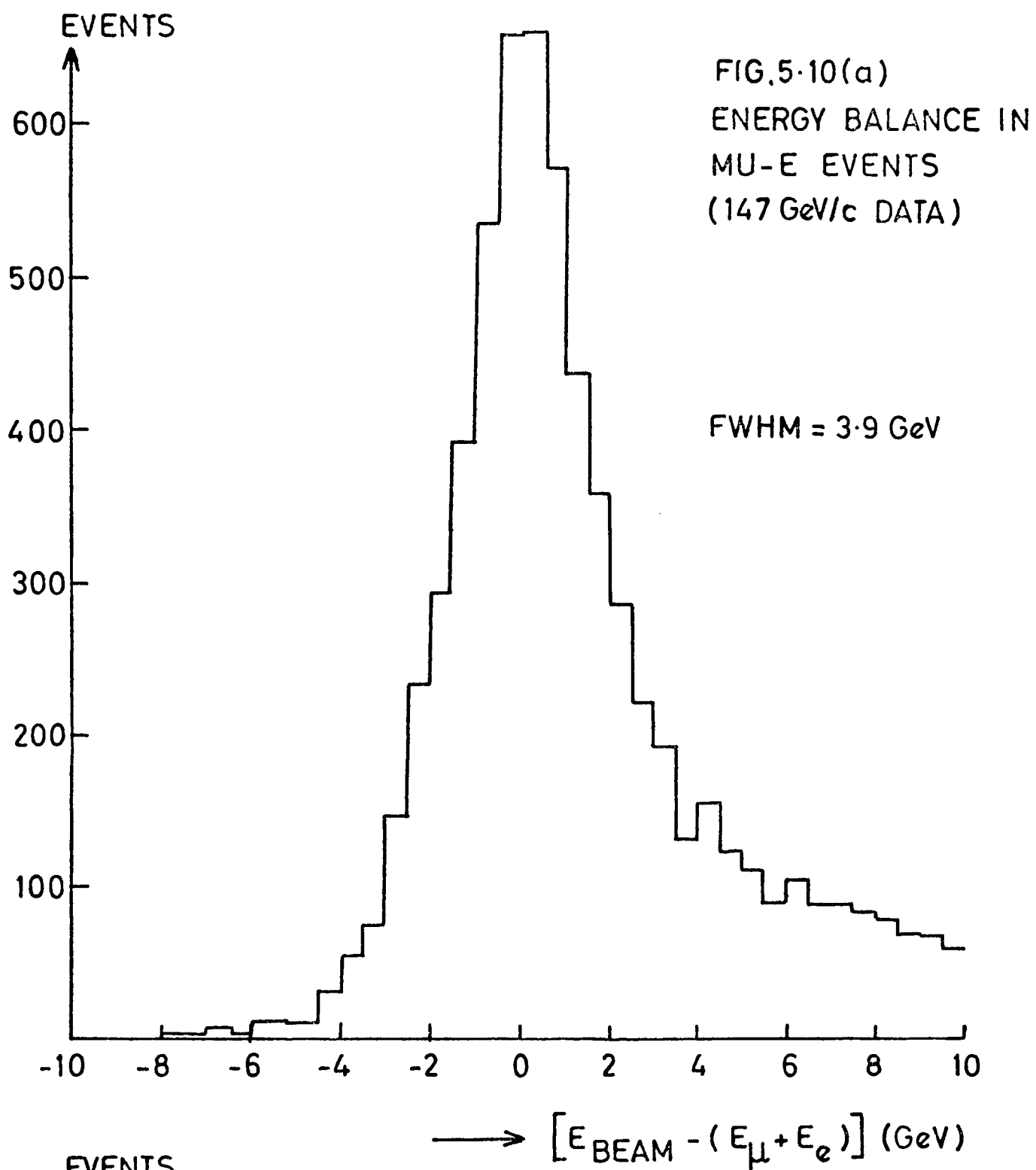


FIG. 5.11 MUON INCLUSIVE CROSS - SECTION vs.
 Q^2 FOR FIXED ν

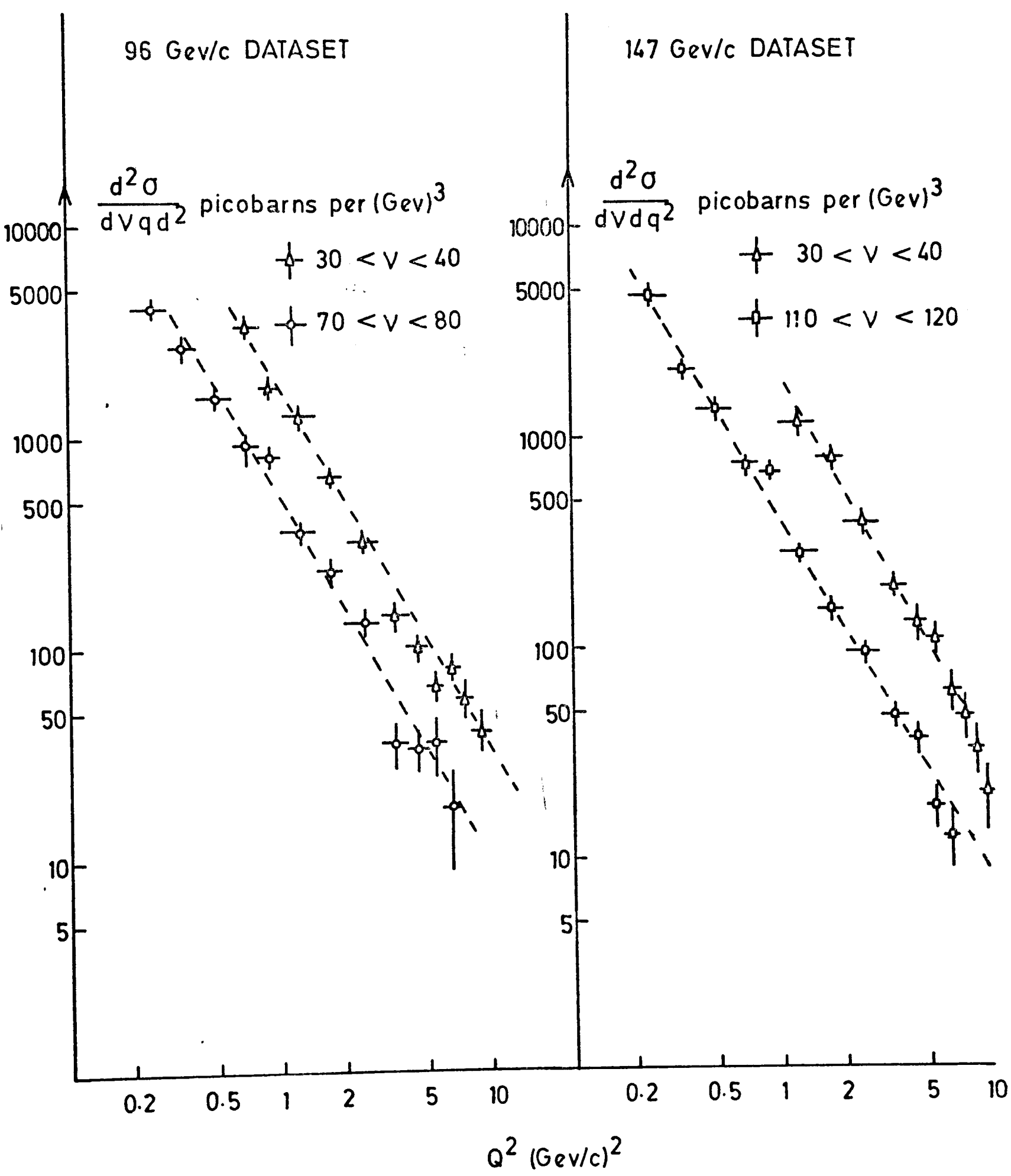


FIG. 5-12
 MUON INCLUSIVE CROSS SECTION vs. ν FOR
 FIXED Q^2 (96 GeV/c DATASET)

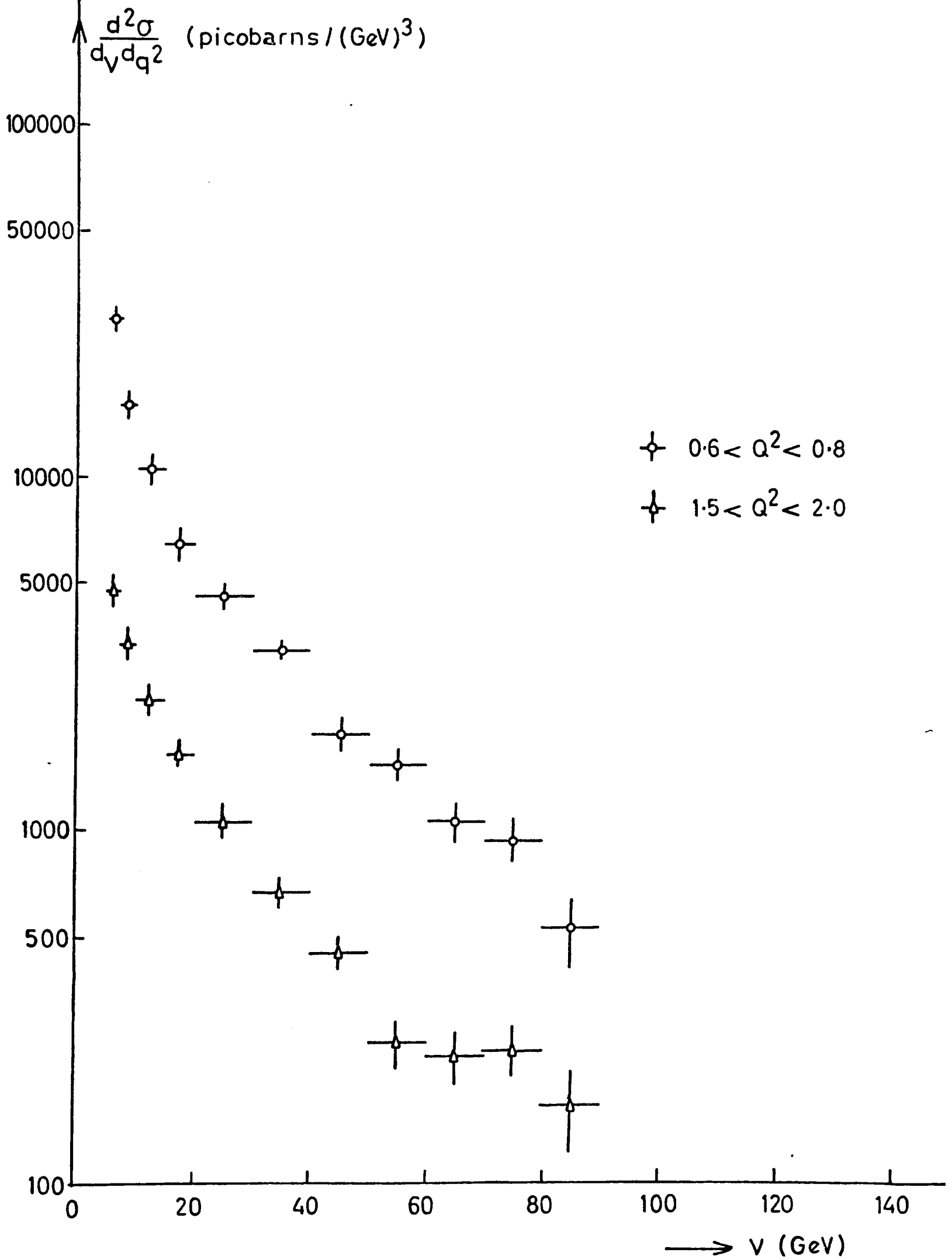


FIG. 5.13

AVERAGE νW_2 vs. ω

Δ 147 GeV/c DATA

\circ 96 GeV/c DATA

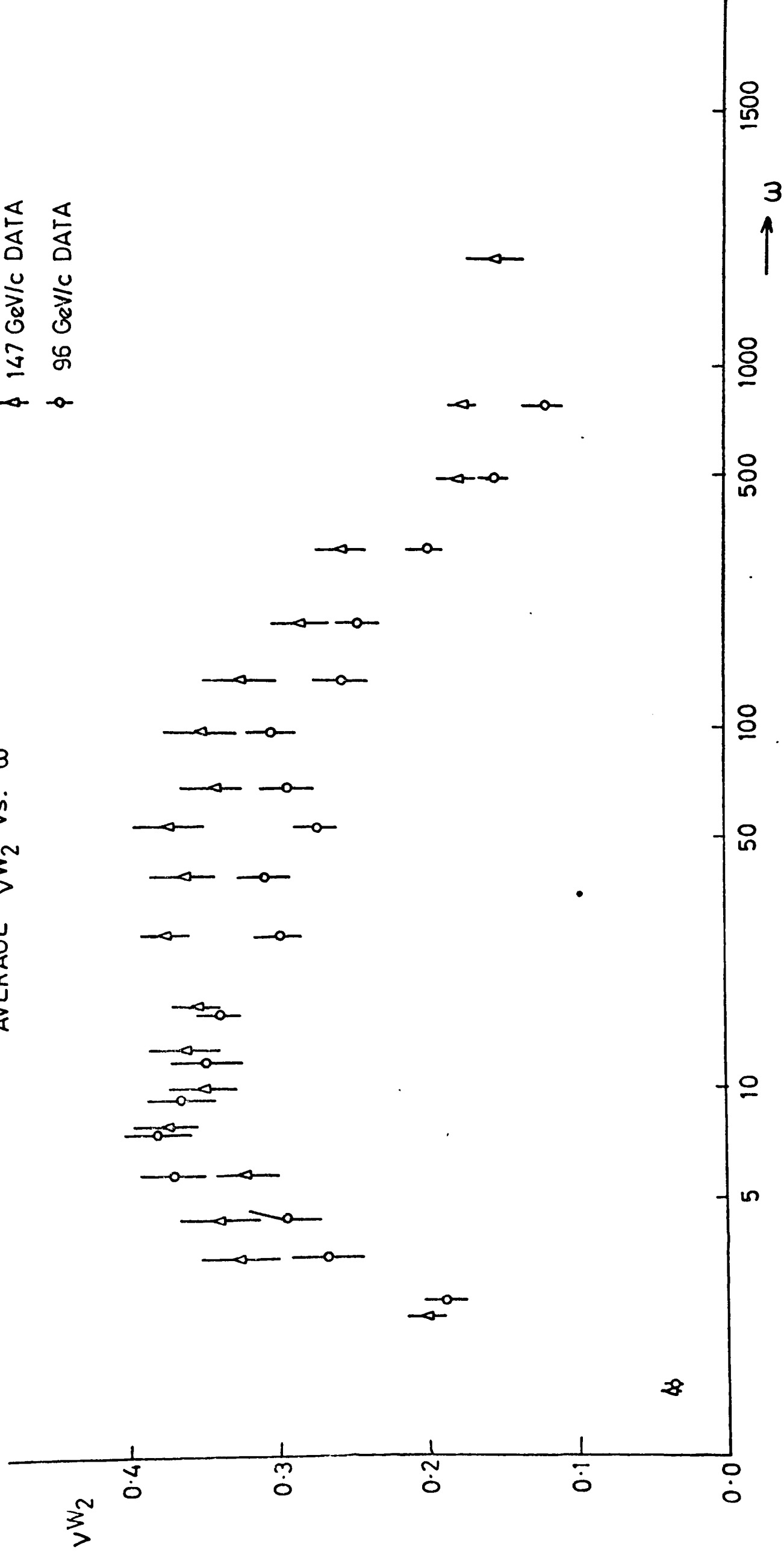


FIG. 5.14 VALUES OF νW_2 AS A FUNCTION OF Q^2 IN VARIOUS BANDS OF ω FOR THE 96 GeV/c DATA $R = 0.18$

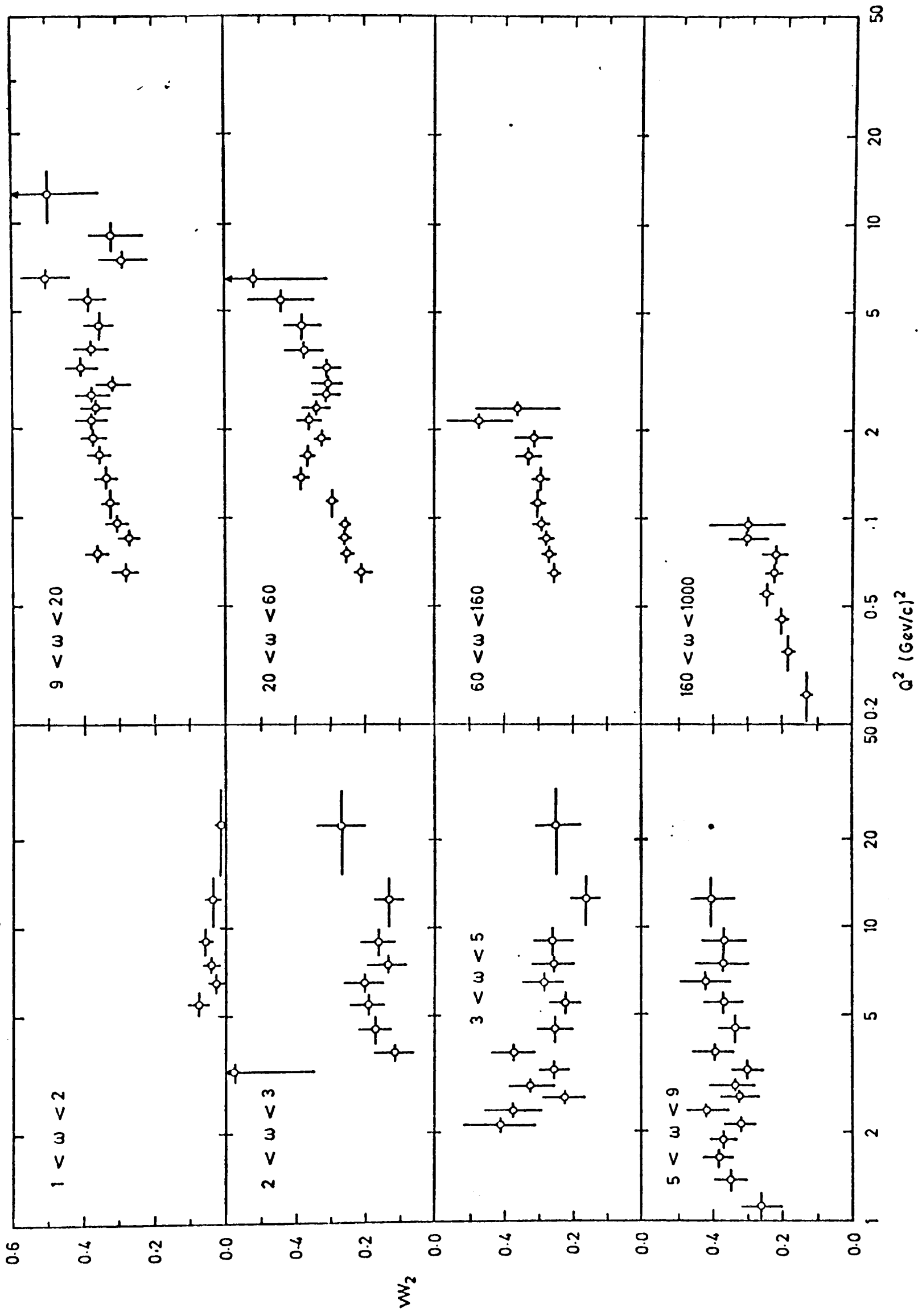


FIG. 5-15 VALUES OF νW_2 AS A FUNCTION OF Q^2 IN VARIOUS BANDS OF ω FOR THE 147 GeV/c DATA $R = 0.18$

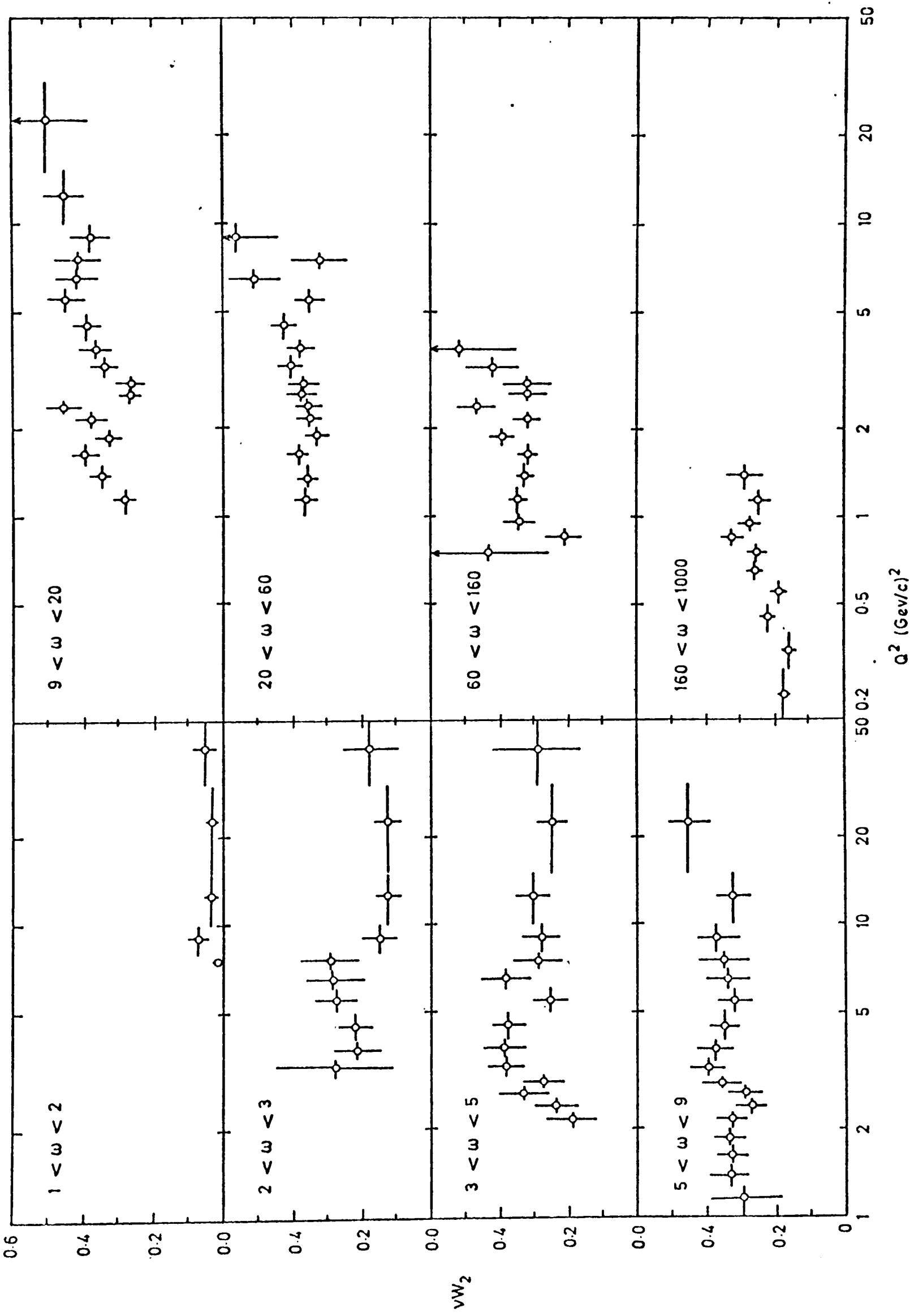
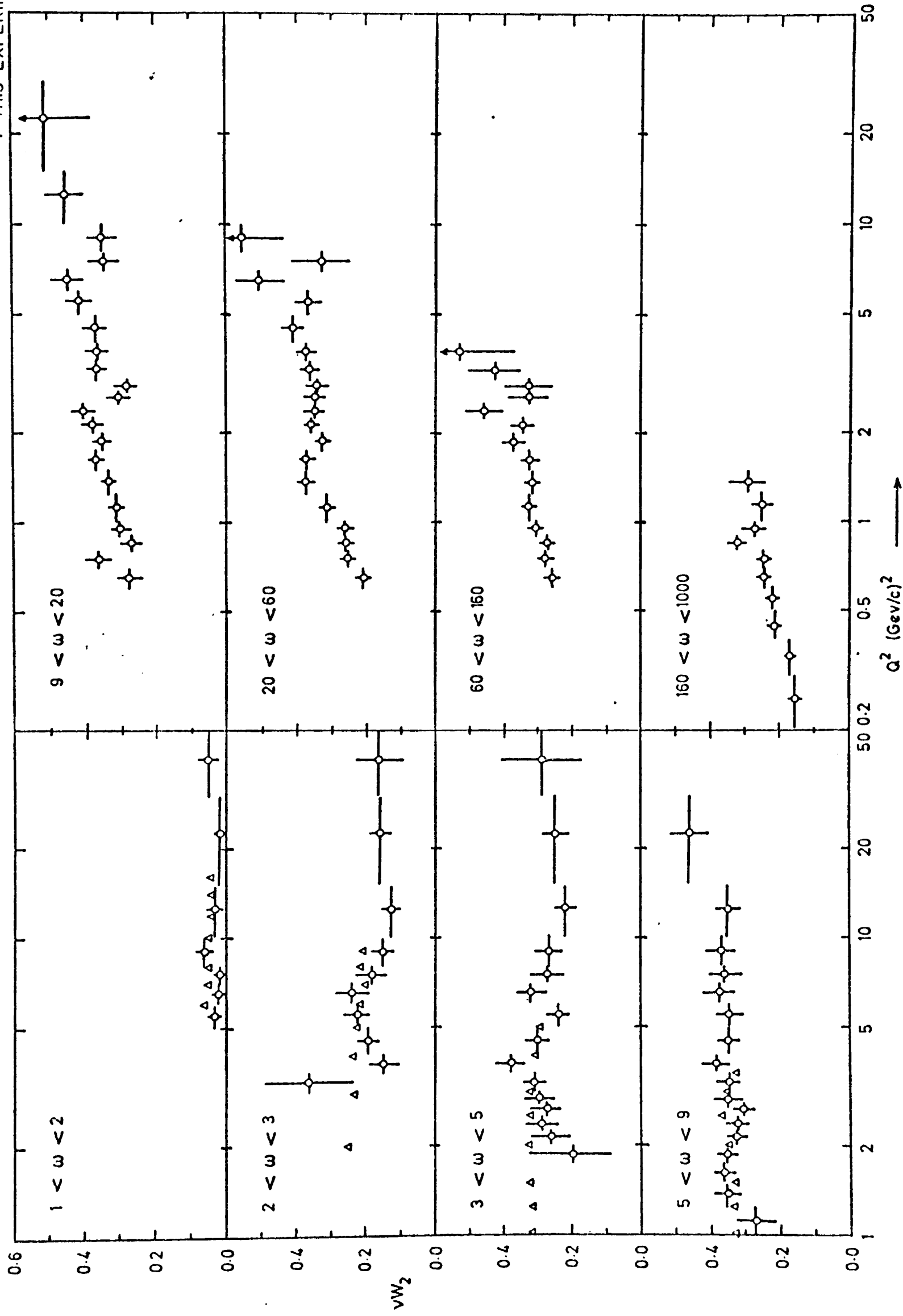


FIG. 5.16 VALUES OF νW_2 AS A FUNCTION OF Q^2 IN VARIOUS BANDS OF ω FOR THE COMBINED DATA $R = 0.18$ Δ SLAC \circ THIS EXPERIMENT



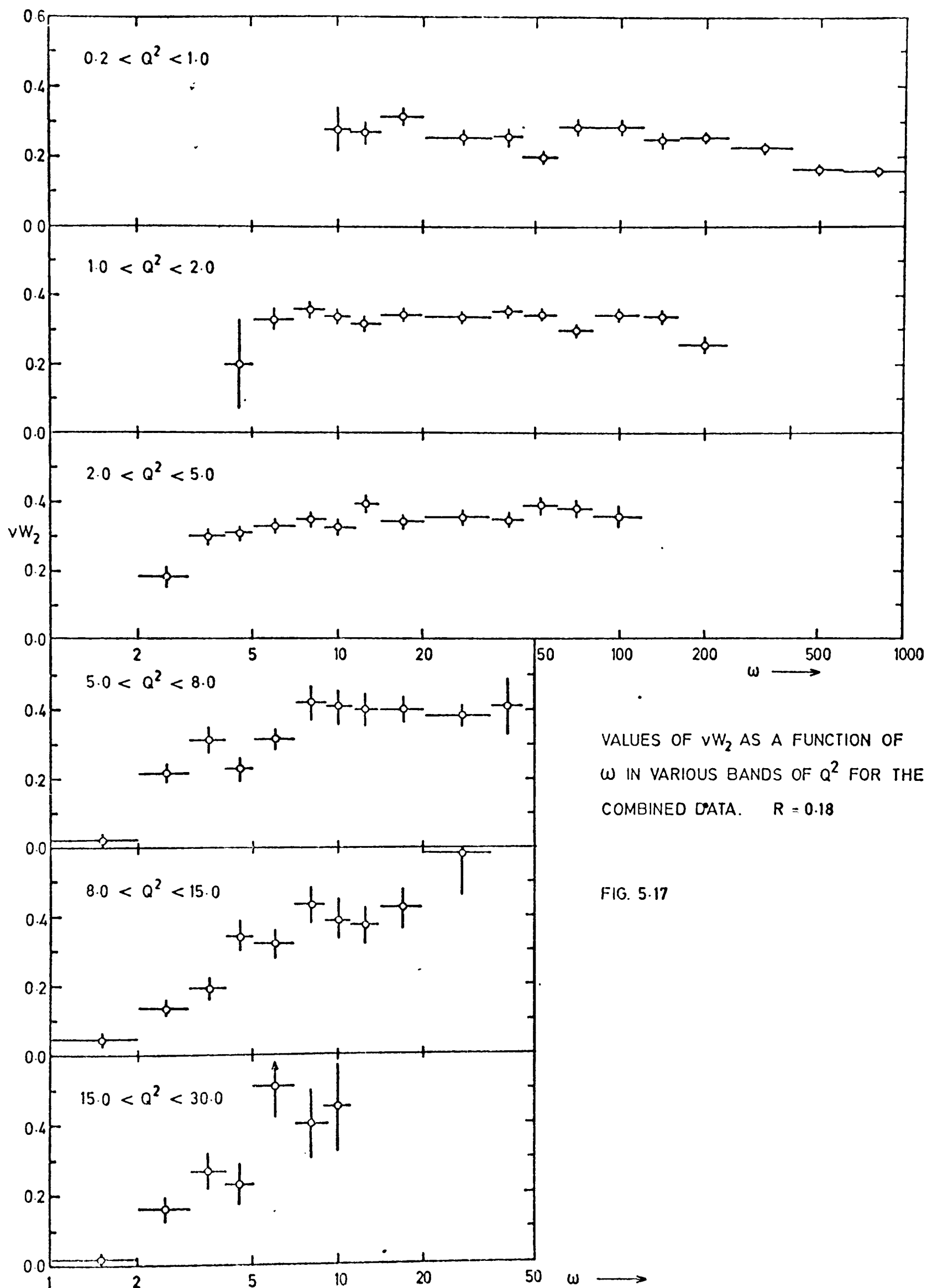


FIG. 5.18
SCALING VIOLATION vs. X

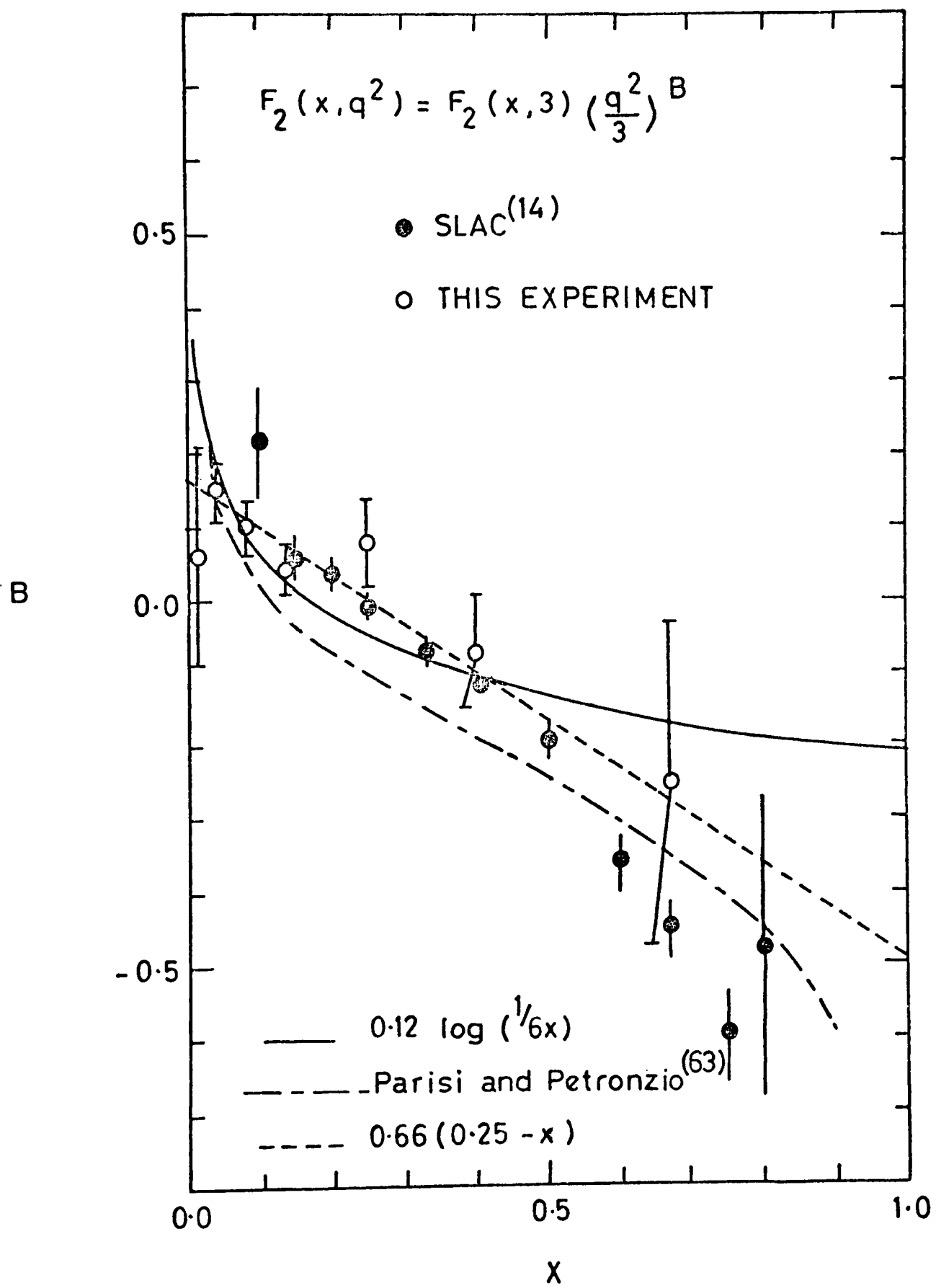


FIG. 5.19

COMPARISON OF VW_2 WITH PREDICTIONS OF GENERALISED VECTOR MESON DOMINANCE

--- GVMD (64)

— GVMD (65)
(including ψ)

\square SLAC (66)

\circ THIS EXPERIMENT

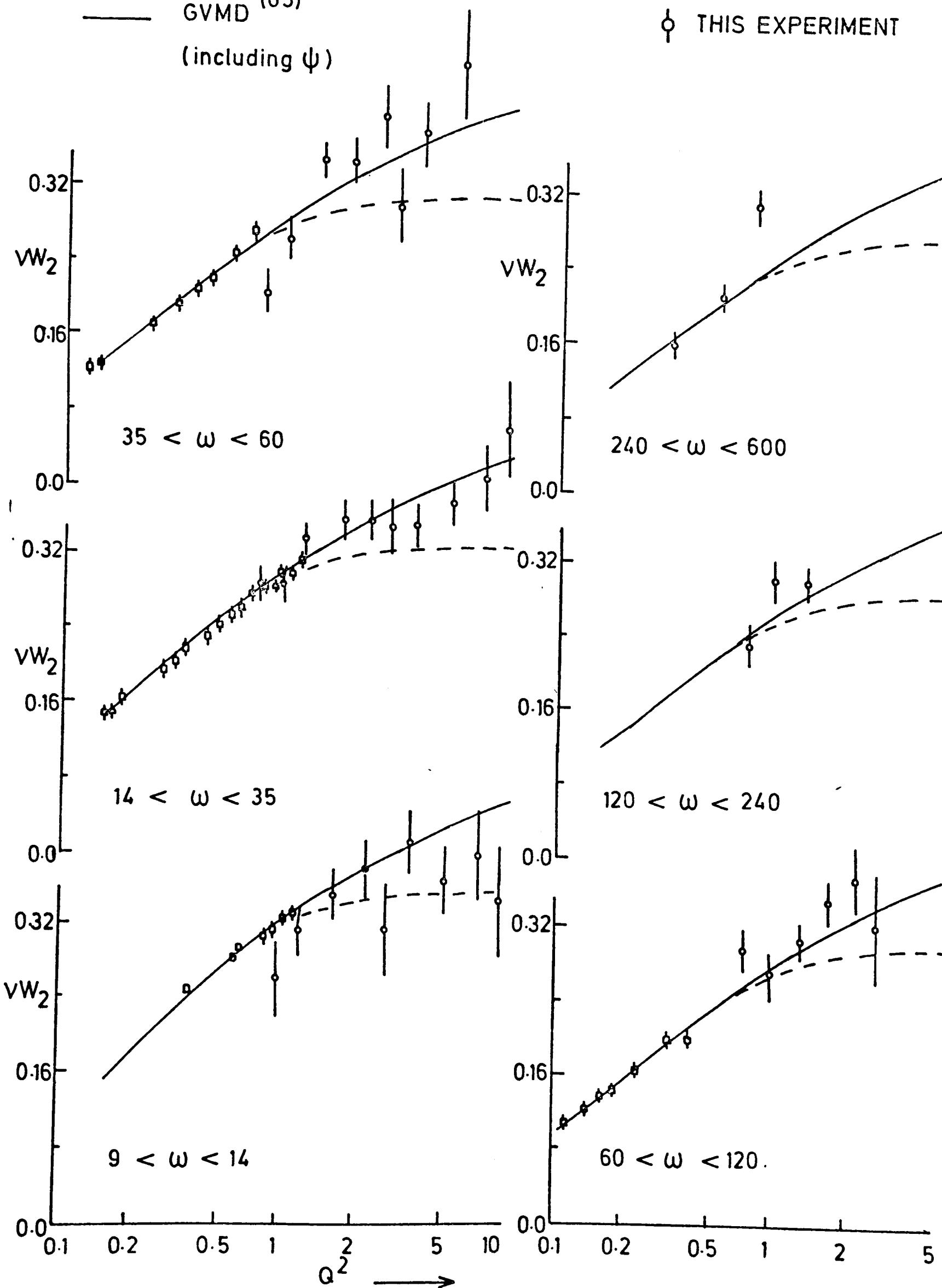


FIG. 5.20

TOTAL VIRTUAL PHOTOABSORPTION CROSS-SECTIONS AS A FUNCTION OF Q^2

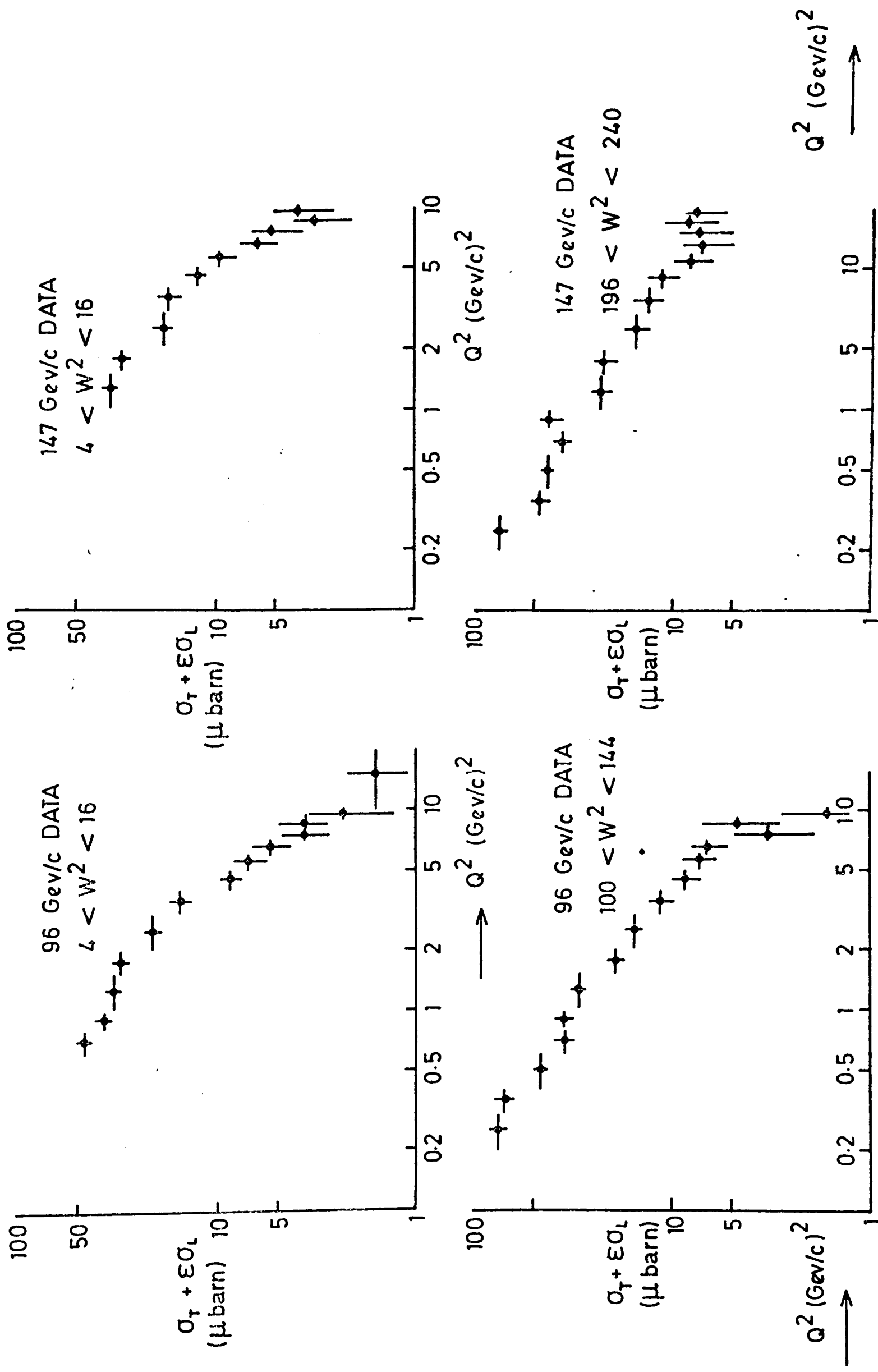
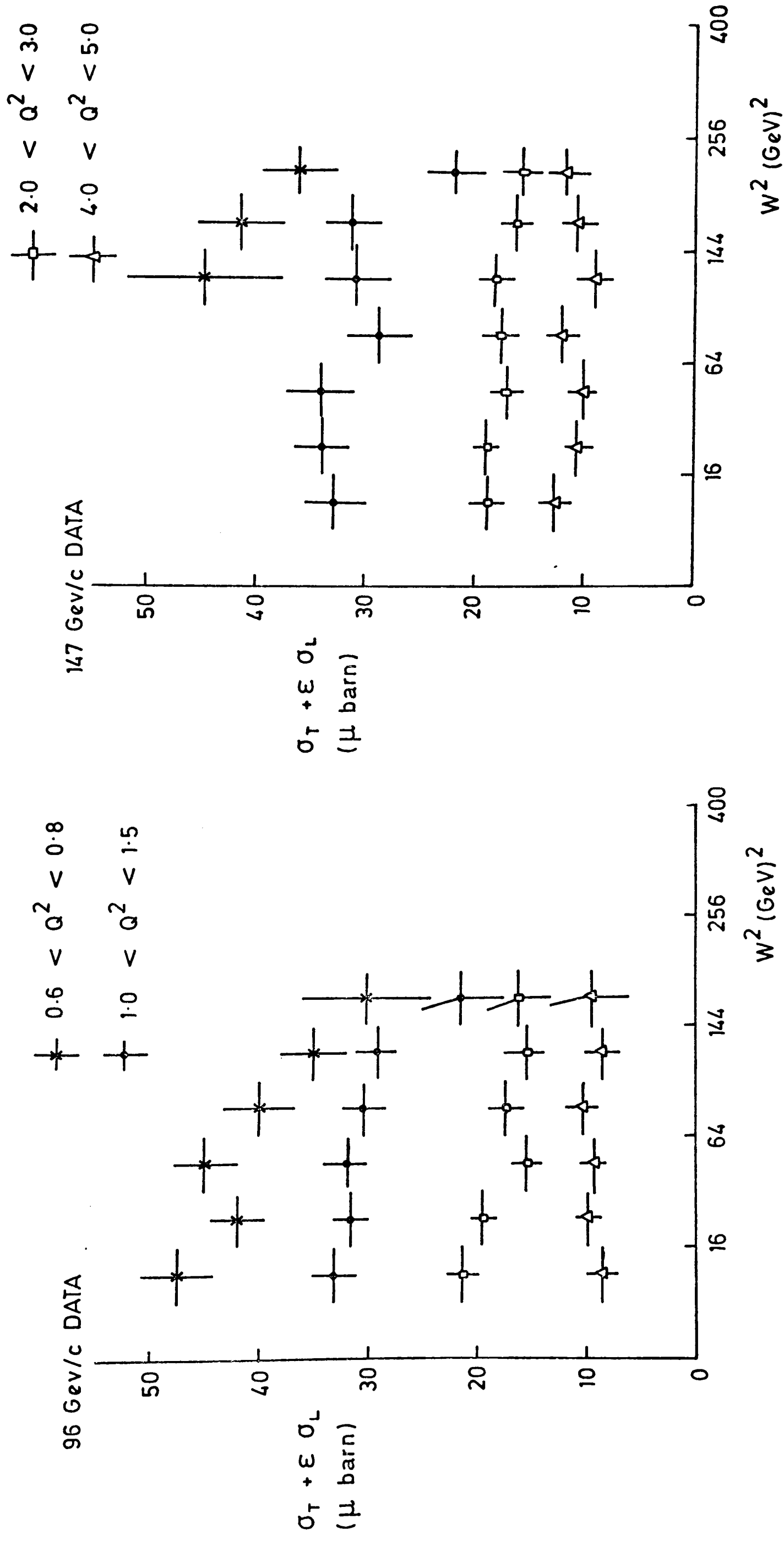


FIG. 5.21

TOTAL VIRTUAL PHOTOABSORPTION CROSS - SECTION VS. W^2



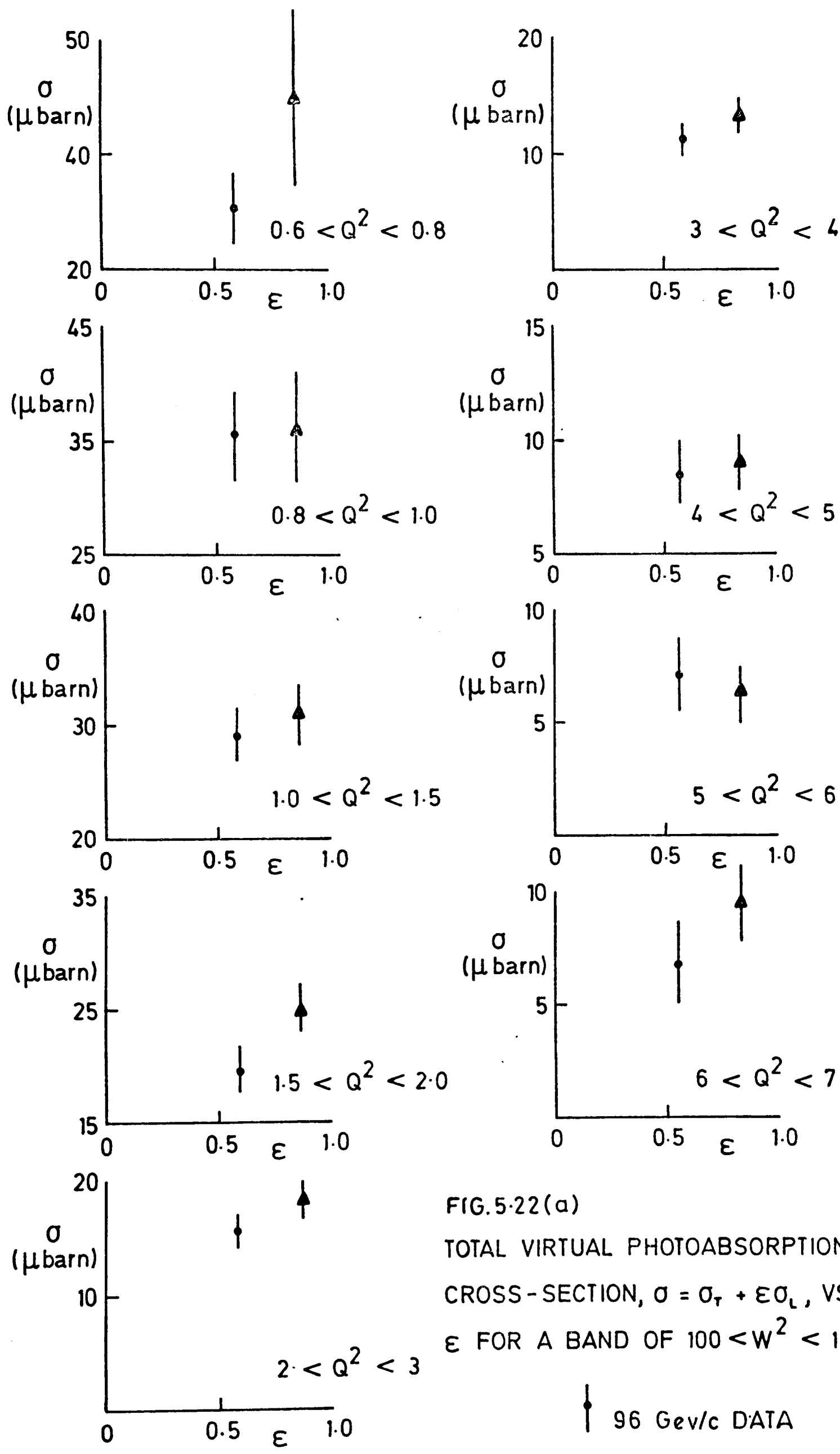


FIG.5-22(a)
 TOTAL VIRTUAL PHOTOABSORPTION
 CROSS-SECTION, $\sigma = \sigma_r + \epsilon\sigma_L$, VS.
 ϵ FOR A BAND OF $100 < W^2 < 144$

\bullet 96 GeV/c DATA
 \blacktriangle 147 GeV/c DATA

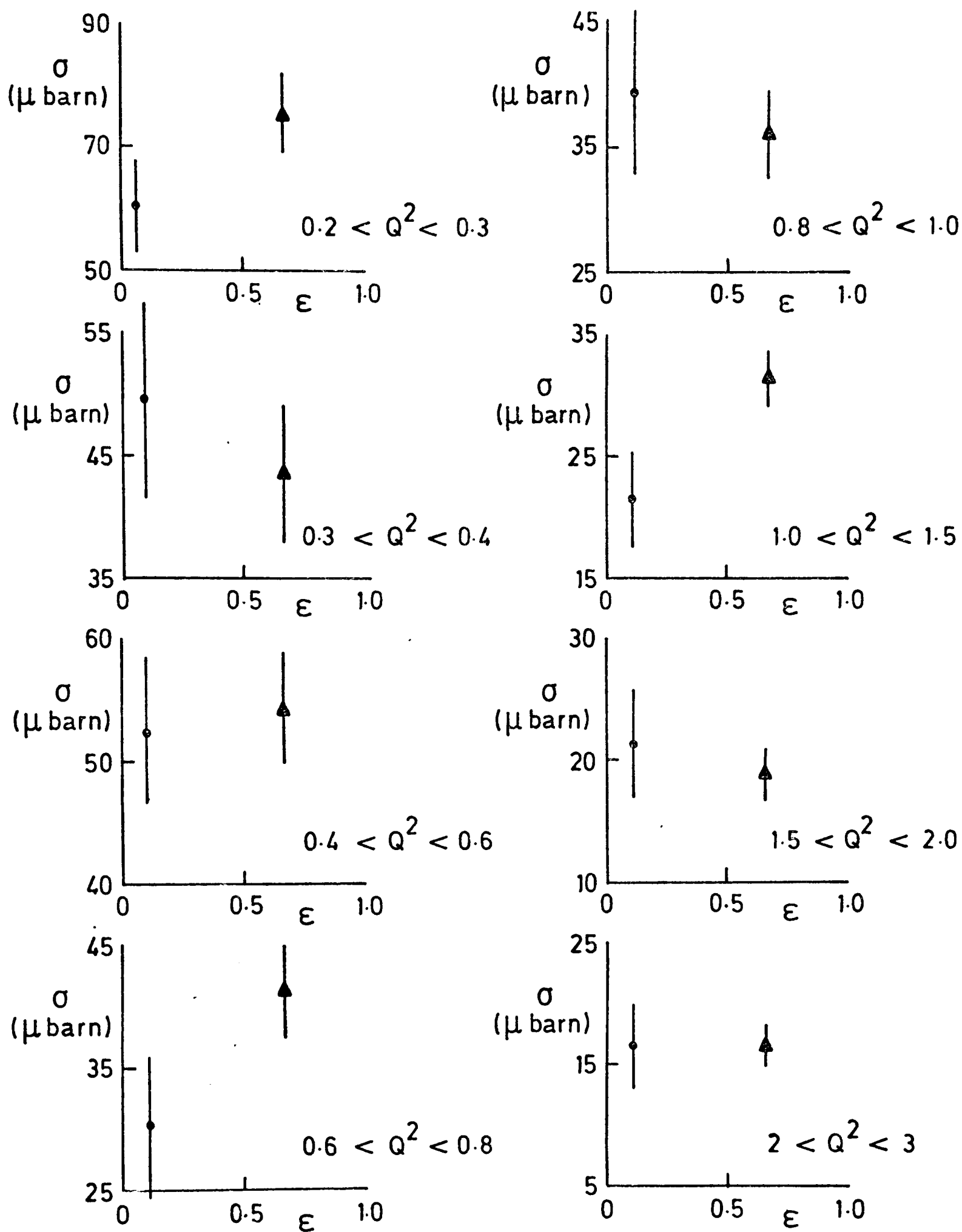


FIG.5-22(b)

TOTAL VIRTUAL PHOTOABSORPTION CROSS - SECTION, $\sigma = \sigma_T + \epsilon \sigma_L$,
VS. ϵ FOR A BAND OF $144 < W^2 < 196$

● 96 GeV/c DATA

▲ 147 GeV/c DATA

Table 5.1 EXTRACTED VALUES OF σ_L , σ_T AND R

Q^2 (GeV/c) ²	W^2 (Gev) ²	σ_L μbarns	σ_T μbarns	R	$\epsilon(147\text{GeV}) - \epsilon(96\text{GeV})$
0.8 - 1.0	64 - 100	20.1±83.8	17.4±71.6	1.55±9.53	0.10
1.0 - 1.5	64 - 100	-16.9±33.8	44.7±29.7	-0.38±0.51	0.10
1.5 - 2.0	64 - 100	6.4±29.2	15.9±25.8	0.40±2.48	0.10
2 - 3	64 - 100	3.9±20.4	14.1±18.2	0.28±1.81	0.10
3 - 4	64 - 100	5.1±18.9	7.4±16.9	0.69±4.71	0.10
0.6 - 0.8	100 - 144	36.1±31.9	13.9±20.1	2.59±6.04	0.26
0.8 - 1.0	100 - 144	2.1±22.9	34.5±15.6	0.06±6.92	0.26
1.0 - 1.5	100 - 144	6.8±13.4	25.1±9.3	0.27±0.62	0.26
1.5 - 2.0	100 - 144	20.8±12.1	7.4±8.6	2.82±4.89	0.26
2 - 3	100 - 144	9.6±8.2	10.0±5.9	0.95±1.39	0.27
3 - 4	100 - 144	6.7±7.9	7.5±5.8	0.89±1.74	0.27
0.2 - 0.3	144 - 196	22.8±16.0	58.7±8.4	0.39±0.33	0.61
0.3 - 0.4	144 - 196	-11.3±16.3	50.5±9.1	-0.22±0.29	0.60
0.4 - 0.6	144 - 196	2.9±13.4	52.3±7.2	0.06±0.26	0.57

COMBINING BINS

1 - 2	64 - 100	-0.35±0.50
2 - 4	64 - 100	0.33±1.69
1 - 2	100 - 144	0.27±0.58
2 - 4	100 - 144	0.92±1.08
1 - 4	64 - 144	0.07±0.34

Note Only the bins with greater than 50 events and $\epsilon(147\text{Gev}) - \epsilon(96\text{GeV})$ greater than 0.1 are tabulated.

Table 5.2 FITS FOR W_2 AND R

Fit 1

$$\nu W_2 = \left[a_1 (1-x)^3 + a_2 (1-x)^4 + a_3 (1-x)^5 \right] \left(1 + a_4 \log \frac{Q^2}{3} \log \frac{\omega}{6} \right)$$

$$R = a_5$$

(a) All the data

Correlation matrix

$a_1 = 0.761 \pm 0.522$	1	1.000				
$a_2 = 1.029 \pm 1.210$	2	-0.996	1.000			
$a_3 = -1.456 \pm 0.698$	3	0.987	-0.997	1.000		
$a_4 = 0.049 \pm 0.002$	4	0.215	-0.230	0.242	1.000	
$a_5 = 0.137 \pm 0.085$	5	0.268	-0.294	0.319	-0.355	1.000
		1	2	3	4	5

NDF = 255
Variance ratio = 1.034

(b) Q^2 greater than 1.0 (GeV/c)² data

Correlation matrix

$a_1 = 1.282 \pm 0.642$	1	1.000				
$a_2 = -0.333 \pm 1.524$	2	-0.997	1.000			
$a_3 = -0.576 \pm 0.900$	3	0.989	-0.997	1.000		
$a_4 = 0.061 \pm 0.015$	4	0.499	-0.519	0.538	1.000	
$a_5 = 0.205 \pm 0.121$	5	0.356	-0.383	0.407	0.171	1.000
		1	2	3	4	5

NDF = 205
Variance ratio = 0.649

Table 5.2 (continued)

Fit 2

$$v^W_2 = \left[a_1 (1-x)^3 + a_2 (1-x)^4 + a_3 (1-x)^5 \right] (1 + a_4 (0.25-x) \log(\frac{Q^2}{a_5}))$$

$$R = a_6$$

(a) All the data

		Correlation matrix					
$a_1=1.071\pm1.071$	1	1.000					
$a_2=-0.331\pm2.060$	2	-0.987	1.000				
$a_3=-0.207\pm0.992$	3	0.888	-0.950	1.000			
$a_4=0.719\pm0.238$	4	0.866	-0.785	0.561	1.000		
$a_5=3.328\pm3.200$	5	-0.858	0.771	-0.539	-0.995	1.000	
$a_6=0.511\pm0.136$	6	0.534	-0.532	0.488	0.456	-0.481	1.000
		1	2	3	4	5	6

$$\text{NDF} = 254$$

Variance ratio = 0.868

(b) Q^2 greater than 1.0 (GeV/c)^2 data

		Correlation matrix					
$a_1= 1.784\pm2.536$	1	1.000					
$a_2=-1.403\pm5.484$	2	-0.999	1.000				
$a_3= 0.045\pm2.831$	3	0.996	-0.998	1.000			
$a_4= 0.609\pm0.200$	4	0.825	-0.831	0.838	1.000		
$a_5= 1.482\pm1.872$	5	-0.956	0.948	-0.934	-0.742	1.000	
$a_6= 0.384\pm0.163$	6	0.243	-0.262	0.288	0.360	-0.111	1.000
		1	2	3	4	5	6

$$\text{NDF} = 204$$
$$\text{Variance ratio} = 0.630$$

TABLE 5.3
CALLAN-GROSS SUM RULE CALCULATION

Data fitted to the form

$$F_2 = \left[\sum_{i=1}^n a_i (1-x)^{i+2} \right] (1+b_1 (0.25-x) \log \frac{Q^2}{3})$$

R = 0.18

$\frac{Q^2}{(\text{GeV}/c)^2}$	x limits of data	$\int_0^1 F_2(x) dx$ (n = 3)	Variance Ratio of Fit	$\int_0^1 F_2(x) dx$ (n = 4)	Variance Ratio of Fit
1-2	0.0025 -0.33	0.178±0.002	1.297	0.188±0.008	1.259
2-4	0.0083 -0.50	0.176±0.001	1.134	0.177±0.001	1.151
4-8	0.0170 -0.67	0.172±0.002	1.705	0.173±0.002	1.707
8-15	0.029 -0.80	0.168±0.004	0.990	0.168±0.004	1.026
15-30	0.050 -0.80	0.164±0.010	0.915	0.161±0.012	1.138

Moving the normalisation of this experiment up by 5% relative to the SLAC-MIT data gives:

1-2	0.181±0.002	1.463	0.189±0.007	1.455
2-4	0.178±0.001	0.961	0.179±0.002	0.977
4-8	0.176±0.002	1.489	0.178±0.002	1.477
8-15	0.173±0.004	0.874	0.174±0.004	0.900
15-30	0.173±0.011	0.914	0.169±0.013	1.113

Values of the integral using data from this experiment only:

$\frac{Q^2}{(\text{GeV}/c)^2}$	x_{\min}	$\int_{x_{\min}}^{0.25} F_2 dx$	$\int_{0.05}^{0.25} F_2 dx$
1-2	0.0025	0.0772±0.0067	0.0606±0.0067
2-4	0.0080	0.0809±0.0018	0.0658±0.0017
4-8	0.0167	0.0811±0.0021	0.0670±0.0019
8-15	0.029	0.0852±0.0033	0.0726±0.0029
15-30	0.05	0.0799±0.0094	0.0799±0.0094

Extrapolation of the data from this experiment to x = 0

$\frac{Q^2}{(\text{GeV}/c)^2}$	$\int_0^{0.25} F_2 dx$	Systematic error from extrapolation
1-2	0.0782±0.0067	0.0003
2-4	0.0809±0.0018	0.0007
4-8	0.0874±0.0021	0.0016
8-15	0.0962±0.0033	0.0030
15-30	0.0989±0.0094	0.0050

Systematic errors
calculated by assuming
a 25% error in the
extrapolation

APPENDIX A

SUMMARY OF THE KINEMATICS OF CHARGED LEPTON-NUCLEON SCATTERING*

Masses

m_l	mass of the lepton
m_e	mass of the electron
m_μ	mass of the muon
M	mass of the proton

Variables

$p = (E, \vec{p})$	four-momentum of the incident lepton
$p' = (E', \vec{p}')$	four-momentum of the scattered lepton
$P = (M, 0)_{lab}$	four-momentum of the target nucleon
$q = (p - p')$	four-momentum of the exchanged virtual photon
E	energy of the incident lepton
E'	energy of the scattered lepton
\vec{p}	three-momentum of the incident lepton
\vec{p}'	three-momentum of the scattered lepton
θ	angle of scattered lepton w.r.t. the incident lepton - i.e. angle between \vec{p} and \vec{p}' .
$\nu = \frac{P \cdot q}{M}$	laboratory energy loss of lepton
$q^2 = -Q^2$	four-momentum transfer squared, $Q^2 \geq 0$.
$W^2 = (q + P)^2$	centre of mass energy squared of the virtual photon-nucleon system.
$S = (p + P)^2$	centre of mass energy squared of the lepton-nucleon system.

* Only the muon inclusive kinematic is summarized here.

APPENDIX A (continued)

$\omega = 1/x$	scaling variables
$\omega' = 1/x'$	scaling variables
$y = v/E$	
K	equivalent photon energy
Γ	transverse virtual photon flux
ϵ	ratio of the longitudinal to transverse virtual photon fluxes

Formulae

$$p^2 = p'^2 = m_\ell^2 \quad ; \quad p^2 = M^2$$

$$v = E_{lab} - E'_{lab}$$

$$Q^2 = -(p-p')^2 = 2(EE' - \vec{p} \cdot \vec{p}' - m_\ell^2)$$

$$Q_{min}^2 = 2(EE' - |\vec{p}| \cdot |\vec{p}'| = m_\ell^2)$$

$$Q^2 = 4EE' \sin^2(\theta/2) + \frac{m_\ell^2 v^2}{EE'}$$

in the limit where terms of orders higher than $\frac{m_\ell^2}{E^2}$ are ignored.

$$W^2 = 2Mv + M^2 - Q^2, \quad S = m_\ell^2 + M^2 + 2ME$$

$$\omega = \frac{2Mv}{Q^2}$$

$$\omega' = 1 + \frac{W^2}{Q^2} = \omega + \frac{M^2}{Q^2}$$

$$K = \frac{W^2 - M^2}{2M}$$

$$\Gamma = \frac{\alpha}{2\pi^2} \frac{K}{Q^2} \frac{E'}{E} \frac{1}{1-\epsilon} \frac{\pi}{EE'}$$

$$\epsilon = \left[1 + \frac{2(Q^2 + v^2) \tan^2 \theta/2}{Q^2 (1 - Q_{min}^2/Q^2)^2} \right]^{-1}$$

APPENDIX A (Continued)

Cross-sections, Form Factors, Structure Functions

G_E	Electric elastic form factor for the nucleon
G_M	magnetic elastic form factor for the nucleon
W_1	inelastic structure functions for
W_2	the nucleon
σ_T	transverse virtual photoabsorption cross-section
σ_L	longitudinal virtual photoabsorption cross-section.
$R = \frac{\sigma_L}{\sigma_T}$	ratio of the longitudinal to transverse virtual photoabsorption cross-sections

for elastic scattering

$$\frac{d\sigma}{dq^2} = \frac{4\pi\alpha^2}{Q^4 (S - M^2)^2} \left[\frac{Q^4}{2} G_M^2 + \frac{\left(G_E^2 + \frac{Q^2}{4M^2} G_M^2 \right)}{1 + \frac{Q^2}{4M^2}} ((S - M^2)^2 - Q^2 W^2) \right]$$

for inelastic scattering

$$\frac{d^2\sigma}{dv dq^2} = \frac{\pi}{|\vec{p}| |\vec{p}'|} \frac{2\alpha^2 |\vec{p}'|}{Q^4 |\vec{p}|} \left[(2EE' - \frac{Q^2}{2}) W_2(Q^2, \nu) + (Q^2 - 2M_\ell^2) W_1(Q^2, \nu) \right]$$

or

$$\frac{d^2\sigma}{dE' d\Omega} = \sigma_{\text{Mott}} [W_2(Q^2, \nu) + 2 \tan^2(\theta/2) W_1(Q^2, \nu)]$$

where

$$\sigma_{\text{Mott}} = \frac{\alpha^2}{4E^2} \frac{\cos^2(\theta/2)}{\sin^4(\theta/2)}$$

APPENDIX A (Continued)

or

$$\frac{d^2\sigma}{dv dq^2} = \Gamma [\sigma_T(Q^2, v) + (\epsilon + \delta) \sigma_L(Q^2, v)]$$

$$\text{where } \delta = \frac{2m_\ell^2(1-\epsilon)}{Q^2}$$

the following relation between σ_T , σ_L , W_1 , W_2 may be written

$$W_1 = \frac{K}{4\pi^2\alpha} \sigma_T ; \quad W_2 = \frac{K}{4\pi^2\alpha} \frac{Q^2}{Q^2+v^2} (\sigma_T + \sigma_L)$$

$$\frac{W_1}{W_2} = \left(1 + \frac{v^2}{Q^2}\right) \left(\frac{1}{1+R}\right)$$

finally F_1 , F_2 are defined as

$$F_1 = 2MW_1 ; \quad F_2 = vW_2$$

REFERENCES

1. R. Hofstadter et al, Ann. Rev. Nuc. Sci. 7, 231 (1957).
2. H. Pilkuhn, Interactions of Hadrons (North Holland, Amsterdam, 1967).
3. S.D. Drell and J.D. Walecka, Ann. Phys. 28, 18 (1964).
4. L.N. Hand, Phys. Rev. 129, 1834 (1963).
5. L.N. Hand, Thesis, Stanford (1961) unpublished.
6. W. Bartel et al, Phys. Lett. 25B, 236 (1967).
7. D.H. Coward et al, Phys. Rev. Lett. 20, 292 (1968).
8. E. Bloom et al, Phys. Rev. Lett. 23, 930 (1969).
9. M. Breidenbach et al, Phys. Rev. Lett 23, 935 (1969).
10. G. Miller et al, Phys. Rev. D5, 528 (1972).
11. J. Friedman and H. Kendall, Ann Rev. Nuc. Sci. 22, 203 (1972).
12. A. Bodek, Thesis, MIT (1972).
13. P.N. Kirk et al, Phys. Rev. D8, 63 (1973).
14. E.M. Riorden et al, SLAC-PUB-1634 (1975).
15. S. Stein et al, Phys. Rev. D12, 1884 (1975).
16. W.B. Atwood, SLAC-Report-185 (1975).
17. Y. Watanabe et al, Phys. Rev. Lett. 35, 898, (1975).
C. Chang et al, Phys. Rev. Lett. 35, 901 (1975).
18. W.A. Loomis et al, Phys. Rev. Lett. 35, 1483 (1975).
H.L. Anderson et al, Phys. Rev. Lett. 36, 1422 (1976).
H.L. Anderson et al, Phys. Rev. Lett. 37, 4 (1976).
19. M. Gell-Mann, Phys. Lett. 8, 214 (1964).
20. K. Gottfried, Phys. Rev. Lett. 18, 1174 (1967).
21. C. Callan and D. Gross, Phys. Rev. Lett. 21, 311 (1968).
22. J. Bjorken, Phys. Rev. 179, 1547 (1969).
23. N. Dombey, Rev. Mod. Phys. 41, 236 (1969).
24. J. Bjorken and E. Paschos, Phys. Rev. 185, 1975 (1969).
25. E. Bloom and F. Gilman, Phys. Rev. Lett. 25, 1140 (1970).

26. F. Close and J. Gunion, Phys. Rev. D4, 742 (1971).
27. C.H. Llewellyn-Smith, Phys. Rev. D4, 2392 (1971).
28. J. Kuti and V. Weisskopf, Phys. Rev. D4, 3418 (1971).
29. J.J. Sakurai and I. Schildknecht, Phys. Lett. 40B, 121 (1972).
30. A. Chodos, R.L. Jaffe, K. Johnson, C.B. Thorn and V. Weisskopf
Phys. Rev. D9, 3471 (1974).
31. H. Georgi and H.D. Politzer, Phys. Rev. Lett, 36, 1281 (1976).
32. D.H. Perkins, Sum Rules in Deep Inelastic Scattering,
Oxford Internal Note (1972).
33. R.P. Feynman, Photon-Hadron Interactions, Benjamin (1972).
34. P. Roy, Theory of Lepton-Hadron Processes at High Energy,
Clarendon Press, Oxford (1975).
35. W.K.H. Panofsky, Proceedings of the 14th International
Conference on High Energy Physics, Vienna (1968).
36. F.J. Gilman, Proceedings of the International Symposium on
Electron and Photon Interactions, Daresbury (1969).
37. J.G. Rutherglen, Proceedings of the International Symposium
on Electron and Photon Interactions, Daresbury (1969).
38. H.W. Kendall, Proceedings of the International Symposium on
Electron and Photon Interactions, Cornell (1971).
39. E. Bloom, Proceedings of the International Symposium on
Electron and Photon Interactions, Bonn, (1973).
40. R.E. Taylor, Proceedings of the International Symposium on
Lepton and Photon Interactions, Stanford (1975).
41. C.H. Llewellyn-Smith, Proceedings of the International
Symposium on Lepton and Photon Interactions, Stanford (1975).
- 42.. Proceedings of the International Symposium on Lepton and
Photon Interactions, Stanford (1975).
43. L.S. Rochester et al, Phys. Rev. Lett. 36, 1284 (1976).
44. R.W. Ellsworth et al, Phys. Rev. 165, 1449 (1968).
L. Camilleri et al, Phys. Rev. Lett, 23, 153 (1969).
I. Kostoulas et al, Phys. Rev. Lett. 32, 489 (1974).
45. W. Toner et al, Phys. Letts. 36B, 251 (1971)
T.J. Braunstein et al, Phys. Rev. D6, 106 (1972).
A. Entenberg et al, Phys. Rev. Lett 32, 1284 (1976).
46. F.H. Combley, Proceedings of the International Symposium on
Lepton and Photon Interactions, Stanford (1975).

47. R. Heisterberg, Thesis, University of Chicago (1976).
48. F.E. Close, Proceedings of the Physics with Polarized Targets at High Energy Meeting, RL-73-088 Rutherford (1973).
49. A.J. Alguard et al, SLAC-PUB-1790 (1976).
50. M. Livingston and J. Blewett, Particle Accelerators, McGraw-Hill (1962).
51. P. Rice-Evans, Sparks, Streamer, Proportional and Drift Chambers, Richelieu (1974).
52. K. Burns et al, Nuc. Inst. Meth. 106, 171 (1973).
T.A. Nunamaker, Nuc. Inst. Meth. 106, 557 (1973).
53. T.A. Nunamaker and D. Turner, Nuc. Inst. Meth. 113, 445 (1973).
T.A. Nunamaker, Rev. Sci. Inst. 42, 1701 (1971).
54. S. Pordes, Thesis, Harvard University (1976).
55. D. Ritson, Techniques of High Energy Physics, Interscience Publishers, Inc. New York (1961).
56. W.A. Loomis, E98 Internal Report (1974).
57. G.I. Kirkbride, Thesis, Oxford University (1976).
58. C. Kittel, Introduction to Solid State Physics, Wiley (1971).
59. E. Wallis, Rutherford Report, RHEL-M-H19.
60. Off-line Analysis Notes, E98 Internal Document (1974)
Oxford Analysis, E98 Internal Document (1975).
61. L. Mo and Y. Tsai, Rev. Mod. Phys. 41, 205 (1969).
62. Y.S. Tsai, Proc. Nuc. Structure Conf. Stanford (1963).
63. G. Parisi and R. Petronzio, Phys. Lett. 62B, 331 (1976).
64. M. Greco, Nuc. Phys. B63, 398 (1973).
G.J. Gounaris, E.K. Manesis and A. Verganelakis, Phys. Lett. 59B, 391 (1975).
65. F.E. Close, D.M. Scott and D. Sivers, Phys. Lett. 62B, 213 (1976).
66. S. Stein et al, SLAC-PUB-1528 (1975).
67. C. Callan and D. Gross, Phys. Rev. Lett. 22, 156 (1969).
68. J. Kogut and L. Susskind, Phys. Rev. D9, 3391 (1974).

DATA TABLE DT2(b) (147Gev data)

RADIATIVE CORRECTION FROM ELASTIC SCATTERING

Q SQRD	Elastic radiative tail $\frac{d^2\sigma}{d\Omega dE}$ in (fermi) ² per GeV															
	0.0	0.0	0.0	0.0	0.0	0.0	0.0	0.0	0.0	0.0	0.0	0.0	0.0	0.0	0.0	0.0
47.50	0.0	0.0	0.0	0.0	0.0	0.0	0.0	0.0	0.0	0.0	0.0	0.0	0.0	0.0	0.0	0.0
42.50	0.0	0.0	0.0	0.0	0.0	0.0	0.0	0.0	0.0	0.0	0.0	0.0	0.0	0.0	0.0	0.0
37.50	0.0	0.0	0.0	0.0	0.0	0.0	0.0	0.0	0.0	0.0	0.0	0.0	0.0	0.0	0.0	0.0
32.50	0.0	0.0	0.0	0.0	0.0	0.0	0.0	0.0	0.0	0.0	0.0	0.0	0.0	0.0	0.0	0.0
27.50	0.0	0.0	0.0	0.0	0.0	0.0	0.0	0.0	0.0	0.0	0.0	0.0	0.0	0.0	0.0	0.0
22.50	0.0	0.0	0.0	0.0	0.0	0.0	0.0	0.0	0.0	0.0	0.0	0.0	0.0	0.0	0.0	0.0
17.50	0.0	0.0	0.0	0.0	0.0	0.0	0.0	0.0	0.0	0.0	0.0	0.0	0.0	0.0	0.0	0.0
12.50	0.0	0.0	0.0	0.0	0.0	0.0	0.0	0.0	0.0	0.0	0.0	0.0	0.0	0.0	0.0	0.0
9.75	0.0	0.0	0.0	0.0	0.0	0.0	0.0	0.0	0.0	0.0	0.0	0.0	0.0	0.0	0.0	0.0
9.25	0.0	0.0	0.0	0.0	0.0	0.0	0.0	0.0	0.0	0.0	0.0	0.0	0.0	0.0	0.0	0.0
8.75	0.0	0.0	0.0	0.0	0.0	0.0	0.0	0.0	0.0	0.0	0.0	0.0	0.0	0.0	0.0	0.0
8.25	0.0	0.0	0.0	0.0	0.0	0.0	0.0	0.0	0.0	0.0	0.0	0.0	0.0	0.0	0.0	0.0
7.75	0.0	0.0	0.0	0.0	0.0	0.0	0.0	0.0	0.0	0.0	0.0	0.0	0.0	0.0	0.0	0.0
7.25	0.0	0.0	0.0	0.0	0.0	0.0	0.0	0.0	0.0	0.0	0.0	0.0	0.0	0.0	0.0	0.0
6.75	0.0	0.0	0.0	0.0	0.0	0.0	0.0	0.0	0.0	0.0	0.0	0.0	0.0	0.0	0.0	0.0
6.25	0.0	0.0	0.0	0.0	0.0	0.0	0.0	0.0	0.0	0.0	0.0	0.0	0.0	0.0	0.0	0.0
5.75	0.0	0.0	0.0	0.0	0.0	0.0	0.0	0.0	0.0	0.0	0.0	0.0	0.0	0.0	0.0	0.0
5.25	0.0	0.0	0.0	0.0	0.0	0.0	0.0	0.0	0.0	0.0	0.0	0.0	0.0	0.0	0.0	0.0
4.75	0.0	0.0	0.0	0.0	0.0	0.0	0.0	0.0	0.0	0.0	0.0	0.0	0.0	0.0	0.0	0.0
4.25	0.0	0.0	0.0	0.0	0.0	0.0	0.0	0.0	0.0	0.0	0.0	0.0	0.0	0.0	0.0	0.0
3.75	0.0	0.0	0.0	0.0	0.0	0.0	0.0	0.0	0.0	0.0	0.0	0.0	0.0	0.0	0.0	0.0
3.25	0.0	0.0	0.0	0.0	0.0	0.0	0.0	0.0	0.0	0.0	0.0	0.0	0.0	0.0	0.0	0.0
2.75	0.0	0.0	0.0	0.0	0.0	0.0	0.0	0.0	0.0	0.0	0.0	0.0	0.0	0.0	0.0	0.0
2.25	0.0	0.0	0.0	0.0	0.0	0.0	0.0	0.0	0.0	0.0	0.0	0.0	0.0	0.0	0.0	0.0
1.75	0.0	0.0	0.0	0.0	0.0	0.0	0.0	0.0	0.0	0.0	0.0	0.0	0.0	0.0	0.0	0.0
1.25	0.0	0.0	0.0	0.0	0.0	0.0	0.0	0.0	0.0	0.0	0.0	0.0	0.0	0.0	0.0	0.0
0.75	0.0	0.0	0.0	0.0	0.0	0.0	0.0	0.0	0.0	0.0	0.0	0.0	0.0	0.0	0.0	0.0
0.25	0.0	0.0	0.0	0.0	0.0	0.0	0.0	0.0	0.0	0.0	0.0	0.0	0.0	0.0	0.0	0.0
NU	2.5	7.5	12.5	17.5	25.0	35.0	45.0	55.0	65.0	75.0	85.0	95.0	105.0	115.0	125.0	135.0

DATA TABLE DT5(b) (96GeV data)

DATA TABLE DT5(c) (96GeV data)

WEIGHTED EVENTS AFTER RADIATIVE TAIL SUBTRACTION

Q SQRD	-5.0	0.0	2.5	5.0	7.5	10.0	15.0	20.0	30.0	40.0	50.0	60.0	70.0	80.0	90.0	100.0
30.00- 50.00 +/-	0	0	0	0	0	0	0	0	0	3	0	0	0	0	0	3
15.00- 30.00 +/-	0	0	0	0	0	0	2	3	16	12	13	5	17	34	30	133
10.00- 15.00 +/-	0	0	0	0	0	2	7	5	17	26	17	4	8	12	27	131
9.00- 10.00 +/-	0	0	0	0	0	2	6	3	5	8	2	1	1	0	0	31
8.00- 9.00 +/-	0	0	0	0	2	4	8	10	11	14	7	3	1	5	8	76
7.00- 8.00 +/-	0	0	0	2	2	3	15	9	16	20	8	3	3	3	2	84
6.00- 7.00 +/-	0	0	0	5	2	10	22	15	24	27	14	11	8	6	7	149
5.00- 6.00 +/-	0	0	0	18	5	11	25	26	32	23	17	13	7	12	5	189
4.00- 5.00 +/-	0	0	0	27	6	21	46	38	47	34	27	17	12	11	8	288
3.00- 4.00 +/-	0	0	0	66	10	67	84	73	103	49	39	23	29	12	10	555
2.00- 3.00 +/-	0	0	0	195	17	133	193	138	160	109	74	52	38	45	18	1156
1.50- 2.00 +/-	0	0	0	198	17	143	195	140	175	112	75	42	38	40	16	1175
1.00- 1.50 +/-	0	0	0	389	25	241	331	246	314	215	127	122	86	60	25	2155
0.80- 1.00 +/-	0	0	0	243	21	176	228	126	215	118	85	72	57	54	22	1397
0.60- 0.80 +/-	0	0	0	470	35	266	353	213	312	230	126	102	68	62	20	2221
0.40- 0.60 +/-	0	0	0	0	0	0	0	0	0	0	0	212	116	105	50	484
0.30- 0.40 +/-	0	0	0	0	0	0	0	0	0	0	0	0	68	91	26	185
0.20- 0.30 +/-	0	0	0	0	0	0	0	0	0	0	0	0	87	138	61	285
0.10- 0.20 +/-	0	0	0	0	0	0	0	0	0	0	0	0	0	0	0	0
0.05- 0.10 +/-	0	0	0	0	0	0	0	0	0	0	0	0	0	0	0	0
0.0 - 0.05 +/-	0	0	0	0	0	0	0	0	0	0	0	0	0	0	0	0
	0	0	0	1615	1081	1515	1045	1447	999	631	693	645	693	334	331	10689
	0	0	0	56	44	52	41	48	38	28	30	29	35	31	0	134

NU GEV

DATA TABLE DT6(b) (147GeV data)

DATA TABLE DT6(d) (147GeV data)

CROSS-SECTIONS IN PICOBARN PER GEV**3

Q SQRD	Muon inclusive cross-section																		$d^2\sigma$ $dvdq^2$																																																																																																																																																																																																																																																																																																																																																																																																																																																																																																																																																																																																																																																																																																																																																																																																																																																																																																																																																																																																																																																																																																																																								
	30.00-	50.00	+/-	0.0	0.0	0.0	0.0	0.0	0.0	0.0	0.0	0.0	0.0	0.0	0.0	0.0	0.0	0.0	0.0	0.0	0.0	0.0	0.0	0.0	0.0	0.0	0.0	0.0	0.0	0.0	0.0	0.0	0.0	0.0	0.0	0.0	0.0	0.0	0.0	0.0	0.0	0.0	0.0	0.0	0.0	0.0	0.0	0.0	0.0	0.0	0.0	0.0	0.0	0.0	0.0	0.0	0.0	0.0	0.0	0.0	0.0	0.0	0.0	0.0	0.0	0.0	0.0	0.0	0.0	0.0	0.0	0.0	0.0	0.0	0.0	0.0	0.0	0.0	0.0	0.0	0.0	0.0	0.0	0.0	0.0	0.0	0.0	0.0	0.0	0.0	0.0	0.0	0.0	0.0	0.0	0.0	0.0	0.0	0.0	0.0	0.0	0.0	0.0	0.0	0.0	0.0	0.0	0.0	0.0	0.0	0.0	0.0	0.0	0.0	0.0	0.0	0.0	0.0	0.0	0.0	0.0	0.0	0.0	0.0	0.0	0.0	0.0	0.0	0.0	0.0	0.0	0.0	0.0	0.0	0.0	0.0	0.0	0.0	0.0	0.0	0.0	0.0	0.0	0.0	0.0	0.0	0.0	0.0	0.0	0.0	0.0	0.0	0.0	0.0	0.0	0.0	0.0	0.0	0.0	0.0	0.0	0.0	0.0	0.0	0.0	0.0	0.0	0.0	0.0	0.0	0.0	0.0	0.0	0.0	0.0	0.0	0.0	0.0	0.0	0.0	0.0	0.0	0.0	0.0	0.0	0.0	0.0	0.0	0.0	0.0	0.0	0.0	0.0	0.0	0.0	0.0	0.0	0.0	0.0	0.0	0.0	0.0	0.0	0.0	0.0	0.0	0.0	0.0	0.0	0.0	0.0	0.0	0.0	0.0	0.0	0.0	0.0	0.0	0.0	0.0	0.0	0.0	0.0	0.0	0.0	0.0	0.0	0.0	0.0	0.0	0.0	0.0	0.0	0.0	0.0	0.0	0.0	0.0	0.0	0.0	0.0	0.0	0.0	0.0	0.0	0.0	0.0	0.0	0.0	0.0	0.0	0.0	0.0	0.0	0.0	0.0	0.0	0.0	0.0	0.0	0.0	0.0	0.0	0.0	0.0	0.0	0.0	0.0	0.0	0.0	0.0	0.0	0.0	0.0	0.0	0.0	0.0	0.0	0.0	0.0	0.0	0.0	0.0	0.0	0.0	0.0	0.0	0.0	0.0	0.0	0.0	0.0	0.0	0.0	0.0	0.0	0.0	0.0	0.0	0.0	0.0	0.0	0.0	0.0	0.0	0.0	0.0	0.0	0.0	0.0	0.0	0.0	0.0	0.0	0.0	0.0	0.0	0.0	0.0	0.0	0.0	0.0	0.0	0.0	0.0	0.0	0.0	0.0	0.0	0.0	0.0	0.0	0.0	0.0	0.0	0.0	0.0	0.0	0.0	0.0	0.0	0.0	0.0	0.0	0.0	0.0	0.0	0.0	0.0	0.0	0.0	0.0	0.0	0.0	0.0	0.0	0.0	0.0	0.0	0.0	0.0	0.0	0.0	0.0	0.0	0.0	0.0	0.0	0.0	0.0	0.0	0.0	0.0	0.0	0.0	0.0	0.0	0.0	0.0	0.0	0.0	0.0	0.0	0.0	0.0	0.0	0.0	0.0	0.0	0.0	0.0	0.0	0.0	0.0	0.0	0.0	0.0	0.0	0.0	0.0	0.0	0.0	0.0	0.0	0.0	0.0	0.0	0.0	0.0	0.0	0.0	0.0	0.0	0.0	0.0	0.0	0.0	0.0	0.0	0.0	0.0	0.0	0.0	0.0	0.0	0.0	0.0	0.0	0.0	0.0	0.0	0.0	0.0	0.0	0.0	0.0	0.0	0.0	0.0	0.0	0.0	0.0	0.0	0.0	0.0	0.0	0.0	0.0	0.0	0.0	0.0	0.0	0.0	0.0	0.0	0.0	0.0	0.0	0.0	0.0	0.0	0.0	0.0	0.0	0.0	0.0	0.0	0.0	0.0	0.0	0.0	0.0	0.0	0.0	0.0	0.0	0.0	0.0	0.0	0.0	0.0	0.0	0.0	0.0	0.0	0.0	0.0	0.0	0.0	0.0	0.0	0.0	0.0	0.0	0.0	0.0	0.0	0.0	0.0	0.0	0.0	0.0	0.0	0.0	0.0	0.0	0.0	0.0	0.0	0.0	0.0	0.0	0.0	0.0	0.0	0.0	0.0	0.0	0.0	0.0	0.0	0.0	0.0	0.0	0.0	0.0	0.0	0.0	0.0	0.0	0.0	0.0	0.0	0.0	0.0	0.0	0.0	0.0	0.0	0.0	0.0	0.0	0.0	0.0	0.0	0.0	0.0	0.0	0.0	0.0	0.0	0.0	0.0	0.0	0.0	0.0	0.0	0.0	0.0	0.0	0.0	0.0	0.0	0.0	0.0	0.0	0.0	0.0	0.0	0.0	0.0	0.0	0.0	0.0	0.0	0.0	0.0	0.0	0.0	0.0	0.0	0.0	0.0	0.0	0.0	0.0	0.0	0.0	0.0	0.0	0.0	0.0	0.0	0.0	0.0	0.0	0.0	0.0	0.0	0.0	0.0	0.0	0.0	0.0	0.0	0.0	0.0	0.0	0.0	0.0	0.0	0.0	0.0	0.0	0.0	0.0	0.0	0.0	0.0	0.0	0.0	0.0	0.0	0.0	0.0	0.0	0.0	0.0	0.0	0.0	0.0	0.0	0.0	0.0	0.0	0.0	0.0	0.0	0.0	0.0	0.0	0.0	0.0	0.0	0.0	0.0	0.0	0.0	0.0	0.0	0.0	0.0	0.0	0.0	0.0	0.0	0.0	0.0	0.0	0.0	0.0	0.0	0.0	0.0	0.0	0.0	0.0	0.0	0.0	0.0	0.0	0.0	0.0	0.0	0.0	0.0	0.0	0.0	0.0	0.0	0.0	0.0	0.0	0.0	0.0	0.0	0.0	0.0	0.0	0.0	0.0	0.0	0.0	0.0	0.0	0.0	0.0	0.0	0.0	0.0	0.0	0.0	0.0	0.0	0.0	0.0	0.0	0.0	0.0	0.0	0.0	0.0	0.0	0.0	0.0	0.0	0.0	0.0	0.0	0.0	0.0	0.0	0.0	0.0	0.0	0.0	0.0	0.0	0.0	0.0	0.0	0.0	0.0	0.0	0.0	0.0	0.0	0.0	0.0	0.0	0.0	0.0	0.0	0.0	0.0	0.0	0.0	0.0	0.0	0.0	0.0	0.0	0.0	0.0	0.0	0.0	0.0	0.0	0.0	0.0	0.0	0.0	0.0	0.0	0.0	0.0	0.0	0.0	0.0	0.0	0.0	0.0	0.0	0.0	0.0	0.0	0.0	0.0	0.0	0.0	0.0	0.0	0.0	0.0	0.0	0.0	0.0	0.0	0.0	0.0	0.0	0.0	0.0	0.0	0.0	0.0	0.0	0.0	0.0	0.0	0.0	0.0	0.0	0.0	0.0	0.0	0.0	0.0	0.0	0.0	0.0	0.0	0.0	0.0	0.0	0.0	0.0	0.0	0.0	0.0	0.0	0.0	0.0	0.0	0.0	0.0	0.0	0.0	0.0	0.0	0.0	0.0	0.0	0.0	0.0	0.0	0.0	0.0	0.0	0.0	0.0	0.0	0.0	0.0	0.0	0.0	0.0	0.0	0.0	0.0	0.0	0.0	0.0	0.0	0.0	0.0	0.0	0.0	0.0	0.0	0.0	0.0	0.0	0.0	0.0	0.0	0.0	0.0	0.0	0.0	0.0	0.0	0.0	0.0	0.0	0.0	0.0	0.0	0.0	0.0	0.0	0.0	0.0	0.0	0.0	0.0	0.0	0.0	0.0	0.0	0.0	0.0	0.0	0.0	0.0	0.0	0.0	0.0	0.0	0.0	0.0	0.0	0.0	0.0	0.0	0.0	0.0	0.0	0.0	0.0	0.0	0.0	0.0	0.0	0.0	0.0	0.0	0.0	0.0	0.0	0.0	0.0	0.0	0.0	0.0	0.0	0.0	0.0	0.0	0.0	0.0	0.0	0.0	0.0	0.0	0.0	0.0	0.0	0.0	0.0	0.0	0.0	0.0	0.0	0.0	0.0	0.0	0.0	0.0	0.0	0.0	0.0	0.0	0.0	0.0	0.0	0.0	0.0	0.0	0.0	0.0	0.0	0.0	0.0	0.0	0.0	0.0	0.0	0.0	0.0	0.0	0.0	0.0	0.0	0.0	0.0	0.0	0.0	0.0	0.0	0.0	0.0	0.0	0.0	0.0	0.0	0.0	0.0	0.0	0.0	0.0	0.0	0.0	0.0	0.0	0.0	0.0	0.0	0.0	0.0	0.0	0.0	0.0	0.0	0.0	0.0	0.0	0.0	0.0	0.0	0.0	0.0	0.0	0.0	0.0	0.0	0.0	0.0	0.0	0.0	0.0	0.0	0.0	0.0	0.0	0.0	0.0	0.0	0.0	0.0	0.0	0.0	0.0	0.0	0.0	0.0	0.0	0.0	0.0	0.0	0.0	0.0	0.0	0.0	0.0	0.0	0.0	0.0	0.0	0.0	0.0	0.0	0.0	0.0	0.0	0.0	0.0	0.0	0.0	0.0	0.0	0.0	0.0	0.0	0.0	0.0	0.0	0.0	0.0	0.0	0.0	0.0	0.0	0.0	0.0	0.0	0.0	0.0	0.0	0.0	0.0	0.0	0.0	0.0	0.0	0.0	0.0	0.0	0.0	0.0	0.0	0.0	0.0	0.0	0.0	0.0	0.0	0.0	0.0	0.0	0.0	0.0	0.0	0.0	0.0	0.0	0.0	0.0	0.0	0.0	0.0	0.0	0.0	0.0	0.0

NU GEV

DATA TABLE DT 7(a) (96 GeV data)

FULL EVENTS

Q SQRD

Q SQRD	1-	2.	3.	4.	5.	7.	9.	11.	14.	20.	35.	45.	60.	80.	120.	160.	240.	400.	600.	1000.	1400.
50.00-70.00	0	0	0	0	0	0	0	0	0	0	0	0	0	0	0	0	0	0	0	0	0
30.00-50.00	0	1	0	0	1	0	0	0	0	0	0	0	0	0	0	0	0	0	0	0	0
15.00-30.00	2	16	8	8	8	9	4	3	0	0	0	0	0	0	0	0	0	0	0	0	0
10.00-15.00	5	11	7	13	25	17	14	8	0	0	0	0	0	0	0	0	0	0	0	0	0
8.00-10.00	6	10	12	9	17	10	16	8	0	7	0	0	0	0	0	0	0	0	0	0	0
7.00- 8.00	3	6	11	5	13	10	11	15	5	7	1	0	0	0	0	0	0	0	0	0	0
6.00- 7.00	2	12	13	9	18	10	19	18	15	21	8	0	0	0	0	0	0	0	0	0	0
5.00- 6.00	5	14	16	9	27	0	18	15	17	26	24	0	0	0	0	0	0	0	0	0	0
4.00- 5.00	0	16	20	19	34	0	27	21	24	35	52	4	0	0	0	0	0	0	0	0	0
3.50- 4.00	0	4	19	20	27	0	21	12	30	24	46	9	0	0	0	0	0	0	0	0	0
3.00- 3.50	0	6	16	17	25	0	21	28	23	36	42	22	9	0	0	0	0	0	0	0	0
2.75- 3.00	0	0	9	12	19	0	12	6	18	21	32	9	13	0	0	0	0	0	0	0	0
2.50- 2.75	0	0	8	7	26	0	11	18	20	21	34	17	19	1	0	0	0	0	0	0	0
2.25- 2.50	0	0	3	18	36	0	23	13	23	35	44	20	26	12	0	0	0	0	0	0	0
2.00- 2.25	0	0	0	15	31	0	25	24	38	33	57	28	33	35	0	0	0	0	0	0	0
1.75- 2.00	0	0	0	1	41	0	44	32	35	49	72	33	33	37	0	0	0	0	0	0	0
1.50- 1.75	0	0	0	0	38	0	51	32	41	74	98	53	50	47	43	0	0	0	0	0	0
1.25- 1.50	0	0	0	0	10	0	65	50	55	91	140	69	84	57	90	2	0	0	0	0	0
1.00- 1.25	0	0	0	0	0	0	19	73	78	123	157	77	87	72	152	67	0	0	0	0	0
0.90- 1.00	0	0	0	0	0	0	0	15	39	62	66	35	45	34	59	68	13	0	0	0	0
0.80- 0.90	0	0	0	0	0	0	0	4	32	65	101	27	42	45	68	57	46	0	0	0	0
0.70- 0.80	0	0	0	0	0	0	0	0	23	94	92	51	41	65	82	49	72	0	0	0	0
0.60- 0.70	0	0	0	0	0	0	0	0	1	68	101	50	27	58	80	63	128	11	0	0	0
0.50- 0.60	0	0	0	0	0	0	0	0	0	0	0	0	0	0	0	0	137	102	0	0	0
0.40- 0.50	0	0	0	0	0	0	0	0	0	0	0	0	0	0	0	0	60	237	0	0	0
0.30- 0.40	0	0	0	0	0	0	0	0	0	0	0	0	0	0	0	0	0	118	166	0	0
0.20- 0.30	0	0	0	0	0	0	0	0	0	0	0	0	0	0	0	0	0	0	275	209	0
TOTAL	23	96	142	163	396	401	395	534	892	1167	504	509	463	583	306	456	468	441	209	0	0
OMEGA	1-	2.	3.	4.	5.	7.	9.	11.	14.	20.	35.	45.	60.	80.	120.	160.	240.	400.	600.	1000.	1400.

DATA TABLE DT7(b) (96 GeV data)

EVENTS WEIGHTED BY ACCEPTANCE

Q SQRD

	1.	2.	3.	4.	5.	7.	9.	11.	14.	20.	35.	45.	60.	80.	120.	160.	240.	400.	600.	1000.	1400.
50.00-70.00 +/-	0	0	0	0	0	0	0	0	0	0	0	0	0	0	0	0	0	0	0	0	0
30.00-50.00 +/-	0	3	3	0	0	0	0	0	0	0	0	0	0	0	0	0	0	0	0	0	0
15.00-30.00 +/-	2	22	6	12	13	33	37	15	0	0	0	0	0	0	0	0	0	0	0	0	0
10.00-15.00 +/-	5	12	4	8	14	28	17	15	35	15	0	0	0	0	0	0	0	0	0	0	0
8.00-10.00 +/-	7	11	3	13	10	18	17	8	9	3	0	0	0	0	0	0	0	0	0	0	0
7.00- 8.00 +/-	4	7	3	13	5	14	12	15	5	2	3	3	0	0	0	0	0	0	0	0	0
6.00- 7.00 +/-	2	14	4	15	10	21	21	19	16	13	13	5	0	0	0	0	0	0	0	0	0
5.00- 6.00 +/-	6	17	5	19	10	31	20	16	18	26	27	6	0	0	0	0	0	0	0	0	0
4.00- 5.00 +/-	0	21	5	26	23	41	32	24	27	38	54	8	3	0	0	0	0	0	0	0	0
3.50- 4.00 +/-	0	5	3	26	26	35	27	15	36	28	48	7	10	0	0	0	0	0	0	0	0
3.00- 3.50 +/-	0	9	4	23	24	35	29	37	29	43	46	7	21	3	0	0	0	0	0	0	0
2.75- 3.00 +/-	0	0	0	14	18	29	18	9	25	26	36	6	9	12	0	0	0	0	0	0	0
2.50- 2.75 +/-	0	0	0	13	12	41	17	27	29	28	38	7	17	1	0	0	0	0	0	0	0
2.25- 2.50 +/-	0	0	0	5	27	54	33	19	32	47	53	8	21	25	11	0	0	0	0	0	0
2.00- 2.25 +/-	0	0	0	0	23	47	37	35	54	46	71	9	30	33	32	0	0	0	0	0	0
1.75- 2.00 +/-	0	0	0	0	1	61	66	47	50	70	94	11	36	34	35	8	0	0	0	0	0
1.50- 1.75 +/-	0	0	0	0	0	57	77	48	61	108	135	14	64	54	47	39	0	0	0	0	0
1.25- 1.50 +/-	0	0	0	0	0	15	97	74	82	132	200	17	91	102	60	87	2	0	0	0	0
1.00- 1.25 +/-	0	0	0	0	0	0	39	118	125	192	241	19	115	124	89	164	60	0	0	0	0
0.90- 1.00 +/-	0	0	0	0	0	0	0	27	68	109	112	14	59	72	52	72	67	11	0	0	0
0.80- 0.90 +/-	0	0	0	0	0	0	0	8	64	125	190	19	50	76	78	95	61	40	0	0	0
0.70- 0.80 +/-	0	0	0	0	0	0	0	0	53	214	207	22	110	84	125	143	60	68	0	0	0
0.60- 0.70 +/-	0	0	0	0	0	0	0	0	3	194	288	24	137	71	137	170	92	130	9	0	0
0.50- 0.60 +/-	0	0	0	0	0	0	0	0	0	0	0	0	0	0	0	0	0	166	90	0	0
0.40- 0.50 +/-	0	0	0	0	0	0	0	0	0	0	0	0	0	0	0	0	0	87	240	0	0
0.30- 0.40 +/-	0	0	0	0	0	0	0	0	0	0	0	0	0	0	0	0	0	0	16	0	0
0.20- 0.30 +/-	0	0	0	0	0	0	0	0	0	0	0	0	0	0	0	0	0	0	0	267	178
TOTAL +/-	26	120	13	185	217	558	585	575	822	1472	1857	776	712	666	778	342	501	459	22	412	178
OMEGA	1.	2.	3.	4.	5.	7.	9.	11.	14.	20.	35.	45.	60.	80.	120.	160.	240.	400.	600.	1000.	1400.

DATA TABLE DT7(c) (96 GeV data)

SD AFTER SUBTRACTION OF RADIATIVE TAIL

EVENTS WEIGHTED BY ACCEPTANCE

Q SORD

	1.	2.	3.	4.	5.	7.	9.	11.	14.	20.	35.	45.	60.	80.	120.	160.	240.	400.	600.	1000.	1400.
50.00-70.00 +/-	0	0	0	0	0	0	0	0	0	0	0	0	0	0	0	0	0	0	0	0	0
30.00-50.00 +/-	0	3	3	0	0	0	0	0	0	0	0	0	0	0	0	0	0	0	0	0	0
15.00-30.00 +/-	2	22	6	12	13	33	36	15	0	0	0	0	0	0	0	0	0	0	0	0	0
10.00-15.00 +/-	5	12	4	8	14	28	17	14	34	0	0	0	0	0	0	0	0	0	0	0	0
8.00-10.00 +/-	7	11	3	13	10	18	17	8	9	15	0	0	0	0	0	0	0	0	0	0	0
7.00-8.00 +/-	4	7	3	13	5	14	12	15	5	8	2	0	0	0	0	0	0	0	0	0	0
6.00-7.00 +/-	2	14	4	15	10	21	21	19	16	21	13	0	0	0	0	0	0	0	0	0	0
5.00-6.00 +/-	6	17	5	19	10	31	20	16	18	26	26	0	0	0	0	0	0	0	0	0	0
4.00-5.00 +/-	0	21	5	26	23	41	32	24	27	38	52	5	0	0	0	0	0	0	0	0	0
3.50-4.00 +/-	0	5	3	26	26	35	27	15	36	27	47	8	0	0	0	0	0	0	0	0	0
3.00-3.50 +/-	0	9	4	23	24	35	29	37	29	43	45	20	8	0	0	0	0	0	0	0	0
2.75-3.00 +/-	0	0	0	14	18	29	18	9	25	26	36	8	11	0	0	0	0	0	0	0	0
2.50-2.75 +/-	0	0	0	13	12	41	17	27	29	27	38	17	16	1	0	0	0	0	0	0	0
2.25-2.50 +/-	0	0	0	5	27	54	33	19	32	47	52	20	23	9	0	0	0	0	0	0	0
2.00-2.25 +/-	0	0	0	0	23	47	37	35	54	46	71	30	32	29	0	0	0	0	0	0	0
1.75-2.00 +/-	0	0	0	0	1	61	66	47	50	70	93	36	33	32	6	0	0	0	0	0	0
1.50-1.75 +/-	0	0	0	0	0	57	76	48	61	108	135	64	53	45	33	0	0	0	0	0	0
1.25-1.50 +/-	0	0	0	0	0	15	96	74	81	131	199	91	101	58	77	1	0	0	0	0	0
1.00-1.25 +/-	0	0	0	0	0	0	30	118	125	191	240	114	122	86	156	49	0	0	0	0	0
0.90-1.00 +/-	0	0	0	0	0	0	0	26	68	109	111	58	71	51	69	61	8	0	0	0	0
0.80-0.90 +/-	0	0	0	0	0	0	0	8	63	125	189	49	76	76	91	55	32	0	0	0	0
0.70-0.80 +/-	0	0	0	0	0	0	0	0	53	212	205	109	83	123	139	55	53	0	0	0	0
0.60-0.70 +/-	0	0	0	0	0	0	0	0	3	193	286	135	69	135	166	87	109	5	0	0	0
0.50-0.60 +/-	0	0	0	0	0	0	0	0	0	0	0	0	0	14	18	12	12	3	0	0	0
0.40-0.50 +/-	0	0	0	0	0	0	0	0	0	0	0	0	0	0	0	0	14	67	0	0	0
0.30-0.40 +/-	0	0	0	0	0	0	0	0	0	0	0	0	0	0	0	0	79	186	0	0	0
0.20-0.30 +/-	0	0	0	0	0	0	0	0	0	0	0	0	0	0	0	0	11	93	93	11	0
TOTAL +/-	26	120	185	217	557	584	573	819	1464	1840	765	696	645	738	308	433	351	280	101	12	0
OMEGA	1.	2.	3.	4.	5.	7.	9.	11.	14.	20.	35.	45.	60.	80.	120.	160.	240.	400.	600.	1000.	1400.

ESTIMATE OF NU*W2 ASSUMING R = 0.180E+00 USING OMEGA IN MILS DATA TABLE DT7(d) (96 GeV data)

Q SQRD	1.	2.	3.	4.	5.	7.	9.	11.	14.	20.	35.	45.	60.	80.	120.	160.	240.	400.	600.	1000.	1400.
50.00-70.00 +/-	0	0	0	0	0	0	0	0	0	0	0	0	0	0	0	0	0	0	0	0	0
30.00-50.00 +/-	0	125	126	-37	-32	-2	0	0	0	0	0	0	0	0	0	0	0	0	0	0	0
15.00-30.00 +/-	14	258	66	223	331	708	2056	4334	0	0	0	0	0	0	0	0	0	0	0	0	0
10.00-15.00 +/-	31	122	37	118	296	423	397	453	1562	-109	0	0	0	0	0	0	0	0	0	0	0
8.00-10.00 +/-	52	148	47	252	252	326	451	300	318	584	0	0	0	0	0	0	0	0	0	0	0
7.00- 8.00 +/-	40	123	50	328	192	342	416	741	216	270	522	0	0	0	0	0	0	0	0	0	0
6.00- 7.00 +/-	20	185	53	283	257	366	528	648	486	503	591	0	0	0	0	0	0	0	0	0	0
5.00- 6.00 +/-	55	164	44	250	183	375	355	383	380	413	491	0	0	0	0	0	0	0	0	0	0
4.00- 5.00 +/-	0	145	36	228	272	321	355	354	348	372	412	654	0	0	0	0	0	0	0	0	0
3.50- 4.00 +/-	0	96	48	315	419	379	414	295	620	352	466	281	-7	0	0	0	0	0	0	0	0
3.00- 3.50 +/-	0	498	204	212	281	283	319	535	368	397	313	373	454	176	0	0	0	0	0	0	0
2.75- 3.00 +/-	0	0	0	278	330	356	312	195	485	366	371	236	422	133	0	0	0	0	0	0	0
2.50- 2.75 +/-	0	0	0	371	175	419	243	493	450	311	317	376	359	92	755	0	0	0	0	0	0
2.25- 2.50 +/-	0	0	0	670	349	448	383	277	411	429	345	355	407	85	433	0	0	0	0	0	0
2.00- 2.25 +/-	0	0	0	0	388	309	331	404	536	325	360	394	414	75	552	0	0	0	0	0	0
1.75- 2.00 +/-	0	0	0	0	144	329	456	417	383	374	355	348	312	56	358	0	0	0	0	0	0
1.50- 1.75 +/-	0	0	0	0	0	387	395	313	343	426	370	440	355	51	347	0	0	0	0	0	0
1.25- 1.50 +/-	0	0	0	0	0	437	371	344	320	362	376	422	450	41	293	0	0	0	0	0	0
1.00- 1.25 +/-	0	0	0	0	0	0	280	367	321	342	292	336	338	37	266	0	0	0	0	0	0
0.90- 1.00 +/-	0	0	0	0	0	0	0	288	312	345	237	296	337	51	264	0	0	0	0	0	0
0.80- 0.90 +/-	0	0	0	0	0	0	0	557	253	314	317	196	278	44	305	0	0	0	0	0	0
0.70- 0.80 +/-	0	0	0	0	0	0	0	0	350	412	264	330	230	37	369	0	0	0	0	0	0
0.60- 0.70 +/-	0	0	0	0	0	0	0	0	307	309	272	301	140	28	292	0	0	0	0	0	0
0.50- 0.60 +/-	0	0	0	0	0	0	0	0	0	0	0	0	0	0	0	0	0	0	0	0	0
0.40- 0.50 +/-	0	0	0	0	0	0	0	0	0	0	0	0	0	0	0	0	0	0	0	0	0
0.30- 0.40 +/-	0	0	0	0	0	0	0	0	0	0	0	0	0	0	0	0	0	0	0	0	0
0.20- 0.30 +/-	0	0	0	0	0	0	0	0	0	0	0	0	0	0	0	0	0	0	0	0	0
TOTAL +/-	34	164	17	253	289	370	390	382	365	359	313	328	291	16	314	285	275	227	175	139	0
OMEGA	1.	2.	3.	4.	5.	7.	9.	11.	14.	20.	35.	45.	60.	80.	120.	160.	240.	400.	600.	1000.	1400.

SO AFTER INELASTIC RADIATIVE CORRECTIONS

DATA TABLE DT7(e) (96 GeV data)

ESTIMATE OF NU*W2 ASSUMING R = 0.180E+00 USING OMEGA

IN MILS

Q SQRD

	1.	2.	3.	4.	5.	7.	9.	11.	14.	20.	35.	45.	60.	80.	120.	160.	240.	400.	600.	1000.	1400.
50.00-70.00 +/-	0	0	0	0	0	0	0	0	0	0	0	0	0	0	0	0	0	0	0	0	0
30.00-50.00 +/-	0	128	-37	-32	0	-2	0	0	0	0	0	0	0	0	0	0	0	0	0	0	0
15.00-30.00 +/-	14	272	227	330	688	400	1937	3939	0	0	0	0	0	0	0	0	0	0	0	0	0
10.00-15.00 +/-	35	131	122	301	422	85	386	429	1433	-109	0	0	0	0	0	0	0	0	0	0	0
8.00-10.00 +/-	58	161	263	258	328	80	445	291	302	526	0	0	0	0	0	0	0	0	0	0	0
7.00-8.00 +/-	41	136	344	197	345	96	412	723	208	250	447	0	0	0	0	0	0	0	0	0	0
6.00-7.00 +/-	26	206	298	265	370	88	526	636	470	474	522	0	0	0	0	0	0	0	0	0	0
5.00-6.00 +/-	70	191	265	188	380	73	354	378	370	394	443	0	0	0	0	0	0	0	0	0	0
4.00-5.00 +/-	0	170	244	281	326	56	354	351	341	358	377	550	0	0	0	0	0	0	0	0	0
3.50-4.00 +/-	0	112	341	433	385	74	414	202	611	341	436	242	-7	0	0	0	0	0	0	0	0
3.00-3.50 +/-	0	585	233	291	287	58	319	531	362	386	296	334	382	0	0	0	0	0	0	0	0
2.75-3.00 +/-	0	0	303	342	359	83	312	193	477	357	354	216	364	0	0	0	0	0	0	0	0
2.50-2.75 +/-	0	0	413	183	424	84	243	489	443	304	303	348	315	755	0	0	0	0	0	0	0
2.25-2.50 +/-	0	0	722	363	450	75	381	274	404	420	331	331	367	365	0	0	0	0	0	0	0
2.00-2.25 +/-	0	0	0	410	312	56	328	399	528	317	347	371	380	477	0	0	0	0	0	0	0
1.75-2.00 +/-	0	0	0	147	326	51	448	410	376	365	342	329	289	319	290	0	0	0	0	0	0
1.50-1.75 +/-	0	0	0	0	385	63	386	306	336	415	358	419	333	318	348	0	0	0	0	0	0
1.25-1.50 +/-	0	0	0	0	416	132	353	331	310	351	363	403	425	274	320	192	0	0	0	0	0
1.00-1.25 +/-	0	0	0	0	0	0	264	344	305	329	281	322	321	250	369	294	0	0	0	0	0
0.90-1.00 +/-	0	0	0	0	0	0	0	263	291	328	228	283	322	249	274	393	304	0	0	0	0
0.80-0.90 +/-	0	0	0	0	0	0	0	504	232	295	303	188	266	289	277	273	305	0	0	0	0
0.70-0.80 +/-	0	0	0	0	0	0	0	0	315	381	251	315	219	349	312	200	220	0	0	0	0
0.60-0.70 +/-	0	0	0	0	0	0	0	0	274	280	256	286	133	277	266	224	235	133	0	0	0
0.50-0.60 +/-	0	0	0	0	0	0	0	0	0	0	0	0	0	0	-42	263	224	133	0	0	0
0.40-0.50 +/-	0	0	0	0	0	0	0	0	0	0	0	0	0	0	0	232	196	133	0	0	0
0.30-0.40 +/-	0	0	0	0	0	0	0	0	0	0	0	0	0	0	0	0	0	0	0	0	0
0.20-0.30 +/-	0	0	0	0	0	0	0	0	0	0	0	0	0	0	0	0	0	0	0	0	0
TOTAL +/-	38	184	270	299	372	22	382	368	348	341	298	311	274	294	304	258	247	200	153	117	0
OMEGA	1.	2.	3.	4.	5.	7.	9.	11.	14.	20.	35.	45.	60.	80.	120.	160.	240.	400.	600.	1000.	1400.

DATA TABLE DT7(f) (96 GeV data)

USING OMEGA

CROSS-SECTIONS PER GEV**2 IN PICOBARN

Q SQRD

	1.	2.	3.	4.	5.	7.	9.	11.	14.	20.	35.	45.	60.	80.	120.	160.	240.	400.	600.	1000.	1400.
50.00-70.00 +/-	0	0	0	0	0	0	0	0	0	0	0	0	0	0	0	0	0	0	0	0	0
30.00-50.00 +/-	0	5	5	0	0	0	0	0	0	0	0	0	0	0	0	0	0	0	0	0	0
15.00-30.00 +/-	5	44	11	25	26	42	111	220	0	0	0	0	0	0	0	0	0	0	0	0	0
10.00-15.00 +/-	44	70	21	46	85	83	51	42	124	53	0	0	0	0	0	0	0	0	0	0	0
8.00-10.00 +/-	153	165	52	156	146	133	125	60	46	16	59	26	0	0	0	0	0	0	0	0	0
7.00- 8.00 +/-	181	201	82	376	165	209	175	53	229	48	38	56	56	0	0	0	0	0	0	0	0
6.00- 7.00 +/-	126	408	118	441	302	308	309	282	155	103	79	32	0	0	0	0	0	0	0	0	0
5.00- 6.00 +/-	565	514	138	556	308	458	304	246	182	129	90	20	0	0	0	0	0	0	0	0	0
4.00- 5.00 +/-	0	692	174	776	704	608	477	361	267	190	108	123	0	0	0	0	0	0	0	0	0
3.50- 4.00 +/-	0	680	342	1552	1579	1050	821	448	716	274	188	64	0	0	0	0	0	0	0	0	0
3.00- 3.50 +/-	0	4484	1359	1359	1429	1064	863	1113	586	432	180	117	115	0	0	0	0	0	0	0	0
2.75- 3.00 +/-	0	0	0	2309	2158	1719	1092	527	1009	525	286	101	127	0	0	0	0	0	0	0	0
2.50- 2.75 +/-	0	0	0	3616	1382	2453	1031	1622	1144	549	304	203	128	0	0	0	0	0	0	0	0
2.25- 2.50 +/-	0	0	0	7462	3368	3230	2008	1130	1298	948	420	246	186	147	0	0	0	0	0	0	0
2.00- 2.25 +/-	0	0	0	0	4506	2808	2192	2086	2156	916	567	360	252	227	0	0	0	0	0	0	0
1.75- 2.00 +/-	0	0	0	0	1942	3825	3933	2811	2015	1391	746	431	261	192	149	0	0	0	0	0	0
1.50- 1.75 +/-	0	0	0	0	0	5611	4590	2851	2450	2161	1078	767	424	269	216	0	0	0	0	0	0
1.25- 1.50 +/-	0	0	0	0	0	7670	6028	4453	3254	2630	1590	1088	807	347	260	137	0	0	0	0	0
1.00- 1.25 +/-	0	0	0	0	0	0	5845	7178	4987	3822	1921	1373	977	519	467	263	0	0	0	0	0
0.90- 1.00 +/-	0	0	0	0	0	0	0	7431	6806	5435	2225	1746	1421	761	518	455	296	0	0	0	0
0.80- 0.90 +/-	0	0	0	0	0	0	0	16337	6831	6238	3771	1480	1510	1144	685	412	345	0	0	0	0
0.70- 0.80 +/-	0	0	0	0	0	0	0	0	11348	10624	4108	3272	1652	1845	1043	410	305	0	0	0	0
0.60- 0.70 +/-	0	0	0	0	0	0	0	0	0	11505	10465	5714	4064	1391	2026	655	419	192	0	0	0
0.50- 0.60 +/-	0	0	0	0	0	0	0	0	0	0	0	0	0	0	0	0	656	404	0	0	0
0.40- 0.50 +/-	0	0	0	0	0	0	0	0	0	0	0	0	0	0	0	0	795	490	0	0	0
0.30- 0.40 +/-	0	0	0	0	0	0	0	0	0	0	0	0	0	0	0	0	0	0	501	0	0
0.20- 0.30 +/-	0	0	0	0	0	0	0	0	0	0	0	0	0	0	0	0	0	0	61	0	0
TOTAL	39	180	19	277	325	836	876	860	1228	2196	2759	1148	1044	968	1107	461	649	526	420	567	502
OMEGA	1.	2.	3.	4.	5.	7.	9.	11.	14.	20.	35.	45.	60.	80.	120.	160.	240.	400.	600.	1000.	1400.

data)

DATA TABLE DT8(a)

(147 GeV

data)

EVENTS

FULL

Q SQPD

	1.	2.	3.	4.	5.	7.	9.	11.	14.	20.	35.	45.	60.	80.	120.	160.	240.	400.	600.	1000.	1400.
TOTAL	26	118	202	213	392	413	323	409	551	832	344	386	351	481	351	476	683	589	1062	207	0
50.00-70.00	0	0	0	0	0	0	0	0	0	0	0	0	0	0	0	0	0	0	0	0	0
30.00-50.00	3	5	5	2	4	0	0	0	0	0	0	0	0	0	0	0	0	0	0	0	0
15.00-30.00	6	12	21	11	37	19	13	11	1	0	0	0	0	0	0	0	0	0	0	0	0
10.00-15.00	6	12	18	23	22	27	18	24	32	6	0	0	0	0	0	0	0	0	0	0	0
8.00-10.00	8	10	11	16	20	20	17	13	21	26	0	0	0	0	0	0	0	0	0	0	0
7.00- 8.00	1	12	10	7	12	14	9	12	19	19	0	0	0	0	0	0	0	0	0	0	0
6.00- 7.00	0	15	17	13	15	19	11	20	24	46	7	0	0	0	0	0	0	0	0	0	0
5.00- 6.00	2	20	19	9	19	23	17	31	34	43	24	4	0	0	0	0	0	0	0	0	0
4.00- 5.00	0	21	32	26	35	35	23	29	51	75	43	39	1	0	0	0	0	0	0	0	0
3.50- 4.00	0	8	13	25	28	24	15	21	31	49	21	37	14	0	0	0	0	0	0	0	0
3.00- 3.50	0	3	30	25	45	29	28	33	27	76	27	39	39	0	0	0	0	0	0	0	0
2.75- 3.00	0	0	14	9	23	19	6	14	25	49	13	19	23	5	0	0	0	0	0	0	0
2.50- 2.75	0	0	4	26	20	20	20	16	16	54	19	21	24	18	0	0	0	0	0	0	0
2.25- 2.50	0	0	2	12	22	22	21	32	40	43	27	29	42	42	0	0	0	0	0	0	0
2.00- 2.25	0	0	0	7	31	29	19	26	48	45	34	45	30	59	0	0	0	0	0	0	0
1.75- 2.00	0	0	0	2	30	41	21	31	38	62	25	33	46	78	32	0	0	0	0	0	0
1.50- 1.75	0	0	0	0	26	29	26	45	48	79	41	39	48	74	57	0	0	0	0	0	0
1.25- 1.50	0	0	0	0	3	35	36	23	57	88	31	39	41	82	94	48	0	0	0	0	0
1.00- 1.25	0	0	0	0	0	8	23	28	39	72	32	42	42	83	114	142	1	0	0	0	0
0.90- 1.00	0	0	0	0	0	0	0	0	0	0	0	0	1	36	30	93	19	0	0	0	0
0.80- 0.90	0	0	0	0	0	0	0	0	0	0	0	0	0	4	17	97	90	0	0	0	0
0.70- 0.80	0	0	0	0	0	0	0	0	0	0	0	0	0	0	7	65	121	0	0	0	0
0.60- 0.70	0	0	0	0	0	0	0	0	0	0	0	0	0	0	0	31	209	1	0	0	0
0.50- 0.60	0	0	0	0	0	0	0	0	0	0	0	0	0	0	0	0	178	74	0	0	0
0.40- 0.50	0	0	0	0	0	0	0	0	0	0	0	0	0	0	0	0	65	318	1	0	0
0.30- 0.40	0	0	0	0	0	0	0	0	0	0	0	0	0	0	0	0	0	191	272	0	0
0.20- 0.30	0	0	0	0	0	0	0	0	0	0	0	0	0	0	0	0	0	5	789	207	0
OMEGA	1.	2.	3.	4.	5.	7.	9.	11.	14.	20.	35.	45.	60.	80.	120.	160.	240.	400.	600.	1000.	1400.

EVENTS WEIGHTED BY ACCEPTANCE

DATA TABLE DT8(b)

(147 GeV data)

Q SQRD																											
50.00-70.00	0	0	0	0	0	0	0	0	0	0	0	0	0	0	0	0	0	0	0	0	0	0	0	0	0	0	0
30.00-50.00	4	7	3	7	11	12	0	0	0	0	0	0	0	0	0	0	0	0	0	0	0	0	0	0	0	0	0
15.00-30.00	7	14	23	12	40	21	14	28	5	5	0	0	0	0	0	0	0	0	0	0	0	0	0	0	0	0	0
10.00-15.00	7	15	22	27	25	30	19	25	34	6	13	0	0	0	0	0	0	0	0	0	0	0	0	0	0	0	0
8.00-10.00	11	13	15	21	25	24	20	15	22	5	28	0	0	0	0	0	0	0	0	0	0	0	0	0	0	0	0
7.00-8.00	1	18	15	10	17	18	11	14	21	5	19	0	0	0	0	0	0	0	0	0	0	0	0	0	0	0	0
6.00-7.00	0	23	25	19	21	26	14	24	28	6	46	7	3	0	0	0	0	0	0	0	0	0	0	0	0	0	0
5.00-6.00	3	31	29	14	30	33	23	41	41	7	44	21	4	3	0	0	0	0	0	0	0	0	0	0	0	0	0
4.00-5.00	0	32	50	40	52	51	32	40	65	9	82	43	7	34	1	0	0	0	0	0	0	0	0	0	0	0	0
3.50-4.00	0	12	30	39	44	36	22	30	43	8	58	22	5	35	11	3	0	0	0	0	0	0	0	0	0	0	0
3.00-3.50	0	5	46	39	70	45	43	50	39	8	101	30	6	40	34	5	0	0	0	0	0	0	0	0	0	0	0
2.75-3.00	0	0	22	14	36	30	10	21	39	8	72	16	4	23	2	0	0	0	0	0	0	0	0	0	0	0	0
2.50-2.75	0	0	7	43	33	33	33	26	25	6	83	26	5	24	14	3	0	0	0	0	0	0	0	0	0	0	0
2.25-2.50	0	0	3	21	38	38	38	56	68	11	71	41	8	38	46	7	0	0	0	0	0	0	0	0	0	0	0
2.00-2.25	0	0	0	13	60	55	35	49	91	13	80	59	68	35	6	53	0	0	0	0	0	0	0	0	0	0	0
1.75-2.00	0	0	0	5	67	92	46	68	82	13	127	49	10	64	10	77	25	5	0	0	0	0	0	0	0	0	0
1.50-1.75	0	0	0	0	71	81	73	122	129	19	199	92	14	88	13	92	47	6	0	0	0	0	0	0	0	0	0
1.25-1.50	0	0	0	0	11	134	140	86	214	29	305	99	112	101	16	134	98	38	5	0	0	0	0	0	0	0	0
1.00-1.25	0	0	0	0	0	44	136	161	217	36	425	171	31	156	25	234	165	128	1	1	0	0	0	0	0	0	0
0.90-1.00	0	0	0	0	0	0	0	0	0	0	0	0	0	5	6	167	73	99	15	3	0	0	0	0	0	0	0
0.80-0.90	0	0	0	0	0	0	0	0	0	0	0	0	0	0	0	21	69	134	72	8	0	0	0	0	0	0	0
0.70-0.80	0	0	0	0	0	0	0	0	0	0	0	0	0	0	0	0	37	147	111	10	0	0	0	0	0	0	0
0.60-0.70	0	0	0	0	0	0	0	0	0	0	0	0	0	0	0	0	0	95	217	1	1	0	0	0	0	0	0
0.50-0.60	0	0	0	0	0	0	0	0	0	0	0	0	0	0	0	0	0	0	236	58	7	0	0	0	0	0	0
0.40-0.50	0	0	0	0	0	0	0	0	0	0	0	0	0	0	0	0	0	0	157	290	1	1	0	0	0	0	0
0.30-0.40	0	0	0	0	0	0	0	0	0	0	0	0	0	0	0	0	0	0	0	224	223	0	0	0	0	0	0
0.20-0.30	0	0	0	0	0	0	0	0	0	0	0	0	0	0	0	0	0	0	0	17	14	0	0	0	0	0	0
TOTAL	34	170	293	327	651	790	709	856	1164	1753	676	720	588	833	515	641	809	554	1035	161	11	161	11	161	11	161	11
OMEGA	1.	2.	3.	4.	5.	7.	9.	11.	14.	20.	35.	45.	60.	80.	120.	160.	240.	400.	600.	1000.	1400.						

SO AFTER SUBTRACTION OF RADIATIVE TAIL

EVENTS WEIGHTED BY ACCEPTANCE

Q SQRD

	1.	2.	3.	4.	5.	7.	9.	11.	14.	20.	35.	45.	60.	80.	120.	160.	240.	400.	600.	1000.	1400.
50.00-70.00 +/-	0	0	0	0	0	0	0	0	0	0	0	0	0	0	0	0	0	0	0	0	0
30.00-50.00 +/-	4	7	3	7	11	12	0	0	0	0	0	0	0	0	0	0	0	0	0	0	0
15.00 30.00 +/-	7	14	23	23	12	40	21	14	28	5	0	0	0	0	0	0	0	0	0	0	0
10.00-15.00 +/-	7	15	22	22	27	25	30	19	25	33	12	15	0	0	0	0	0	0	0	0	0
8.00-10.00 +/-	11	13	15	15	21	25	24	20	15	22	27	6	0	0	0	0	0	0	0	0	0
7.00- 8.00 +/-	1	18	15	15	10	17	18	11	14	21	18	5	0	0	0	0	0	0	0	0	0
6.00- 7.00 +/-	0	23	25	25	19	21	26	14	24	28	45	7	6	0	0	0	0	0	0	0	0
5.00- 6.00 +/-	3	31	29	29	14	30	33	23	41	41	43	7	19	3	0	0	0	0	0	0	0
4.00- 5.00 +/-	0	32	50	50	40	52	51	32	40	65	82	10	41	1	0	0	0	0	0	0	0
3.50- 4.00 +/-	0	12	30	30	39	44	36	22	30	43	57	8	21	10	0	0	0	0	0	0	0
3.00- 3.50 +/-	0	5	46	46	39	70	45	43	50	39	100	12	30	30	0	0	0	0	0	0	0
2.75- 3.00 +/-	0	0	22	22	14	36	30	10	21	39	72	10	16	21	3	0	0	0	0	0	0
2.50- 2.75 +/-	0	0	7	7	43	33	33	33	26	25	83	11	25	23	12	0	0	0	0	0	0
2.25- 2.50 +/-	0	0	3	3	21	38	38	38	56	68	70	11	41	38	32	0	0	0	0	0	0
2.00- 2.25 +/-	0	0	0	0	13	60	55	35	49	91	79	12	58	68	47	0	0	0	0	0	0
1.75- 2.00 +/-	0	0	0	0	5	67	92	46	68	81	127	16	49	59	71	22	0	0	0	0	0
1.50- 1.75 +/-	0	0	0	0	0	71	81	73	122	129	199	23	91	85	87	38	0	0	0	0	0
1.25- 1.50 +/-	0	0	0	0	0	11	134	140	85	213	304	33	98	112	130	89	30	0	0	0	0
1.00- 1.25 +/-	0	0	0	0	0	0	43	135	160	217	424	52	171	198	230	158	103	1	0	0	0
0.90- 1.00 +/-	0	0	0	0	0	0	0	0	0	0	0	0	0	0	165	70	87	9	0	0	0
0.80- 0.90 +/-	0	0	0	0	0	0	0	0	0	0	0	0	0	0	20	66	124	56	0	0	0
0.70- 0.80 +/-	0	0	0	0	0	0	0	0	0	0	0	0	0	0	0	36	138	86	0	0	0
0.60- 0.70 +/-	0	0	0	0	0	0	0	0	0	0	0	0	0	0	0	0	91	177	1	0	0
0.50- 0.60 +/-	0	0	0	0	0	0	0	0	0	0	0	0	0	0	0	0	0	177	16	0	0
0.40- 0.50 +/-	0	0	0	0	0	0	0	0	0	0	0	0	0	0	0	0	0	203	29	0	0
0.30- 0.40 +/-	0	0	0	0	0	0	0	0	0	0	0	0	0	0	0	0	0	141	214	1	0
0.20- 0.30 +/-	0	0	0	0	0	0	0	0	0	0	0	0	0	0	0	0	0	22	17	1	0
TOTAL +/-	34	170	293	327	650	788	707	854	1160	1742	668	708	572	799	479	571	672	424	720	89	89
OMEGA	1.	2.	3.	4.	5.	7.	9.	11.	14.	20.	35.	45.	60.	80.	120.	160.	240.	400.	600.	1000.	1400.

DATA TABLE DT8(d) (147 GeV data)

ESTIMATE OF NU*W2 ASSUMING R = 0.180E+00 USING OMEGA IN MILS

Q SJRD

	1.	2.	3.	4.	5.	7.	9.	11.	14.	20.	35.	45.	60.	80.	120.	160.	240.	400.	600.	1000.	1400.
50.00-70.00 +/-	0	0	0	0	0	0	0	0	0	0	0	0	0	0	0	0	0	0	0	0	0
30.00-50.00 +/-	52	173	272	628	740	740	-35	0	0	0	0	0	0	0	0	0	0	0	0	0	0
15.00-30.00 +/-	32	119	287	205	513	417	475	1388	1604	0	0	0	0	0	0	0	0	0	0	0	0
10.00-15.00 +/-	33	116	243	407	268	470	400	495	580	1350	0	0	0	0	0	0	0	0	0	0	0
8.00-10.00 +/-	68	132	212	396	332	450	515	335	385	657	0	0	0	0	0	0	0	0	0	0	0
7.00- 8.00 +/-	12	252	293	261	299	445	367	417	494	373	0	0	0	0	0	0	0	0	0	0	0
6.00- 7.00 +/-	0	241	368	357	278	486	337	512	442	574	670	0	0	0	0	0	0	0	0	0	0
5.00- 6.00 +/-	22	228	300	193	271	421	389	595	440	362	491	864	0	0	0	0	0	0	0	0	0
4.00- 5.00 +/-	0	178	338	350	311	421	347	375	441	413	568	631	891	0	0	0	0	0	0	0	0
3.50- 4.00 +/-	0	168	273	480	360	407	322	382	389	379	375	588	703	0	0	0	0	0	0	0	0
3.00- 3.50 +/-	0	215	333	351	427	374	463	458	257	473	368	473	542	-30	0	0	0	0	0	0	0
2.75- 3.00 +/-	0	0	345	205	344	391	309	370	478	287	523	584	332	435	306	0	0	0	0	0	0
2.50- 2.75 +/-	0	0	152	507	262	351	448	300	207	482	374	337	376	432	432	0	0	0	0	0	0
2.25- 2.50 +/-	0	0	355	209	245	336	424	530	456	327	472	424	585	566	566	0	0	0	0	0	0
2.00- 2.25 +/-	0	0	0	170	304	393	309	370	478	287	523	584	332	435	306	-40	0	0	0	0	0
1.75- 2.00 +/-	0	0	0	358	279	493	313	394	328	349	329	374	450	434	434	797	0	0	0	0	0
1.50- 1.75 +/-	0	0	0	0	0	373	323	521	384	400	443	397	439	370	370	346	-74	0	0	0	0
1.25- 1.50 +/-	0	0	0	0	0	244	400	258	446	426	328	347	339	361	361	417	385	0	0	0	0
1.00- 1.25 +/-	0	0	0	0	0	0	317	320	297	386	365	390	326	390	390	443	309	706	0	0	0
0.90- 1.00 +/-	0	0	0	0	0	0	0	0	0	0	0	0	314	481	481	327	346	256	0	0	0
0.80- 0.90 +/-	0	0	0	0	0	0	0	0	0	0	0	0	0	252	252	234	369	436	0	0	0
0.70- 0.80 +/-	0	0	0	0	0	0	0	0	0	0	0	0	0	0	0	486	299	309	0	0	0
0.60- 0.70 +/-	0	0	0	0	0	0	0	0	0	0	0	0	0	0	0	0	357	304	517	0	0
0.50- 0.60 +/-	0	0	0	0	0	0	0	0	0	0	0	0	0	0	0	0	0	295	152	0	0
0.40- 0.50 +/-	0	0	0	0	0	0	0	0	0	0	0	0	0	0	0	0	0	292	262	507	0
0.30- 0.40 +/-	0	0	0	0	0	0	0	0	0	0	0	0	0	0	0	0	0	0	193	193	0
0.20- 0.30 +/-	0	0	0	0	0	0	0	0	0	0	0	0	0	0	0	0	0	0	217	200	200
TOTAL +/-	36	176	296	324	323	394	378	390	377	402	392	411	387	404	404	375	334	306	216	213	200
OMEGA	1.	2.	3.	4.	5.	7.	9.	11.	14.	20.	35.	45.	60.	80.	120.	160.	240.	400.	600.	1000.	1400.

DATA TABLE DT8 (e) (147 GeV data)

SO AFTER INELASTIC RADIATIVE CORRECTIONS

ESTIMATE OF NU*W2 ASSUMING R = 0.180E+00 USING OMEGA IN MILS

Q SQRD

	1.	2.	3.	4.	5.	7.	9.	11.	14.	20.	35.	45.	60.	80.	120.	160.	240.	400.	600.	1000.	1400.
50.00-70.00 +/-	0	0	0	0	0	0	0	0	0	0	0	0	0	0	0	0	0	0	0	0	0
30.00-50.00 +/-	56	180	274	614	697	-35	0	0	0	0	0	0	0	0	0	0	0	0	0	0	0
15.00-30.00 +/-	34	126	255	206	503	395	438	1234	1362	0	0	0	0	0	0	0	0	0	0	0	0
10.00-15.00 +/-	37	127	254	416	268	459	384	465	514	1103	0	0	0	0	0	0	0	0	0	0	0
8.00-10.00 +/-	75	150	224	407	334	444	501	321	356	558	0	0	0	0	0	0	0	0	0	0	0
7.00-8.00 +/-	14	293	312	269	303	441	359	401	454	322	0	0	0	0	0	0	0	0	0	0	0
6.00-7.00 +/-	0	287	396	368	281	483	331	496	418	508	502	0	0	0	0	0	0	0	0	0	0
5.00-6.00 +/-	24	277	328	200	273	419	383	579	420	330	395	621	0	0	0	0	0	0	0	0	0
4.00-5.00 +/-	0	220	380	365	313	417	343	367	424	383	495	493	891	0	0	0	0	0	0	0	0
3.50-4.00 +/-	0	212	322	505	362	401	316	375	376	355	337	490	522	0	0	0	0	0	0	0	0
3.00-3.50 +/-	0	273	392	373	428	368	455	449	250	446	335	411	422	-30	0	0	0	0	0	0	0
2.75-3.00 +/-	0	0	402	219	342	382	155	294	381	486	266	331	362	222	0	0	0	0	0	0	0
2.50-2.75 +/-	0	0	181	557	264	343	436	291	201	458	345	302	318	327	0	0	0	0	0	0	0
2.25-2.50 +/-	0	0	413	228	242	324	410	512	441	311	438	384	506	443	0	0	0	0	0	0	0
2.00-2.25 +/-	0	0	0	192	309	369	298	357	459	274	498	533	292	349	-40	0	0	0	0	0	0
1.75-2.00 +/-	0	0	0	0	275	463	296	377	314	333	308	344	402	363	595	0	0	0	0	0	0
1.50-1.75 +/-	0	0	0	0	377	306	343	492	365	382	417	358	397	320	271	0	0	0	0	0	0
1.25-1.50 +/-	0	0	0	0	230	363	449	236	419	404	310	323	310	321	348	290	0	0	0	0	0
1.00-1.25 +/-	0	0	0	0	0	291	288	281	272	363	346	366	302	352	387	249	706	0	0	0	0
0.90-1.00 +/-	0	0	0	0	0	0	0	0	0	0	0	0	290	439	292	291	193	0	0	0	0
0.80-0.90 +/-	0	0	0	0	0	0	0	0	0	0	0	0	0	229	212	319	342	0	0	0	0
0.70-0.80 +/-	0	0	0	0	0	0	0	0	0	0	0	0	0	0	438	264	252	0	0	0	0
0.60-0.70 +/-	0	0	0	0	0	0	0	0	0	0	0	0	0	0	0	0	316	254	517	0	0
0.50-0.60 +/-	0	0	0	0	0	0	0	0	0	0	0	0	0	0	0	0	0	252	803	0	0
0.40-0.50 +/-	0	0	0	0	0	0	0	0	0	0	0	0	0	0	0	0	0	252	119	0	0
0.30-0.40 +/-	0	0	0	0	0	0	0	0	0	0	0	0	0	0	0	0	0	255	219	507	0
0.20-0.30 +/-	0	0	0	0	0	0	0	0	0	0	0	0	0	0	0	0	0	41	17	814	0
TOTAL +/-	40	205	328	342	323	376	352	364	356	379	365	375	347	355	325	284	258	258	181	178	152
OMEGA	1.	2.	3.	4.	5.	7.	9.	11.	14.	20.	35.	45.	60.	80.	120.	160.	240.	400.	600.	1000.	1400.

[illegible]

DATA TABLE DT9(a) (96GeV data)

Total virtual photoabsorption cross-section

SO AFTER INELASTIC RADIATIVE CORRECTIONS

ESTIMATE OF CROSS SECTION IN MICROBARN

Q SQRC	4.0	16.0	36.0	64.0	100.0	144.0	196.0	240.0	324.0	400.0
50.00	0.0	0.0	-0.000	0.790	-0.027	-0.053	0.0	0.0	0.0	0.0
+/-	0.0	0.0	0.0	0.791	0.0	0.0	0.0	0.0	0.0	0.0
30.00	0.0	0.424	2.039	2.376	1.693	10.653	-0.003	0.0	0.0	0.0
+/-	0.0	0.300	0.551	0.623	0.663	4.010	0.0	0.0	0.0	0.0
15.00	0.0	1.636	2.151	4.052	3.539	3.736	58.032	0.0	0.0	0.0
+/-	0.0	0.579	0.523	0.730	0.804	1.175	29.226	0.0	0.0	0.0
10.00	0.0	2.396	3.273	4.312	2.719	1.661	-0.104	0.0	0.0	0.0
+/-	0.0	1.198	1.159	1.367	1.231	1.289	0.0	0.0	0.0	0.0
9.00	0.0	3.640	6.148	6.658	5.894	4.801	34.763	0.0	0.0	0.0
+/-	0.0	1.287	1.452	1.572	1.675	2.085	25.369	0.0	0.0	0.0
8.00	0.0	3.734	5.658	7.594	6.243	3.373	9.522	0.0	0.0	0.0
+/-	0.0	1.182	1.277	1.553	1.574	1.483	10.215	0.0	0.0	0.0
7.00	0.0	5.506	6.985	10.441	9.941	6.775	17.479	0.0	0.0	0.0
+/-	0.0	1.299	1.278	1.676	1.827	1.844	10.887	0.0	0.0	0.0
6.00	0.0	7.097	8.134	9.478	7.543	7.123	10.364	0.0	0.0	0.0
+/-	0.0	1.321	1.214	1.449	1.632	1.632	5.056	0.0	0.0	0.0
5.00	0.0	8.781	9.903	9.309	10.130	8.575	9.430	0.0	0.0	0.0
+/-	0.0	1.312	1.186	1.284	1.526	1.593	4.014	0.0	0.0	0.0
4.00	0.0	15.194	13.407	14.462	11.631	11.348	8.709	0.0	0.0	0.0
+/-	0.0	1.554	1.227	1.417	1.440	1.571	3.121	0.0	0.0	0.0
3.00	0.0	21.535	19.696	15.676	17.353	15.557	16.582	0.0	0.0	0.0
+/-	0.0	1.550	1.242	1.252	1.459	1.530	3.232	0.0	0.0	0.0
2.00	0.0	31.463	26.159	25.286	21.346	19.601	21.215	0.0	0.0	0.0
+/-	0.0	2.242	1.641	1.879	1.889	2.068	4.392	0.0	0.0	0.0
1.50	0.0	33.236	31.885	32.134	30.461	29.124	21.677	0.0	0.0	0.0
+/-	0.0	1.863	1.507	1.824	1.968	2.167	3.881	0.0	0.0	0.0
1.00	0.0	37.440	33.222	37.742	34.413	35.745	39.128	0.0	0.0	0.0
+/-	0.0	2.792	2.232	2.887	3.058	3.292	6.773	0.0	0.0	0.0
0.80	0.0	47.775	42.166	45.260	39.995	35.298	30.177	0.0	0.0	0.0
+/-	0.0	3.205	2.576	3.110	3.203	2.988	5.668	0.0	0.0	0.0
0.60	0.0	0.0	0.0	0.0	66.852	47.252	52.575	0.0	0.0	0.0
+/-	0.0	0.0	0.0	0.0	10.596	3.060	6.133	0.0	0.0	0.0
0.40	0.0	0.0	0.0	0.0	0.0	70.921	49.564	0.0	0.0	0.0
+/-	0.0	0.0	0.0	0.0	0.0	7.299	7.902	0.0	0.0	0.0
0.30	0.0	0.0	0.0	0.0	0.0	74.139	60.127	0.0	0.0	0.0
+/-	0.0	0.0	0.0	0.0	0.0	6.587	7.569	0.0	0.0	0.0
0.20	0.0	0.0	0.0	0.0	0.0	0.0	0.0	0.0	0.0	0.0
+/-	0.0	0.0	0.0	0.0	0.0	0.0	0.0	0.0	0.0	0.0
0.10	0.0	0.0	0.0	0.0	0.0	0.0	0.0	0.0	0.0	0.0
+/-	0.0	0.0	0.0	0.0	0.0	0.0	0.0	0.0	0.0	0.0
0.0	0.0	0.0	0.0	0.0	0.0	0.0	0.0	0.0	0.0	0.0
+/-	0.0	0.0	0.0	0.0	0.0	0.0	0.0	0.0	0.0	0.0

DATA TABLE DT10(a) (147GeV data)

SO AFTER SUBTRACTION OF RADIATIVE TAIL

EVENTS WEIGHTED BY ACCEPTANCE

Q SQRC	0+/-	0	0+/-	0	4+/-	2	5+/-	3	7+/-	3	7+/-	4	11+/-	9	6+/-	6	0+/-	0
50.00	0+/-	0	0+/-	0	4+/-	4	27+/-	5	35+/-	6	36+/-	6	24+/-	6	24+/-	11	0+/-	0
30.00	0+/-	0	5+/-	2	12+/-	4	43+/-	7	38+/-	7	39+/-	6	28+/-	5	25+/-	7	0+/-	0
15.00	0+/-	0	11+/-	4	31+/-	6	17+/-	5	13+/-	4	11+/-	4	8+/-	3	8+/-	4	0+/-	0
10.00	0+/-	0	10+/-	4	14+/-	4	26+/-	6	22+/-	5	10+/-	3	10+/-	3	11+/-	3	0+/-	0
9.00	0+/-	0	9+/-	4	24+/-	6	25+/-	6	22+/-	5	21+/-	5	7+/-	3	12+/-	4	0+/-	0
8.00	0+/-	0	19+/-	5	36+/-	7	46+/-	8	34+/-	6	33+/-	6	22+/-	5	13+/-	4	0+/-	0
7.00	0+/-	0	30+/-	7	52+/-	9	73+/-	10	57+/-	8	27+/-	5	26+/-	5	18+/-	4	0+/-	0
6.00	0+/-	0	57+/-	9	53+/-	5	90+/-	11	82+/-	10	47+/-	7	44+/-	7	33+/-	6	0+/-	0
5.00	0+/-	0	102+/-	13	119+/-	13	157+/-	15	111+/-	12	91+/-	10	70+/-	9	50+/-	7	2+/-	1
4.00	0+/-	0	187+/-	17	245+/-	19	310+/-	23	236+/-	19	181+/-	16	129+/-	12	82+/-	9	7+/-	3
3.00	0+/-	0	328+/-	24	474+/-	29	664+/-	55	403+/-	37	321+/-	28	249+/-	18	116+/-	11	10+/-	3
2.00	0+/-	0	370+/-	31	491+/-	35	0+/-	0	120+/-	25	207+/-	29	158+/-	16	114+/-	11	3+/-	2
1.50	0+/-	0	682+/-	55	993+/-	71	0+/-	0	0+/-	0	158+/-	28	233+/-	21	130+/-	12	6+/-	3
1.00	0+/-	0	0+/-	0	0+/-	0	0+/-	0	0+/-	0	0+/-	0	362+/-	31	212+/-	16	16+/-	5
0.80	0+/-	0	0+/-	0	0+/-	0	0+/-	0	0+/-	0	0+/-	0	127+/-	16	167+/-	15	11+/-	5
0.60	0+/-	0	0+/-	0	0+/-	0	0+/-	0	0+/-	0	0+/-	0	304+/-	25	372+/-	21	26+/-	7
0.40	0+/-	0	0+/-	0	0+/-	0	0+/-	0	0+/-	0	0+/-	0	0+/-	0	0+/-	0	0+/-	0
0.30	0+/-	0	0+/-	0	0+/-	0	0+/-	0	0+/-	0	0+/-	0	0+/-	0	0+/-	0	0+/-	0
0.20	0+/-	0	0+/-	0	0+/-	0	0+/-	0	0+/-	0	0+/-	0	0+/-	0	0+/-	0	0+/-	0
0.10	0+/-	0	0+/-	0	0+/-	0	0+/-	0	0+/-	0	0+/-	0	0+/-	0	0+/-	0	0+/-	0
0.0	0+/-	0	0+/-	0	0+/-	0	0+/-	0	0+/-	0	0+/-	0	0+/-	0	0+/-	0	0+/-	0

W2 GEV**2
1.0

400.0

DATA TABLE DT10(c)

Total virtual photoabsorption cross-section

ESTIMATE OF CROSS SECTION IN MICROBARN

Q SQRD	4.0	16.0	36.0	64.0	100.0	144.0	196.0	240.0	324.0	400.0
50.00	0.0	0.0	0.863	0.822	1.022	1.220	2.093	6.510	0.0	0.0
+/-	0.0	0.0	0.503	0.412	0.461	0.616	1.723	6.575	0.0	0.0
30.00	0.0	0.724	0.900	1.902	2.692	3.263	2.641	6.706	0.0	0.0
+/-	0.0	0.363	0.285	0.381	0.470	0.565	0.626	2.904	0.0	0.0
15.00	0.0	1.461	2.609	3.730	4.023	5.164	4.677	7.992	0.0	0.0
+/-	0.0	0.488	0.513	0.614	0.692	0.855	0.887	2.287	0.0	0.0
10.00	0.0	3.656	3.728	5.121	4.814	5.323	5.287	9.042	0.0	0.0
+/-	0.0	1.387	1.125	1.370	1.456	1.698	1.809	4.123	0.0	0.0
9.00	0.0	2.854	5.492	6.610	7.047	4.153	5.356	10.608	0.0	0.0
+/-	0.0	1.079	1.297	1.445	1.667	1.401	1.746	3.406	0.0	0.0
8.00	0.0	4.557	6.699	5.525	6.263	7.814	3.160	9.422	0.0	0.0
+/-	0.0	1.266	1.343	1.238	1.441	1.808	1.263	2.958	0.0	0.0
7.00	0.0	5.437	7.735	8.344	8.058	10.371	9.115	9.144	0.0	0.0
+/-	0.0	1.218	1.292	1.435	1.501	1.909	1.952	2.593	0.0	0.0
6.00	0.0	7.918	6.203	10.691	11.088	6.896	8.794	10.366	0.0	0.0
+/-	0.0	1.303	1.066	1.472	1.642	1.397	1.748	2.386	0.0	0.0
5.00	0.0	10.724	10.504	10.347	12.705	9.767	12.205	14.876	-0.055	0.0
+/-	0.0	1.323	1.177	1.286	1.560	1.474	1.857	2.549	0.0	0.0
4.00	0.0	15.597	15.455	13.367	12.851	14.356	14.638	17.352	26.222	0.0
+/-	0.0	1.421	1.231	1.284	1.420	1.606	1.803	2.492	16.839	0.0
3.00	0.0	17.936	19.510	17.834	18.921	15.948	18.960	20.041	25.889	0.0
+/-	0.0	1.311	1.187	1.311	1.554	1.734	1.772	2.208	9.626	0.0
2.00	0.0	31.050	26.704	27.974	23.640	27.894	22.019	28.939	34.970	0.0
+/-	0.0	2.588	1.913	2.253	2.348	2.673	2.342	3.121	13.683	0.0
1.50	0.0	37.098	36.586	36.139	31.188	34.459	36.204	28.193	35.874	0.0
+/-	0.0	3.204	2.605	2.977	2.893	2.966	2.638	2.729	12.206	0.0
1.00	0.0	0.0	0.0	0.0	39.669	40.241	41.638	50.738	16.494	0.0
+/-	0.0	0.0	0.0	0.0	8.234	5.542	4.102	4.861	14.859	0.0
0.80	0.0	0.0	0.0	0.0	0.0	56.107	47.598	44.774	29.221	0.0
+/-	0.0	0.0	0.0	0.0	0.0	8.791	4.210	4.173	16.295	0.0
0.60	0.0	0.0	0.0	0.0	0.0	0.0	62.377	52.213	58.698	0.0
+/-	0.0	0.0	0.0	0.0	0.0	0.0	5.282	3.911	18.046	0.0
0.40	0.0	0.0	0.0	0.0	0.0	0.0	49.490	58.391	59.161	0.0
+/-	0.0	0.0	0.0	0.0	0.0	0.0	6.152	5.160	23.856	0.0
0.30	0.0	0.0	0.0	0.0	0.0	0.0	84.824	93.896	97.378	0.0
+/-	0.0	0.0	0.0	0.0	0.0	0.0	7.056	5.415	24.854	0.0
0.20	0.0	0.0	0.0	0.0	0.0	0.0	0.0	0.0	0.0	0.0
+/-	0.0	0.0	0.0	0.0	0.0	0.0	0.0	0.0	0.0	0.0
0.10	0.0	0.0	0.0	0.0	0.0	0.0	0.0	0.0	0.0	0.0
+/-	0.0	0.0	0.0	0.0	0.0	0.0	0.0	0.0	0.0	0.0
0.0	0.0	0.0	0.0	0.0	0.0	0.0	0.0	0.0	0.0	0.0
+/-	0.0	0.0	0.0	0.0	0.0	0.0	0.0	0.0	0.0	0.0

W2 GEV*2
1.0

Total virtual photoabsorption cross-section

[illegible]